

*Imperial College London
Department of Surgery and Cancer*

Cable-Driven Parallel Mechanisms for Minimally Invasive Robotic Surgery

Timo Joric Corman Oude Vrielink
January 2019

Submitted in part fulfilment of the requirements for the degree of
Doctor of Philosophy in Surgery and Cancer of Imperial College London
and the Diploma of Imperial College London

Declaration

This thesis contains original work from the author and any work that is not from the author is referenced accordingly.

The copyright of this thesis rests with the author. Unless otherwise indicated, its contents are licensed under a Creative Commons Attribution-Non Commercial 4.0 International Licence (CC BY-NC).

Under this licence, you may copy and redistribute the material in any medium or format. You may also create and distribute modified versions of the work. This is on the condition that: you credit the author and do not use it, or any derivative works, for a commercial purpose.

When reusing or sharing this work, ensure you make the licence terms clear to others by naming the licence and linking to the licence text. Where a work has been adapted, you should indicate that the work has been changed and describe those changes.

Please seek permission from the copyright holder for uses of this work that are not included in this licence or permitted under UK Copyright Law.

Timo Joric Corman Oude Vrielink

Abstract

Minimally invasive surgery (MIS) has revolutionised surgery by providing faster recovery times, less post-operative complications, improved cosmesis and reduced pain for the patient. Technological developments in MIS are focused on further decreasing the invasiveness of procedures, by using yet smaller and fewer incisions or using natural orifices as entry point, while expanding the number of therapies that can be performed minimal invasively. These developments include surgical robotics with novel sensing technologies, control methods and mechanical designs. However, many robotic systems still suffer from technical challenges such as sufficient instrument dexterity and payloads, leading to limited adoption in clinical practice.

Cable-driven parallel mechanisms (CDPMs) have unique properties, which can be used to overcome existing challenges in surgical robotics. These beneficial properties include high end-effector payloads, efficient force transmission and a large configurable instrument workspace. However, the use of CDPMs in MIS is largely unexplored. This thesis is dedicated to exploring the use of cable-driven parallel mechanisms for minimally invasive robotic surgery, through the development of multiple prototypes. The developed prototypes are used to demonstrate different minimally invasive access methods in which CDPMs are introduced into the body. The ESD CYCLOPS is a bimanual robot for flexible endoscopic surgery in the gastrointestinal tract. The prototype has been evaluated during benchmarking and *in vivo* porcine studies and demonstrates the ability to provide high dexterity and high end-effector payloads in tortuous anatomical pathways. A second prototype, CDAQS, was developed to demonstrate the use of CDPMs for estimating end-effector forces for application in haptic feedback. The system was evaluated during a palpation user study with 21 surgical trainees and demonstrated that haptic feedback could be used to increase the nodule detection rate. As CDAQS was developed as a lab-based system, a third prototype was developed to provide the benefits of haptic feedback to MIS: SIMPLE. This system provides a second MIS access method by using multiple microports to directly guide the cables through tissue into the body. Similar to multi-port laparoscopic surgery, the port positions can be configured to ensure adequate workspace for the surgical procedure. SIMPLE has been evaluated for the use in an automated raster scan to identify tissue stiffness. A third access method is shown in which two other proof-of-concept systems, the

neuroCYCLOPS and the microCYCLOPS, use a tubular tissue retractor to create a MIS pathway into the body. Additionally, an optimisation method has been developed in which CDPMs are configured to comply with clinical workspace requirements and constraints.

The research presents the first structured exploration of CDPMs for MIS. By focusing on the minimally invasive access method, the thesis provides a framework, which can be used by researchers, engineers and clinicians to identify future opportunities of CDPMs in MIS. The prototypes demonstrate that this type of mechanism has several key advantages for surgical applications in which haptic feedback, safe automation or a high payload are required. These advantages, combined with the different access methods, demonstrate that CDPMs can have a key role in the advancement of MIS technology.

Acknowledgements

I would like to express my sincere gratitude to Dr George Mylonas and Professor the Lord Ara Darzi for the unique opportunity to work in an inspirational environment on cutting-edge research within the field of surgical robotics. In particular I would like to thank Dr George Mylonas for his dedicated support during my PhD, and for being always open for new ideas. I would also like to thank the ERANDA Rothschild Foundation for providing the financial support required during this PhD.

I would like specially thank my academic 'brothers' at the HARMS Lab, Alexandros Kogkas, Ming Zhao, Mark Runciman, Fernando Avila-Rencoret for their friendship and mutual experiences, in both dinners, BBQs and drinks but also in late-night work sessions. Also, I would like to thank Mafalda Camara, James Dilley, Ismael Omar and Dr Philip Pratt for sharing the best office in London and for all the social events together.

I would also like to thank my family. I am very proud and grateful to have such an amazing and supportive family, and realize every day again how lucky I am with that. I would like to show special thanks for Sonja and Cees for being so supportive over the last few months of my PhD. Lastly I would like to thank uncle - well Tio - Tarpon for always being such a great source of inspiration.

Table of contents

Chapter 1	<i>Introduction</i>	28
1.1	A Brief History of Robotics in Surgery	28
1.1.1	Background technological developments	28
1.1.2	The development of minimally invasive surgery	29
1.1.2.1	Single-port surgery, Natural Orifice Endoscopic Surgery and Natural Orifice Transluminal Endoscopic Surgery	30
1.1.3	Early surgical robotic systems	32
1.1.4	Recent commercial developments	33
1.2	Motivation	34
1.3	Objectives	37
1.4	Overview of the proposed research method	37
1.5	Thesis Outline	38
1.6	Contribution	38
Chapter 2	<i>Cable-Driven Parallel Mechanisms</i>	40
2.1	Core Principle	40
2.1.1	Types of CDPM	41
2.2	Mechanics of CDPMs	42
2.2.1	Kinematics	42
2.2.2	Force equilibrium	44
2.2.3	Optimal Tension Distribution	44
2.2.4	Controllable Workspace	46
2.2.5	Workspace Calculation	47
2.3	Applications of cable-driven parallel mechanisms in different industries	48
2.4	Technical advantages of CDPMs	52
2.5	Limitations of CDPMs	53
2.6	Summary	55
Chapter 3	<i>End-effector mechanisms and actuation methods in Minimally Invasive Surgical Therapeutic Robotics</i>	56
3.1	Aims and scope of the literature review	56
3.2	Endoscopic Surgical Robotic Systems	58
3.2.1	Rigid Endoscopic Robotic System	59
3.2.1.1	Multi-port robotic systems	59
3.2.1.2	Single-port Surgical Robotic Systems	61

3.2.1.3	Robotic systems designed for higher payloads	66
3.2.2	Flexible Endoscopic Robotic Systems	68
3.2.2.1	Flexible robotic systems for Endoscopic Submucosal Dissection	74
3.2.2.2	Variable stiffness mechanisms	76
3.3	Other surgical robotic platforms.....	77
3.4	Overview of mechanical analysis	81
3.4.1	Endoscopic robotic systems	81
3.4.2	Other surgical platforms.....	83
3.4.3	Synthesis.....	83
Chapter 4	<i>ESD CYCLOPS for bimanual endoluminal surgery.....</i>	86
4.1	Clinical Background	86
4.1.1	Techniques for providing traction	88
4.1.2	Endoscope stabilisation	91
4.2	ESD CYCLOPS	92
4.3	Deployable Scaffold	96
4.3.1	Clinical requirements.....	96
4.3.2	Parametric design.....	98
4.3.3	Scaffold parameterization and instrument workspace	100
4.3.4	Overtube curvature	102
4.3.5	Scaffold parameters and manufacturing.....	104
4.4	Bench-testing	105
4.4.1	Force exertion.....	105
4.4.2	Control Accuracy	107
4.5	Pre-clinical validation	109
4.5.1	Ex vivo validation	109
4.5.2	In vivo validation	110
4.6	Discussion.....	112
Chapter 5	<i>Cable-driven parallel mechanisms with force-sensing capabilities</i>	114
5.1	Haptic feedback in minimally invasive surgery	114
5.2	The CDAQS system	119
5.2.1	System architecture.....	120
5.2.2	Control system.....	120
5.2.3	Force estimator	122
5.3	Benchmarking the CDAQS system for force sensing.....	123
5.3.1	Direct measurement on loadcell	123
5.3.2	Estimation on plain silicone phantoms	124
5.3.2.1	Repeated force measurements	126
5.3.2.2	Indentation depth.....	127

5.4	Palpation study	129
5.4.1	Blind palpation study.....	130
5.4.2	Visual-Haptic comparison study	131
5.4.3	Results	131
5.5	Discussion.....	132
Chapter 6	<i>SIMPLE: a CDPM for safe autonomous surgical tasks</i>	134
6.1	Autonomy in Surgery	135
6.1.1	Clinical need for autonomy	135
6.1.2	Levels of Autonomy	136
6.1.3	Autonomy in surgical robotics.....	137
6.2	Autonomous tasks using the CDAQS System	140
6.2.1	Positional accuracy	141
6.2.1.1	Step response	141
6.2.1.2	Linear motion	142
6.2.1.3	Circular motion	143
6.2.1.4	Repeatability task	144
6.2.2	Robustness analysis on positional accuracy	145
6.2.3	Raster scan	148
6.2.4	Overview of autonomous motions with CDAQS	148
6.3	The SIMPLE system	149
6.3.1	Prototype.....	150
6.3.1.1	Abdominal motor units	151
6.3.1.2	External Scaffold	152
6.3.1.3	Transperitoneal arm	153
6.3.1.4	Cable actuation and transmission	153
6.3.1.5	Actuation of the shaft.....	155
6.4	System Assembly.....	156
6.5	Validation	158
6.5.1	Feasibility of Intra-abdominal cable assembly	158
6.5.2	Benchmarking.....	159
6.5.3	Raster scanning	159
6.6	Discussion.....	162
Chapter 7	<i>Workspace optimisation for surgical applications</i>	167
7.1	Optimization Algorithm	167
7.2	Case study: procedure-specific optimization of the ESD CYCLOPS.....	168
7.2.1	Workspace optimization using a theoretical task space	170
7.2.2	Workspace optimization using a surgical task space	173
7.2.2.1	Collecting the task space	173
7.2.2.2	Recorded Data	174

7.2.2.3	Optimization results	175
7.2.3	Discussion ESD CYCLOPS optimization	176
7.3	Case Study: Patient-specific optimization of the SIMPLE system	178
7.3.1	Design vector and Objective function	180
7.3.2	Task space definition	182
7.3.3	Manual Configuration.....	184
7.3.4	Optimized Systems	185
7.3.5	Discussion of the SIMPLE Optimization	187
7.4	Conclusion.....	189
Chapter 8	<i>Research Synthesis and Discussion</i>	190
8.1	Development framework for cable-driven parallel mechanisms	190
8.1.1	End-effector Workspace Size	191
8.1.2	Minimally invasive access method	192
8.1.3	Framework synthesis.....	193
8.2	Discussion and future work.....	196
8.3	Conclusion.....	199
Appendices.....		201
A.1	Dimensions cable entry points of the ESD CYCLOPS.....	201
A.2	First generation scaffold of the ESD CYCLOPS	202
A.3	neuroCYCLOPS and microCYCLOPS	203
A.4	CYCLOPS da Vinci Instrument	206
A.5	Cable coordinates of the CDAQS system	209
A.6	The results of the subjective evaluation of the palpation study	210
A.7	Parametric fitting of the forward kinematics of the transperitoneal shaft	212
A.8	Algorithm structure used for workspace optimisation.....	213
A.9	Linear-least squares method for calculation of the robot-mounting point of the transperitoneal arm	214
A.10	Anatomical Landmarks selected using CT-images	215

List of Figures

Figure 1.1 - The results (publications and citations) of a search on the topic Natural Orifice Transluminal Endoscopic Surgery in the Web of Science database (performed 27 December 2018).	32
Figure 1.2 – (a) The da Vinci® Xi system at the patient side. ©2019 Intuitive Surgical, Inc. (b) The surgeon seated at the console. ©2019 Intuitive Surgical, Inc. (c) The endoWrist® articulated tip. ©2019 Intuitive Surgical, Inc.	33
Figure 1.3 – The first prototype of the CYCLOPS system in 2014. A six-cable CDPM is used to control the overtube in 5 degrees of freedom.[34] ©2014 IEEE	35
Figure 1.4 – Three CDPMs developed for MIS. (a) The planar wire robot developed for epicardial MIS [37]. (b) The Light Endoscope Robot (LER) using a CDPM for orientation of an endoscope. Image source: [38]©2002 IEEE. (c) The MRI compatible planar CDPM used for positioning a biopsy needle [36] ©2008 IEEE.	36
Figure 1.5 - An artistic representation of a bimanual version of the CYCLOPS system for flexible endoscopy.	37
Figure 2.1 – The core concept of the cable-driven parallel mechanisms.	41
Figure 2.2 – Types of CDPM: fully constrained (a) , cable-suspended (b) , hybrid (c) and multi-link (d) .	41
Figure 2.3 - The vectors used for the derivation of the kinematics.	43
Figure 2.4 – (a) The NIST robocrane [1] used for painting airplanes. Image courtesy: N.E. Wasson Jr./US Technologies. (b) A CDPM used for 3D printing. Image courtesy: IAAC - Institute for Advanced Architecture of Catalonia (c) The IPAnema robot suggested for placement of solar panels[25]. Image courtesy: Fraunhofer IPA. (d) The CableRobot for simulation purposes. Image courtesy: Fraunhofer IPA, Philipp Miermeister.	48
Figure 2.5 - (a) The Skycam [30] used for broadcasting sport events. Image source: [50](b) A CDPM used for the digitizing of 3D objects [51]. ©2007 IEEE (c) A small scale model of the FAST radiotelescope, which has been built in China in 2016. Image source: [52].	50
Figure 2.6 – (a) The IPAnema 3 robot used for haptic feedback [57]. (b) A planar upper limb rehabilitation device for on desktops [55]. (c) The String-man for gait rehabilitation [39]. ©2007 IEEE. (d) The CAREX exoskeleton using a hybrid CDPM for upper limb rehabilitation. Image source: [58]. ©2015 IEEE (e) The NeReBot for upper limb rehabilitation. Image source: [40]©2005 IEEE (f) A multi-link CDPM for lower limb rehabilitation [56]. ©2015 by ASME	51

Figure 3.1 – Three different types of remote-centre of motion mechanisms used for minimally invasive surgery. (a) a double parallelogram RCM mechanism. Image source: [20]©2015 by ASME. (b) spherical RCM mechanism. Image source: [21]©2006 IEEE. (c) a ‘virtual’ RCM in which a robotic arm is constrained at a fixed point. Image source: [22] ©2007 IEEE.	60
Figure 3.2 – (a) The VeSPA instruments (Intuitive Surgical, Inc.). Image source: [33]. (b) The LER system adapted by Berkelman et al. for single-port robotic surgery. Image source: [36].	62
Figure 3.3 – (a) The system developed by Choi et al. with a modified elbow joint for high end-effector payloads [37]. ©2014 IEEE. (b) The da Vinci SP® end-effector (Intuitive Surgical, Inc.). Image source: [38]. (c) The HVSPS developed at TU München [39].	63
Figure 3.4 – Two single-port systems using continuum mechanisms as manipulators. (a) the SPORT system. Image courtesy: Titan Medical, Inc. (b) The SURS system [48] ©2015 IEEE.	65
Figure 3.5 – Three different designs with a parallel structure to provide higher forces at the instrument tip. (a) The PLAS system for single-port surgery with high force requirements uses a parallel plate spring [58]. (b) A single port system with parallel links at the joints to enable forces up to 15 Newton [59]. (c) The double-screw drive mechanisms used developed at Waseda University to provide high stiffness articulated joints [61] ©2007 IEEE.	67
Figure 3.6 – (a) Endosamurai system (Olympus Corp., Japan). Image source: [70]. (b) The R-Scope (Olympus Corp., Japan). Image source:[77] . The Anubiscope (IRCAD & Karl Storz Endoskope). Image source: [75].	69
Figure 3.7 – (a) Medrobotics Flex® Robotic System . Permission for use of image granted by Medrobotics Corporation. (b) The Cobra system (USGI Medical, Inc.). Image source: [83].(c) the DDEST™ system developed by Boston Scientific Corp. Image Source: [69].	70
Figure 3.8 – (a) The MASTER system developed by Phee et al. [91] ©2009 IEEE. (b) The laser sintered flexible robot developed by the MiMed group, TU München [92]. Image Source: [93] ©Feussner et al.	71
Figure 3.9 – The two components of the system designed in collaboration with Samsung [98] (a) The joints design used to increase the joint stiffness and payload. Image source: [98]. (b) The variable stiffness flexible shaft with the instruments mounted on it. Image source: [99].	73
Figure 3.10 – (a) The system developed by Lehman et al. which is anchored on the inside wall of the peritoneum. Image source: [104]. (b) The reconfigurable concept using several modules developed by Harada et al. [106] ©2009 IEEE (c) The reconfigurable system earlier developed by Harada et al., developed with magnetic anchoring to the peritoneum [107] ©2012 IEEE.	74
Figure 3.11 – Three devices developed for ESD procedures. (a) The LumenR™ Tissue Retraction System (Boston Scientific Corp., USA). Image source: [111]. The Endolifter (Olympus Corp., Japan). Image source: [112]. (c) The articulated instruments developed at Kyushu University, Japan [113]. .	75

Figure 3.12 – Two MRI compatible robot systems for prostate interventions. (a) The MIRIAM robot. Image courtesy: DEMCON Advanced Mechatronics BV. (b) The MrBot [130]. Reprinted with permission of MedReviews®, LLC. Mozer PC, Partin AW, Stoianovici D. Robotic image-guided needle interventions of the prostate. Rev Urol. 2009;11(1):7-15. All rights reserved.	78
Figure 3.13 – Different configurations of CRISP [138]. The straight needle instruments have hooks at the end which are used to attach the needle to the continuum flexible shaft, thereby becoming a parallel assembly ©2016 IEEE.	80
Figure 3.14 – An overview of mechanisms used for MIS based on the findings from literature.....	84
Figure 4.1 – (a) Endoscopic Mucosal Resection and (b) Endoscopic Submucosal Dissection.....	87
Figure 4.2 – A number of clinical techniques used for providing tissue traction during ESD. (a) The clip-and-line method. Image source: [19]. (b) The clip-and-line method with an additional clip to redirect the cable. Image source: [18]. (c) The S-O clip using a spring and two clips. Image source: [21].(d) The ring-shaped thread method developed by Mori et al. [23] (e) The hybrid percutaneous method in which a clip-and-line is used combined with a small needleport to provide traction.[24] (f) The cross-counter technique developed by Okamoto et al. [25].	89
Figure 4.3 – The DiLumen C2™ system for ESD. Image courtesy: Lumendi Ltd.	92
Figure 4.4 – The ESD CYCLOPS. Top-left: The scaffold containing the endoscope and the two overtubes controlled by CDPMs. Flexible instruments are inserted into the overtubes to perform surgery. ©2018 IEEE. Bottom-left: The undeployed scaffold. The scaffold is placed directly after the steerable tip of the endoscope during navigation. Right: The components of the system. (A) The scaffold covered by a soft silicone sleeve. (B) Bowden cables used to guide the actuation cables and the flexible instruments along the endoscope. (C) The endoscope. (D) A flexible needle is inserted into the endoscope’s working channel and used to lift the mucosa by injecting a liquid. (E) The diathermy instrument. (F) A cable splitter. (G) A motor unit containing 6 motors. (H) Mechanism for opening and closing of the grasper. ©2018 IEEE.	93
Figure 4.5 – An overview of the hardware of the ESD CYCLOPS. ©2018 IEEE.....	95
Figure 4.6 – The inflatable scaffold which is an alternative approach to the ESD CYCLOPS scaffold presented in this chapter. ©2018 IEEE.	96
Figure 4.7- The bowel’s tortuosity varies strongly between patients, as shown in the 3D segmentations of CT-scans. Image source: [52].....	97
Figure 4.8 – The scaffold design and parameters used to adjust the system to clinical requirements.....	99
Figure 4.9 – The workspace for scaffold thickness t , corresponding to a colon diameter of 50mm (Transverse, American).	101
Figure 4.10 – The relationship of the scaffold circumference to workspace.....	101
Figure 4.11 - The workspace for different height-to-width ratios.	101

Figure 4.12 – The workspace for $r = 0.5$ (left) and $r = 1.0$ (right) with the tension factor as isolines. The dots indicate the reachable poses by both instruments. The red circle is as reference for a 20mm diameter lesion. The circumference used represents the mean diameter of American transverse colon.	102
Figure 4.13 – The curvature in the overtube is defined by the angle required for the tip to reach a point 15mm in front of the scaffold from a chosen homing pose ζ_h	103
Figure 4.14 - The workspace for curvatures determined by $y_{com} = [0, 0.05, \dots, 0.5]w$. The vertical lines indicate the y_{com} for the geometric centre and at $y_{com} = w/4$	103
Figure 4.15 – The workspace of both instruments when determining the curvature with y_{com} at $0.3w$, $0.4w$ and $0.5w$ (left to right)	103
Figure 4.16 – The workspace of the left (green) and right (blue) instrument. A 20mm red circle is used to simulate a lesion.	104
Figure 4.17 – The scaffold undeployed (left) and deployed (right).....	105
Figure 4.18 – The setup used for measuring the forces with the loadcell (A) and the clamped overtube (B). The images show the clamping method for the straight overtube (left) and overtube with straight angles representing the curved (right). ©2018 IEEE.....	106
Figure 4.19 – Each of the cable forces and the measured end-effector force using the Nano17. The data shown is for a straight overtube with a motion from the workspace boundary into the x +direction. ©2018 IEEE.	106
Figure 4.20 – Left: The setup for the tracing task. Right: The results of the 7 users. The bottom-right task is performed by participant 4 on the da Vinci robot. ©2018 IEEE.	108
Figure 4.21 – (a,b) ESD performed on chicken skin. (c) The endoscope with the undeployed scaffold on it before insertion into the porcine stomach. (d) The insufflated stomach with the scaffold inserted. (e) ESD performed in the stomach. (f)The dissected mucosa of the stomach.	109
Figure 4.22 – The first animal trial with the scaffold partly deployed, showing a clear view of the gastrointestinal tract and the setup. ©2018 IEEE.....	110
Figure 4.23 – The second animal trial. (a) The scaffold fully deployed. (b) The marking of the lesion. (c) The flexible needle is inserted into the endoscope’s working channel, and shown here while injecting underneath the mucosa of the marked lesion. (d) Circumferential dissection of the marked lesion. (e) The dissection just before perforation of the bowel. (f) The bowel collapses inwards due to the loss of pressure.	111
Figure 4.24 - The addition of a serial link should contribute to an increase of workspace.	112
Figure 5.1 - Different locations at which force sensors are placed to measure forces at the instrument tip.....	116

Figure 5.2 – Using a parallel structure to enable accurate force sensing at the proximal end of the instrument [7] ©2018 IEEE.	116
Figure 5.3 – The DLR Mirosurge system. The centre image shows the articulated end-effector mounted on a Stewart-Gough platform (Right). Each of the links of the Stewart Platform has a strain gauge used to sense forces in 6 DoF at the instrument tip. Image sources: [13][14].	117
Figure 5.4 – The CYCLOPS dVI, in which the CDPM is used integrated into a surgical instrument mounted on the da Vinci robot. Image source: [17]. Left: The system mounted on the da Vinci Robot. Right: The end-effector with endoscopic probe, controlled with a planar CDPM.....	118
Figure 5.5 – (a) The CDAQS system with 6 actuation cables to provide 5 DoF. (a) The aluminium frame used for mounting of the motors and the endoscope. (c) One of the motor units, showing the cable pathway from the cable spool to the end-effector. Image source: [18].....	119
Figure 5.6 – Schematics of the control architecture implemented in the CDAQS system. Image source: [18].	121
Figure 5.7 – The end-effector force estimation compared to a ground truth loadcell, here shown for control setting CS2. <i>F_{est}, comp</i> represents the force estimation when the pose that is tracked by an a tracker systemImage source: [18].	123
Figure 5.8 – The controller values for each motor while exerted forces on the loadcell, here shown for control setting CS1.5.	124
Figure 5.9 - The measured and estimated forces for the hard and soft silicone phantoms (Sylgard and Ecoflex, respectively). The accuracy of the estimation is visible in the ratio between the measured and the estimated forces.	125
Figure 5.10 – The measured displacement of the end-effector for commanded velocities.....	126
Figure 5.11 – The estimated stiffness based on the measured displacement and the estimated forces.	126
Figure 5.12 – The consecutive repeated (n = 10) force estimation and measurement for CS2 at 1mm/s on the Sylgard phantom.....	127
Figure 5.13 - The force estimation of <i>F_{est}</i> with the mean and range of $[-2\sigma, 2\sigma]$ at different velocities (n = 10).	127
Figure 5.14 – The controller with control settings CS2 on the Ecoflex 00-30 phantom at different indentation depths. Each indentation is a 2mm increment increase of the previous, hence the 20th is an indentation input of 40mm depth.....	128
Figure 5.15 – The cable tension during indentations (see Figure 5.14) of cables 3 and 4. Cable 3 has the lowest tension overall, displaying slackness at around the 17th indentation. Cable 4 has the highest measured tensions, which remains below the total estimated force.....	128

Figure 5.16 – The ratio between the estimated and measured forces. The encircled data points represent indentation depths where at least one cable shows slackness.....	129
Figure 5.17 – The first indentation steps of the IDC controller on ecoflex.	129
Figure 5.18 – (a) The experimental setup for the palpation user study. Covering the aluminium frame during the user study prevents direct vision of the probe. (b) The haptic device in an upright position. A silicone phantom and the probe are shown in the display. Image source: [18].....	130
Figure 6.1 - The CDAQS system with markers placed on the ports and end-effectors.....	141
Figure 6.2 – The circular task (blue) shown for three repetitions with controller settings $GPD = 1.0$. The end-effector pathway shows a high repeatability as the three separate circles cannot be distinguished visually. The pathway shows deformation of the circle towards an ellipse. The fitting of the ellipse is so accurate that the ellipse is hidden behind the pathway, making only the axes of the ellipse visible.	143
Figure 6.3 – The 3D position of the end-effector during the repeatability task of 100 random motions. All dimensions given are in metre.	145
Figure 6.4 – The linear trajectory of the instrument to singularity planes.	146
Figure 6.5 – The tension factor as part of the linear motion from the centre of the scaffold to the singularity. Blue: raw data. Red: the moving average over 50 samples.	146
Figure 6.6 - The linear motions at different x starting positions. The singularity plane lies around $x = 70$ and this can be seen in the motion along the x -axis when reaching this plane. All dimensions are in millimetre.	147
Figure 6.7 – The circular task at different heights cx in the workspace. The upper-most circle ‘hits’ the singularity plane, shown by the difference in the shape. All dimensions are in millimetre.	147
Figure 6.8 – Raster scan on the phantoms used in the user study presented in chapter 5. The color of each pixel represents the estimated force at a specific indentation. The indentation are performed along the x -axis, resulting in a 35x35 grid with a spatial resolution of 2mm on the YZ -plane. Image source: [39].....	148
Figure 6.9 – The main concept of SIMPLE.	150
Figure 6.10 - The SIMPLE prototype shown from the outside (left) and from the inside (right).....	150
Figure 6.11 –The abdominal motor unit and its components. The cable pathway (red) is guided into the abdomen via a single pulley. The RCM is mounted on the scaffold.	151
Figure 6.12 – The RCM mechanism adapted from [43]. Rotation around the two axes is used to set the orientation. The images on the right show the cross-section for an RCM at 5mm and 15mm depth.	151

Figure 6.13 – The scaffold made with thermoplastic materials. The position of the scaffold and each of the ports is calibrated using passive optical trackers.	152
Figure 6.14 - The transperitoneal arm shown attached to the UR5 robot (left) and when placed into the scaffold (right).	153
Figure 6.15 - Pathway (in red) for the first and second cables through the transperitoneal arm.	154
Figure 6.16 – Pathway of cable 3, placed at the entry port of the transperitoneal arm.	154
Figure 6.17 - The transmission mechanism for articulation of the tip of the transperitoneal arm. ...	155
Figure 6.18 – Two different approaches to connect the cables. (a) “inside-out”: a device is used to insert the port in the desired position and couple the cables outside of the body. (b) “Outside-in”: the cable with a barbed-tip is inserted into the microport and manipulated with a U-shaped shaft. A mechanism, such as seen in the Capio OPEN ACCESS is used to connect the cable to the overtube.	157
Figure 6.19 – Stills of the video assembly method using the brass insertion tool. The video shows the second attempt to connect two cables, which took 59 seconds at the second attempt.	158
Figure 6.20 – The force estimation (red) compared to the ground truth measurements (blue), for motions in the X+, Y+ and Y- directions, respectively.	159
Figure 6.21 – The setup used for the raster scan. A loadcell is used at the base of the pillar for measuring the ground-truth forces.	160
Figure 6.22 - Silicone/PLA phantom used for the staircase experiments.	160
Figure 6.23 – Comparison between the loadcell measurements (A) and the force estimation (B) of the same raster scan. The difference between both force maps is shown in (C) and is calculated as $\Delta F = F_{est} - F_{meas}$. The force map is 25x25 pixels for the raster scan with a 1mm resolution.	160
Figure 6.24 - The raster scan performed on each letter. The top row shows the CAD model used to create the phantoms, the middle row shows the force images as collected with the system. The bottom row shows the fitting of affine transformation of the contours of the letters to points in the dataset. The parameters for the affine transformation are shown in Table 6.11.	162
Figure 6.25 – Possible configurations for using SIMPLE in NOTES: (a) Endoscope stabilisation. (b) A combination of endoscope stabilisation with additional cable-driven elbow joints to provide high forces and sufficient stiffness during manipulation.	165
Figure 6.26 – An example of a cable-suspended CDPM used for tissue retraction.	166
Figure 7.1 – The definition of the dimensions for the design vector.	169
Figure 7.2 – The objective function used for the optimization of the ESD CYCLOPS.	170
Figure 7.3 – The optimized systems with the theoretical ESD task space shown in blue. The workspace of the left and right instruments are yellow and red, respectively. In all cases, an outer circumference	

equal to a 70mm diameter colon was used. All dimensions in the figures are in millimetres. The percentage of the task space reached and the workspace volumes are shown in Table 7.1. **(a)**, **(b)** and **(c)** are the systems found for optimization for a 20mm, 30mm, and 40mm lesion. **(d)** is the combined system using the left instrument of configuration (a) and the right instrument of configuration (c). 171

Figure 7.4 – Side view of the **(a)** left and **(b)** right cable configurations of the combined optimized system (Figure 7.3d). All dimensions are in millimetres. 173

Figure 7.5 – The aluminium rig used for the collection of the task space. A dummy task space is shown in the figure; this was used for early validation of the algorithm before proceeding to the data collection during an ESD with ex vivo tissue. 174

Figure 7.6 – The modified instruments used for data collection. The top instrument was used for diathermy cutting, and the bottom instrument for grasping. 174

Figure 7.7 – The motor unit used for the CYCLOPS system was used for actuation of the grasper. ... 174

Figure 7.8 – The data collection of the ESD task on ex vivo chicken tissue. 175

Figure 7.9 – The forces at the tip of the grasper (left instrument) along the x, y, z axes. 175

Figure 7.10 – The 3D pointcloud of each of the instruments during the simulated ESD task. All dimensions are in millimetre. 175

Figure 7.11 – The yaw, pitch and roll of the instruments (**top**: left instrument, **bottom**: right instrument). 175

Figure 7.12 – The systems optimized using the recorded task space. The workspaces without external forces of the left and right instrument are indicated in green and yellow, respectively. The percentages of the task space and the workspace volume are shown in Table 7.2. All dimensions are in millimetres. **(a)** The configuration found for single-curved instruments and a scaffold designed for a 70mm diameter colon. **(b)** The configuration found for a 70mm diameter colon with double-curved instruments. **(c)** The double curvature optimized configuration for a 60mm diameter colon. 176

Figure 7.14 – The left instrument (grasper) of the single curvature configuration placed at a specific position of the recorded task space. 177

Figure 7.14 – The STL files obtained from the pneumoperitoneal simulation study. 179

Figure 7.15 – Schematics used for the calculation of the cable entry points on the transperitoneal arm. 179

Figure 7.17 – The objective function used for optimization of the SIMPLE system. 182

Figure 7.17 – The fitting of the abdominal wall inner surface (left) and the viscera (right). All dimensions are in millimetre. 183

Figure 7.18 – The axial (left) and sagittal planes indicating a point on the right liver lobe, left medial section.	183
Figure 7.19 – The parameterized surfaces and landmarks Appendix (A), Umbilicus (Um), Right Renal Hilum (RRH), Left Renal Hilum (LRH), the selected point on the liver (L) and the cystic duct of the gallbladder (G). All dimensions are in millimetre.....	184
Figure 7.20 – The manual configured system, optimized for the selected point on the surface of the liver. A 60mm sphere is shown in the figure as task space. All dimensions are in millimetre.....	184
Figure 7.21 – Manual configuration for a bimanual system for the reaching of points on the liver surface. The workspace of the left and right instrument are shown in red and purple, respectively. The peritoneum and the abdominal viscera are shown in light grey and green, respectively. The dimensions are given in millimetre.	185
Figure 7.22 – The single-instrument system which was optimized using a task space positioned at the selected point on the liver. All dimensions are in millimetre.	186
Figure 7.23 – Results found for an optimized bimanual system. All dimensions are in millimetre. ...	186
Figure 7.24 – The system in a configuration in which the overtube is reversed. Note that in this case cables 2, 4 and 6 are the rear cable, as opposed to the systems shown in earlier optimizations.....	187
Figure 7.25 – An optimized configuration when the visceral surface constraint is removed.....	188
Figure 8.1 – An overview of the CDPM prototypes.....	191

List of Tables

Table 2.1 – A summary table of the technical advantages and limitations of CDPMs.....	55
Table 3.1 – An overview of endoscopic robotic systems found in literature. Multiport systems and other systems for which insufficient technical information was found are omitted from the table. The term “snake-like” is used when there is redundancy in the DoF but no explicit technical description of the mechanism is found. Such mechanisms are therefore either a continuum or a serial redundant mechanism. *Theoretical payload. ** payload without any increase in positional error. ***Measured for a single segment. **** Calculated for the forces at tip of single section, using theoretical joint torque. *****Measured for a single joint at 75mm distance.....	82
Table 4.1 - Each anatomical section of the colon with the length and diameter in an American and Japanese study. For each section the percentage of non-polypoid lesions and ESDs are included. The two right columns indicate the percentage of non-polypoid lesions found and ESDs performed at each section.....	98
Table 4.2 - The workspace volume, overlap and surface area at the tissue plane. The circumference is calculated based on the mean diameter of the Sigmoid (S), Descending Colon (D) and Transverse (T) of the Japanese population, using the Transverse and Ascending Colon (A) for the American population (See Table 4.1). Rather than the cecum, the P95 percentile ($P95 = \mu + 2\sigma$) of the ascending bowel is used as the largest diameter.....	102
Table 4.3 – Parameters of the final scaffold design.	104
Table 4.4 – The dimensions of the scaffold when deployed and undeployed.....	104
Table 4.5 - The measured forces at the tip of a straight and curved overtube.	105
Table 4.6 – The results of the ellipse tracing task ($n = 7$). Values are the same as [63].....	108
Table 5.1 – The dimensions and properties of the CDAQS system. Table is adopted from [18].	120
Table 5.2 – The comparison between ground truth measurement and the force estimation for different control settings.	123
Table 5.3 - The range of means and standard deviations found for F_{est} and F_{meas} for each of the velocities [1,5,10,20,50] mm/s.....	127
Table 5.4 – The results of the blind palpation study. The first and second trials are compared statistically, using the Wilcoxon Signed-rank for the nodule detection rate and the repeated-measures t-test for the maximum indentation forces. Normality of the distribution of the forces has been confirmed with the Shapiro-Wilk test.	132

Table 5.5 – The quantitative results of the visual-haptic comparison study. The first and second trials are compared statistically, using the Wilcoxon Signed-rank test for the nodule detection rate and the repeated-measures t-test for the maximum indentation forces and completion time. Normality of the distribution of the forces and the completion time was confirmed using the Shapiro-Wilk test.	132
Table 6.1 - The step response for different controller settings, with steady state error ε , rise time tr and settling time ts	142
Table 6.2 - The accuracy of the linear motion, shown in the length of the path and the RMSE for different control modes.	142
Table 6.3- Accuracy of the circular motion around the X-axis, starting from centre of scaffold ($X0 = [0,0,0,0,0,0]$).....	143
Table 6.4 - Accuracy of the circular motion for $GPD = 1.0$ around x,y,z axis.	144
Table 6.5 - The mean and standard deviation of a repeated repositioning task at different control conditions (n= 100).....	145
Table 6.6 - The accuracy of the linear motion in x,y,z direction at different heights cx in the workspace.	146
Table 6.7 - The tensions factor for each circular motion at different proximities to the singularity plane at $cx = 70mm$	148
Table 6.8– Dimensions of the values given in equations (6.1)-(6.2) and Figure 6.17.	156
Table 6.9 - The ratio for the maximum measured and estimated forces $r = \frac{maxF_{est}}{maxF_m}$ at different linear velocities.	159
Table 6.10 - The average value for each step (inner 8x8 samples) and the difference between the measured and estimated value.	161
Table 6.11 - The fitted parameters for affine transformation of the reference image to the force map, as described in eq.(6.7) and (6.8). $c1$ and $c2$ represent scaling on the x and y-axis, respectively.	162
Table 7.1 – The optimized systems for 20,30 and 40mm lesions. As a comparison, the 20mm lesion is included of the ESD CYCLOPS, as configured in chapter 4. For each instrument, the combined system uses the configuration from the optimization which has the largest workspace volume, and therefore uses the left instrument configuration found for 20mm optimization and the right instrument configuration for 40mm optimization.....	172
Table 7.2 – The size of the workspace and the percentage of the task space for the optimized configurations shown in Figure 7.12.	176
Table 7.3 – The results of the manually configured single and double instrument system when targeting a selected point on the liver surface. All dimensions are in millimetre.	185

Table 7.4 – The optimized system for a 30mm sphere placed at the selected position on the liver surface. The workspace was evaluated for 30mm, 60mm, and 80mm task spaces.	186
Table 8.1 – The CDPM prototypes categorized according to type of pathway and workspace size (WS) relative to entry port size A_{entry} . The colours indicate systems which can be used for force-sensing (blue), systems that require a scaffold that is deployed/assembled (yellow), or both (green).....	194
Table 8.2 – The classification of several minimally invasive access methods using the same principles as the grid presented above in Table 8.1.	195

List of Acronyms

3D	<i>Three Dimensional</i>
CDAQS	<i>CYCLOPS Data Acquisition System</i>
CDPM	<i>Cable-driven Parallel Mechanism</i>
COM	<i>Centre of Motion</i>
CT	<i>Computer Tomography</i>
CYCLOPS dVI	<i>CYCLOPS da Vinci Instrument</i>
DoF	<i>Degree of Freedom</i>
dVRK	<i>da Vinci Research Kit</i>
EMR	<i>Endoscopic Mucosal Resection</i>
ESD	<i>Endoscopic Submucosal Dissection</i>
ESTD	<i>Endoscopic Submucosal Tunnel Dissection</i>
GI	<i>Gastrointestinal</i>
IK	<i>Inverse Kinematics</i>
LESS	<i>LaparoEndoscopic Single-site Surgery</i>
MIS	<i>Minimally Invasive Surgery</i>
MRI	<i>Magnetic Resonance Imaging</i>
NHS	<i>The British National Health Service</i>
NOES	<i>Natural Orifice Endoluminal Surgery</i>
NOTES	<i>Natural Orifice Transluminal Endoscopic Surgery</i>
OR	<i>Operating Room</i>
OTD	<i>Optimal Tension Distribution</i>
PC	<i>Personal Computer</i>
PD	<i>Proportion-Derivative</i>
PLA	<i>Polylactic Acid, a thermoplastic used for 3D printing.</i>
POEM	<i>Peroral endoscopic Myotomy</i>
RMIS	<i>Robot-Assisted Minimally Invasive surgery</i>
RMSE	<i>Root-Mean Square Error</i>
SBC	<i>Single-board Computer</i>
SILS	<i>Single-Incision Laparoscopic Surgery</i>
SIMPLE	<i>Single-Incision MicroPort LaparoEndoscopic</i>
SMA	<i>Smart-Memory Alloy</i>
SPAS	<i>Single-Port Access Surgery</i>
SPS	<i>Single-Port Surgery</i>
TEMS	<i>transanal endoscopic microsurgery</i>
TEO	<i>Transanal Endoscopic Operation</i>

<i>TF</i>	<i>Tension Factor</i>
<i>TORS</i>	<i>Transoral Robotic Surgery</i>
<i>UDP</i>	<i>User Datagram Protocol</i>
<i>vNOTES</i>	<i>transvaginal NOTES</i>

List of Mathematical Symbols

n	Number of cables
m	Number of controllable degrees of freedom
i	Cable index number
ζ	End-effector pose
l_i	Length of cable i
$\vec{p}_i, \vec{p}_{i,g}$	Vector of the attachment point of cable i in the local reference frame of the end-effector and the global reference frame, respectively. $\mathbb{R}^{3 \times 1}$
P	Matrix containing the n global cable attachment points $\vec{p}_{i,g}$, $\mathbb{R}^{3 \times n}$
\vec{b}_i	The scaffold entry point of cable i in the global reference frame, $\mathbb{R}^{3 \times 1}$
B	Matrix containing the n global cable entry points, $\mathbb{R}^{3 \times n}$
\vec{v}_i	Vector representing the actuation cable i from the global attachment point $\vec{p}_{i,g}$ to the entry point \vec{b}_i
\vec{u}_i	The normalized cable vector \vec{v}_i
R	Rotation matrix $\in \mathbb{R}^{3 \times 3}$
A	Structure matrix $\in \mathbb{R}^{6 \times n}$
J	Jacobian matrix ($J = A^T$)
t_i	Tension in cable i
\vec{t}	Cable tension vector $\in \mathbb{R}^{n \times 1}$
$\vec{t}_{min}, \vec{t}_{max}$	Vectors containing the minimum and maximum allowable cable tensions, respectively. $\in \mathbb{R}^{n \times 1}$
\vec{w}	External wrench vector on the end-effector $\in \mathbb{R}^{6 \times 1}$
\vec{F}_{ext}	External force vector on the end-effector $\in \mathbb{R}^{3 \times 1}$
K	Stiffness matrix $\in \mathbb{R}^{6 \times 6}$
Ω	Diagonal matrix with cable lengths l_i
ρ	Radius of the cable spool
q_i	Rotational angle of the cable spool
τ	Torque exerted on the cable spool shaft
V_t, V_o	Total and overlapping volume of the end-effectors workspace, respectively
A_s	Overlapping surface area of the end-effector workspace at a given plane

List of Publications

Saracino*, A, Oude Vrielink*, TJC , Menciassi, A, Sinibaldi, E , Mylonas, G. *Haptic intracorporeal palpation using a cable-driven parallel robot: a user study*, IEEE Transaction on Biomedical Engineering, submitted.

Contributions: *Technical development of the CDAQS system, including the modification of the software code (see description below regarding the SIMPLE system) to enable force sensing and a GUI for use during the user study and benchmarking. Additionally, I applied for the ethics and recruited the participants. The preparation of the user studies, the experiments themselves and the documentation was in close collaboration with Arianna Saracino.*

Fathi, J, Oude Vrielink, TJC, Runciman, M, Mylonas, G. *A Deployable Soft Robotic Arm with Stiffness Modulation for Assistive Living Applications*, IEEE International Conference for Robotics and Automation (ICRA 2019), *accepted*.

Contributions: *Supervision of the student Johnny Fathi during his MRes thesis.*

Oude Vrielink, TJC, Darzi, A, Mylonas, G. *A SIMPLE surgical robot concept: a bimanual single-port system with intrinsic force-sensing capability*, 8th Joint Workshop on New Technologies for Computer/Robot Assisted Surgery (CRAS) 2018.

Contributions: *Idea conception, technical development and early stage validation of the SIMPLE system. Technical development included the full design and manufacturing of the system. Additionally, the software was rewritten from the ground-up with a new software architecture which is soft real-time (Linux-based), modular for other CDPM mechanisms (e.g. CDAQS) and can be easily extended by new classes and hardware when required.*

Oude Vrielink*, TJC, Gonzalez-Bueno Puyal*, J, Kogkas, Mylonas, G. *Intuitive gaze-control of a robotized flexible endoscope*, IEEE/RSJ International Conference on Intelligent Robots and Systems (IROS 2018), 1-5 October 2018.

Contributions: *Technical benchmarking of the system, documentation and presentation. The system was part of the MRes thesis of Juana Gonzalez-Bueno Puyal, who I supervised and provided with technical assistance.*

Oude Vrielink, TJC, Patel, N, Darzi, A, Mylonas, G, *The CYCLOPS Robotic system for Endoscopic submucosal dissection of gastrointestinal cancers*, International Congress of the European Association of Endoscopic Surgery (EAES 2018), June 2018, London, UK.

Contributions: *Technical research and development, abstract writing and presenting.*

Oude Vrielink, TJC, Zhao, M, Darzi, A, Mylonas, GP, *ESD CYCLOPS: A new robotic surgical system for GI surgery*, IEEE International Conference for Robotics and Automation (ICRA 2018), Brisbane, Australia.

Contributions: *Development and validation of the prototype. Mechatronics were largely based on the first CYCLOPS prototype (2014).*

Pittiglio G, Kogkas A, Oude Vrielink TJC, Mylonas G, *Dynamic control of cable driven parallel robots with unknown cable stiffness*, IEEE International Conference for Robotics and Automation (ICRA 2018), Brisbane, Australia.

Contributions: *Supervision and technical assistance of the student Giovanni Pittiglio during his MRes thesis. As the student has a strong theoretical and control background, I developed the hardware and mechatronics.*

Miyashita K, Oude Vrielink, TJC, Mylonas, G, *A cable-driven parallel manipulator with force sensing capabilities for high-accuracy tissue endomicroscopy*, International Journal of Computer Assisted Radiology and Surgery, 2018.

Contributions: *Supervision and technical assistance of the student Kiyoteru Miyashita during his MRes thesis. Specific technical assistance regarded the code required for controlling the system.*

Oude Vrielink, TJC, Darzi A, Mylonas G, *Pre-clinical in vivo validation of the CYCLOPS surgical system for ESD (prize winner)*, International Society for Medical Innovation and Technology (iSMIT 2017)

Contributions: *Development of the ESD CYCLOPS (see ICRA 2018 paper for specific details), preparing and performing the ex vivo and in vivo animal trials. Writing of the abstract. The work was presented by Dr. Mylonas at the conference due to a second upcoming animal trial.*

Avila-Rencoret* F, Oude Vrielink*, TJC, Elson DS, Mylonas et al., *EndoSDR: Concurrent Endoscopic Screening, Diagnosis, and Removal of GI cancers* (prize winner), Business Engineering and Surgical Technologies Innovation Symposium (BEST 2016).

Contributions: *joint collaboration on preparation and pitching.*

Oude Vrielink, TJC, Darzi, Mylonas G, “microCYCLOPS: A Robotic System for Microsurgical Applications”, 6th Joint Workshop on New Technologies for Computer/Robot Assisted Surgery (CRAS) 2016.

Contributions: *The development, evaluation and documentation of the microCYCLOPS prototype and presentation at the CRAS conference. Existing software was modified for the requirements of the prototype.*

Oude Vrielink TJC, D.Z. Khan, H.J. Marcus, A. Darzi, G.P. Mylonas, “neuroCYCLOPS: A Novel System for Endoscopic Neurosurgery”, Conference Proceedings Hamlyn Symposium on Medical Robotics, 2016.

Contribution: *The design, manufacturing and evaluation of the neuroCYCLOPS prototype. In addition, the core concept that enables manual control was developed.*

Khan DZ, Oude Vrielink TJC, Marcus H, Darzi A, Mylonas et al., *NeuroCYCLOPS: development and preclinical validation of a robotic platform for endoscopic neurosurgery*, European Association of Neurosurgical Societies (EANS 2016), Publisher: European Association of Neurosurgical Societies

Contribution: Technical development of the neuroCYCLOPS.

Patent application GB 1806943.5. SIMPLE: Single Incision Micro Ports Laparoscopic Endosurgery

Contribution: *Generation of the core concept using the microports to solve technical challenges in MIS. Brainstorming with other inventors led to the additional ideas regarding applications and scaffold design.*

Chapter 1

Introduction

1.1 A Brief History of Robotics in Surgery

1.1.1 Background technological developments

The first developments in surgical robotics went hand in hand with the development of minimally invasive surgery (MIS) and industrial robotics. An important background development that made MIS possible was the development of minimally invasive visualisation methods. The development of the X-ray, Computer Tomography (CT) and Magnetic Resonance Imaging (MRI) technology enabled imaging for diagnostic purposes and improved planning for therapy. Another essential visualisation method for many MIS procedures is the endoscope, a long and slender surgical instrument that enables surgeons to look into the body through a natural orifice or small incision. The first prototypes of endoscopes were described by Hippocrates as far back as 400BC, in the form of an anoscope, but it was not until the invention of fibre optics in 1954 [1][2] and the rod-led endoscope that the technology had matured enough to be used in surgery [3]. The development of endoscopic tools enabled the first laparoscopic appendectomy, which was performed in 1981 by Dr Kurt Semm [4]. The rigid endoscope has since become widely used in laparoscopy, but also in other domains such as arthroscopy, thoracoscopy and endoscopic neurosurgery. Fibre optics technology also enabled the development of the first fully flexible fibrescope in 1958 [5]. Flexible fibrescopes developed to flexible endoscopes, which are now essential for many gastrointestinal, urological, gynaecological and bronchoscopic procedures.

At the same time with developments in minimally invasive surgery, technological developments in electronics and computing in the second half of the 20th century led to the creation of the first industrial robot, the Unimate [6]. The Unimate was used to automate assembly lines in hazardous conditions. The higher accuracy, repeatability and cost-effectiveness of these industrial robots eventually led to the wide-spread automation seen in modern factories. Other applications of robotics were in hazardous environments hostile to human life - the deep sea, space, nuclear reactors – and the performance of highly dangerous tasks, such as bomb detonation. In general, these types of robotic systems are not autonomous or pre-programmed, but are controlled by a human operator from a distance; this is referred to as teleoperation. Teleoperated robots are essential for the performance of tasks in environments that require complex decision-making, and while further developments in computational power, new mechanical designs, computer vision and artificial intelligence make autonomy in complex environments increasingly feasible, autonomous robots still do not outperform human capabilities.

1.1.2 The development of minimally invasive surgery

The best-known form of MIS is laparoscopy. A clear advantage of laparoscopic surgery is the use of smaller incisions for the insertion of surgical instruments, in contrast to the large incisions required for surgeons to be able to use their own hands when performing open surgery. The smaller incision size has many benefits for patients, such as faster recovery time, fewer post-operative complications, less pain, less analgesics and improved cosmesis due to the reduction of visible scar tissue. Also, the shorter hospital stay - days rather than weeks, or even same-day discharge – reduces the strain on the healthcare system in terms of hospital bed occupation and care needs [7]. However, the clinical benefits of laparoscopic surgery notwithstanding, these procedures are technically challenging to perform for the surgeon. The access points into the abdomen, via trocars, limit the laparoscopic instruments to 4 degrees of freedom of motion (DoF). The entry points also result in the counter-intuitive mirroring of the instruments motion, also referred to as the ‘fulcrum’ effect. The added complexities that follow require additional training for laparoscopic skills and result in prolonged operation times [8]. In addition, the suboptimal ergonomics, in which awkward positions must be maintained for a longer period of time, has caused an increase in musculoskeletal problems among surgeons. Despite the fact that it is more challenging to perform, the clinical advantages of laparoscopic surgery have resulted in its wide-spread adoption for many surgical procedures [9].

1.1.2.1 *Single-port surgery, Natural Orifice Endoscopic Surgery and Natural Orifice Transluminal Endoscopic Surgery*

Laparoscopic surgery typically uses three to four ports. Single-Incision Laparoscopic Surgery (SILS)¹ further reduces the number of ports in order to further decrease invasiveness. Additionally, SILS leads to an improved cosmesis which can be further improved when using the umbilicus - a naturally occurring scar –, resulting in virtually scarless surgical interventions. However, SILS is even more technically challenging than conventional laparoscopic surgery. In addition to the “fulcrum effect”, SILS also involves instrument mirroring, in which the left hand controls the instrument that is visually displayed on the right, and vice versa. Another challenge is the effect of multiple instruments crowding around the port – a phenomenon also referred to as “sword-fighting” – which, among others, limits the surgeon’s freedom of motion. In contrast to conventional laparoscopic surgery, SILS has not seen wide adoption in clinical practice, as its technical challenges outweigh the incremental clinical advantage it brings. An extensive systematic review of SILS pelvic and abdominal procedures showed an incremental improvement of post-operative recovery times for certain procedures [10]. A multi-centred randomized controlled trial published in 2017 comparing multi-port and single-port cholecystectomy showed similar technical challenges, but reported an overall improvement in patient satisfaction for cosmesis [11]. Longer operative times have been reported, although this can be improved by training. Studies with regard to colorectal [12], gynaecological [13] and urological [14] surgical procedures yielded similar findings. The most important findings of the abovementioned studies are that SILS procedures do not increase perioperative and postoperative complications, which shows feasibility and safety of the method. Overall, the main opportunity for improvement of SILS lies in the development of instruments and surgical techniques that reduce the technical challenges and make procedures more intuitive.

While SILS, as an example of a specific single-port surgical technique is indeed minimally invasive, other MIS techniques exist. *Natural Orifice Endoscopic Surgery (NOES)*² uses existing anatomical points of entry to gain access into the body. It is typically the mouth or the anus that serves as the access point, but other natural pathways such as the urethra or the nose are also used. Flexible endoscopy plays a major role in NOES to access the gastrointestinal (GI) tract or the bronchi, for which there exists a variety of instruments in different sizes, with names referring to the anatomy of interest (e.g. colonoscope, sigmoidoscope, gastroscope, bronchoscope). For anatomies with a

¹ In literature variations of the term single-port surgery are used, such as Laparoendoscopic Single-site Surgery (LESS), Single-Port Access Surgery (SPAS), Single-Port Surgery (SPS) and Single-Incision laparoscopic Surgery (SILS).

² The term *NOES* is not widely used. One occasionally encounters the term *endoluminal surgery*, but often the procedure is referred to according to the specific access method used: transanal, transnasal, transoral, peroral etc.

relatively short and straight access pathway, rigid endoscopes are also sometimes used, such as the rigid cystoscope for transurethral access. The number of surgical techniques that can be performed via NOES is still very limited, however, although it does play an important role in the removal and prevention of early stage cancers. In the GI tract, the removal of lesions (e.g. polyps) with a snare is a common practice in many screening procedures. Although these are mostly performed using a simple snare (e.g. Endoscopic Mucosal Resection (EMR)), more advanced therapeutic techniques have also been developed, e.g. Endoscopic Submucosal Dissection (ESD) and Peroral Endoscopic Myotomy (POEM).

Another development in MIS techniques is *Natural Orifice Transluminal Endoscopic Surgery* (NOTES). NOTES uses an existing anatomical entry into the body, after which (unlike NOES) it passes through an anatomical border to access a second lumen³. Examples of NOTES access methods are transvaginal and transgastric, used to access the peritoneal cavity. The first transgastric NOTES procedure was published in 2004 by Kalloo et al., in which liver biopsies were taken in a porcine study [15]. An earlier paper on transvaginal NOTES⁴ on a patient was published in 2001, in which a laparoscope was introduced through the vagina wall, while introducing small 2-mm and 5-mm instruments through the abdomen for gynaecological surgery [16]. The hybrid technique was also used to perform other surgeries, including a cholecystectomy [17] and appendectomy [18]. Many other transgastric, transvaginal and even transanal NOTES studies rapidly followed [19]. However, while interest in NOTES grew, it was not adopted into clinical practice, and the number of publications and citations has been steadily decreasing in recent years (Figure 1.1); furthermore, a number of important challenges have yet to be solved. One of the main challenges is the development of new endoscopic instruments which could be used for suturing, tissue traction and counter traction and endoscope stabilization [20][21]. Despite the decline in interest, a few recent randomized control trials showed that NOTES resulted in similar or better clinical outcomes than laparoscopic surgery[22][23]. These findings primarily relate to the transvaginal access method, but taking a wider perspective, they provide an important stimulus to further improve medical technology in order to make the procedure more accessible.

³ the term *lumen* is derived from Latin (where it means “source of light”) and is used in anatomy to describe the space inside a hollow organ, which is typically tubular.

⁴ the author of this paper used the term culdolaparoscopy, rather than NOTES. Culdoscopy had already existed in gynaecology since 1938, but was predominantly used for diagnostic purposes. The working group Natural Orifice Surgery Consortium for Assessment and Research (NOSCAR) created the term NOTES and was not aware of the earlier instances of NOTES in gynaecology [20]. While the error has been rectified in a later white paper [21], the work by Kalloo et al. [15] is often regarded as the first use of NOTES.

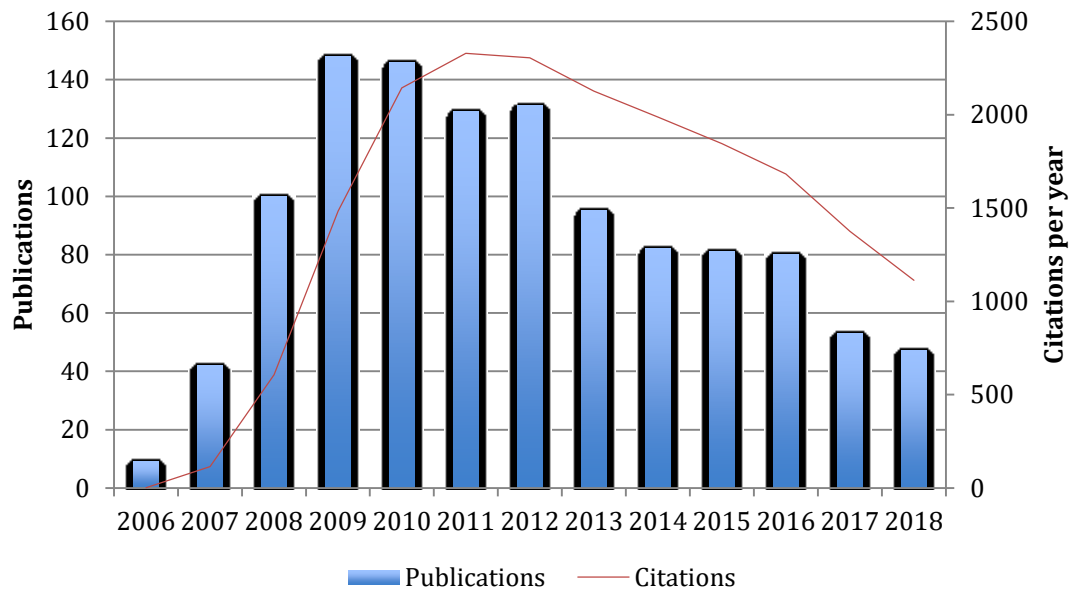


Figure 1.1 - The results (publications and citations) of a search on the topic Natural Orifice Transluminal Endoscopic Surgery in the Web of Science database (performed 27 December 2018).

1.1.3 Early surgical robotic systems

Minimally invasive surgery has been made possible by the unprecedented technological developments of the last half-century. In the past few decades we have witnessed the emergence of a new field, in which robotics were introduced into surgery. The first use of a robotic system for surgery was in 1985, when a UNIMATE PUMA 200 industrial arm was used to target a brain tumour for tissue biopsy [24]. The same concept was used in Switzerland to develop technology [25] that later became the Neuromate system (which is technology now owned by Renishaw plc, UK). In 1992, another industrial arm was adapted for automated bone milling for total hip arthroplasty, later leading to the development of the Robodoc system. Developments of the Robodoc system spurred the development of other robotic bone milling systems such as the Acrobot [26] and Caspar [27]. Another early development was the Probot, a robot used to perform transurethral resection of the prostate [28].

The first robotic system to obtain FDA approval in 1994 was the AESOP endoscope manipulator developed by Computer Motion, Inc. A next-generation system used the AESOP for endoscopic manipulation and added two surgical instruments; the result was the Zeus robot. A second company, Intuitive Surgical Inc., developed the similar da Vinci® Surgical System (Figure 1.2), and became the market leader in robotic procedures, with 4,986 surgical systems in use around the world at the end

of 2018⁵. An important innovation of the da Vinci system is the endoWrist®, which is located at the tip of the rigid instrument shaft and mimics the function of the human wrist to provide additional dexterity. Systems in recent generations have been developed for single-port robotic surgery.

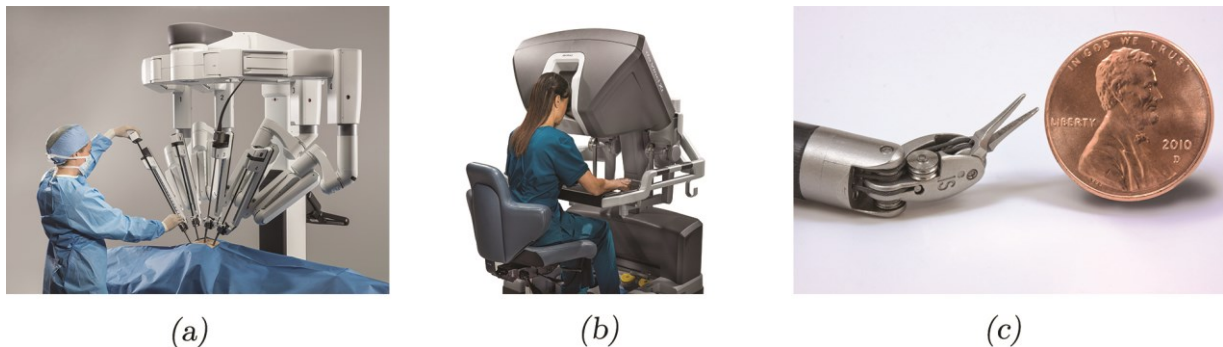


Figure 1.2 – (a) The da Vinci® Xi system at the patient side. ©2019 Intuitive Surgical, Inc. (b) The surgeon seated at the console. ©2019 Intuitive Surgical, Inc. (c) The endoWrist® articulated tip. ©2019 Intuitive Surgical, Inc.

The RAVEN system is a lightweight MIS surgical system developed for telesurgery [29]. The system was used in the NASA Extreme Environment Mission Operations (NEEMO) project, together with Stanford Research International's (SRI) M7 system and the AESOP system. An improved version of the system was developed and used as an academic research platform, RAVEN-II, containing a wristed end-effector [30]. SRI developed the M7 surgical robot in 1998 for use in military and aeronautic contexts [31]. Weighing only 15 kg, the system was designed for open surgery and provided haptic feedback and tremor filtering. The MiroSurge system was developed in 2010 by the German aerospace agency DLR, combining a 10 kg lightweight robotic arm (Miro) with 10mm laparoscopic instruments with an integrated 7 DoF force sensor in the tip [32]. The cable-driven instruments have a universal joint to provide an additional 2 DoF to the instrument.

1.1.4 Recent commercial developments

While the da Vinci system has remained dominant over the last decade, several companies have recently launched new robotic platforms. The Senhance™ robotic system (Transenterix), formerly called the Telelap ALF-X, obtained FDA approval in May 2018 for laparoscopic inguinal hernia and laparoscopic cholecystectomy surgery. Another company, Cambridge Medical Robotics (CMR Surgical, Ltd.), is developing a cost-effective, versatile and portable system for laparoscopic surgery with their new Versius system. Verb Surgical Inc., founded by Verily Life Sciences LLC and Ethicon, Inc. (subsidiaries of Alphabet, Inc. and Johnson & Johnson, respectively) is also developing a new robotic system. While it is not yet clear exactly what Verb is developing, expectations are high, due to the large corporations backing it. The term *Digital Surgery* suggest strong emphasis on the use of

⁵ This figure (4,986) is based on the Q4 2018 Preliminary Financial Data Table published by Intuitive Surgery, and represents the number of systems as on the 31st of December 2018. The annual report for 2018 has not yet been published.

sophisticated data processing and machine learning technology, which would be in line with the strengths of the mother company Alphabet Inc. Medtronic Inc. is expected to launch a new robotic system in the upcoming years, and is said to be based on the earlier mentioned MiroSurge technology. Other developments is the Sina system (Sina Robotics and Medical Innovators Co., Ltd.) in Iran and the Mantra robot (SS Innovations, Ltd) in China. The latter aims has a similar approach as CMR Surgical by developing a cost-effective surgical system, for a global population.

Recently developed systems for flexible endoscopy include the Flex® Robotic System (Medrobotics, Corp.) and the Monarch™ (Auris Health, Inc.). The Flex Robotic System has received FDA approval for both transoral and colorectal procedures. Auris Health Inc., having received more than half a billion US dollars' investment, announced that it had received FDA clearance for their Monarch system in March 2018. This system was designed for the improved diagnosis and treatment of lung cancers.

While this short overview outlines the general background of the commercial activities in the area of surgical robotics, it represents but the tip of the iceberg. A great many developments have taken place at institutions and companies throughout the world, especially in recent years. A more extensive overview of different surgical robotics will be provided later on in this thesis. Technical challenges still limit the use of robotic systems for SILS, NOES and NOTES, which prevents a radical improvement of surgical outcomes through novel technology; this will be discussed in more detail in section 1.2.

1.2 Motivation

Despite the many developments in MIS and in surgical robotics, certain issues have yet to be resolved. Challenges remain in the lack of haptic feedback, large operating footprint, limited dexterity and high capital costs. The most recent robotic systems seem to tackle few of these aspects for conventional laparoscopic approaches, and it will be exciting to see how these prove themselves in the near future. However, since these systems have primarily been developed for conventional laparoscopic approaches, they are not easily adapted for other forms of minimally invasive surgery, such as SILS, NOES and NOTES. Despite the recent development of many new systems for these types of MIS, technical challenges in terms of workspace, dexterity and payload remain [33].

The CYCLOPS system (Figure 1.3) represents a completely different approach to MIS, providing bimanual instrument dexterity and high payloads [34]. A unique aspect of the CYCLOPS system is the mechanical actuation of the instruments, which uses a cable-driven parallel mechanism (CDPM). A CDPM is best described as a Steward-Gough platform in which the rigid links have been replaced by cable actuation. The cables are attached to the so-called 'overtube' in which conventional

endoscopic instruments can be placed for surgery. An outer structure, or *scaffold*, is used to provide support and direction to the actuation cables. A first prototype of the CYCLOPS was developed in 2014, in which a single instrument system with a rigid scaffold was used to provide end-effector forces of up to 65 Newton. Additionally, an analysis was performed which illustrated that the large workspace can be adapted to specific clinical needs by changing the cable entry points into the scaffold.

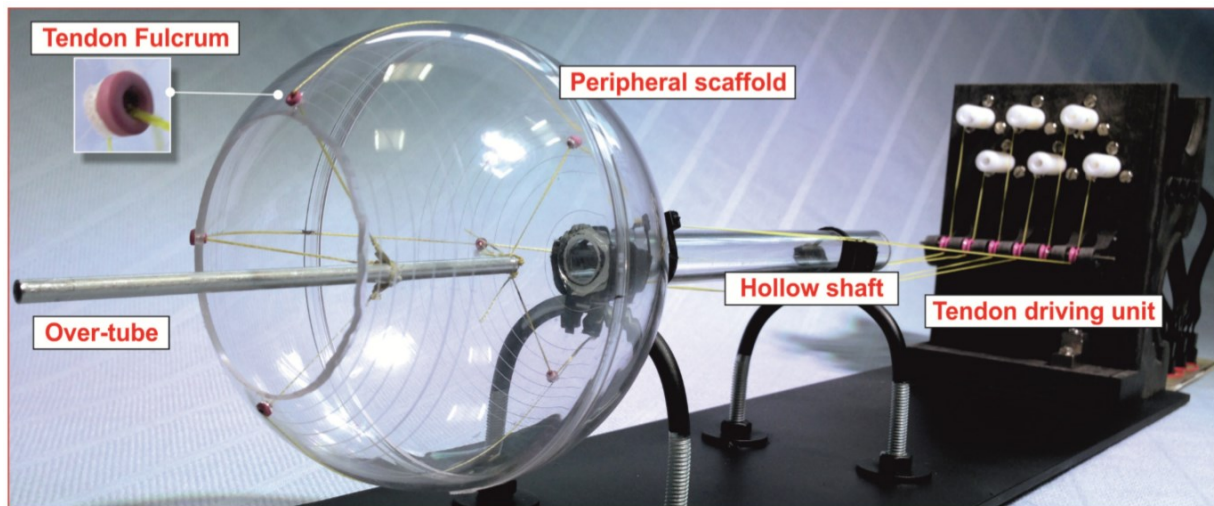


Figure 1.3 – The first prototype of the CYCLOPS system in 2014. A six-cable CDPM is used to control the overtube in 5 degrees of freedom.[34] ©2014 IEEE.

The use of CDPMs in MIS is limited to only a few examples (Figure 1.4). In 2003, the Light Endoscope Robot (LER) was presented [35]. Initial prototypes of the LER used a hybrid CDPM (i.e. a cable-driven mechanism combined with a single rigid link) to control the orientation of the endoscope. The group behind LER also developed the Light Puncture Robot (LPR) in 2004. The LPR is a belt-driven parallel mechanism developed for the positioning of biopsy needles within an MRI or CT bore [36]. It uses a four-cable planar design, providing intrinsic compliance in the out-of-plane direction to adapt to the shape and motion of the abdomen while breathing. Another planar CDPM was developed in 2014 for MIS epicardial interventions [37]. The system is inserted into the pericardial sac through a 20mm cannula and adheres to the heart through suction. The three-cable planar CDPM is able to mobilize a therapeutic needle over a large workspace along the surface of the heart.

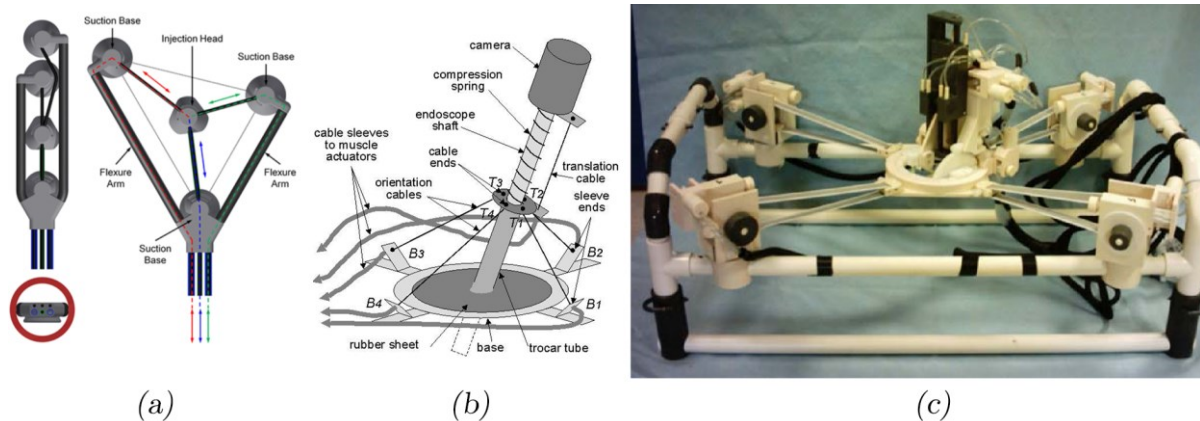


Figure 1.4 – Three CDPMs developed for MIS. (a) The planar wire robot developed for epicardial MIS [37]. (b) The Light Endoscope Robot (LER) using a CDPM for orientation of an endoscope. Image source: [38]©2002 IEEE. (c) The MRI compatible planar CDPM used for positioning a biopsy needle [36] ©2008 IEEE.

With the exception of these examples, many applications of CDPMs in MIS remain largely unexplored. The 2014 prototype of the CYCLOPS system showed potential technical and clinical benefits, but the system was not yet adapted to the many clinical requirements. Firstly, the cables were guided in a straight path from the motors to the entry points on the scaffold. Many surgical procedures, especially in flexible endoscopy, require a tortuous access pathway, and therefore a transmission mechanism should be included in further developments. Secondly, a full *bimanual* prototype had not yet been realized and the workspace needs for specific procedures not explored. Additionally, the scaffold was made out of a large rigid sphere, prohibiting the use of the system for surgery. The scaffold mechanism must be adapted to comply with the clinical needs for surgery in terms of access method, instrument workspace and size. All these aspects are required for further clinical translation of the mechanism, and depend on the specific clinical needs. The instrument workspace depends on the configuration of the cables, and therefore the workspace can be adapted to specific procedural requirements. An artistic representation of such a system for flexible endoscopy can be seen in Figure 1.5.

This thesis focuses on further development of cable-driven parallel mechanisms for minimally invasive surgery and highlights future developments that can contribute to the solution of existing problems in minimally invasive surgical robotics.

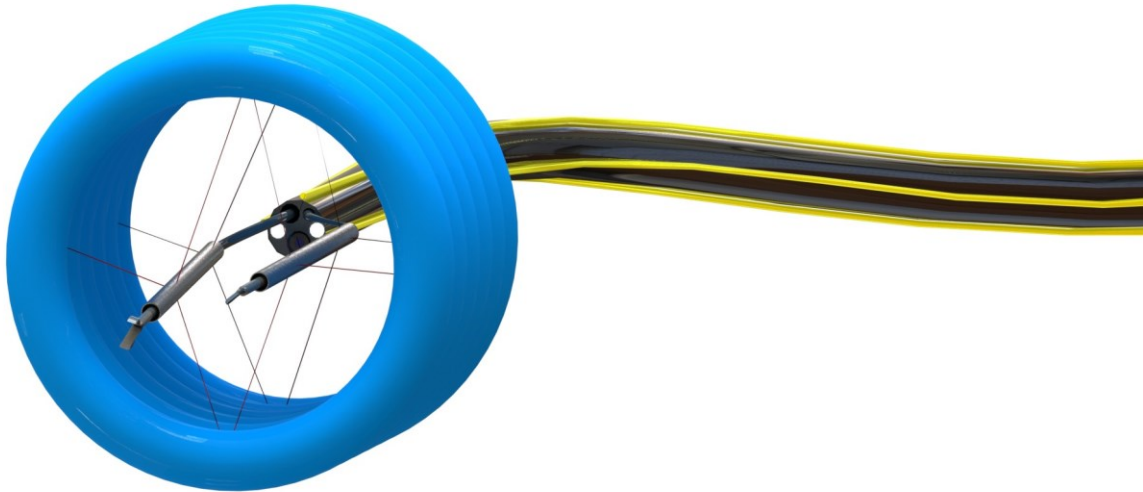


Figure 1.5 - An artistic representation of a bimanual version of the CYCLOPS system for flexible endoscopy.

1.3 Objectives

The objectives of this thesis are:

- To identify key technical advantages and disadvantages of CDPMs compared to other robotic architectures for MIS
- To identify minimally invasive access methods for use with CDPMs
- To identify clinical applications of CDPMs
- To develop a research framework that allows identifying future MIS applications for Cable-Driven Parallel Surgical Robotics

1.4 Overview of the proposed research method

The thesis is divided into a literature review and a section on the development and validation of prototypes. The main focus of the literature review is on the first objective: identifying the key technical advantages and disadvantages of the CDPM compared to other (robotic) architectures. An overview of different mechanical solutions for surgical robotics is given, based on important aspects during surgical tasks, such as dexterity, access method and tissue traction. The focus lies primarily on rigid and flexible endoscopic systems designed for NOES/NOTES and SILS. However, certain other mechanisms for such applications as endovascular, percutaneous and orthopaedic surgery also give insight in clinical requirements, leading to a choice for a particular mechanical design, and are therefore relevant to discuss. The synthesis of the literature study compares the CDPM to existing surgical systems and identifies opportunities for clinical applications.

The second and more extensive part of the thesis concerns the research and development of CDPM prototypes for MIS. The access method remains one of the most important challenges for CDPMs and hence prototypes are developed in specific ways to cover the different methods: endoluminal, transluminal, transparenchymal and extraluminal. Other technical challenges regarding workspace are discussed, and addressed in the light of clinical applications.

Based on the literature review and the experimental analysis of the prototypes, the thesis' discussion involves a framework with guidelines for the future development of CDPMs in the MIS domain. The framework is intended to help researchers and engineers identify future clinical opportunities. As the framework is based on early-stage development of CDPMs in the surgical field, it also highlights the domains in which further research is needed and the research questions that need addressing for CDPMs in MIS.

1.5 Thesis Outline

The thesis is structured to accommodate the research method described above. Chapter 2 introduces technical aspects of CDPMs, followed by the literature on surgical robots in Chapter 3. The ESD CYCLOPS was developed based on the initial concept of 2014, and has been brought to a further stage of development in which pre-clinical *in vivo* animal trials are conducted, which is described in Chapter 4. Chapter 5 comprises an evaluation of the CDPM principle for force-sensing applications, such as haptic palpation. Based on the findings from this chapter, the SIMPLE surgical system is discussed in chapter 6. Chapter 7 describes an optimization method to adapt the CDPM instrument workspace to procedure and patient-specific requirements. The method has been used to optimize the workspace of the ESD CYCLOPS and SIMPLE. In Chapter 8, the framework is synthesized, and future opportunities of CDPMs in MIS are suggested.

1.6 Contribution

This thesis makes the following contributions:

- An overview of mechanical architectures used in recent surgical robotic systems.
- The development of the first bimanual surgical robot for endoluminal surgery based on a CDPM: the ESD CYCLOPS. The ESD CYCLOPS provides high end-effector forces and thereby shows a unique advantage of CDPMs for the use in flexible endoscopic surgery.
- Identification of the use of CDPMs for end-effector force-sensing capabilities without the need of additional sensors inside the body. The force-sensing capabilities have been

demonstrated for palpation and autonomous scanning tasks.

- Development and patenting of a novel access method for the use of CDPMs inside the body: the Single-Incision MicroPort LaparoEndoscopic (SIMPLE) system. The system brings the force-sensing capabilities which were demonstrated earlier to SILS.
- Development of the microCYCLOPS and neuroCYCLOPS, illustrating the use of the CDPM adapted combination with tissue retraction devices. The neuroCYCLOPS illustrates a mechanical solution for manual, rather than robotic, control of the CDPM.
- Illustration of the capacity for patient- and procedure-specific optimization of CDPMs based on pre-operative imaging data.
- A framework for researchers, designers and engineers for the identification of opportunities for future development of CDPMs in MIS.

Chapter 2

Cable-Driven Parallel Mechanisms

This chapter serves as an introduction to cable-driven parallel mechanisms (CDPMs) in general. The core principle and the various types of CDPMs are discussed first, followed by the mechanical theory and key concepts for workspace calculation used throughout the thesis. To better understand the versatility of CDPMs, a brief overview of their usage for various (mainly industrial) applications is given. These applications serve as a context in which to discuss the advantages of CDPMs, such as the CYCLOPS system. The limitations of the mechanism are also described in this chapter.

2.1 Core Principle

The basic principle of CDPMs is shown in Figure 2.1. CDPMs use a plurality of actuation cables placed in a parallel fashion to manipulate an end-effector in space. Changing the length of the actuation cables controls the end-effector's pose. The principle is similar to Stewart-Gough platforms, with the main difference that the rigid links are replaced with flexible cables. An encapsulating base structure, referred to as *scaffold* throughout this thesis, is used as a support from which the cable's length is changed. The points at which the cables enter the scaffold and are attached to the end-effector are referred to as the cable *entry points* and *attachment points*, respectively. The prototypes developed in this thesis use a hollow tubular end-effector, which is referred to as the *overtube*.

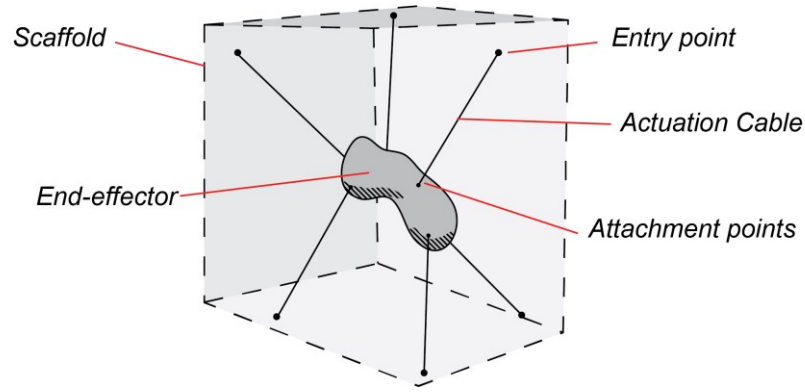


Figure 2.1 – The core concept of the cable-driven parallel mechanisms.

Note that while the term CDPM is used in this thesis, such robotic mechanisms are sometimes referred to as *cable-driven parallel robots* (CDPR) in the literature. The terms *wire* and *tendon* are also used instead of *cable* (e.g. *wire robot* or *wire-driven parallel mechanism*). Other designations refer to the similarity with Stewart platforms, e.g. *tendon-based Stewart platforms*.

2.1.1 Types of CDPM

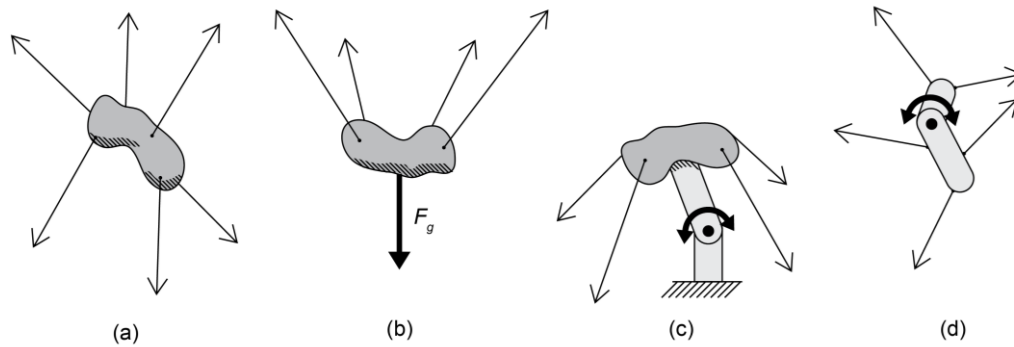


Figure 2.2 – Types of CDPM: fully constrained **(a)**, cable-suspended **(b)**, hybrid **(c)** and multi-link **(d)**.

The term “CDPM” is generally used to refer to one of two types of cable-driven parallel mechanisms: *fully constrained* or *completely/redundantly restrained* (Figure 2.2a) and *cable-suspended* or *under-constrained parallel mechanisms* (Figure 2.2b). The difference between these two mechanisms mainly lies in the ability to exert wrench on the end-effector. Cable-suspended parallel mechanisms, or *suspended CDPMs*, are dependent on an external counter-force for control. Most applications use gravity as the counter-force (e.g. [39][40]), though other sources of counter-force exist, e.g. helium-balloons [41][42]. As the counter-force is a passive force, it is not possible to use cable tension to increase the internal forces of the mechanism, and thereby exert a wrench with the end-effector. In contrast, fully constrained CDPMs can apply additional tension to the cables to increase the end-effector stiffness or to create a wrench on the end-effector. For fully-constrained

CDPMs, the number of cables determines the controllable DoF of the end-effector, and as these cables can only be used for pulling, not pushing, the number of cables n must be always larger than the number of controllable DoF m : $n \geq m + 1$.

An object in 3D space can have a maximum of 6 degrees of freedom, which is the case for CDPMs. An object in space can be constrained in such a way to allow for a combination of translational (T) and rotational (R) DoF, leading to a total of 15 combinations (i.e. for 2 DoF this would be RR, RT, TT; for 3 DoF, RRR, RRT, RTT, TTT, etc.). In contrast, as Verhoeven shows [43], CDPMs can only be controlled in 6 different motion combinations (T, TT, RTT, TTT, RRTTT and RRRTTT). This is related to the fact that no torques can be exerted on the end-effector without also exerting forces (i.e. the number of rotational DoF is always smaller than or equal to the translational DoF). Simultaneously, the number of translational DoF determines whether the end-effector is constrained to a line, a plane or a 3D space (for T, TT and TTT respectively). As rotation is not possible for an object constrained to a line and only possible in one direction in a plane, the combinations RT and RRTT are also unfeasible. Note that, as mentioned previously, the specific motion combination does not dictate the number of cables.

Two other types of CDPMs are the hybrid mechanism and the multi-link mechanism (Figure 2.2c,d). As the name suggests, when multiple linkages joint together as end-effector, these are referred to as multi-link CDPMs (e.g. [44][45]). Hybrid mechanisms use a passive joint in which the cables are used to articulate the end-effector [46][47]. The main advantage of CDPMs of this type is that they can act as an *open chain* (i.e. serial mechanisms). Such mechanisms are in general referred to as *hybrid*, as it combines the closed-chain parallel actuation with an open-chain serial configuration [48]. One benefit of this type of mechanism is that it does not need to be encapsulated by the base-frame (or scaffold).

2.2 Mechanics of CDPMs

This section discusses a number of key concepts that are used throughout the thesis, such as kinematics, optimal tension distribution and workspace calculation.

2.2.1 Kinematics

The pose of the end-effector ζ is determined by the length l_i of the $i = 1, \dots, n$ cables. As seen in Figure 2.3, the vectors \vec{v}_i describing the cables can be determined based on the difference between the cable entry points \vec{b}_i and the pose-dependent attachment points $\vec{p}_{i,g}(\zeta)$:

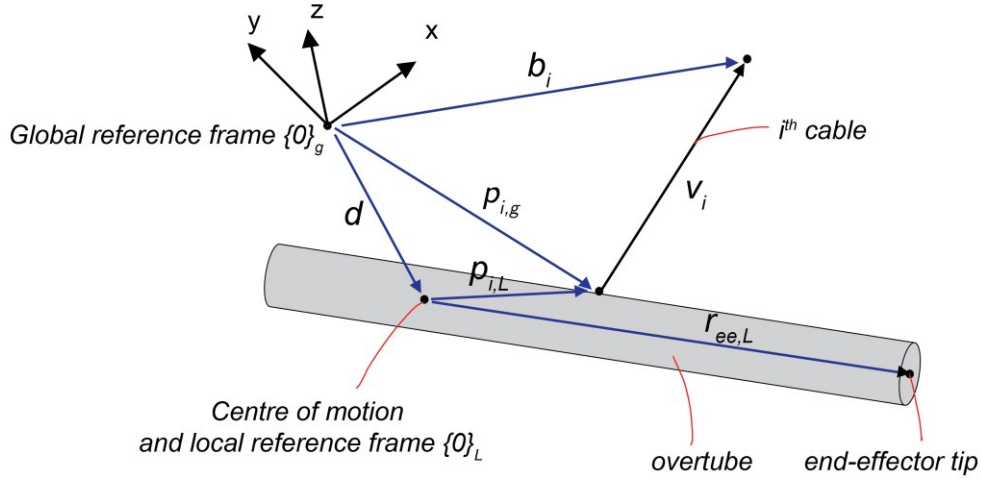


Figure 2.3 - The vectors used for the derivation of the kinematics.

$$\vec{v}_i = \vec{b}_i - \vec{p}_{i,g}(\zeta), \quad (2.1)$$

in which $\vec{b}_i, \vec{p}_{i,g} \in \mathbb{R}^{3 \times 1}$. The length of the cable is $l_i = \|\vec{v}_i\|$. Equation (2.1) can be written in matrix format as $V = B - P$, in which V, B and P represent the matrix of cable vectors, entry points and attachment points in $\mathbb{R}^{3 \times n}$. For a 6DoF system ($m = 6$), the end-effector pose is $\zeta = [x, y, z, \alpha, \beta, \gamma]$. Throughout this thesis, the yaw, pitch and roll angles are used for α, β and γ . The cable attachment points in the global coordinate frame $p_{i,g}$ can be calculated by taking the coordinates in the local end-effector frame, p_i , for the end-effector pose ζ :

$$p_{i,g}(\zeta) = R(\alpha, \beta, \gamma) p_i + \begin{bmatrix} x \\ y \\ z \end{bmatrix} \quad (2.2)$$

The rotation matrix $R(\alpha, \beta, \gamma)$ for the used yaw, pitch and roll angles is:

$$R(\alpha, \beta, \gamma) = \begin{bmatrix} \cos(\alpha) \cos(\beta) & \cos(\alpha) \sin(\beta) \sin(\gamma) - \cos(\gamma) \sin(\alpha) & \sin(\alpha) \sin(\gamma) + \cos(\alpha) \cos(\gamma) \sin(\beta) \\ \cos(\beta) \sin(\alpha) & \cos(\alpha) \cos(\gamma) + \sin(\alpha) \sin(\beta) \sin(\gamma) & \cos(\gamma) \sin(\alpha) \sin(\beta) - \cos(\alpha) \sin(\gamma) \\ -\sin(\beta) & \cos(\beta) \sin(\gamma) & \cos(\beta) \cos(\gamma) \end{bmatrix}$$

In this thesis, motors are used to rotate a spool around which the cables are wound, thereby changing the cable length l_i . The cable length is dependent on the spool radius ρ and the angle in radians of motor rotation q_i : $\Delta l_i = \rho(q_i - q_{i,0})$. The initial motor position $q_{i,0}$ is obtained through calibration.

One of the technical challenges of CDPM is that, while the inverse kinematics are easy to compute, computation of the forward kinematics is cumbersome. This is best understood with reference to equations (2.1) and (2.2), from which it can be seen that the motor pose q_i can be easily

calculated algebraically for a desired end-effector pose ζ , i.e. an algebraic function exists for $q_i(\zeta)$. This mapping from desired end-effector space to joint space is referred to as the *inverse kinematics*. The non-linear trigonometric functions in the rotation matrix $R(\alpha, \beta, \gamma)$ and the L2-norm for cable length calculation impede the finding of an analytical description of the opposite relationship, i.e. the *forward kinematics* for mapping the desired joint space to an end-effector space: $\zeta(\vec{q})$ with $\vec{q} = [q_1, \dots, q_n]^T$. However, even for systems without a rotation matrix (i.e. translational CDPMs), calculation of the forward kinematics remains difficult. Equations (2.1) and (2.2) are underdetermined with more cables n than controllable DoF m , and as a result multiple end-effector poses can be found for the same cable lengths. Hence, no single unique solution exist for the forward kinematics; rather, an optimal solution can be found numerically.

2.2.2 Force equilibrium

The force equilibrium equation for CDPMs is defined as:

$$A(\zeta)\vec{t} + \vec{w} = 0 \quad (2.3)$$

In which \vec{t} is the vector describing the tension in the cables, \vec{w} is the external wrench and A is the pose-dependent structure matrix composed from of the cable unit vectors $\vec{u}_i = \frac{\vec{v}_i}{\|\vec{v}_i\|}$ and the cable attachment points $p_{i,g}$:

$$A = \begin{bmatrix} u_1 & \dots & u_n \\ p_{1,g} \times u_1 & \dots & p_{n,g} \times u_n \end{bmatrix}^T \quad (2.4)$$

The structure matrix is also the transpose of the Jacobian, i.e. $J = A^T$. The stiffness of the end-effector can be calculated using the structure matrix [49]:

$$K(\zeta, \vec{t}) = kJ^T \Omega J + \frac{d}{d\zeta} J^T \vec{t} \quad (2.5)$$

with k being the cable stiffness per length and the diagonal matrix Ω containing the cable lengths l_i . The left component of the equation is only pose-dependent, while the right component increases depending on both the pose and the cable pre-tension.

2.2.3 Optimal Tension Distribution

The redundancy in actuation also affects the ability to find a required cable tension for a given pose. Therefore, a finite set of solutions exists for solving equation (2.3) with respect to the cable tension \vec{t} . Also, the cable tension must be positive to prevent slackness and must be limited to the maximum forces the cables can resist without failure. The *optimal tension distribution* (OTD) is the

best cable tension found within the range between the minimum and maximum cable tensions, t_{min} and t_{max} , respectively. In the literature, several different approaches for calculating the optimal tension distribution exist.

The *minimum norm solution* [50] uses the Moore-Penrose pseudoinverse to solve equation (2.3). The tension distribution in the cables will have a minimum norm and a null space component [51]:

$$\vec{t} = \vec{t}_{mn} + \vec{t}_{null} \quad (2.6)$$

For which

$$\vec{t}_{mn} = -A^+ \vec{w}$$

$$\vec{t}_{null} = \lambda_c (I - A^+ A) \mathbf{1}$$

$$A^+ = A^T (A A^T)^{-1}$$

Where λ_c is a scalar constant such that all the cable tensions lie between t_{min} and t_{max} . The choice of λ_c influences whether a feasible solution is found, and hence for this purpose an iterative search algorithm can be used [52]. The minimum norm approach is suggested to be appropriate for an initial workspace estimation, as feasible points might be excluded from the calculation [51].

A second method is to use the *L1-norm* for numerical optimization:

$$\begin{aligned} & \min_{\vec{t}_r} 1^T \vec{t} \\ \text{s. t. } & A \vec{t} = -\vec{w} \\ & \vec{t}_{min} \leq \vec{t} \leq \vec{t}_{max} \end{aligned} \quad (2.7)$$

$\vec{t}_r \in \mathbb{R}^{(n-m) \times 1}$ represents the tension vector in the redundant cables. The redundant cable can be mathematically expressed in terms of the other cables (\vec{t}_{nr}) by dividing the structure matrix in equation (2.3) in a redundant and non-redundant matrix ($A = [A_{nr} | A_r]$):

$$\vec{t}_{nr}(\vec{t}_r) = -A_{nr}^{-1} \vec{w} - A_{nr}^{-1} A_r \vec{t}_r \quad (2.8)$$

Linear programming optimization techniques can be used to solve this problem with high computational efficiency [51]. For a single redundancy (i.e. $n - m = 1$), an analytical solution for the L1-norm exists giving even higher computational efficiency without compromising accuracy [51], [53].

An L2-norm optimization problem has also been proposed in the literature, in which the objective function in equation (2.7) becomes $\|\vec{t}\|_2^2$. However, this method was demonstrated to be more computationally expensive than the L1-norm, without a clear advantage in terms of accuracy

[51]. Another L2-norm method which, to the author's knowledge, does not exist in the literature regarding CDPMs is:

$$\begin{aligned} & \min_{\vec{f}} \|A\vec{t} - \vec{w}\|_2 \\ \text{s. t. } & \vec{t}_{\min} \leq \vec{t} \leq \vec{t}_{\max} \end{aligned} \quad (2.9)$$

This approach is used in other fields of computer science, and is referred to as the *bounded variable least-squares*. The approach is simple and efficient and therefore a good candidate for the calculation of the optimal tension distribution.

2.2.4 Controllable Workspace

A pose is said to be controllable if a set of cable tensions \vec{t} can be found within the maximum and minimum cable tensions. Additionally, controllability is lost when the *rank* of the structure matrix decreases and becomes lower than the m controlled DoF: $\text{rank}(A) < m$. The loss of rank occurs when the structure matrix becomes singular, and this is typically seen at the boundaries of the workspace. As seen in the previous section, the optimal tension distribution is dependent on both pose ζ and wrench \vec{w} . Hence controllability, and thus the workspace, are influenced by the external wrench. Where this thesis refers to *workspace*, this means the *reachable workspace* with no external wrench. When calculating the workspace for a specific external wrench, the term *wrench-feasible workspace* is used.

The condition number is a metric used to describe the quality of a specific pose within the dexterous workspace. The condition number of the Jacobian matrix represents the dexterity of the system: $CN(J) = \frac{\lambda_{\max}}{\lambda_{\min}}$, in which λ_{\max} and λ_{\min} represent the eigenvalues of the Jacobian matrix. Similarly, the condition number of the stiffness matrix can be used for a measure of quality of stiffness in all DoF [54]. The condition number of the Jacobian, however, does not always accurately represent the dexterity of the system [55]. The tension factor (TF) has therefore been suggested as more suitable alternative. The TF is the ratio of the minimum over the maximum cable tension:

$$TF = \frac{\min(t)}{\max(t)} \quad (2.10)$$

The tension factor can be used to estimate the proximity of the end-effector position to the boundaries of the workspace. For an entire workspace, the quality can be quantified by using the *global tension index* [55], in which the tension factor over the workspace is integrated over the entire volume:

$$GTI = \frac{\int TF(\zeta)dV}{\int dV} \quad (2.11)$$

The GTI can be used when comparing different cable configurations, as will be important for the optimization routines in Chapter 7.

2.2.5 Workspace Calculation

Finding the feasibility of a single pose requires an estimation of the cable tensions using the optimal tension distribution, as discussed in previous sections. However, as a result of the redundancy of actuation, no algebraic solution exists, which is reflected in the absence of a general equation that defines feasibility as a function of the end-effector pose. As a result, each pose in the workspace needs to be evaluated for feasibility, requiring the discretization of a search space along each of the controllable DoF of the system. The search space is defined as a space with the dimension of the number of DoF m , i.e. in \mathbb{R}^m . For each dimension dim_j with $j = 1, \dots, m$ the space is discretised over the range $\{dim_{j,min}, dim_{j,max}\}$ by stepsize $\Delta_j = (dim_{j,max} - dim_{j,min})/n_j$, where n_j is the number of evaluations along the j th dimension. The total number of pose evaluations is the product of the evaluations along each axis: $n_{SP} = \prod_{j=1}^m n_j$. With a smaller stepsize Δ_j , the accuracy increases, but so does the number of iterations. For example, for a system with x, y, z, β, γ DoF the search space can be discretized into $n_{SP} = n_x n_y n_z n_\beta n_\gamma$ pose evaluations. Over a cubic search space of 50x50x50mm discretized in steps of 1mm and with both angles discretized over 20 steps, this requires 50 million poses to be evaluated to obtain the workspace. The computation becomes especially cumbersome for workspace optimization, requiring the full workspace to be evaluated for each step in the optimization process.

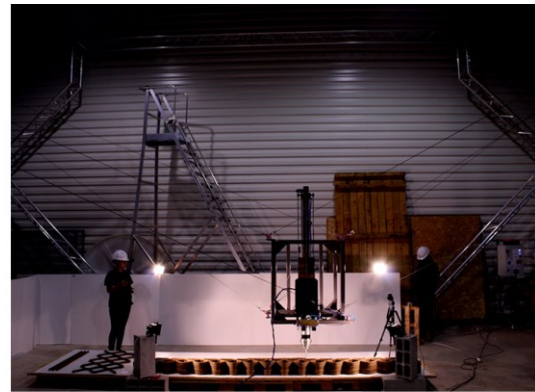
The chord method [56] has been proposed to increase computational efficiency. The method first iteratively finds an initial point at the boundary of the workspace, from which it starts to follow the boundary. The method therefore does not require calculating all the points within the boundaries, hence saving computational time. The method has been predominantly developed for planar parallel systems and for use in spatial CDPMs (in \mathbb{R}^3 cartesian space) one axis still needs to be discretized. The main disadvantage of this approach, however, is that the method can be used to find the *boundary* but not the *quality* of the workspace. To assess the quality of the workspace (section 2.2.4) all the intermediate points have to be used, and therefore the discretized search method is used throughout this thesis.

2.3 Applications of cable-driven parallel mechanisms in different industries

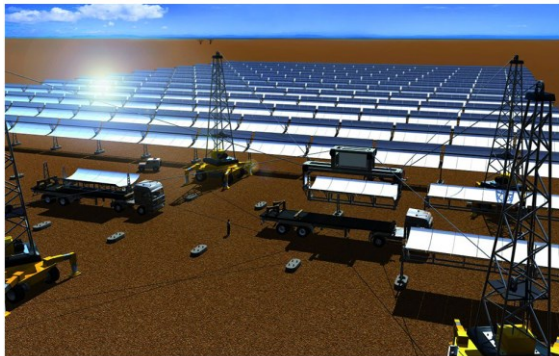
Cable-driven parallel mechanisms are found in a wide range of applications. A number of overviews of systems are given in the literature, e.g. in Gosselin (2014) [57] and Qian et al (2018)[58]. These types of mechanisms are found in a wide variety of applications, such as radio telescopes [59][60], industrial weight lifting [61][40][39], assembly [62][63][64], manufacturing [46][65][66][67], stadium cameras [68][69], environment sensing for terrestrial and aquatic applications [70][71], haptic devices [72][73][74][75][76], rehabilitation [77][78][79][80], search and rescue [42][81][82], motion simulators [83][84][85], and wind tunnel tests [52][86]. A selection of systems is shown in Figure 2.4-2.6.



(a)



(b)



(c)



(d)

Figure 2.4 – (a) The NIST robocrane [39] used for painting airplanes. Image courtesy: N.E. Wasson Jr./US Technologies. (b) A CDPM used for 3D printing. Image courtesy: IAAC - Institute for Advanced Architecture of Catalonia (c) The IPAnema robot suggested for placement of solar panels[63]. Image courtesy: Fraunhofer IPA. (d) The CableRobot for simulation purposes. Image courtesy: Fraunhofer IPA, Philipp Miermeister.

Cable-suspended parallel robots are used in many heavy lifting applications. Dagalakakis et al. proposed a suspended CDPM for lifting and positioning heavy structures in shipbuilding applications, in which additional stability and stiffness was required [40]. Further developments in heavy lifting applications can be seen in the NIST Robocrane [39], in which a suspended CDPM is placed within a

lightweight aluminium octahedral scaffold. Another application of the NIST robocrane is seen in Figure 2.4a. Manufacturing applications of suspended CDPMs are found in applications such as large-scale machining [65] and 3D printing [15][16] (Figure 2.4b). The IPAnema is a CDPM platform which is being evaluated for further industrial applications [61]. One of the possible applications for the IPAnema robot is the assembly of large-scale solar panels. As such, the scaffold is envisioned as consisting of multiple tower trucks bearing the cable-winches [63](Figure 2.4c). At a smaller scale, the low inertia of CDPM platforms was exploited by Kawamura et al. to develop a high-speed but energy-efficient platform for assembly purposes [62]. The system reached accelerations of up to 43g. Another CDPM for high dynamic assembly applications is the WARP system [64]. A hybrid parallel mechanism for high speed manufacturing is the DeltaBot, a modified conventional delta robot in which the rigid links are replaced by cables. The system has a central pneumatic shaft and thus is best defined as a hybrid CDPM [46].

The heavy weight lifting and high dynamic capabilities of CDPMs exploited for assembly and manufacturing purposes are excellent properties for the simulation of motion, such as in vehicle simulators [84][83](Figure 2.4d) and a virtual hang-glider [85]. CDPMs are also used for a walking platform for virtual reality and gait analysis applications [87]. Each foot is placed on a separate CDPM structure to provide support during the required motion. CDPMs have also been proposed for haptic interfaces for use in simulated environments, e.g. having large workspaces [76][73] or body-mounted haptic devices [74][72]. One range of CDPM haptic devices is the SPIDAR, with systems which are finger-tip mounted or handheld at different sizes, with the largest size fully immersing the human operator [73]. Other CDPMs are being developed for sports applications such as tennis and rowing [75]. CDPMs are often used for haptic devices due to their safe human-machine interaction by means of cables (as opposed to robots with rigid arms), their low mass and large workspace. Their low inertia enables better-quality haptic rendering at higher frequencies. Another benefit is that cables are relatively non-intrusive, which is also one of the main reasons for the use of cables in wind tunnels [52][86], where they enable the control of model aircrafts in 6DoF without the aerodynamics being influenced by the support suspension system.

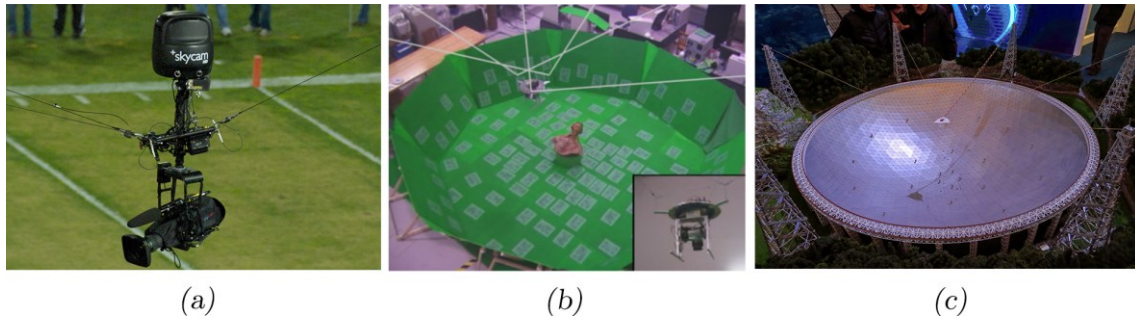


Figure 2.5 - (a) The Skycam [68] used for broadcasting sport events. Image source: [88](b) A CDPM used for the digitizing of 3D objects [89]. ©2007 IEEE (c) A small scale model of the FAST radiotelescope, which has been built in China in 2016. Image source: [90].

Another use of CDPMs can be found in the control of sensors. This includes the probably best-known uses of wire robots: the Skycam [68] (Figure 2.5a), SpiderCam and Cablecam [69]. These systems are primarily used for sports events in stadiums to hover cameras over the field. Deschênes et al. [89] developed a suspended CDPM used for the 3D surface reconstruction of objects by collecting a large dataset of images from different angles (Figure 2.5b). CDPMs are also used to control sensors in the measurement of terrestrial and aquatic environments, as seen in the NIMS. The NIMS RD is a sensorized cable robot which can be deployed between two tall objects, such as trees, to scan the environment along a line trajectory [71] or planar surface [70]. The largest cable-driven parallel robots are found in radio telescopes. The FAST telescope is a radio telescope with a 500m diameter dish [59](Figure 2.5c). A suspended CDPM is used to control the position of the detector, hovering above the dish. Another radio telescope which uses a CDPM is the Large Adaptive Reflector (LAR). The LAR uses an inverted suspended CDPM in which the counter-force is not gravity, but is provided by a large helium aerostat [60]. The system is designed to work in combination with a 200m diameter parabolic reflector with a focal length of 500m, at which distance the detector is suspended. Aerostats have also been developed for use in rescue missions; sensors placed on the balloon can detect signs of people buried beneath rubble after an earthquake [42]. Other deployable CDPMs have also been suggested for rescue operations, e.g. to lift rubble [82] or people [81]. In rescue missions, the use of such CDPMs has been proposed for their large workspace and being deployable, while remaining lightweight and compact. This allows these systems to be transported through hard-to-reach and remote areas, e.g. regions in which the roads have been destroyed or simply do not exist.

An interesting CDPM is when planar systems are used to follow the contour of a convex surface, as described by Voss et al. [91]. The concept of contour-following by a planar system is used in medicine in which the LPR and epicardial robot mentioned in Chapter 1, as two examples. Another example is the Tele-Echography Robot (TER), which uses a planar belt-driven CDPM for ultrasonic

scanning [92]. In all these applications, the off-plane compliance of planar systems is used for following of the soft tissue surface, and the absence of the rigid links makes the system lightweight and inherently safe.

Another medical application of CDPMs is in rehabilitation. The MariBot was developed as a suspended CDPM for upper limb neuro-rehabilitation for stroke patients [78]. Alternative configurations for upper limb rehabilitation include a full 3D CDPM design (MACARM robot) [79], a hybrid exoskeleton for the arm [80] (Figure 2.6d) and a planar desk-mounted CDPM by Jin et al. [93] (Figure 2.6e). The String-man is a body-mounted CDPM developed for body stabilization and force perturbation during gait rehabilitation [77] (Figure 2.6c). Another interesting approach for lower limb rehabilitation is the affixation of cables to both the upper and lower parts of the leg [94] (Figure 2.6f). As such, the knee joint is part of the kinematics and thus can be seen as a multi-link CDPM with a knee acting as the joint in the end-effector. A major reason for the use of CDPMs in rehabilitation is their lightweight construction and the ability to adjust the cables for specific clinical needs.

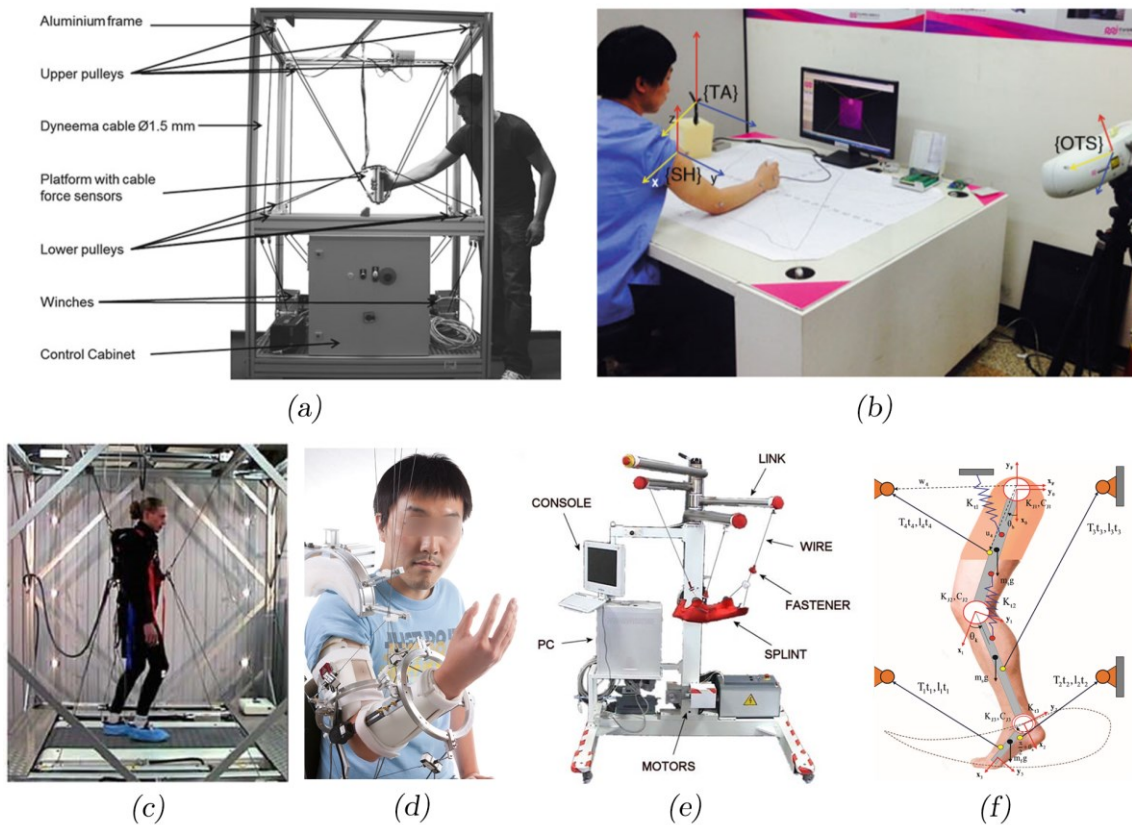


Figure 2.6 – (a) The IPAnema 3 robot used for haptic feedback [95]. (b) A planar upper limb rehabilitation device for on desktops [93]. (c) The String-man for gait rehabilitation [77]. ©2007 IEEE. (d) The CAREX exoskeleton using a hybrid CDPM for upper limb rehabilitation. Image source: [96]. ©2015 IEEE (e) The NeReBot for upper limb rehabilitation. Image source: [78]©2005 IEEE (f) A multi-link CDPM for lower limb rehabilitation [94]. ©2015 by ASME.

2.4 Technical advantages of CDPMs

The wide range of applications for which CDPMs are used illustrates the versatility of the mechanism. By analysing the reasons why the developers and researchers have selected the CDPM for their application yields the following overview of technical advantages:

- *Workspace size and configurability* – The workspace of CDPMs is directly dependent on the size of the scaffold, and we thus find examples of workspaces that range from few centimetres to half a kilometre. The mechanism is therefore easily scaled to suit different workspace requirements. The configurability of CDPMs can also be seen in the ability to change the mechanism to fit specific needs, e.g. for rehabilitation purposes. The system workspace is directly related to the cable *entry point* on the scaffold and the cable *attachment points* on the end-effector.
- *High dynamic capabilities* – High-speed applications of CDPMs can be found in manufacturing and assembly. It is possible to achieve high speeds because the cables enable the exertion of high forces, while the mechanism itself has low mass and thus inertia. CDPMs generally have low inertia because they do not incorporate great numbers of, often heavy, moving structures, such as the rigid links in serial robotics.
- *Deployable structures* – Due to low weight and workspace configurability of CDPMs, it is possible to create them as deployable structures. Such systems are found in rescue and sensor applications in often hard-to-reach locations.
- *High payload and efficient force transmission* – The fact that CDPMs are used for manufacturing, construction and cranes shows that the mechanism is well-suited for heavy lifting applications. The high payload can be attributed to the efficient force transmission from actuator forces to forces in the end-effector. This efficiency is realized by distributing loads across multiple actuators and lower influences of torques on each joint. The overall benefit becomes clearer when considering serial robots, in which the lowest joint in the chain has to bear the loads of all the forces exerted on the end-effector. In addition, the length of the serial mechanisms results in large torque at the base joint. CDPMs generally have lower torque effects because they carry loads between or close to cable attachment points.

- *Low costs* – The cost saving aspect is often mentioned in many applications, and should be considered in comparison to serial mechanisms. The first cost-saving aspect of CDPMs is that they do not need strong mechanical links as a support structure, hence saving manufacturing and material costs. A second aspect relates to the more efficient force transmission, as discussed above, which allows for smaller actuators without compromising on functionality.

2.5 Limitations of CDPMs

This section describes the limitations of CDPMs, of which some will affect the use of CDPMs in MIS. Most limitations relate to technical aspects such as control and optimization, these are addressed throughout the thesis.

One limitation of CDPMs is that the cables are only able to pull and not push. As a result, in *fully-constrained* CDPMs, the *attachment points* on the end-effector need to be encapsulated by the scaffold structure. In contrast to the attachment points, however, the end-effector can be elongated to reach outside of the scaffold structure, as seen in the first CYCLOPS prototype. *Hybrid* and *suspended* mechanisms can extend these attachment points outside the frame using rigid elements or external forces. The need for an encapsulating scaffold poses a challenge with regard to MIS, and is one of the main reasons why the combination of MIS and CDPMs seems counter-intuitive. This thesis will present multiple different ways to create such a scaffold for MIS.

Another limitation relating to the cables' sole ability to pull is the redundancy of actuators for control (i.e. the previously mentioned $n \geq m + 1$). The addition of a counter-force can be used to reduce the redundancy, as seen in cable-suspended parallel mechanisms in which gravity is purposefully used as counter-force. Another method to develop non-redundant CDPMs is the addition of springs to maintain a positive tension in the cable, as explored by Liu et al. [97]. In such mechanisms, one or more compliant elements (i.e. spring) are added to one end of the cables to create a pretension, or to act directly as a counter-force on the end-effector. The different configurations explored by Liu [98] showed that the method could be successfully applied to planar and spatial CDPMs (3 Cartesian DoF). Note that the number of cables entering the scaffold is not reduced (but the number of actuators required for control). The explored spatial CDPM mechanism had 6 cables entering the scaffold, which can be seen as still having cable redundancy (rather than an actuation redundancy). Similarly, in other research, such as [99], actuation redundancy rather than cable redundancy is addressed. A benefit of non-redundant actuation mechanisms, however, is the reduction in the number of actuators, which can save costs spent on mechatronics.

Cable-collision (or cable interference) can also occur for CDPMs with rotational DoF, as discussed by Verhoeven [43]. For purely translational CDPMs, cable collision is not possible, as multiple cables attached to a single point cannot cross each other. In systems that do enable rotational DoF, grouping attachment points to multiple single points prevents cable-collision. In the first CYCLOPS prototype, the front cables and back cables are attached close to others of their kind; one might say they are grouped into a single front and a rear attachment point. For such systems, as shown by Verhoeven, cable-collisions only occur in the event of very large rotations that generally lie outside the feasible workspace of the mechanisms. The cable configurations of the prototypes developed in this thesis fall under this category and no cable-collision has occurred during usage. The CYCLOPS system is susceptible to another type of cable collision, as it combines two adjacent CDPMs to offer bimanual instrument control. Specifically, cable-collision can occur when there is an overlap in 3D space in which an attachment point of one instrument can be manipulated within the workspace of any of the attachment points of the other instrument. It is immediately clear that this is not the case for the original CYCLOPS, but this must be taken into consideration in new designs. During the thesis this type of cable collision is prevented by strictly separating the space spanned by the attachment points of the instruments from each other. It is also important to realize that cable collisions in CDPMs have limited effects, in contrast to collisions between rigid links, which often lead to violent mechanical failure. Cables will simply bend, primarily resulting in a change in the end-effector position. Even then, cable collision can be modelled [100] in the workspace, calculated, and purposefully embedded in the control system. Other methods for the detection of collisions are described in the literature, such as [101].

A third, more technical limitation of CDPMs is the calculation of the forward kinematics (section 2.2.1). In contrast to serial mechanisms, it is easy to algebraically compute the inverse kinematics of parallel mechanisms, but the forward kinematics requires numerical calculation. For normal control, the inverse kinematics equations are used to calculate the joint space (i.e. motor) positions for a desired pose of the end-effector. When the end-effector pose has to be calculated based on the motor position, however, it is necessary to use the forward kinematics. In the control of a system, the forward kinematics are used for calibrations in which the position is derived through measurement of the cable lengths. As this is computationally complex, other calibration strategies are used, such as [102][103][70]. The forward kinematics is also required for the calculation and optimization of the end-effector workspace, which leads to lengthy numerical computations, as discussed in section 2.2.5.

A final important aspect that can be seen as a limitation of CDPMs is the use of cables itself. Since the cables can only pull, not push, slackness occurs when the cable tension becomes too low

($t = 0$). Such slackness results in a loss of controllability, as it effectively results in the complete loss of one of the CDPM's actuation cables. To prevent this problem, it is necessary to calculate the cable tensions; this is referred to as the *optimal tension distribution* (section 2.2.3). Another important aspect relating to the cables is the stiffness of the cables, which is relatively low when compared to their rigid parallel counterparts (e.g. Stewart platform). Several models exist for the inclusion of cable elasticity in control methods, such as [104][105][106]. Finally, the use of cables may lead to cable sagging, in which the weight of the cables prevents them from maintaining a straight line. However, cable sagging is primarily an issue in larger systems and therefore unlikely to affect systems used for MIS.

2.6 Summary

This chapter provided a brief introduction to CDPMs and the applications for which they are used. These applications were used to illustrate the benefits and limitations of CDPMs (Table 2.1). The benefits include high payloads, workspace configurability and low costs. Limitations exist primarily in the areas of control and optimization. A number of key technical concepts relating to kinematics, workspace and control were also discussed. To understand how the benefits of CDPMs can be taken advantage of in MIS, Chapter 3 provides an overview of surgical robotic systems.

<i>Technical Advantages</i>	<i>Limitations</i>
<ul style="list-style-type: none"> • (Re-)configurable workspace and size • High dynamic capabilities • Compatible with deployable structures • High payload and efficient force transmission • Low costs • Inverse Kinematics are computationally inexpensive 	<ul style="list-style-type: none"> • An encapsulating support structure required (predominantly for <i>fully-constrained</i> CDPMs) • Redundancy of actuators/cables • Possible cable-collision • Forward Kinematics are computationally expensive • Possible cable slackness

Table 2.1 – A summary table of the technical advantages and limitations of CDPMs.

Chapter 3

End-effector mechanisms and actuation methods in Minimally Invasive Surgical Therapeutic Robotics

This chapter provides an overview of types of mechanical systems used in minimally invasive surgical robotics. This overview is used to determine in which areas challenges exist, and how, given the technical advantages discussed in previous chapter, cable-driven parallel mechanisms (CDPMs) may be used to realise improvements in MIS.

3.1 Aims and scope of the literature review

The aim of this literature review is to provide an overview of existing surgical robotic systems, and to find relationships between mechanical design choices and the clinical functions the systems are designed to perform.

Minimally invasive surgery is defined, in this literature study, as surgical procedures and interventions aimed at minimization of the trauma to healthy or critical tissues. While laparoscopic surgery is the best-known type of MIS (and sometimes used as a synonym), this literature study, in adopting this definition, holds to a wider notion of MIS, including systems used for flexible endoscopy, neurosurgery and percutaneous interventions. The resultant wider scope grants better insight into what technical solutions are used for specific problems and where opportunities lie for

CDPMs, and is thus conducive to the fulfilment of objective one of the thesis⁶. In neurosurgery, for instance, MIS has obvious benefits: it minimises trauma in the brain and avoids critical brain structures. Out of the scope of this literature study are non-contact therapeutic MIS technologies involving the emission of energy into the patient, as the challenges which these systems face are completely different from the challenges of systems that mechanically interact with tissues. An example of such a technology is High-Intensity Focused Ultrasound (HIFU) in which ultrasonic waves are used to achieve ablation of tissue, without the need for any incision [107]. Other examples are energy-emitting technologies such as those used in radiotherapy (e.g. Gamma Knife, CyberKnife). Similarly, untethered micro robots (e.g. [108]) and solutions which use magnetic fields as the main method of actuation [109] of a surgical instrument are left out of the scope, as their therapeutic applications are still limited and they do not incorporate mechanical links.

With regard to the term *robotics*, this review also applies a broader sense of the word, in which robotics is not limited to systems that are autonomous or pre-programmed. Tele-operated master-slave devices, in which a human controller is responsible for the actions of the system, are included within this definition. These account for the majority of surgical robotic systems. Handheld devices are sometimes described as ‘robotic’. However, with this definition it becomes hard to distinguish between conventional surgical (e.g. laparoscopic) instruments and robotic instruments. Therefore, systems with a direct mechanical interface between the surgeon’s input and the instrument’s actions are excluded. There are a number of exceptions to this, specifically in systems where the mechanical linkage is flexible (e.g. flexible torsion cables, pull/push cables) and in which the transmission mechanism can theoretically be of arbitrary length. An example of this is the flexible endoscopic STRAS Robotic system [110], which derives from the earlier-developed manually controlled AnubiScope (Karl Storz, Germany). The endoscope and the instruments of the bimanual system were originally controlled by rotating multiple dials, making complex procedures cumbersome. As the system is mechanically driven by tendon-sheath mechanisms, the dials can easily be converted into mechatronic actuation (i.e. leading to the STRAS system). Similarly, other currently manual systems are included in this literature study.

The focus of this review lies on *endoscopic surgical robotics* and is discussed in section 3.2. Endoscopic surgical robotic systems can be subdivided into rigid and flexible endoscopic systems (section 3.2.1 and 3.2.2, respectively); the available mechanical solutions and technical challenges

⁶ As given in Chapter 1: “To identify key technical advantages and disadvantages of CDPMs compared to other robotic architectures for MIS”

differ significantly between these two subcategories. Rigid endoscopic systems can be further subdivided in multiport and single ports system (section 3.2.1.1 and 3.2.1.2, respectively).

However, the field of surgical robotics has a wide range of surgical disciplines, which are not limited to endoscopy alone. Surgical robotics developed for applications such as image-guided surgery and interventions and microsurgery have their own set of design requirements, which have led to the choice of specific mechanical designs. This is important in order to illustrate for what applications specific mechanical designs are successful, and to evaluate whether these types of mechanisms can bring advantages in other fields of MIS surgery. As such, section 3.3 includes a short overview of image-guided surgical robotic systems and microscopic surgical systems.

3.2 Endoscopic Surgical Robotic Systems

Endoscopic surgical systems have been reviewed in earlier academic works, such as Vitiello et al. (2013)[33], Diaz et al. (2015) [111], Zhao et al. (2015) [112] and Simaan et al. (2018) [113]. Yeung et al. provided an overview of endoscopic robotic platforms, including mechanically controlled systems, in 2012 and 2016 [114][115]. Endoscopic surgical systems discussed in these reviews and others are described in sections 3.2.1 and 3.2.2.

Almost all systems described in these reviews use cable-driven, snake-like mechanisms to achieve end-effector dexterity. In such systems, the actuation units (commonly DC motors) are placed far from the surgical end-effector to allow for miniaturization of the instruments. However, as is mentioned by almost all authors, achieving sufficient force and motion accuracy are major issues, which are a result of cable friction and hysteresis. The same conclusion is drawn in a review concerning actuation mechanisms for MIS robotic systems (2016) [116], where a distinction is made with regard to the way in which the cable is guided from the actuator to the end-effector. The use of pulley guides is seen in mechanisms such as the da Vinci EndoWrist®, the benefit of which is relatively low friction. For flexible endoscopic systems, pulley guidance is often not feasible, resulting in the use of a tendon-sheath mechanism (TSM). While TSMs make it possible to pass through tortuous paths, the associated higher friction is a major challenge in achieving accurate control and providing sufficiently high forces with the surgical instruments. The friction also presents difficulties with regard to force sensing capabilities, which are required for surgical robotics to be implemented in intelligent systems with complementary situational awareness [117]. An overview of different types of segments used in SILS and NOTES platforms is given in [118], showing the wide diversity of compositions of segments with different DoF in these systems. As the authors argue, this is due to the fact that there is no clear data on what is the optimal configuration for surgery, partly due to the lack of clear design specifications.

3.2.1 Rigid Endoscopic Robotic System

3.2.1.1 Multi-port robotic systems

The first generations of the da Vinci® system and other older systems such as Zeus and AESEOP are all based on the use of robotics for performing multi-port laparoscopic surgery. Other systems include Senhance™ (TransEnterix Inc.), DLR MiroSurge, Raven and Versius® (CMR Surgical Ltd.). Surgical robotics in this area focus on improving intuitiveness by eliminating the fulcrum effect for the operator and replicating wrist movements at the end-effector, and by focusing on ergonomics, e.g. by creating a comfortable master console instead of requiring surgeons to spend hours standing while using laparoscopic instruments. The Senhance™ system was developed using conventional laparoscopic instruments as a control interface, including the fulcrum effect, but measures the forces at the proximal end of the surgical instrument to provide haptic feedback to the surgeon.

The mechanical design of multi-port extraluminal surgical systems predominantly focuses on two aspects: (I) the external mechanism providing tool positioning via a remote centre-of-motion (RCM, see Figure 3.1) around the entry point, and (II) the development of articulated end-effectors to increase the DoF in the body. The primary function of the RCM is to safely control the rigid surgical instrument within the body, without violating the constraints imposed by the entry port on the skin. The use of an RCM is seen in all multi-port extraluminal surgery (e.g. da Vinci®, Zeus, RAVEN, LER, Senhance™, MiroSurge, TISKA®[119]) and also in endoscope positioning systems (e.g. FIPS®[120], ViKY® (Endocontrol SA), SoloAssist II (AktorMed GmbH), FreeHand (Freehand 2010 Ltd), Endoassist, COBRASurge, EMARO (Riverfield Inc)). The da Vinci® and FIPS® (a derivative of the ARTEMIS [121] system), for instance, have been designed for use with a parallelogram to provide a RCM. The RAVEN uses a spherical linkage RCM mechanism. Parallel manipulators are also used in academic multiport systems, such as the PRAMiSS [122], in which the hexapod mechanism is coupled with a robotic arm to provide for micrometre tip accuracy through the RCM. While many mechanical solutions exist, software-controlled ‘virtual’ RCMs can be used for the same purpose. An extensive overview of RCM mechanisms up to 2012 is given in [123]. While new surgical robotic systems have been developed since, these systems still use similar RCMs as those described in earlier reviews. The use of virtual RCMs has been adopted in more recent commercial systems (Versius®, Senhance™). In particular, virtual RCMs in the Versius® system enable the use of conventional, and increasingly less expensive, robotic arms instead of dedicated hardware. Another recent academic development, the S-Surge system, combines a parallelogram with additional parallel links to provide 2DoF control around an RCM, with an additional 1 DoF for insertion of the surgical instrument [124]. The instrument itself has 4 DoF, offered by rotation, grasping and an articulated wrist. The advantage of the system is the low weight and size of the design, comprising a single controllable arm of 4.7Kg with 34x18x20cm

dimensions. It should be noted that the use of RCMs is not limited to multi-port extraluminal procedures only; they can also be found in single-port systems using a rigid shaft and percutaneous robotic systems.

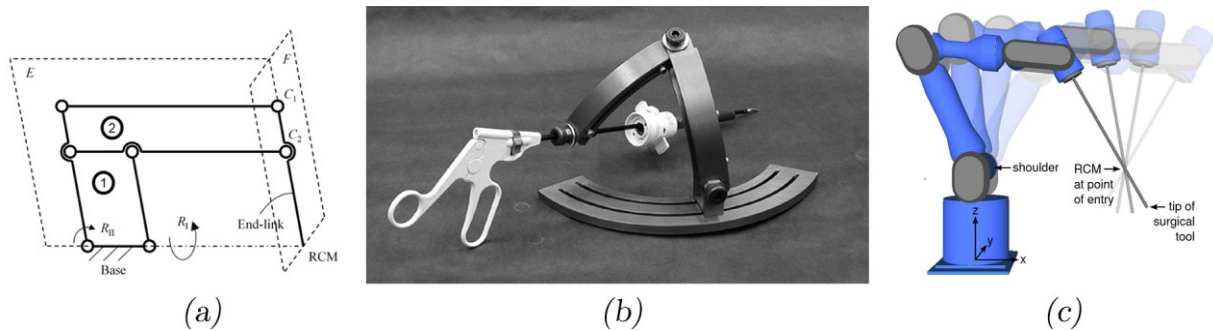


Figure 3.1 – Three different types of remote-centre of motion mechanisms used for minimally invasive surgery. (a) a double parallelogram RCM mechanism. Image source: [125]©2015 by ASME. (b) spherical RCM mechanism. Image source: [126]©2006 IEEE. (c) a ‘virtual’ RCM in which a robotic arm is constrained at a fixed point. Image source: [127] ©2007 IEEE.

The structure supporting the multiple slave arms, is responsible for a system’s footprint in the operating room (OR). The da Vinci system uses a centralized support structure with multiple passive arms to position the RCM and instruments over the patient. The Senhance™ system has multiple overarching arms on large carts that can be positioned to the specifications of a surgery. Both the da Vinci® and Senhance™ system take up a considerable amount of space inside the OR. Systems with smaller OR footprints are CMR’s Versius system, which uses much smaller carts supporting conventional robotic arms. Another method used to decrease OR footprint is the use of the bed-mounted robotic arms, as in the DLR’s MiroSurge system. Based on the patents filed by Verb Surgical, it seems that they are considering the table-mounted approach for their new system [128]. Another method for OR footprint reduction is to suspend the robotic system from the ceiling, as shown in the EndoPar system [129].

The articulated end-effectors of the surgical instruments are essential for the performance of more complex tasks, such as knot-tying and suturing. In robotic surgery, the EndoWrist is considered to be one of the key factors contributing to the success of the da Vinci system. Other examples of wristed instruments can be found in MiroSurge, RAVEN, and SOFIE [130]. In these systems, the wristed tip mimics the human wrist, offering additional DoF to the end-effector. While da Vinci®, MiroSurge and RAVEN are actuated through cables, SOFIE uses a geared mechanism for the wrist and a cable mechanism for the articulation of each jaw of the grasper. Wristed instrument tips are also found in handheld instruments, e.g. Radius [131], SILS™ Hand Instruments (Medtronic Inc.), RealHand® (Novare Surgical Systems, Inc.), FlexDex™ (FlexDex, Inc.), HandX™ (Human Xtension, Ltd.).

The development of new types of wristed mechanisms receives much attention within the academic community. An example is the hyper-finger, in which a decoupling ring is introduced between each segment to decouple the wire actuation of the two rotational DoF at each joint [132]. An extensive classification and overview of wristed instruments (including patents, and commercial and academic systems) has been provided by Jelinek et al. [133].

3.2.1.2 Single-port Surgical Robotic Systems

While the systems mentioned above were all developed to use multiple entry ports, there is a general movement towards decreasing invasiveness and reducing systems to a single port. By using the umbilicus as the entry point, patient cosmesis is further increased, resulting in virtually scarless surgical interventions. Another benefit is that these systems can often be used for a wider range of MIS applications, including endoluminal procedures (e.g. transoral surgery or transanal endoscopic microsurgery). The terminology used in literature to describe single-port systems varies; terms used include Laparoendoscopic Single-site Surgery (LESS), Single-Port Access Surgery (SPAS), Single-Port Surgery (SPS) and Single-Incision laparoscopic Surgery (SILS). This literature review uses the acronym SPS, mostly because the primary focus of this review is on single-port systems, rather than specific laparoscopic systems. While flexible endoscopic systems also can be referred to as single-port, the current section is mainly concerned with SPS using rigid scopes; flexible SPS systems are discussed in sections 3.2.2. This distinction is made because the rigid shaft allows for mechanisms that require a straight pathway; as such, there are specific clinical and technical differences between rigid and flexible systems.

The first single-port procedures were performed by surgeons introducing multiple straight laparoscopic instruments through a single incision. While further developments brought pre-curved instruments to facilitate and improve tissue triangulation, this further complicated laparoscopy as in addition to the fulcrum effect, it also introduced mirrored instrument motion. The mirroring is the result of the crossing of the instruments at the port, due to which an instrument shown on the left is controlled by the right hand and vice versa. While there is evidence that this approach has been successful in general surgery [10], it has not yet seen wide-spread adoption. As with conventional laparoscopy, it is thought that opportunities to overcome these technical challenges may be found in robotics.

In robotics, there are two types of approaches for the performance of surgery through a single incision, depending on whether the instruments are integrated in a single shaft or not. The latter method (not integrated) resembles single-incision laparoscopic surgery by multiple instruments through a single incision, in which each instrument can be individually inserted and controlled. The 'X'-configuration, in which instruments cross, is the most evident example of such systems. The use of the da Vinci system for single-port surgery has been explored for applications such as single-port nephrectomies [134], prostatectomies [135] and transvaginal NOTES [136]. However, despite successes, instrument collision remains an issue. Intuitive Surgical introduced the single-port VeSPA instruments for the da Vinci Si as an alternative to conventional multi-port instruments (Figure 3.2a)[137]. These semi-rigid instruments are inserted through a multichannel single-incision port that

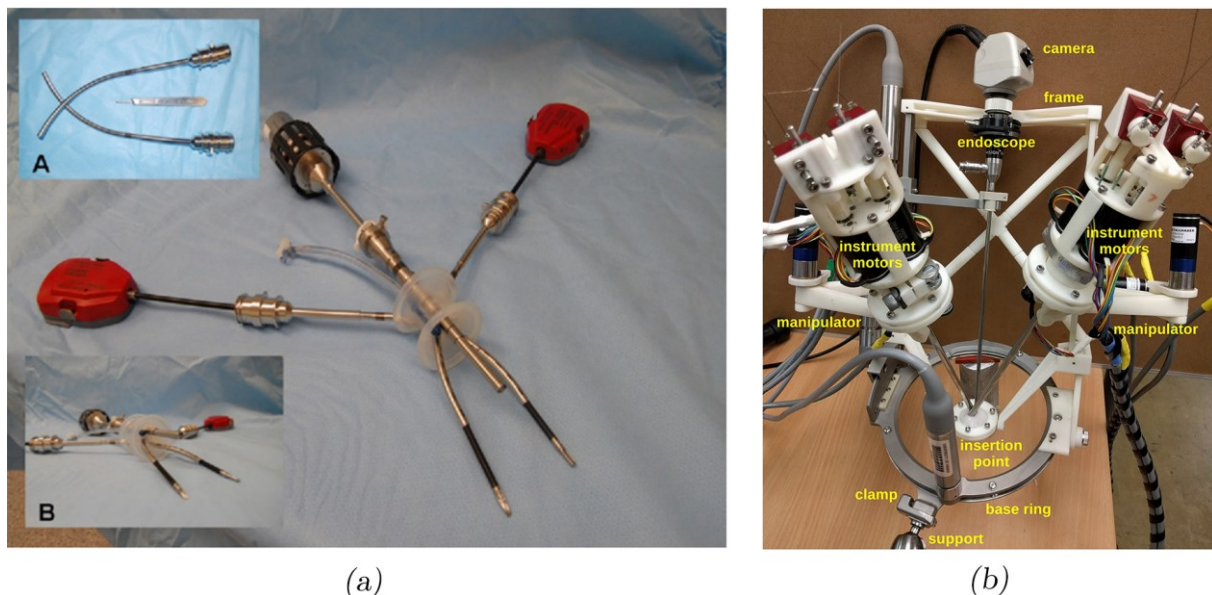


Figure 3.2 – (a) The VeSPA instruments (Intuitive Surgical, Inc.). Image source: [137]. (b) The LER system adapted by Berkelman et al. for single-port robotic surgery. Image source: [140].

has pre-bent rigid cannulas to bend the VeSPA instruments, thereby providing instrument triangulation. The main limitation of the system is the lack of an endoWrist to provide sufficient end-effector DoF and the reduced range of motion during surgery, making complex procedures cumbersome [138]. Berkelman et al., who previously developed the LER system, also introduced a single-incision version of the system which uses two rigid instruments with articulated tips instruments (Figure 3.2b) [139][140]. Choi et al. developed a similar system using two instruments with a specific parallel elbow joint to enable high end-effector payloads [141] (Figure 3.3a).

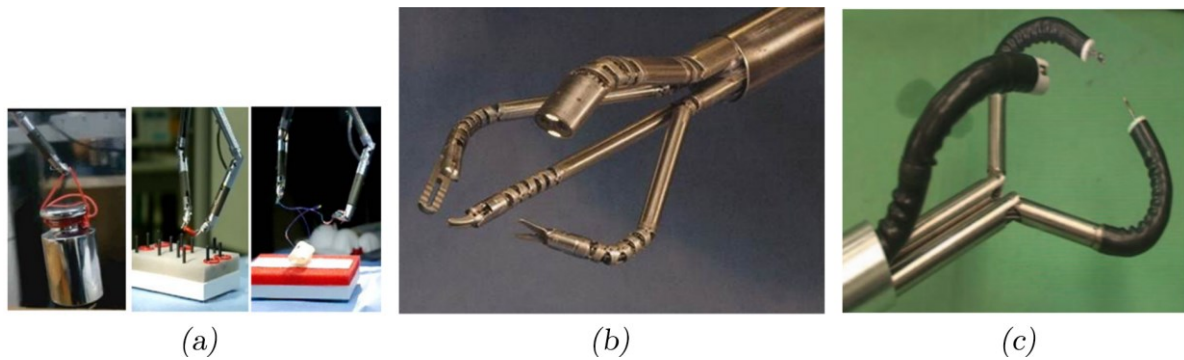


Figure 3.3 – (a) The system developed by Choi et al. with a modified elbow joint for high end-effector payloads [141]. ©2014 IEEE. (b) The da Vinci SP® end-effector (Intuitive Surgical, Inc.). Image source: [142]. (c) The HVSPS developed at TU München [143].

A second approach is to integrate all instruments into a main shaft, and individually controlling multiple instruments at distal end of the shaft. As illustrated in [118], the single shaft requires the articulated instruments to have multiple segments to achieve sufficient triangulation. The specific mechanical topology and actuation methods vary between commercial and academic systems, but with a few exceptions, these systems can be classified as redundantly actuated serial or continuum mechanisms. In both cases, there is motion redundancy in the system, i.e. the DoF in the system are higher than the number of individually controllable actuators.

Intuitive Surgery developed a new generation da Vinci robot specifically for single-port surgery: the da Vinci SP® system (FDA clearance June 2018). The main shaft contains the endoscope and two deployable surgical instruments with articulated tips (Figure 3.3b). The articulated tip has two sections; one ‘elbow’ joint that provides instrument triangulation and a second snake-like mechanism, which can ostensibly be classified as a redundantly actuated cable-driven serial mechanism. The benefit of integrating multiple instruments into a single shaft is that it makes it possible to use the same system for such surgeries as transoral robotic surgery (TORS) [144]. The HVSPS (Figure 3.3c), a system with similarities to the Da Vinci SP, was developed at TU München [145]. It uses an elbow joint combined with a redundantly actuated serial mechanical wrist. The elbow mechanism is actuated by a cable mechanism, but this leads to a high force reduction of factor 50. Due to this ratio, the forces on the tip are low and the system is able to achieve end-effector forces of up to 1.6N. The HVSPS has also been explored for NOTES applications [143]. The mechanics of the system were not altered, and still required the use of a rigid shaft, and was evaluated based on a simulated transsigmoidal cholecystectomy. The micro-IGES (Imperial College London) was specifically developed for Transanal Endoscopic MicroSurgery (TEMS). The system is adapted to the confined workspace of the rectum and uses two cable-driven redundantly actuated serial

mechanisms, providing a total of 7 DoF. The instruments are able to exert a force of up to 3.5N, with a maximum calculated cable tension of 65N [146].

TransEnterix has been developing a single-port system, called the SurgiBot (after being denied FDA approval in 2016, the technology was transferred to a Chinese company for commercialization in China [147]). The main concept is based on the previously developed manually controlled SPIDER system, and using a multichannel cannula to insert two flexible instruments, a scope and, if required, another rigid instrument. The tips of two flexible instruments are controlled via a hollow snake-like mechanisms, referred to as *Instrument Delivery tubes* [148]. While not specifically disclosed by the manufacturer, it is clear based on images that four cables are used for control of the end-effector, indicating redundancy in actuation and hinting towards either a redundantly actuated serial mechanism or a continuum mechanism. An important addition to the mechanism is the use of a parallel structure, a bar mechanism, at the distal tip to offer stability and triangulation for the flexible instruments. The bar mechanism provides the same functionality as the elbow joint in other systems. In 2017, a group of the Tianjin University developed a system similar to the SPIDER in which the main shaft containing both instruments can be articulated and locked via a variable stiffness mechanism [149].

Continuum mechanisms have received attention from multiple researchers [150][151][152][153][154]. The SPORT Surgical system⁷ (Figure 3.4b) originated from academic research under the name IREP and features a dual-arm system that can be inserted through a 15mm port [151]. Both arms are snake-like continuum mechanisms with 4 DoF, each supported by a 2-DoF parallelogram. Push-pull Nitinol rods are used for control and are actuated externally. The SURS system (2014) [152] uses two 6 DoF surgical arms consisting of two distal continuum segments (Figure 3.4b). The system can be deployed through a 12mm diameter port. One of the main limitations of the system is its inability to cope with high payloads, showing a large deflection at loads of 2N. The NeuRobot (2002) offers bimanual control of three 1mm diameter articulated surgical instruments [155] and a 4mm scope through a 10mm port. The system uses a brain dilation device for insertion and accessing of the area requiring dissection. However, the instruments only have a single joint, which restricts the workspace considerably. Another similar system, SiromanS, was developed in 2011 at the University of Chonman, with a focus on increasing the workspace [154]. The developers successfully increased the workspace by using a continuum mechanism at the instrument tip; however, the implementation required a 20mm port and used two 4mm flexible instruments. For

⁷ Titan Medical Inc. is planning for FDA approval in 2019 [378].

neurosurgical applications, positional accuracy may well be considered to be even more important than in other procedures, and the end-effector accuracy of 1.35mm found in the latest version [156] may be problematic. The iSnake is another robot developed as a single-port system at Imperial College London. The original iSnake [157] was primarily a flexible shaft with embedded motors (and is further discussed in section 3.2.2); an adaptation of the system using a rigid shaft was subsequently developed in which two 4DoF continuum instruments were used in *in vivo* porcine trials [153].



Figure 3.4 – Two single-port systems using continuum mechanisms as manipulators. (a) the SPORT system. Image courtesy: Titan Medical, Inc. (b) The SURS system [152] ©2015 IEEE.

Serial mechanisms, when not redundantly actuated, have been demonstrated to be able to exert higher forces than their redundantly actuated counterparts. The ARAKNES SPRINT system (2010) uses multiple-link serial mechanisms, controlled via joint gears to provide two instruments with six DoF each [158]. Two DoF are actuated using an external motor with rigid shaft transmission. The remaining four DoF are actuated by on-board motors (elbow and wrist articulation). The system was designed to exert at least 5N end-effector forces, and this has been confirmed experimentally while moving at a speed of 1m/s. The speed is important as in many systems the payload is measured for a static pose, which is generally higher than the forces a system can deliver while moving.

Virtual Incision, Corp. also developed a system with on-board motors with the aim to create single-port technology in the form of a small portable device. The system originates from earlier academic research [159]. The system shows the use of a geared mechanism for actuation of 2 serial links, with a total of 5 Dof per surgical instrument. The gripper is actuated with small DC motors placed in the last link of the end-effector. The force exertion capability is high, with a theoretical end-effector force of 30N in all directions [160]. The footprint in the OR is impressively small, and the cross-sectional area of the shaft is with 4.13cm² comparable to other single-incision devices.

Different names were used during the initial development of the system, including SISR [161], CubReich-Bot, and Lou-Bot [160].

A recent commercial product for SILS is the manually controlled SymphonX™ (Fortimedix Surgical BV). The system is introduced via a 15mm trocar port and uses two 5mm instruments. Two additional channels (5mm and 3mm) are used for additional instruments and for the endoscope. The system has received both FDA and CE marking. No extensive clinical study has been performed using the system. Based on the images published by Fortimedix, the system appears to use a cable-driven continuum mechanism to convey the motion of the handles at the instrument tip.

3.2.1.3 *Robotic systems designed for higher payloads*

The force exertion capability has been identified as an issue by many researchers, leading to the development of new mechanisms with specific joint designs. One such design can be found in the PLAS Robotic system (2014), in which serial links are used to control two instruments integrated into a single shaft (Figure 3.5a). In order to be able to sustain higher payloads, PLAS uses a plate spring mechanism for the rotation instead of conventional actuation using a cable-driven antagonistic mechanism. Each of the two arms has 6 DoF and is able to sustain payloads of >14N [162]. Another group used a hybrid rigid parallel bar-mechanism for the development of a high-payload single-port robotic device system [163]. As a result, the 7mm instrument was able to lift >15N with its articulated joint. The forces were transmitted using an outer sliding shaft placed around the straight rigid shaft, acting as a parallel mechanism. A completely different approach for articulating distal tips of surgical instruments was developed by Sekiguchi et al. at Waseda University, Japan [164]. Their system consists of an articulated main shaft (2DOF) with a camera; two surgical instruments are guided through the shaft. It uses a specific mechanism called a double-screw drive mechanism (Figure 3.5c), which involves 3 parallel-placed universal joints connecting the distal tip to the main instrument shaft [165]. The universal joint allows each parallel shaft to bend in 2 DoF, while the length of two of the three parallel shafts can be extended/contracted by a screw mechanism enabling 2 DoF flexion of the distal tip. The third shaft does not vary its length, but is used for additional functionality such as gripping. Including the rotation/insertion, this makes for a total of 5 DoF. The system was validated in an *in vivo* porcine animal study [166]. One of the limitations encountered was the small workspace of the end-effectors for abdominal surgery.

Other research has focused on developing new joints or actuation mechanisms, though this has not (yet) led to the development of a full bimanual system. Shin et al. (2013) developed an elbow joint mechanism using a sliding slot mechanism to achieve forces of up to 9.2N at 75mm from the joint [167]. In 2014, Hong et al. developed a mechanism similar to [164] with a parallel structure to

achieve higher rigidity [168]. The use of parallel links to control a wristed end-effector was previously illustrated in the MIPS system, which sought to achieve high accuracy and high payload capacity [169]. Another use of parallel joints can be found in [170]. Another proof-of-concept was shown using parallel kinematics, demonstrating an ability to accurately control the instrument during a high-speed motion while loaded with a 4N load [171]. The main goal of this system is to use the parallel structure for the measurement of haptic forces on the tip. Lee et al. (2012) showed a proof-of-concept using a serial chain of 4-bar parallel mechanisms [172]. The parallel mechanisms are used to provide high payloads while keeping the arm lightweight and relatively compact. Unfortunately, neither the workspace nor the payload of the system was explored experimentally.

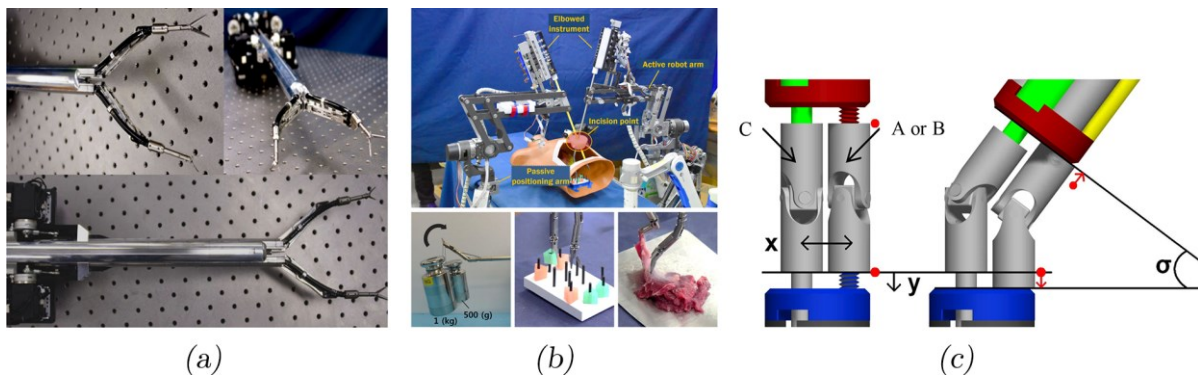


Figure 3.5 – Three different designs with a parallel structure to provide higher forces at the instrument tip. (a) The PLAS system for single-port surgery with high force requirements uses a parallel plate spring [162]. (b) A single port system with parallel links at the joints to enable forces up to 15 Newton [163]. (c) The double-screw drive mechanisms used developed at Waseda University to provide high stiffness articulated joints [165] ©2007 IEEE.

All but one of the above systems (the exception being the PLAS Robotic System [162]) are categorized as parallel mechanisms. Even the PLAS system can be regarded as having some form of parallel links, since it incorporates plate springs, which are a compliant version of a bar mechanism such as in [162]. One mechanism not discussed in this section but mentioned earlier is the SPORT surgical system. This system uses a parallel bar mechanism to offer stability at the elbow joints of the continuum mechanisms. While these solutions show that high force exertion can be realized, most parallel structures are reliant on the sliding of (semi-rigid) elements. These mechanisms are therefore well suited for systems with a rigid shaft, but the same concepts will lose part of their qualities when applied to flexible endoscopic systems. Semi-flexible elements required to convey the sliding motion will need to run alongside or inside the endoscope, and will influence the stiffness and dexterity of the endoscope when too rigid. When too compliant, however, these transmission mechanisms lose much of their ability to provide stable support, and therefore a trade-off needs to be sought between sufficient instrument stability and endoscope dexterity. Additionally, friction between the endoscope

and the transmission mechanism is introduced when the endoscope is navigated through a tortuous pathway, introducing errors on positional accuracy. However, depending on specific clinical needs in terms of positional accuracy and forces, such parallel constructions might still be worth exploring.

3.2.2 Flexible Endoscopic Robotic Systems

The development of flexible endoscopic systems has received attention from traditional endoscope manufacturers aiming to transform their systems, which are predominantly used for screening and diagnostics, to make them suitable for full therapy. Olympus Corporation, having the largest market share in endoscopy, developed a flexible endoscopic system named the EndoSamurai [173]. Each of the two surgical end-effectors is controlled in 5DoF. An additional proximal elbow was added to allow for better triangulation. The system shows capabilities in bimanual tasks like suturing, endoscopic submucosal dissection (ESD) and full-thickness resection [174]. While the force exertion capability has not been explored, one study mentions that force is a limiting factor when using the system for traction and countertraction of larger manoeuvres [175]. Aside from being a snake-like mechanism, the specific mechanism and actuation method for the arms is not clear. Another system developed by Olympus is the R-scope [176]. The first generation of this system was an endoscope specifically modified for the performance of ESD, by providing lifting capability of a grasper inserted in one of the two instrument channels. A second version was developed for NOTES, by also providing lateral deflection to the instrument mounted in the second instrument channel [177]. One of the drawbacks of this system has been found to be the complexity of its manual control; furthermore, it does not provide sufficient degrees of freedom for the instruments to be used in NOTES [178].

In 2010, Karl Storz developed the manually controlled Anubiscope system [179] in collaboration with IRCAD in Strasburg. They adapted the flexible endoscope, itself a redundant serial mechanism, to include two surgical graspers that are deployed at the end of the device. An additional elbow joint was added to provide additional triangulation to the instruments. Recently, a robotic version of the system was launched in the form of the STRAS system [110]. A second generation (STRAS v2) has been evaluated and demonstrated 0.9N tip bending forces and a 3.9mm+-1.89mm repeatability on the position. While this is large, the user in the loop can compensate for it. The system was successfully able to perform multiple ESDs on an *in vivo* pig model [180].

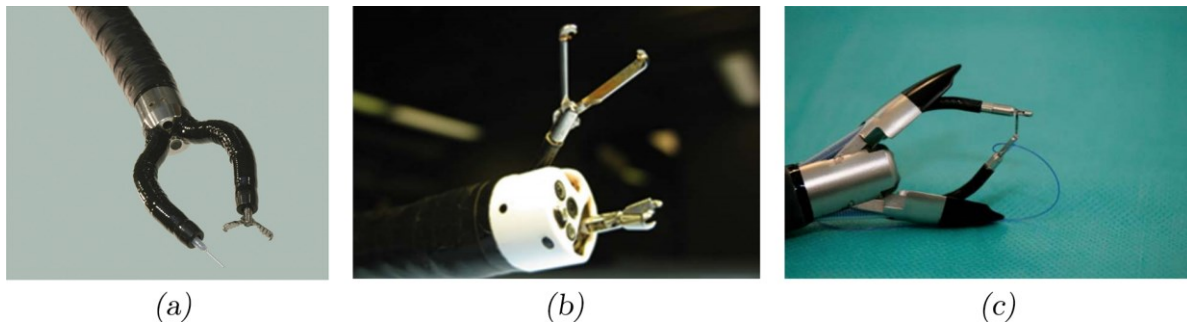


Figure 3.6 – (a) Endosamurai system (Olympus Corp., Japan). Image source: [174]. (b) The R-Scope (Olympus Corp., Japan). Image source:[181] . The Anubiscope (IRCAD & Karl Storz Endoskope). Image source: [179].

In collaboration with Pentax, a Japanese research group evaluated the use of three endoscopes for bimanual surgery: a larger scope with two 7mm instrument channels, in which two inner endoscopes of 4.9mm were placed [182]. The instrument channels of the inner endoscopes were used for the insertion of 2mm flexible endoscopic instruments. While the system enabled the physicians to remove the mucosal layer in an *in vivo* porcine model, one of the drawbacks was the complexity of controlling the system.

In addition to endoscope manufacturers, other companies have recently begun developing flexible endoscopic robotic systems as well. The Medrobotics Flex® Robotic System uses a combination of a variable stiffness sheath with a flexible inner system to perform transoral robotic surgery, and obtained FDA approval in 2015. In 2017 and 2018, additional FDA approval was obtained for colorectal, gynaecological, thoracic and urologic surgeries. The main concept of the Flex system is based on the previously developed technology of the HARP system [183]. HARP was originally designed for cardiac surgery, and also has been referred to as CardioARM [184]. The system uses two concentric snake robots which can change stiffness by tensioning the cables within the mechanism. The outer snake has three cables for steering and stiffening, whereas the inner has only one cable to change the stiffness. The change in stiffness is achieved by the joint design in which spherical joints slide over each other; when cables are tensioned, the friction between these joints increases, thereby stiffening the entire structure. While the HARP concept is mainly concerned with providing access methods for flexible endoscopy, the Flex system adds two manual controlled flexible endoscopic instruments to the tip to perform transoral surgery (TORS) [185][186].

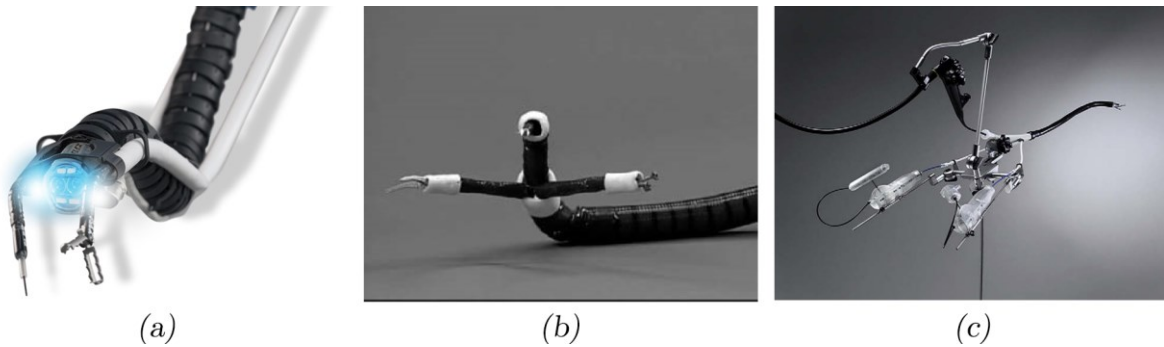


Figure 3.7 – (a) Medrobotics Flex® Robotic System . Permission for use of image granted by Medrobotics Corporation. (b) The Cobra system (USGI Medical, Inc.). Image source: [187].(c) the DDES™ system developed by Boston Scientific Corp. Image Source: [173].

USGI Medical, Inc. developed the Incisionless Operating Platform™(IOP), which is based on the previously developed technology of the Transport and Cobra systems [188][187]. The Transport system is a flexible overtube that acts as a variable stiffness mechanism, and thereby is able to lock the entire structure for NOTES purposes. The overtube system provides two instrument channels, but similar to other dual-channel endoscopes no additional articulation is provided at the distal end and therefore tissue triangulation remains a challenge [189]. By combining the Transport with the Cobra system, the two instruments and an articulated camera can be controlled individually from the main shaft. The instrument triangulation capabilities of are still limited in the IOP system; however, the system's feasibility for the performance of transgastric cholecystectomy and gastric bariatric procedures has been demonstrated [190].

The Direct drive endoscopic system (DDES™) developed by Boston Scientific Corporation is a manually controlled endoscopic sheath from which two instruments can be controlled [191]. The flexible sheath contains three working channels, one for the optic and two for the flexible instruments. The flexible instruments are controlled in 5 DoF each, while the guide sheath has an additional 2DoF. In benchmark tests, suturing and knot-tying were shown to be complex but feasible. One main limitation described by the authors was the lack of proper triangulation and robustness during the tasks. The system was used to perform gastric EMR/ESD in an *in vivo* animal study, but it still took considerable time to perform the procedure [192].

EndoVia Medical, Inc. (now part of Hansen Medical) developed the ViaCath⁸ system for robotic surgery within the GI tract (NOES and NOTES) [193]. An early version of the system consisted of instruments with a flexible backbone which could be actuated in 6 DoF (4 bending, 1 rotation, 1 translation). Tests revealed that the system had a low force exertion capability of only 0.5N. The

⁸ The ViaCath system is partly based on the earlier developed Laprotek system.

main reason for this had to do with the compliance and the redundant actuation of the flexible backbone. A later version used a cable-driven serial mechanism with 6 joints to increase the stiffness of the system. A stiffness of 1.15deg/mNm was reported, which can be used to approximate stiffness at the tip, located at 75cm from the tip: 1mm tip displacement would require 0.009N of force (or, when linearized, 1.4N to bend the instrument 90 degrees). The authors acknowledge that forces can be increased by accounting for the friction within the instruments, though it is unlikely that this will drastically increase the forces at the tip.

In 2008, Phee et al. developed a robotic add-on to a conventional flexible endoscope that provides two instruments in order to enable the performance of complex surgical tasks [194]. The anthropomorphic design is based on the human arm, and provides 5 DoF to the surgical end-effector. Actuation is performed by cables, guided through a flexible sheath (Bowden) along the endoscope. Two antagonistic cables are used to articulate a single DoF, and are simultaneously actuated by a single DC motor placed at the proximal end of the endoscope. A more advanced version of the system, called MASTER, was used to perform advanced endoluminal and transluminal surgery during *in vivo* animal studies [195](Figure 3.8a). Force capacity tests of the system showed that the mechanism is able to exert forces up to 5.2N at the end-effector. The system is currently undergoing clinical trials and belongs to a Singaporean company called EndoMaster Pte Ltd.



Figure 3.8 – (a) The MASTER system developed by Phee et al. [195] ©2009 IEEE. (b) The laser sintered flexible robot developed by the MiMed group, TU München [196]. Image Source: [197] ©Feussner et al.

A group in Hong Kong developed flexible instruments using a continuum mechanism. An early stage design was developed in 2014 [198] and optimised for ESD in 2016 [199]. The 6mm instruments are used in combination with the Transport system, which had sufficiently large working channels. The continuum mechanism in each flexible instrument is actuated by four SMA cables guided through a tendon-sheath assembly from external motors to the end-effectors. An important part of

the control method included compensation of non-linear behaviour of the tendon-sheath mechanism (e.g. backlash and hysteresis). The system is able to lift 48gram of weight, which they considered sufficient for ESD when taking alternative triangulation strategies into account. Bardou et al. presented a bimanual system using flexible hollow arms in which surgical instruments are placed [200]. The system provides 4 DoF with each arm, which are actuated via cables. A group at TU München developed a bimanual flexible robot that can be manufactured through selective laser sintering [196] (Figure 3.8b). The system is based on a continuum mechanism actuated by push rods, and a cable for additional control. The system was validated in a weight-lifting test and was able to exert forces of 2-5N.

Zhao et al. developed a bimanual flexible surgical system that uses continuum mechanisms to provide dexterity to the instruments [150]. While the system is manually driven, the system can be easily converted to a full robotic system; they did so with a single-port version of the system, which was described above as the SURS system. The manual fully flexible system was able to lift weights of 200g, and 500g when a large part of the proximal continuum mechanism was constrained.

An academic group from Japan developed a scorpion-shaped endoscopic surgical robot for NOTES and single-port surgery [201]. It uses cables to actuate each of its two instruments, of which one is used for the opening and closing of the surgical instruments and the other four are actuated in antagonistic pairs to bend the flexible backbone in 2 DoF. The system was designed to exert forces of up to 3N with each instrument.

A single-port system with a flexible shaft was developed in Korea (2015), in collaboration with Samsung. This system comprises two sections; a 3 DoF flexible shaft and two 7DoF instruments [202]. The elbow and the shoulder joints of the mechanism are designed to achieve high accuracy and payloads. The joints consist of serial links with a cable-actuated rolling gear mechanism. The cable forces are amplified and the cable motion is reduced through the use of a pulley mechanism at the joints. Hence, a larger proximal motion is required to realize an angular motion at the tip, enhancing accuracy and improved force transmission enabling higher end-effector payloads. Another interesting aspect of the system is the use of a variable stiffness mechanism for the flexible shaft, based on the mechanism described in Kim et al. [203]. The mechanism uses rolling joints that can be used to increase stiffness by increasing the tension in the antagonistic cables.

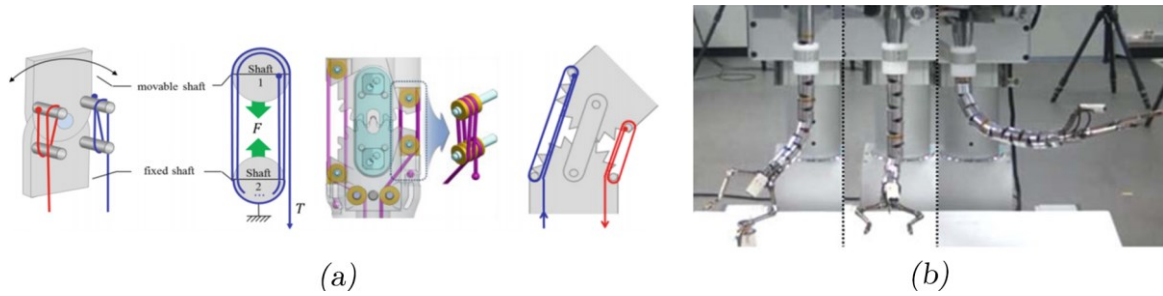


Figure 3.9 – The two components of the system designed in collaboration with Samsung [202] (a) The joints design used to increase the joint stiffness and payload. Image source: [202]. (b) The variable stiffness flexible shaft with the instruments mounted on it. Image source: [203].

Another Korean group from KAIST University is exploring the same mechanism in their development of a surgical robot. The K-Flex system uses the variable stiffness mechanism as main shaft which holds two surgical instruments. While there are as yet no extensive academic publications on the system, the system was presented at the Hamlyn Symposium on Medical Robotics 2018 [204] and won the Surgical Robotic Challenge [205].

The iSnake is a system developed at Imperial College London in 2011 [157] [206]. The serial structure comprises multiple segments with on-board motors, as a working channel and an outer diameter of 12.5mm. To accommodate the motors, the segment lengths are 35mm or 40mm for 1 DoF and 2 DoF articulation, respectively. Individual segments were tested for forces, which revealed that the joint design allowed for an average force of 0.57N at the end of a single segment, corresponding to 24mNm torque [206]. While tip forces for a full mechanism have not been evaluated, a calculation based on the five segments (3 yaw, 2 universal joints), each 42mm in length, yields tip forces of 0.11N. The limited force exertion capability of the embedded micromotor design led to a change in actuation method in the latest version, the i²snake [207]. The i²snake uses a redundantly actuated cable-driven serial mechanism with rolling joints. The improved torsion of each link has not been evaluated experimentally, and thus it is not clear whether the new joint design has resulted in a payload improvement. Unlike in earlier systems, the snake mechanism is used as the main shaft with four working channels, which allows for flexible endoscopic surgery.

Lehman et al. developed a bimanual robot that anchors to the peritoneal wall using magnets. The two arms are actuated by on-board permanent magnet DC motors and tethered to a control unit outside of the body [208] (Figure 3.10a). The system has a diameter of 26mm, and each instrument arm can be extended axially to increase the workspace of the system. The system has shown feasibility in performing cholecystectomy during *in vivo* animal trials [209].

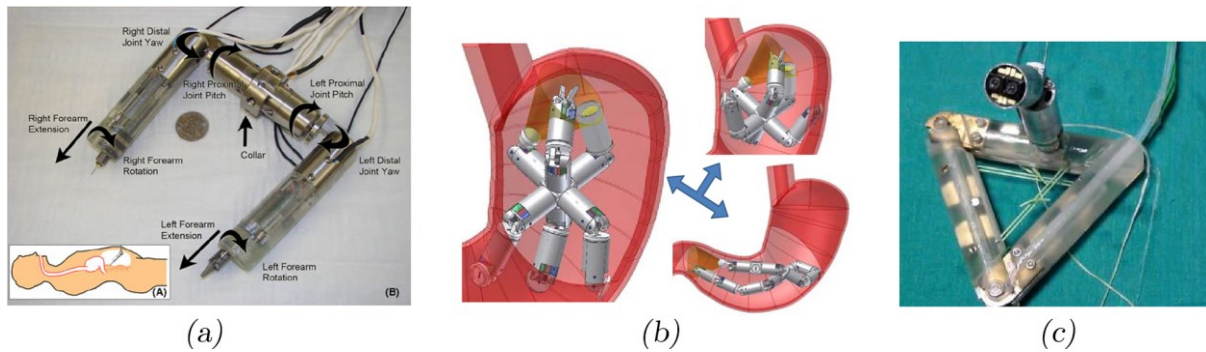


Figure 3.10 – (a) The system developed by Lehman et al. which is anchored on the inside wall of the peritoneum. Image source: [208]. (b) The reconfigurable concept using several modules developed by Harada et al. [210] ©2009 IEEE (c) The reconfigurable system earlier developed by Harada et al., developed with magnetic anchoring to the peritoneum [211] ©2012 IEEE.

Attempts have also been made to develop reconfigurable modular systems for MIS. As these are often untethered, they are strictly speaking not flexible endoscopic systems, but are best categorized as NOES and NOTES. Harada et al. proposed a reconfigurable system consisting of modules that each contain integrated motors for actuation of joints and active elements, such as a grasper [210] (Figure 3.10b). The standard (or structural) module consists of two miniature DC motors to provide axial rotation and 90 degrees joint articulation. Another module was created as a gripper for biopsies. In addition to the two DC motors, each module has a battery and wireless control board resulting in an overall module diameter and length of 15.4mm and 36.5mm, respectively. Permanent magnets are used for connection between modules. Considering the number of components integrated within a single module the size of is impressive. However, the main limitation of the system is providing sufficient torsion for high payloads. The authors only mention a maximum theoretical motor stall torque of 10.6mNm, but taking the length and weight of each module (5.6 grams), the torque is barely sufficient to lift the weight of three serially linked modules. Tognarelli et al. developed another reconfigurable system based on the same modules [211]. This system has the advantage that it is magnetically mounted to the abdominal wall and primarily intended for visualization. Tortora et al. expanded the range of purposes by adding other modules for the performance of surgical tasks, such as graspers and cameras [212]. A gripper module demonstrated end-effector forces of up to 1.2N. The proposed modules can be assembled using a magnetic coupling mechanism described in [213].

3.2.2.1 Flexible robotic systems for Endoscopic Submucosal Dissection

A specific group of robotic systems has been developed for ESD. ESD is an advanced therapeutic technique to remove early stage gastrointestinal cancers via a flexible endoscope. The complexity ESD has sparked engineers and clinicians to developed new techniques and devices. Systems mentioned earlier have been developed for ESD [110][176][199]. Many of these systems offer general bimanual dexterity, and therefore can be seen as more widely applicable for other

procedures. Another type of approach is the development of mechanisms that are specifically tuned to a specific procedure, in particular for ESD. A recent (2017) review of robot-assisted devices for ESD was given in [214]. Providing traction is seen as one of the most important aspects in ESD – an importance which is illustrated by the often creative methods developed to achieve it, such as the use of forceps actuated by external magnets, the introduction of miniature 2-mm percutaneous graspers to lift the tissue, or weights to let gravity assist with traction; other techniques often employ clips attached to lines. While these methods are interesting on their own merit, they fall out of the scope of the current literature review; instead, they will be discussed in Chapter 4.

The LumenR™ Tissue Retraction System [215] is a flexible system specifically developed for ESD (Figure 3.11a), which was acquired by Boston Scientific in 2016. The system uses a deployable operating chamber with two instrument guides which can be controlled in 3 DoF, and a 4th DoF is created through retraction and extension of the flexible endoscopic instruments relative to the instrument guides. Both instruments are used as graspers to lift the submucosal layer, while a third electrocautery instrument is used via the endoscope's biopsy channel to dissect the tissue.

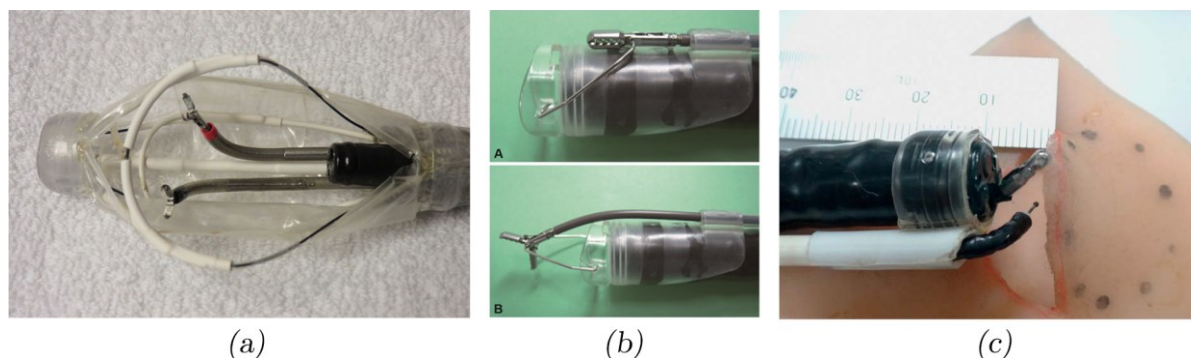


Figure 3.11 – Three devices developed for ESD procedures. (a) The LumenR™ Tissue Retraction System (Boston Scientific Corp., USA). Image source: [215]. The Endolifter (Olympus Corp., Japan). Image source: [216]. (c) The articulated instruments developed at Kyushu University, Japan [217].

Gafford et al. developed a robotic add-on for conventional endoscopes by using Smart Memory Alloy (SMA) to create a ‘swiping’ motion [218][219]. SMAs are metal alloys that change material properties at different temperatures and this behaviour can be used to ‘programme’ specific shapes at a temperature, providing features such as a straight rod bending when changing its temperature. To increase the low response frequencies typical for SMAs, the device was equipped with a fluidic cooling channel, resulting in 10 sweeping motions per minute. The system has not been validated in any user studies or *ex vivo* trials. It should be noted however that the design does not account for a second instrument, which is typically required to lift the tissue for cutting and provide countertraction, as explicitly stated in this editorial [220].

In 2015, Olympus developed the EndoLifter (Figure 3.11b), another add-on for conventional endoscopes, which in contrast to Gafford et al.'s device could only provide traction [216]. The study was performed on an *ex vivo* porcine stomach, not showing clear benefits in terms of procedural time. No further *in vivo* studies could be found in the literature. A similar add-on device, the Impact Scooter, provides an additional exterior working channel to help with traction [221]. This system has been successfully used in patient trials for ESD in the rectum. Between 2006 and 2013, the system was successfully used for ESD in the oesophagus of 107 patients, without a single perforation [222]. It should be noted, however, that it cannot be excluded that all procedures were performed by the same endoscopist, leading to possible bias in the result.

Nakadate et al. (2014) developed an articulated 2.6 mm wire-driven instrument which could be manually controlled by a joystick specifically developed for the system [217] (Figure 3.11c). The system was tested with one articulated instrument inserted into the working channel, and a second mounted with a cap on the outside of the channel. The system was successfully used by endoscopists (both experts and novices in ESD) to perform ESD in *ex vivo* gastric porcine studies, proving itself to be a promising and cost-effective solution. Two experts used the system to perform *in vivo* gastric ESD on pigs. A 2018 study of 30 colonic ESDs performed on 10 pigs compared ESD performed using two of the articulated instruments (n = 15) to conventional ESD (n = 15) [217]. The same Kyushu University group developed the Robotic-Assisted Flexible Endoscope (RAFE) [223]. The RAFE is an add-on to the proximal dials of the endoscope to make any conventional endoscope robotic. The system showed success when performing several tasks, including ESD on *ex vivo* porcine stomach. The system did not use any additional articulated end-effectors and the group remarked that future steps will be to integrate the articulated 2.6mm instruments in the robotic system.

3.2.2.2 Variable stiffness mechanisms

The flexibility of the main endoscopic shaft is often a point of focus in the development of robotic systems. The shaft needs to be compliant enough to be able to navigate through tortuous paths, but should also provide stability when performing a surgical task. Variable stiffness systems were discussed above in the context of the FLEX robotic system, the IOP [189], the newest version of the SPIDER system [149], the SAIT [202] and the K-Flex System [204]. While these are specific mechanisms that have been applied to bimanual surgical systems, there are more examples of academic work focused on variable stiffness mechanisms for surgical devices, e.g. granular [224] and layer jamming mechanisms [225]. However, these mechanisms have not yet been used to create bimanual systems. Another system being developed using the concept of variable stiffness is the Constraint Serpentine Tendon-Driven Mechanism (CSTM) developed at the National University of Singapore in 2015 [226]. The basis of the mechanism is a tubular redundantly actuated serial

mechanism, in which a constraint tube is inserted to constrain a desired length at the proximal side of the serial mechanism. The system has not been validated to determine its maximum force exertion; however, even in the highest stiffness mode, the system showed considerable deformation when only 0.1N force was applied at the tip. Variable stiffness mechanisms are not only found in surgical robotics, but also in the field of soft robotics [227].

3.3 Other surgical robotic platforms

This section gives a brief overview of surgical robotic platforms that do not use endoscopic visualisation. Many of these systems rely extensively on imaging modalities used in radiology - such as CT, MRI and X-ray – for image-guidance. Endovascular catheterization and percutaneous diagnoses and therapies, especially, are largely dependent on pre-and intra-operative imaging for planning and path correction. Similarly, intra-operative images are also essential for path planning in the field of MIS neurosurgery. In robot-assisted orthopaedic surgery, the surgeon often has a direct visualization of the procedure; however, the robot uses pre-operative images combined with stereotactic markers to assist the surgeon during the operation. Overall, the accuracy and efficacy of robotic systems in these different applications are highly dependent on pre- or intra-operative images and the accuracy of overlaying these images with the robot's frame of reference.

Percutaneous interventions use needles inserted into the skin to access parts within the body for therapeutic and diagnostic purposes. Needle biopsies are a common way of getting pathological tissue information of suspicious lesions, and are used for the diagnosis of breast, prostate and liver diseases. Medical imaging modalities (CT, MRI, US) are commonly used to guide the needle to the right location to ensure that the biopsy is taken from the correct tissue. Therapeutic percutaneous interventions include brachytherapy – in which small radioactive seeds are placed within a tumour – and tissue ablation. As in diagnostics, percutaneous therapeutic interventions require accurate needle control and the ability to verify that the needle is placed correctly. The neurosurgical placement of needles within the brain is subject to similar requirements. Robotics can help to accurately position the needle-tip based on the findings from pre- and intra-operative imaging. As tissue can cause needle deflection, a higher accuracy can be achieved by correcting the needle position using intra-operative imaging. Without robotics, intra-operative repositioning during intra-operative CT/X-ray can expose the surgeons to higher doses of radiation and necessitate the wearing of heavy protective lead vests. Also, the limited workspace within a closed-bore make needle re-adjustment without the help of a robot cumbersome. Another method used with percutaneous robots to achieve end-effector accuracy is the implementation of an external positioning platform. With compliant instruments such as needles, this approach is only useful once there is an online feedback on the real position of the instrument tip, as seen in MRI/CT images. Parallel mechanisms

are a commonly used method to achieve high positional accuracy and stiffness, e.g. in the CT-Bot [228], MrBot [229], MIRIAM [230] (Figure 3.12). The compactness of parallel mechanisms is an additional benefit, specifically when adapted for a closed-bore system. One specific parallel mechanism, already mentioned earlier in this thesis is the Light Puncture Robot (LPR) [36]. This system uses a belt-driven parallel mechanism, equivalent to a planar CDPM, to place and orientate the needle before insertion. The intrinsic off-plane compliance of the planar system is used to adapt the translational motion to the shape of the patient. Many of these interventional robots also are equipped with remote centres of motion, equivalent to the mechanisms discussed in section 3.2.1.1. An overview of interventional robotic systems is given by Cleary et al. (2006) [231] and Arnolli et al. (2015) [232].



Figure 3.12 – Two MRI compatible robot systems for prostate interventions. (a) The MIRIAM robot. Image courtesy: DEMCON Advanced Mechatronics BV. (b) The MrBot [233]. Reprinted with permission of MedReviews®, LLC. Mozer PC, Partin AW, Stoianovici D. Robotic image-guided needle interventions of the prostate. Rev Urol. 2009;11(1):7-15. All rights reserved.

One major challenge in endovascular operations is the navigation of the catheter and guidewire assembly through the long and tortuous vasculature. Combined with the aforementioned radiological imaging techniques, robotics can help achieve more intuitive navigation with less exposure to radiation. Recent developments in endovascular robotics are summarized by Rafii-Tari et al. (2013) [234] and Ghamraoui (2018) [235]. Commercial endovascular catheter systems include the Magellan and Sensei X systems (both technology owned by Auris Health, Inc since 2016), the CorPath system (Corindus Vascular Robotics, Inc.) and Amigo (Catheter Precision, Inc). CorPath and Amigo use standard (pre-bent) catheters and guidewires, whereas the Magellan and Sensei X systems have a wire-driven steerable catheter tip. Another system is the Niobe system (Stereotaxis, Inc) that uses large magnets to pull and thereby navigate a compliant catheter through the vasculature.

Several robotic systems have been developed for neurosurgery, with a particular focus on stereotactic systems. In 1985, the first robotic neurosurgery was performed with the UNIMATION

PUMA 200 industrial robot [24]. A needle biopsy was taken and guided using of a CT scan and a stereotactic frame. The Neuromate (Renishaw plc) and the ROSA robot (Medtech, SA) are commercial robotic systems for stereotactic guidance of instruments, such as biopsy needles and neuroendoscopy. These systems are capable of high positional accuracy combined with the sub-millimetre positioning accuracy of industrial serial robotics with joint integrated motors and encoders. Another system for neurosurgery that uses industrial arms is the Pathfinder robot [236]. A few head-mounted systems are being explored for stereotactic neurosurgery, including the NexFrame (MedTronic) and the ClearPoint (MRI Interventions, Inc); these are attached to the skull for accurate placement of needles or other devices, such as electrodes, for deep brain stimulation. Mazor Robotics Ltd. has two robotics systems for spinal surgery, the Mazor X™ and the Renaissance® robot. The Mazor X uses a serial robotic arm to achieve accuracy. The Renaissance robot uses a frame attached to the patient spine and a small hexapod robot mounted on top of this.

One of the main applications of robotics in orthopaedic surgery is implants for knee and hip replacements. Pre-operative imaging and planning, combined with intra-operative stereotaxic, is used to provide accurate robotic milling and drilling. Many commercial orthopaedic surgical robots use serial arms, such as the RIO robot (Stryker Corp.), the NAVIO™ robot (Smith & Nephew, plc), the TSolution One® (Think Surgical, Inc.)⁹ and the previously used CASPAR robot¹⁰. It is important to mention that while the accuracy of all these serial robotic arms is high, the positional accuracy during a procedure is largely dependent on the co-registration of pre-operative images with the patient and robot for surgery.

Continuum mechanisms are a common type of design used to provide a steerable tip with low structural complexity and elements. An extensive review of continuum mechanisms in medicine is given by Burgner-Kahrs et al. (2015) [237]. The review includes an overview of continuum mechanisms by medical application, varying from endovascular and cardiac surgery to neurosurgery. Another review of percutaneous needle-tip steering is provided by Van den Berg et al. (2015) [238].

Concentric tube robots, sometimes also referred to as active cannulas, are another type of continuum mechanisms explored for surgical robotics. The concept uses thin tubes with a set curvature that are concentrically placed within each other. By telescopically sliding and axially rotating the tubes relative to each other, resulting in a tentacle-like motion. A review of concentric tube robotics in medical robotics was provided by Gilbert et al. in 2016 [239]. An interesting approach using continuum robots is seen in the Continuum Reconfigurable Incisionless Surgical

⁹ Formerly known as the ROBODOC system.

¹⁰ The company behind the CASPAR robot went bankrupt removing the system from the market.

Parallel (CRISP) system (Figure 3.13), which combines parallel robotic kinematics with a continuum robot for additional stiffness and the ability to exert higher forces when required [240]. CRISP uses thin ‘incisionless’ needle instruments with loops at the tip, used to assemble the parallel and reconfigure the system inside the body. The needle instruments are used to facilitate with the motion and enhance the stiffness of the main flexible shaft. The complexity of path planning in this configuration has received further attention in subsequent development [241].

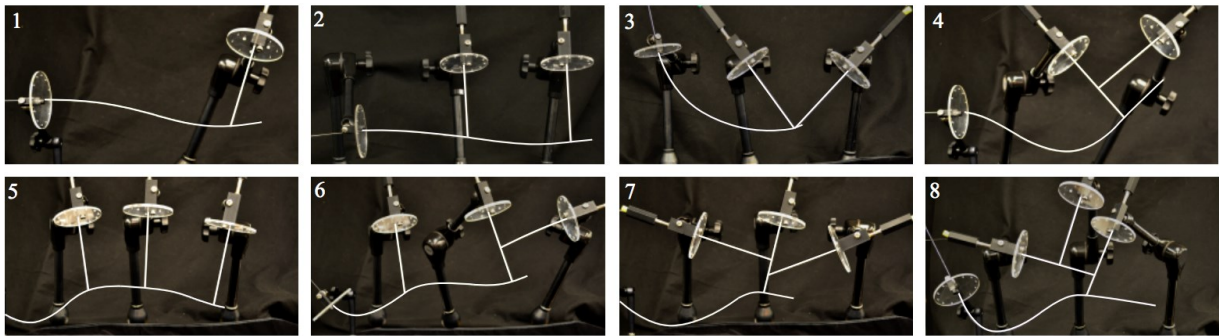


Figure 3.13 – Different configurations of CRISP [240]. The straight needle instruments have hooks at the end which are used to attach the needle to the continuum flexible shaft, thereby becoming a parallel assembly ©2016 IEEE.

The use of parallel structures has also been explored for other continuum structures. Simaan et al. developed the multi-backbone snake-like distal tip [242]. The mechanism is based on a central backbone surrounded by three other backbones. The outer backbones can be extended and retracted to create an overall bending of the continuum tip, and thus acting as a parallel continuum mechanism. The outer backbones are hollow; a superelastic push-pull rod is passed through them to actuate a miniature parallel mechanism at the tip of the instrument. These so-called ‘parallel continuum mechanisms’ were further explored through mathematical modelling by Black et al. (2018) [243]. Of specific interest for later chapters is the use of the continuum Stewart-Gough configuration to sense forces at the end-effector by measuring tension at the joints.

Microsurgical robotic systems focus on providing the surgeon with high accuracy under microscopic vision through motion scaling and tremor filtering of the master input¹¹. While they are in certain cases being replaced by endoscopes to provide better visualization, not all procedures will benefit from this. For instance, ophthalmic surgery remains a field in which most operations are performed using microscopes. Applications exist in ophthalmic, neuro and microvascular surgery. An example of such a system is the JPL RAMS system. It contains a serial manipulator with multiple

¹¹ The term “microsurgical” is in the clinical context is used to describe microscopic visualization, however, many engineers use this term to describe the micrometer precision.

cable-driven joints with a theoretical 10 micrometre positional accuracy [244][245]. The accuracy of the system has not been illustrated experimentally, but based on the findings of other serial manipulators in endoscopic surgical robots it is expected that friction and hysteresis has a major influence on the performance and accuracy. The high accuracy requirement is the reason for the adoption of hexapod – or Stewart-Gough – platforms in precision robotic surgical applications. One of the first systems developed for microsurgical applications [246] used a parallel mechanism to provide micrometre accuracy. The URS Evolution 1 hexapod robot was also used for accurate positioning and control of instruments for neuroendosurgery [247]. The hexapod form was chosen because it offered six degrees of freedom and a 20 micrometre positional accuracy. Another use of a hexapod for neuroendosurgery is seen in [248]. Another important aspect is the repeatability and robustness of the positional accuracy, which can be guaranteed even under high payloads. A parallel mechanism for eye surgery is proposed with the Intra-Ocular Dexterous Robot (IODR) [249]. A concentric tube robot with 2 DoF is mounted on a parallel Stewart-Gough platform to provide positioning of the surgical instrument within the eye. Similar as in other examples, the parallel structure was chosen to provide rigidity, compactness and accuracy for the surgical tool.

3.4 Overview of mechanical analysis

3.4.1 *Endoscopic robotic systems*

Table 3.1 gives an overview of the endoscopic robotic systems discussed in this chapter. The challenges that current endoscopic systems must overcome differ depending on their shaft design. For multi-port systems, the rigid shaft for each instrument provides sufficient stiffness to translate forces to the tip of the instrument. These systems are constrained by the trocar ports, and most systems include an articulated tip (e.g. endoWrist) in order to provide sufficient dexterity. Dexterity and instrument clashing remain an issue when introducing multiple instruments through a single port.

A more common design in single-port systems is the integration of multiple instruments within a single rigid or flexible shaft. For single-port and NOTES systems, there is a trade-off between instrument diameter and instrument triangulation and payload capabilities. To achieve sufficient instrument triangulation, the most commonly applied technique is to incorporate additional joints (often an elbow joint), placed in a serial fashion. While this provides dexterity, many systems are redundantly actuated and therefore will inherently deform when external loads are applied. Also, as the articulated sections of the instruments are often long, forces on the tip result in large moments in the tip. One mechanism that is frequently used to increase payload capacity takes the form of a parallelogram for extra support of the elbow joints. Typically, these mechanisms use rigid links to

transmit forces and therefore cannot be easily adapted for flexible shafts. Similarly, the high payload capacities of direct transmission systems, such as the Virtual Incision, are attributable to the use of a rigid shaft.

	System	Year	Main Shaft	Mechanism Type	Transmission	Forces	DoF
SPS	Virtual Incision [159]–[161]	2013	Rigid	Geared Shaft + Embedded motors	Rigid shaft, gears	30N*	4DoF
	ARAKNES SPRINT [158]	2010	Rigid	Geared Shaft + Embedded motors	Rigid shaft, gears	5N	6DoF
	SURS [152]	2015	Continuum	Continuum	Push-pull backbone	2N	6DoF
	HVSPS [143], [145]	2012	Continuum	Serial + Redundant Serial	Cables	1.6N	6DoF
	PLAS [162]	2014	Rigid	Parallel Joint	Rigid shaft /Plate spring	>14N	6DoF
				Serial	Cables		
	Hwang et al [163]	2017	Rigid	Parallel joint	Rigid shaft	>15N	6DoF
				Serial	Cables		
	Matich et al [171]	2015	Rigid	Parallel (joint)	Sliding shaft	4N**	5DoF
	SAIT [202]	2015	Flexible	Serial	Cables	-	7DoF
	Lee et al [172]	2012	Rigid	Parallel joint	Rigid shaft	-	5DoF
				Serial	Cables		
	Sekiguchi [164]	2010	Rigid, articulated tip	Parallel	Flexible torsion shaft	-	4DoF
NOTES/NOES	NeuRobot [155]	2002	Rigid	Serial	-	-	3DoF
	SiromanS [154]	2011	Rigid	Continuum	Cables	0.9N	5DoF
	microIGES	2017	Rigid	Redundant Serial	Cables	3.5N	7DoF
	Endosamurai [173]	2009	Flexible	Snake-like	-	-	5DoF
	Anubiscope [179]	2010	Flexible	Snake-like	-	-	3DoF
	STRAS [110], [180]	2013	Flexible	Snake-like	Cables	0.9N	3DoF
	MASTER [194], [195]	2008	Flexible	Serial	Cables	5.2N	5DoF
	TUM system [250]	2014	Flexible	Continuum	Push rods/ Cables	2-5N	3DoF
	i ² Snake [207]	2018	Flexible	Redundant Serial	Cables	0.57N***	5DoF
	ViaCath I [193]	2007	Flexible	Continuum	Cables	0.5N	6DoF
	ViaCath II [193]	2007	Flexible	Serial	Cables	3N	6DoF
	DDES [251]	2009	Flexible	Snake-like	-	-	5DoF
	LumenR [215]	2016	Flexible	Pre-bent tubes	Flexible shaft	-	4DoF
	Zhao et al [150]	2013	Flexible	Continuum	Push-pull wires	-	5DoF
	Lehman et al [208], [209]	2009	No shaft (Tethered)	Embedded motor	-	5N	4DoF
	Scorpion shaped endoscopic Surgical Robot [201]	2010	Flexible	Continuum	Cables	3N	2DoF
	Lau et al [199]	2016	Flexible	Continuum	Cables	0.47N	4DoF
	Harada et al [210]	2009	No shaft (Wireless)	Embedded motor	Gears	0.3N****	-
	Tortora et al [212]	2013	No shaft (Wireless)	Embedded motor	Gears	1.2N	4DoF
	Shin et al [167]	2013	Rigid	Serial	Cables	9.21N*****	6DoF

Table 3.1 – An overview of endoscopic robotic systems found in literature. Multiport systems and other systems for which insufficient technical information was found are omitted from the table. The term “snake-like” is used when there is redundancy in the DoF but no explicit technical description of the mechanism is found. Such mechanisms are therefore either a continuum or a serial redundant mechanism. *Theoretical payload. ** payload without any increase in positional error. ***Measured for a single segment. **** Calculated for the forces at tip of single section, using theoretical joint torque. *****Measured for a single joint at 75mm distance.

Another challenge for flexible endoscopic systems is the lack of stability of the flexible shaft during surgery. For most flexible systems, tip payload capacity is evaluated while the main shaft is clamped in place. In practice, however, a flexible shaft in soft tissue does not provide a stable environment, which may result in even lower maximum payloads [118]. Variable stiffness mechanisms are often introduced as a method to offer a stable platform from which surgery can be performed.

For most systems, however, it is not clear what the appropriate clinical force requirements are, and the low payloads might be more than sufficient for certain surgical procedures; for example, the forces required for suturing may be lower than the forces required to handle the gallbladder during a cholecystectomy. Hence, the requirements for robotic systems designed for specific procedures are likely less demanding than for general-purpose robotic systems.

3.4.2 Other surgical platforms

Where possible in terms of space, many surgical applications use serial mechanical systems with motors and encoders at the joints, similar to conventional industrial arms. An inherent benefit of such mechanisms is the sub-millimetre positional accuracy achieved through the direct actuation and measurement of the joint. This is in contrast to the serial mechanisms found in single-port surgery that use cables to transmit positions. Endoscopic robotic systems with integrating micromotors use the same principle of providing actuation near the joint, however, this results in relatively large segments while the payload remains limited. Another observation with regard to other surgical robotic applications is how frequently parallel Stewart-Gough platforms are used to achieve compactness and micrometre accuracy control of surgical instruments, which remain accurate even under high payloads. As mentioned in chapter 2, the Stewart-Gough platforms share many similarities with CDPMs, including their relative compactness and high payload capacity.

3.4.3 Synthesis

An overview of the type of mechanisms found in literature is shown in Figure 3.14. Generally speaking, snake-like mechanisms (i.e. serial redundant and continuum mechanisms) are found in applications that require dexterity for navigation through a small entry channel (e.g. endovascular). A small entry channel is indeed required for MIS, but this should not be at the expense of the ability to perform the surgery once the area of interest has been reached. Snake-like mechanisms, however, have proven to have low end-effector payloads, which can be a problem when performing surgery, especially for NOES and NOTES. Systems that have micromotors integrated near the actuated joints suffer similar problems because the miniaturization of the motors drastically reduce their torques and thus the end-effector payload. However, even when miniaturizing the motors to the extent in

which the payloads become too low to perform surgery, these mechanisms are bulky and less dexterous in comparison with snake-like mechanisms. In contrast, the use of parallel joints or geared shaft mechanisms increases the payload capabilities of the end-effector, but require a (semi-)rigid transmission mechanism and are therefore less suitable for tortuous pathways. The contrasting requirements of on one side the compliance for navigation and on the other side stability for surgery are therefore a major challenge in MIS.

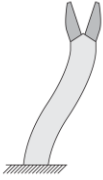
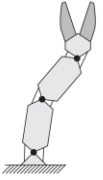
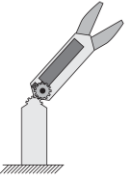
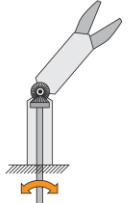
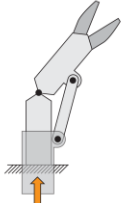
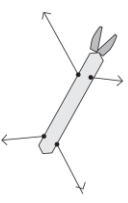
	Continuum	Serial			Parallel	
		Serial (redundant) 	Embedded Motors 	Geared shaft mechanism 	Parallel Joint 	CDPM 
DoF of instrument	++	++	+	+	+	+
Payload at instrument tip	--	--	--	++	+	++
Access through a tortuous pathway	++	++	+	--	--	+
Performing a task within a confined space	++	++	-	+/-	+	-

Figure 3.14 – An overview of mechanisms used for MIS based on the findings from literature.

CDPMs, as highlighted in Chapter 2, have high end-effector payloads due to the distribution of forces over all actuation cables. Additionally, the flexible actuation cables can be guided through a tortuous pathway by using a tendon-sheath mechanism. The main challenge with CDPMs for MIS is the need for the cable entry points (and thus the scaffold) to encapsulate the instrument workspace. A minimum amount of space is required for the CDPM to perform a surgical task and this is directly related to the instrument workspace. Additionally, in many MIS procedures the instrument workspace is larger than the access port. Therefore, the access method required to introduce the CDPM to the desired location into confined spaces is an essential aspect that needs to be solved before using CDPMs in MIS. The prototypes in the following chapters are developed to research different MIS access methods for CDPMs. The first method is demonstrated by the ESD CYCLOPS in Chapter 4. The prototype exploits the rapid deployability of CDPMs and uses this to introduce the system through a small access port and deploy the scaffold within the body. A second method to deploy a CDPM is shown with the SIMPLE system, which is discussed in Chapter 6. A third MIS access method, which does not use an outer structure that is deployable is used by the microCYCLOPS and neuroCYCLOPS (Appendix A.3)

Another interesting development in surgical robotics is the use of parallel continuum configurations to sense end-effector forces, as explored by Black et al. As mentioned earlier, one of the limitations of MIS robotic systems is the lack of haptic feedback. The same concept for the sensing of end-effector forces can be used for CDPMs, which is explored in Chapter 5 and implemented in the SIMPLE system in Chapter 6.

Chapter 4

ESD CYCLOPS for bimanual endoluminal surgery

This chapter discusses the ESD CYCLOPS, which uses a CDPM for flexible endoscopy. First, a clinical background is given about the current need for such a system, including alternative approaches to current clinical needs. The ESD CYCLOPS is discussed and validated in an *in vitro* benchmarking study and *ex vivo* and *in vivo* pre-clinical animal trials.

4.1 Clinical Background

Gastrointestinal (GI) cancers are one of the leading causes of mortality and morbidity in the world. In 2018, there were 685,800 new cases of oesophageal, gastric and colorectal cancers and an estimated 389,800 gastrointestinal cancer-related deaths in Europe [252]. Colorectal cancer was the second largest cause of death, with an estimated 242,000 deaths. In the United Kingdom, bowel cancer was responsible for 41,804 new cancers cases and 16,384 deaths in 2016 [253]. In the United States, GI cancers together accounted for a total of 183,780 new cases and 77,280 deaths in 2018 [254] (gastric, oesophageal and colorectal). With an estimated 50,630 deaths, colorectal cancer mortality is the highest among GI cancers and the second highest when compared to all cancers (after lung cancer).

Surgical resection can be used to remove gastrointestinal cancers; however, even when performed laparoscopically, it is still considered an invasive procedure. The surgical resection of

colorectal cancer requires the removal of a section of the tract and either an anastomosis to reconnect the two ends of the tract, or a stoma. As such, the laparoscopic resection of colorectal cancer is associated with a higher complication rate than endoscopic resection [255].

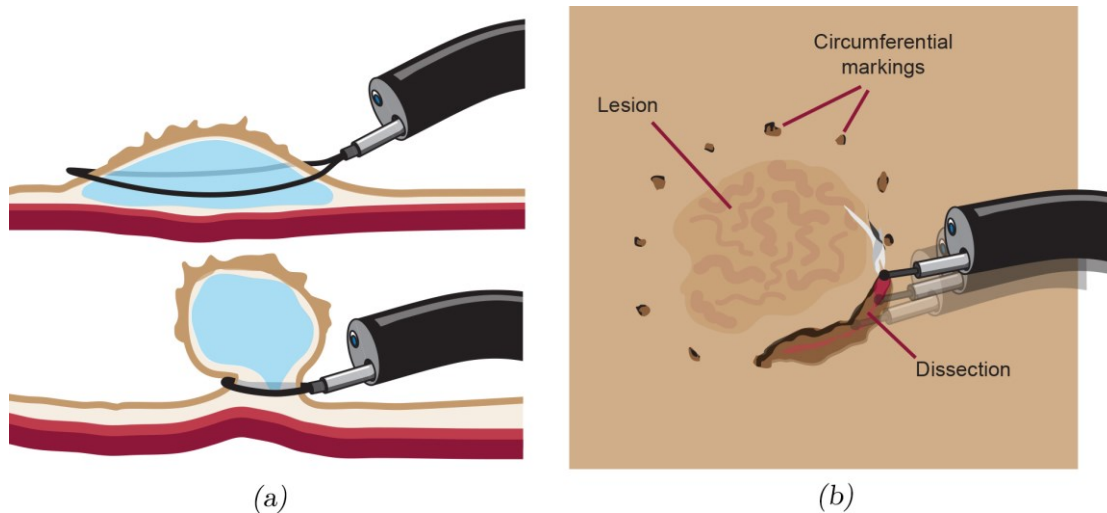


Figure 4.1 – (a) Endoscopic Mucosal Resection and (b) Endoscopic Submucosal Dissection.

Endoscopic resection can be used for the minimally invasive removal of pre-cancerous lesions (adenomas) and early-stage GI cancer. The endoscopic removal of polypoid lesions, polypectomy, is performed using a snare inserted into the biopsy channel of an endoscope. Non-polypoid adenomas [256] (i.e. flat or depressed lesions) are more challenging to detect and remove, and are more likely to develop into adenocarcinomas. Endoscopic Mucosal Resection (EMR) and Endoscopic Submucosal Dissection (ESD) are two endoscopic techniques (Figure 4.1) which can be used to remove lesions which have not yet invaded the deeper tissue layers (submucosal and muscular layers [257]). Both techniques typically use a submucosal injection to lift the mucosal layer from the underlying tissue. During EMR, the mucosa is resected using a snare placed over the elevated mucosal tissue. Other techniques include the use of a suction cup to elevate the tissue before removal with the snare [258]. EMR is successful for *en bloc* removal of non-polypoid lesions smaller than 20mm, but requires piecemeal resection for larger lesions, referred to as Endoscopic Piecemeal Mucosal Resection. However, piecemeal EMR is often associated with a high recurrence rate, in particular for malignant lesions [259].

ESD, in contrast, uses a knife (typically in the form of electrocautery) to remove lesions by dissecting the submucosal layer. ESD can be used for *en bloc* dissection of lesions of all sizes, i.e. also for lesions larger than 20mm. *En bloc* removal of lesions using ESD results in a lower local recurrence rate than piecemeal EMR [260][261]. In addition, *en bloc* resection is beneficial for the detection of negative tumour margins during pathological analysis and subsequent follow-up treatment [262]. In

contrast, for piecemeal EMR the assessment of tumour margins is difficult. However, ESD is associated with a higher bleeding and perforation rate than EMR [263]. ESD is also a challenging therapeutic procedure to perform, which is reflected in the long procedure times and long learning curves. Nevertheless, ESD is the preferred technique for lesions larger than 20mm [264].

The complexity of ESD arises from the need to perform a cutting motion with an instrument inserted into the working channel of a flexible endoscope. The instrument can only move along the axis of the channel, hence the endoscope tip is controlled to provide dexterity at the instrument tip. Another requirement is the need of counter-traction to cut and remove tissue out of view while dissecting underneath the lesion. Traction can be achieved by using a dual-channel endoscope with a flexible grasper placed in the second working channel. However, this method still is seen as cumbersome, as the second instrument can only be moved in a parallel fashion relative to the knife, leading to a plethora of different solutions to provide traction [265][266]. An overview of traction methods used in ESD is presented in section 4.1.1. Specific techniques for endoscopic submucosal tunnel dissection (ESTD) are not discussed¹². Another aspect that makes ESD complex to perform is the mechanical compliance of flexible endoscopes, which is a major challenge in both NOES and NOTES procedures [20]. Compliance is required for navigation through the GI tract but decreases the positional stability of the endoscope leading to challenges in maintaining an adequate view and effective interacting with tissue. Devices that are used to provide stability of the endoscope are discussed in section 4.1.2. An overview of robotic methods was provided in Chapter 3.

4.1.1 Techniques for providing traction

The clip-and-line method uses an endoscopic clip attached to a thin line (often dental floss or silk). The clip is attached to the mucosal layer, after which the line can be pulled to get a clear view of and access to the submucosal layer [267] (Figure 4.2a). An obvious shortcoming of this method is that traction is only provided in a single direction, which is dictated by the pathway along which the body was accessed (i.e. anus or mouth). An alternative setup involves the use of two clips to redirect the line to a desired direction before it is guided away [268] (Figure 4.2b). A multi-centred randomized controlled trial was published in 2018 assessing clinical outcomes of gastric ESD with and without the use of the clip-and-line method [269]. The study showed that the method was not beneficial for the average ESD case; for gastric lesions located at the upper and middle greater curvature, however, the method led to a lower perforation rate and reduced operating times.

¹² ESTD is a novel clinical technique for the performance of peroral endoscopic myotomy (POEM) to treat oesophageal achalasia [379].

The use of internally anchored clip-and-line assemblies has also been evaluated. The S-O Clip is a miniature spring with a conventional clip at one end and nylon loops at the other. The spring can be inserted through the biopsy channel, and after the first clip is connected to tissue, a second clip is used to stretch the spring and provide counter-traction (Figure 4.2c) [270]. A clinical study with 50 patients showed that S-O clips were safe to use and resulted in reduced operating times when compared to conventional ESD [271]. A similar concept using an elastic band instead of a spring was demonstrated by Parra-Blanco et al. [272]. Mori et al. (2017) introduced the ring-shaped thread method that uses a thread (instead of a spring) with multiple clips to provide traction. The main difference between this method and the use of S-O clip is that the ring thread method use of insufflation to enlarge the colorectal tract, thereby controlling the degree of traction. A clinical study with 45 patients showed reduced operating times compared to conventional ESD [273].

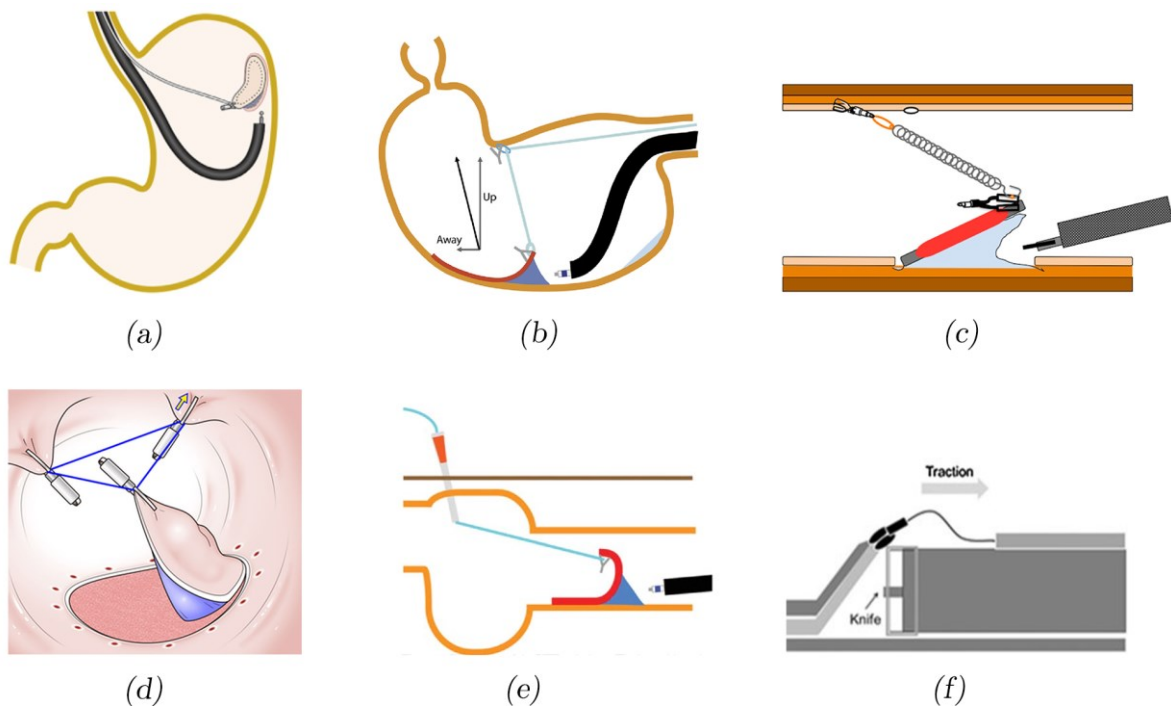


Figure 4.2 – A number of clinical techniques used for providing tissue traction during ESD. (a) The clip-and-line method. Image source: [269]. (b) The clip-and-line method with an additional clip to redirect the cable. Image source: [268]. (c) The S-O clip using a spring and two clips. Image source: [271]. (d) The ring-shaped thread method developed by Mori et al. [273] (e) The hybrid percutaneous method in which a clip-and-line is used combined with a small needleport to provide traction.[274] (f) The cross-counter technique developed by Okamoto et al. [275].

Traction can also be achieved with the use of magnetically actuated forceps, in which an external magnet is used to provide the traction [276][277]. Magnetic traction was recently shown to be feasible in one patient with a colorectal tumour (2017) [278], and even more recently (2018) in fifty patients with gastric lesions [279]. In addition to the need for a large external magnet, this method

requires the complete retraction and reinsertion of the endoscope halfway through the procedure in order to introduce the internal magnet-and-clip. Another external force-based method is to use gravity [280]. This method uses a clip with a small weight, and thus requires reorientation of the patient when traction in other directions is required, which can be impractical and will only be feasible for a fixed set of body orientations (and thus directions).

It is also possible to use a transluminally inserted thin percutaneous grasper to offer traction during ESD [281][282]. Chen et al. describe a hybrid technique combining a percutaneous grasper and the clip-and-line technique [274], in which a transgastric percutaneous catheter is used to guide the clip-and-line and achieve a desired direction. These techniques are used in gastric and oesophageal ESD. Whether the technique is suitable for colorectal ESD is not explored, however the purposeful perforation of the bowel will likely lead to an increase of post-operative complication rates.

There exist a number of solutions that use traction devices placed along the exterior of a conventional endoscope. Okamoto et al. developed the cross-counter technique, an adaption of the clip-and-line method for colorectal ESD [275]. In this method, a thin wire is guided through an external tube along the endoscope shaft. A clip is attached to the tissue, and the wire is used to pull the mucosa over a transparent cap attached to the tip of the endoscope so that the electrocautery instrument can reach beneath the submucosa. Another alternative to the clip-and-line method is the use of a conventional flexible endoscopic instrument alongside the endoscope, in which a second grasper in the biopsy channel is used to manoeuvre the flexible grasper to the desired tissue location [283]. A variation of the method involved the addition of a controllable bend at the tip of the external grasper [284]. For more tortuous paths, e.g. in the colon, this method would make the navigation of the instrument to the region of interest a cumbersome task. Other systems using an external channel for additional traction were discussed in Chapter 3. These systems include the EndoLifter [216], Impact Scooter [221][222] and the systems developed by Nakadate et al. [217].

Traction can also be provided by introducing an additional thinner endoscope with a grasper placed in the biopsy channel, as shown in [285][286]. Another paper presented a solution where the second endoscope was inserted transnasally to assist the gastric ESD [287]. While this method has been shown to be feasible, the addition of another endoscope requires additional hands during the procedure and leads to crowding of instruments in narrow parts of the tract.

Endoscopy companies have also developed dedicated endoscopes for ESD. One such dedicated endoscope is the R-scope, developed by Olympus (also mentioned in Chapter 3). The R-scope has two articulated working channels to control instruments, the first providing an up-down motion for

grasping and lifting tissue, and a second a sweeping (left-right) motion. In 2006, the system was evaluated in clinical studies in Europe [176] and Japan [288], demonstrating that the system could be successfully used to remove neoplastic gastric lesions. ESD performed with the R-scope among 20 Japanese patients was retrospectively compared to conventional ESD (n=40), showing shorter procedural times (57.9 ± 29.7 min versus 92.8 ± 58.9 min, respectively) but no clear difference in complications. In the European study (not a comparative study), the procedure was still found to be challenging, which was reflected in the length of the procedures. One of the drawbacks of the R-scope is the number of dials, which complicates the instrument's manual control.

The aforementioned approaches have not yet replaced conventional ESD. Many clinical techniques offer limited control over the counter-traction and do not provide the additional instrument control required to drastically reduce procedure times and perforations. Other systems, including a number of robotic systems discussed in Chapter 3, have limited payload capacities, which is partly due to the inefficient force transmission of serial and continuum mechanisms.

4.1.2 Endoscope stabilisation

In addition to limited dexterity for retraction, endoscope stabilisation also complicates ESD. Several systems have been specifically developed to control the endoscope stiffness, with so-called variable stiffness mechanisms. A number of systems have already been mentioned in Chapter 3. The topic has received specific attention by researchers with overviews of variable stiffness mechanisms for endoscopes given in [289], and specifically for NOTES in [187].

Another method to provide a stable endoscope tip is by using the surrounding tissue as support. One common method is the use of one or two balloons at the tip of the endoscope, which is a method used in enteroscopy to navigate through the small-intestine. In colonoscopies the integration of a balloon is less common, however, the NaviAid™ G-EYE system (SMART Medical systems Ltd.) has a balloon integrated in the bending tip and used for tissue retraction. The balloon offers stability to the colonoscope, but can also be used to straighten colonic folds for improved visualisation of the tissue surface. This is important for the detection of polyps, which can be missed when hidden behind tissue, and is yet another important reason leading to the introduction of new add-on devices such as Endocuff Vision® (Olympus Corp.). Instead of a balloon, the EndoCuff uses flexible 'arms' to straighten colonic folds and provide endoscope stabilization.

The DiLumen™ EIP oversheath (Lumendi Ltd) is a recent development that uses a double balloon technique specifically for therapeutic interventions. The first balloon is integrated into the oversheath and affixed just before the steerable section of the endoscope's tip, and is used for endoscope stabilization. The second balloon is located at the tip of the endoscope and can be

extended forwards along two rails. By inflating both balloons, the DiLumen EIP device creates a working area around the lesion (the so-called ‘therapeutic zone’) which can be used to inflate and stretch the colonic folds. Additionally, the distal balloon can be equipped with clips to provide mucosal traction by extending the balloon further along the guides. In 2018, this system with clips was compared to conventional cap-assisted ESD in *ex vivo* animal trials and one *in vivo* animal trial, demonstrating a significant decrease in operating time [290]. A similar result was found when performing the ESD in *ex vivo* tissue when the therapeutic zone was filled with water [291]. The system has been FDA-approved and CE-marked (2018), and a bimanual version of the system is being developed for ESD (DiLumen C2™).



Figure 4.3 – The DiLumen C2™ system for ESD. Image courtesy: Lumendi Ltd.

The combination of endoscope stabilisation and tissue counter-traction, as seen in the DiLumen system, are important to reduce the complexity of ESD procedures. Another important aspect is the dexterity of the surgical instruments. This current chapter discusses how CDPMs can be used to provide instrument dexterity, while providing a stable platform for the endoscope. The system is based on the original CYCLOPS system and adapted to flexible endoscopy to perform ESD.

4.2 ESD CYCLOPS

The ESD CYCLOPS is a CDPM system developed as a bimanual surgical robotic system mounted on conventional flexible endoscopes (Figure 4.4). The outer scaffold of the CDPM is deployable and is used for endoscope stabilization. A small clamp is fixated around the endoscope at a few centimetre distance from the steerable tip of the endoscope. The clamp is used to push and rotate the undeployed scaffold during navigation. During deployment the endoscope is able to move independent from the scaffold and is retracted behind the instruments. The CDPM itself is used to

provide sufficient payload and instrument dexterity to perform ESD in the colon. Both aspects are evaluated during benchmarking and pre-clinical studies (section 4.4.1 and 4.5, respectively).

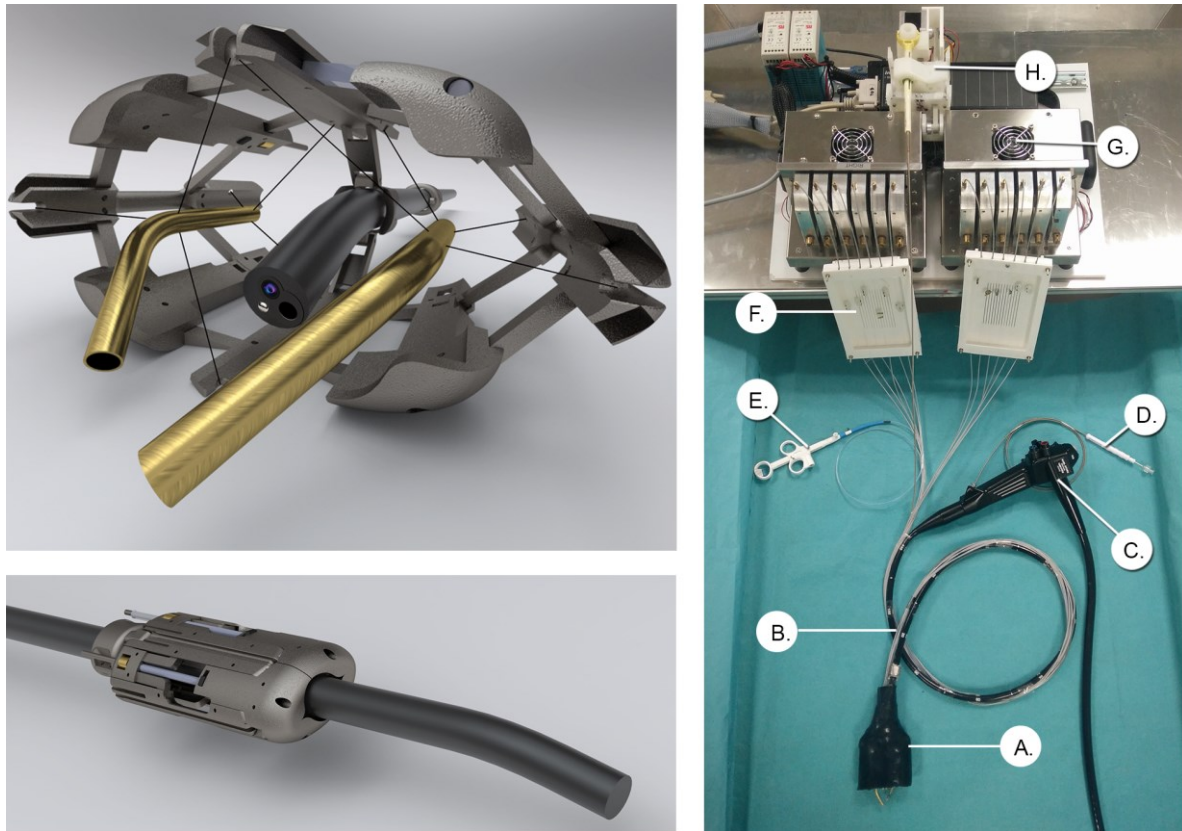


*Figure 4.4 – The ESD CYCLOPS. **Top-left:** The scaffold containing the endoscope and the two overtubes controlled by CDPMs. Flexible instruments are inserted into the overtubes to perform surgery. ©2018 IEEE. **Bottom-left:** The undeployed scaffold. The scaffold is placed directly after the steerable tip of the endoscope during navigation. **Right:** The components of the system. (A) The scaffold covered by a soft silicone sleeve. (B) Bowden cables used to guide the actuation cables and the flexible instruments along the endoscope. (C) The endoscope. (D) A flexible needle is inserted into the endoscope’s working channel and used to lift the mucosa by injecting a liquid. (E) The diathermy instrument. (F) A cable splitter. (G) A motor unit containing 6 motors. (H) Mechanism for opening and closing of the grasper. ©2018 IEEE.*

The system comprises two CDPMs, each using 6 cables to control a curved overtube in 5 DoF (x, y, z, yaw, pitch). Bowden cables (1.4mm Round wire coil, Asahi Intecc, Japan) are used as conduits to guide the actuation cables from the deployable scaffold along the endoscope to the motor units located outside the body. A PTFE inner cable is added to reduce the friction between the actuation and the Bowden cables. The flexible endoscopic instruments are guided along the shaft of the endoscope and placed in the overtubes. The overtube curvature is introduced to increase the overlap of the instruments required for ESD.

The surgeon controls the instruments using haptic controllers (Geomagic Touch, 3D Systems, USA). The force feedback that the haptic controllers can provide is only used to indicate the

boundaries of the workspace in which the surgeon can operate. The boundaries are determined by the coordinates of the attachment point and thus represent the theoretical boundaries in which the centre of motion (COM) is able to move. The endoscopic view is provided to the surgeon via a display. The surgeon activates a grasper using a button on the haptic device. The electrocautery is controlled by a foot pedal to activate the current generator (Erbe Elektromedizin GmbH, Germany). A cable splitter is placed in-between to electrically insulate the steel Bowden cables from the mechatronics unit, which is required when using electrocautery. An additional function of the cable splitter is to facilitate the exchange of scaffolds without having to rewire the cables at the motor side.

The schematics of the mechatronics can be seen in Figure 4.5. A brushless DC motor (2232S024BX4 CCD, Faulhaber, Germany) with a 25:1 gear assembly (22F) is used to actuate each cable. Each motor drives a 9mm diameter motor spool around which the actuation cable is rolled. The actuation cable is guided to the cable-splitter along three pulleys, of which the middle pulley is mounted on a loadcell (LCL-020, Omega Engineering, Inc., USA) to measure the tension of the cables. The loadcell analogue inputs are digitized using an Instrunet i100 (GW Instruments, Inc. USA) 14-bit DAQ interface, resulting in a theoretical 5.4mN resolution. The tension in the cables is used as a safety setting to prevent cable failure, triggering a release at forces higher than 60N. Typically this is only triggered when cables are displaced from their pulleys or when the system is incorrectly calibrated.

The position of the haptic device's handle is mapped and scaled to fit the slave coordinates, and the desired motor positions are calculated for the desired end-effector pose. The mapping is based on the motion of the end-effector as it is displayed to the user, i.e. an upward motion is mapped to an upward motion on the screen. The inverse kinematics are used to translate the desired end-effector position to the motor angle. The motor controllers are set to position control. A CAN interface (IXXAT USB-to-CAN V2, HMS Industrial Networks AB, Sweden) is used to send the desired pose to the motors. Graspers are opened and closed by a stepper motor (103H5208-5240, Sanyo Denki, Japan), which controls a linear motion. The control software of the system is largely based on the code developed for the first CYCLOPS prototype [34]. Other control software used in other prototypes (see Chapter 5 and later) have been developed during this thesis.

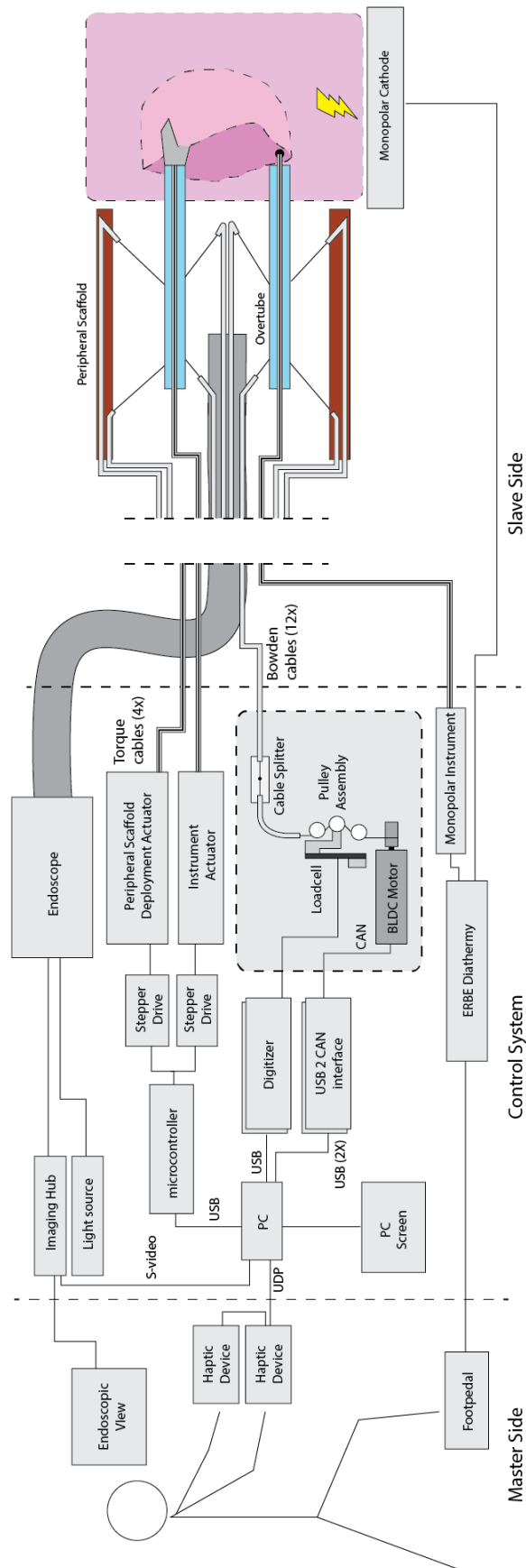


Figure 4.5 – An overview of the hardware of the ESD CYCLOPS. ©2018 IEEE.

4.3 Deployable Scaffold

An important aspect of the system is the deployable scaffold. A silicone sleeve (Ecoflex 00-20, Smooth-on, Inc., USA) is used to cover the scaffold and prevent damage to soft tissue. The system is introduced and navigated into the body while undeployed, and is subsequently deployed to perform ESD. The deployable scaffold is based on a four-bar mechanism, which is used for its compactness and robustness, and allows the creation of a scaffold which is adjusted to the scale required for performing ESD in a pre-clinical setting. Another advantage of the four-bar mechanisms is that the shape of the scaffold can be parametrized to the clinical requirements for performing ESD. The clinical design requirements are first discussed in section 4.3.1, and the parameterization of the scaffold in section 4.3.3.

An alternative approach for the development of such a deployable system is to use an inflatable toroidal structure, as shown in Figure 4.6. The manufacturing of the inflatable structure for a scaffold at scale is currently being explored by another PhD candidate at the department [292]. However, many of the results of this chapter, including the workspace analysis of the instruments, are important for the development of an inflatable scaffold.

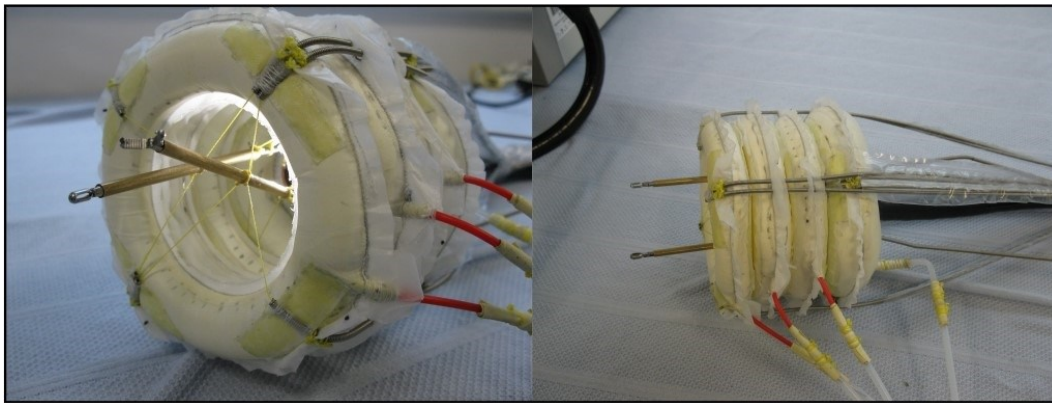


Figure 4.6 – The inflatable scaffold which is an alternative approach to the ESD CYCLOPS scaffold presented in this chapter. ©2018 IEEE.

4.3.1 Clinical requirements

The size of lesions which must be removed by ESD is an important factor in the workspace considerations of the robotic system. A large meta-study of 22 studies and 2841 ESDs showed that the median of the means of these studies was 32.4mm with a range of means of 6.2-43.6mm [293]. The upper range was determined by a specific study in which ESD was performed on large colorectal cancers ($43.6 \pm 16\text{mm}$) [294].

The diameter of the bowel depends on the location along the tract and also varies per population. Table 4.1 shows the bowel diameter and length for an American [295] and a Japanese population [296]. Equally relevant is the prevalence of non-polypoid lesion locations in terms of the anatomical location [297] and the frequency of ESD performed in each location [298]. The shape and tortuosity of the colon can change considerably between patients, as shown in Figure 4.7. The biomechanical properties of the transversal colon have been evaluated for cadaveric and fresh samples from surgery [299]. The stress-strain curves of the samples showed that the tissue initially could be stretched with little increase in stress. Tests performed on the axial and transversal tissue direction showed an increase of stress at $\mu = 18.4\%$ and $\mu = 33.3\%$ ($n = 50$), respectively.

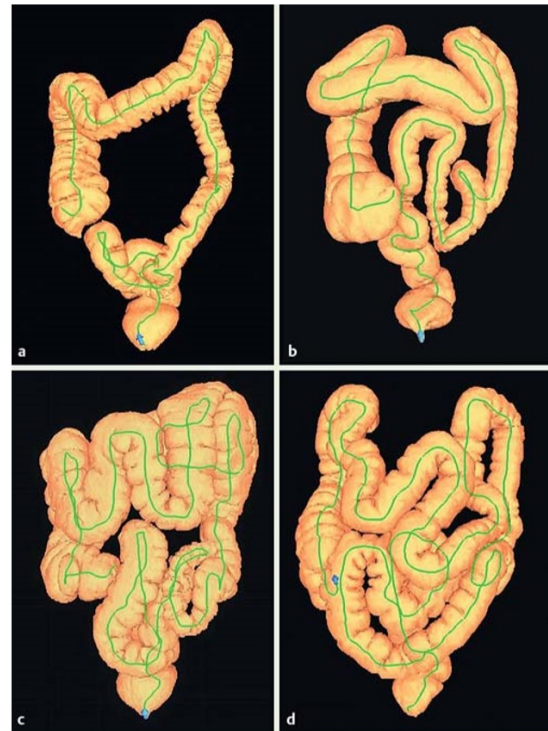


Figure 4.7- The bowel's tortuosity varies strongly between patients, as shown in the 3D segmentations of CT-scans. Image source: [295].

The force requirements for ESD depend on whether the graspers or electrocautery are being used, with the former requiring the highest forces in order to provide traction. A number of studies have performed analyses of the force requirements for the grasper. One *in vivo* porcine study involving a laparotomy showed mean forces of $1.13N$ with a maximum estimated force of $2.26N$ [300] to lift gastric mucosa. In another study, a rigid device was developed to measure interaction forces during tissue pulling and lifting [301]. In an *in vivo* porcine study, tissue located 10 centimetres into the rectum was manipulated, showing forces of $0.89 \pm 0.21N$ and $0.58 \pm 0.31N$ for lifting and pulling, respectively. Data collection during an ESD on *ex vivo* chicken tissue yielded similar forces as the aforementioned two studies (Chapter 7). The forces on the electrocautery have not been explored extensively, with one basic study mentioning a force range of 300-400mN to dissect *ex vivo* porcine gastric tissue [218].

In the broader context of NOTES, it is expected that higher forces are required for the grasper. $5N$ forces have been registered for the lifting of a section of colon [302]. The earlier-mentioned study into ESD forces also explored the forces required for NOTES and NOES, and indicated forces of $11.55N$ to lift the stomach and $6.42N$ for laparoscopically mobilizing the sigmoid [300]. The maximum forces required for NOTES can also be further estimated by looking at internal organ

weights. A large cadaver study ($n = 684$) showed the liver to be one of the heaviest internal organs, with a weight of 1831 ± 384 grams for Caucasian males with height between 176-190cm [303]. Many other organs (spleen, pancreas, kidneys) have a weight of approximately 180 grams. These weights translate to approximately $18N$ and $1.8N$. It is safe to say that lifting the entire liver is probably not required in most (if any) MIS procedures; however, this can serve as an ideal upper limit.

	American [295] $n = 505$		Japanese [296] $n = 920$		non-polypoid adenomas[297] $n = 307^{13}$	ESD performed [298] $n = 1111^{14}$
	Diameter [mm]	Length [cm]	Diameter [mm]	Length [cm]		
Cecum	75.7 ± 12.2	6.7 ± 1.9	47.7 ± 8.5	4.12 ± 0.82	31,3%	13,9%
Ascending	61.3 ± 11.1	23.1 ± 6.8	49.1 ± 16.8	15.7 ± 3.3		33,3%
Transverse	50.0 ± 8.5	58.3 ± 13.6	42.2 ± 9.9	38.8 ± 8.6	32,2%	
Descending	38.3 ± 7.2	33.0 ± 8.0	33.2 ± 9.2	18.3 ± 4.5	30,6%	19,4%
Sigmoid	34.5 ± 7.1	49.0 ± 12.9	33.2 ± 6.4	35.3 ± 10.0		
Rectum	64.6 ± 10.6	19.5 ± 3.1	37.5 ± 10.4	17.3 ± 1.7	5,9%	33,3%

Table 4.1 - Each anatomical section of the colon with the length and diameter in an American and Japanese study. For each section the percentage of non-polypoid lesions and ESDs are included. The two right columns indicate the percentage of non-polypoid lesions found and ESDs performed at each section

4.3.2 Parametric design

The scaffold is described parametrically in order enable adjustment to different clinical needs in terms of colon diameter (Figure 4.8). The scaffold is symmetrical along the XZ plane and the XY plane, and each quadrant consists of two four-bar mechanisms. Each four-bar mechanism is fully determined by two angles θ_1 and θ_2 . In reality it is cumbersome to control both angles, and it becomes more practical to control the length a . The angles θ_1 and θ_2 are by default only fully determined by length a when the scaffold is fully deployed and undeployed position. If a fully determined system is required, a thin parallel link can be added, which constrains the angles to each other: $\theta_1 = \theta_2$.

¹³ The original study reports a total of 2770 lesions, of which only the non-polypoid lesions are used to calculate the percentages. Both neoplastic and non-neoplastic are included as in this calculation as often it is not clear before undergoing pathological examination. Lesions of all sizes are included in this data.

¹⁴ For ESD performed on lesions larger than 20mm.

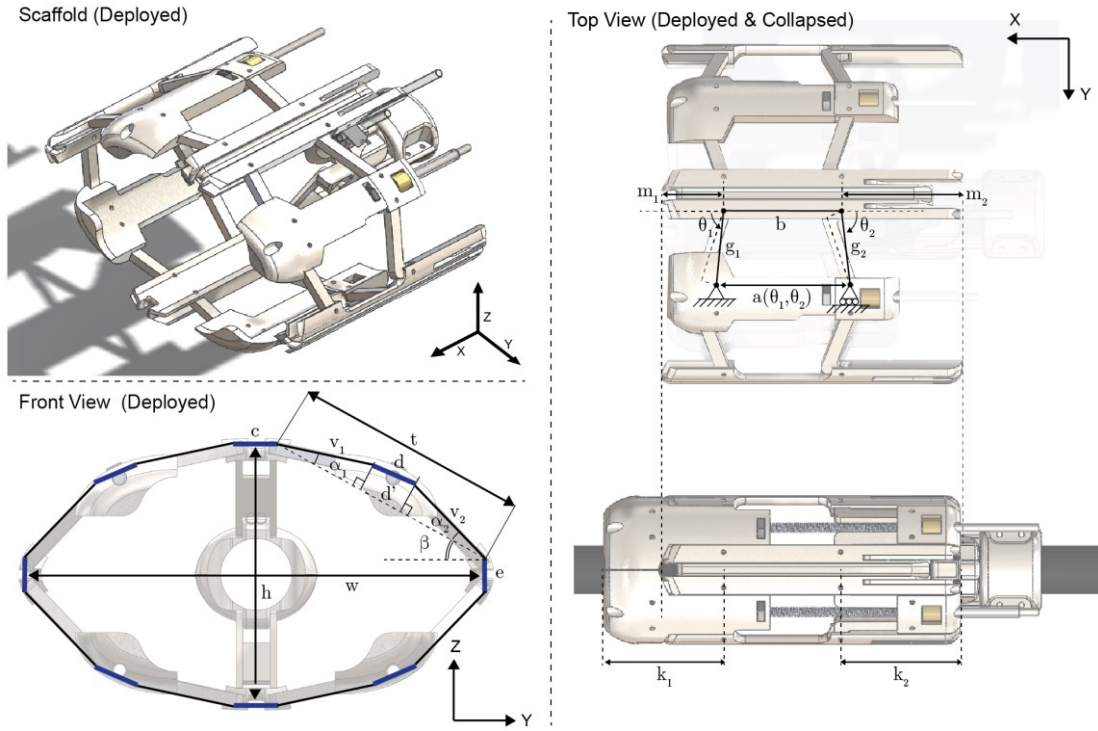


Figure 4.8 – The scaffold design and parameters used to adjust the system to clinical requirements.

The height and width of the system in the ZY-plane are found thus:

$$\begin{aligned} h &= e + 2\|t_v\| \sin(\beta) \\ w &= c + 2\|t_v\| \cos(\beta) \end{aligned} \quad (4.1)$$

where t_v represents the distance between the side bar and top bar:

$$\|t_v\| = d' + v_1 \cos(\alpha_1) + v_2 \cos(\alpha_2) \quad (4.2)$$

in which d' represents the projection of line d on the vector $t_v \in \mathbb{R}^2$. The projection of the links g_i on the ZY-plane is v_i . Thus,

$$\begin{aligned} d' &= \sqrt{d^2 - (v_1(\theta_1) \sin(\alpha_1) - v_2(\theta_2) \sin(\alpha_2))} \\ v_i(\theta_i) &= g_i \sin(\theta_i) \end{aligned} \quad (4.3)$$

The design parameters are $b, c, d, e, \beta, \alpha_1, \alpha_2, g_1$ and g_2 . The angle β determines the ratio between the height and the width, and when c and e are small approximates the tangent: $r = \frac{h}{w} \approx \tan(\beta)$. The angles α_1 and α_2 are responsible for the convexity, and thus the elliptical shape of the scaffold. The circumference of the scaffold, in the YZ-plane, can be found as follows: $circum = 4d + 2c + 2e + 8g \sin(\theta)$. The maximum and minimum height and width of the scaffold can be found by equation (4.3), and the maximum value of v_i :

$$v_{i,min} = g_i \sin(\theta_{i,min})$$

$$v_{i,max} = \begin{cases} g_i & \text{if } \frac{\pi}{2} \in [\theta_{i,min}, \theta_{i,max}] \\ g_i \sin(\theta_{i,max}) & \text{otherwise} \end{cases} \quad (4.4)$$

Hence, using equations (4.1)-(4.4), the maximum and minimum height and widths can be found.

The length of the scaffold also depends on whether it is deployed or not, and can be found as follows:

$$L_{undeployed} = b + h_1 + h_2 + g_1 \cos(\theta_{1,min}) + g_2 \cos(\theta_{2,min})$$

$$L_{undeployed} = b + m_1 + m_2 \quad (4.5)$$

Note that these equations are for an inward-deploying scaffold, as shown in Figure 4.8. When requiring an outward-deploying scaffold, the equations (4.5) simply reverse, i.e. $L_{deployed,out} = L_{undeployed}$ and $L_{undeployed,out} = L_{deployed}$.

4.3.3 Scaffold parameterization and instrument workspace

The scaffold parameters are determined by using the colon sizes shown in Table 4.1. Many parameters are dependent on practical considerations, such as the size required for manufacturing, and thus the main parameters that are adjusted to change the deployed scaffold size are g_1 and g_2 . While the scaffold can be designed to be tapered (e.g. $g_1 > g_2$), a parallel configuration is much more practical for most sections in the colon, thus $g_1 = g_2 = g$. Another parameter that can be modified relatively easily is the angle β , representing the height over width ratio of the scaffold, i.e. $r(\beta) = h/w$. A third parameter that has not received much attention, but has a clear influence on the workspace, is the thickness of the scaffold wall t .

A study is performed to evaluate the effect of each of these parameters g , β and t . The values of the other parameters are as set as in the final scaffold, as shown in Table 4.3. Unless indicated otherwise, the other variables remain the same. The dimension of g is chosen to by default represent the transverse colon of the American population, enabling scaffold deployment in all sections of the colon except for the descending and the sigmoid colon. When undeployed the scaffold diameter is smaller than any of the colon diameters shown in Table 4.1. The positions of the entry points as a function of the scaffold size, and the overtube dimensions and the cable attachment points on the overtube can be found in Appendix A.1. For the calculation of the workspace, a minimum and maximum cable tension of $0N$ and $60N$ is used. In each case, the total volume of workspace of both instruments V_t , the volume of workspace at which both instruments overlap V_o and the surface area A_s of the overlapping workspace at a plane representing the colon wall is given.

Figure 4.10 and Table 4.2 show how g can be varied to adapt the scaffold for a selected size of the colon (adopted from Table 4.1). As a reference, a 20mm lesion has a surface area of 3.1cm^2 . The figure shows that, as expected, the workspace increases for larger colon dimensions. The effect of the ratio $r(\beta)$ for a fixed circumference is shown in Figure 4.11. It can be seen that the volume of the workspace is larger for a higher ratio r . However, the surface area increases initially, but reaches an optimum around $r = 0.4$.

When looking more closely at the data (Figure 4.12), one also sees that the quality of the workspace is much better for the more elliptical scaffold shape. Increasing the thickness t has a strong detrimental effect on the workspace (Figure 4.9). This result imposes clear constraints for the scaffold's dimensions and illustrates that great care should be taken in future developments for inflatable scaffold structures.

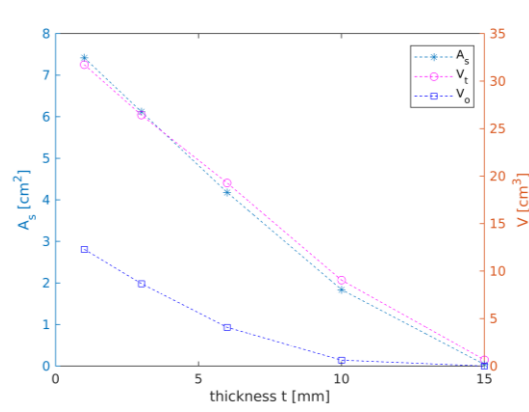


Figure 4.9 – The workspace for scaffold thickness t , corresponding to a colon diameter of 50mm (Transverse, American).

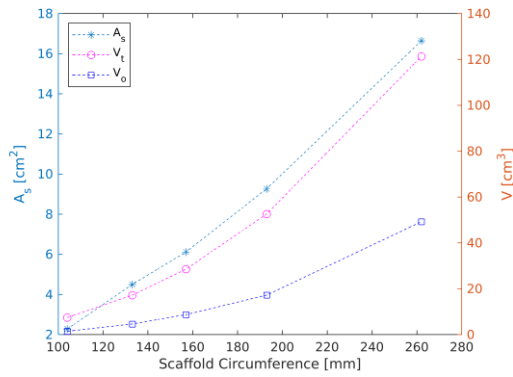


Figure 4.10 – The relationship of the scaffold circumference to workspace.

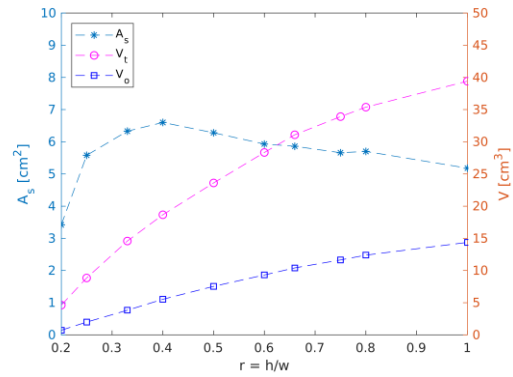


Figure 4.11 - The workspace for different height-to-width ratios.

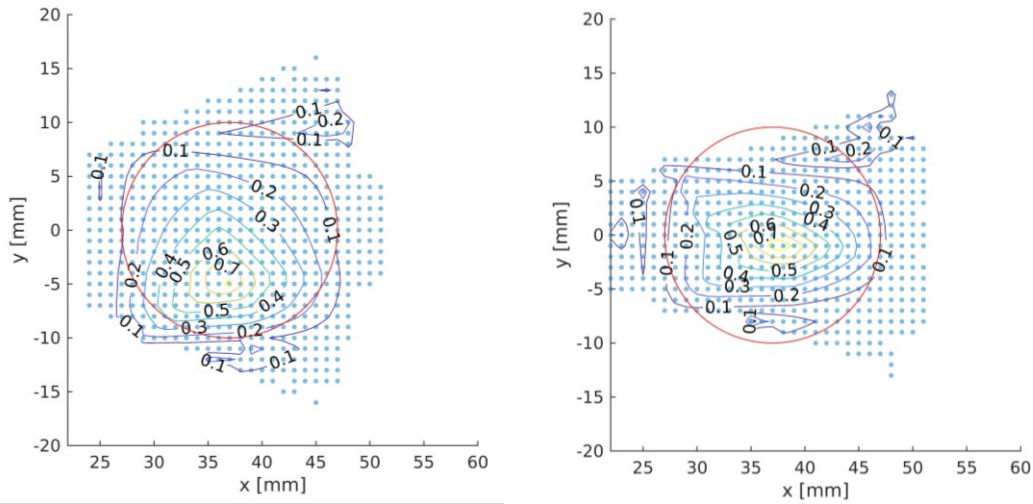


Figure 4.12 – The workspace for $r = 0.5$ (left) and $r = 1.0$ (right) with the tension factor as isolines. The dots indicate the reachable poses by both instruments. The red circle is as reference for a 20mm diameter lesion. The circumference used represents the mean diameter of American transverse colon.

Section	Circumference	g	V_t	V_o	A_s
S + D, Japanese	104mm	7.7mm	$7.5cm^3$	$1.4cm^3$	$2.3cm^2$
T, Japanese	133mm	12.4mm	$17.2cm^3$	$4.6cm^3$	$4.5cm^2$
T, American	157mm	14.4mm	$28.5cm^3$	$8.7cm^3$	$6.1cm^2$
A, American	193mm	18.9mm	$52.6cm^3$	$17.2cm^3$	$9.3cm^2$
$P_{95}(A)$, American	262mm	27.5mm	$121.3cm^3$	$49.2cm^3$	$16.6cm^2$

Table 4.2 - The workspace volume, overlap and surface area at the tissue plane. The circumference is calculated based on the mean diameter of the Sigmoid (S), Descending Colon (D) and Transverse (T) of the Japanese population, using the Transverse and Ascending Colon (A) for the American population (See Table 4.1). Rather than the cecum, the P_{95} percentile ($P_{95} = \mu + 2\sigma$) of the ascending bowel is used as the largest diameter.

4.3.4 Overtube curvature

In previous workspace calculations the curvature of the overtube was always determined by placing the local COM halfway between the coordinate points along all three axes, i.e. at pose $\zeta_c = [0, w/4, 0, 0, 0]$ (Figure 4.13). From this point, the curvature was determined thus that the tip reached a point located 15mm in front of the front cables (at point $[37, 0, 0]$ with the front cables at $b_z = 22$). This enables maximum translation of the end-effector along each axis to dissect the largest lesions.

However, the curvature can be determined in many arbitrary ways, and it is not clear how the shape will influence the workspace of the end-effector on the surface. We know that for CDPMs the highest quality of workspace is within the geometric centre between the entry points [54]. Hence, this is another possible starting point for determining the overtube curvature. The geometric centre of the entry points resembles the pose used in previous workspace calculations (ζ_c) and can be

calculated by taking the mean of the x, y, z coordinates of the entry point matrix B_m : $\zeta_\mu \approx [0, w/6, 0, 0, 0]$.

To understand what curvature is best, the global COM of the overtube used to determine the curvature can be moved along the y -axis¹⁵. Figure 4.14 shows the effect on the workspace of changes in the COM position for a scaffold with the dimensions given in Table 4.3. The y position relative to the scaffold width w is given, with $w = 63.4\text{mm}$. Looking at the individual workspace surfaces (Figure 4.15), it is clear that the best workspace is found at around $y_{com} = 0.4w$.

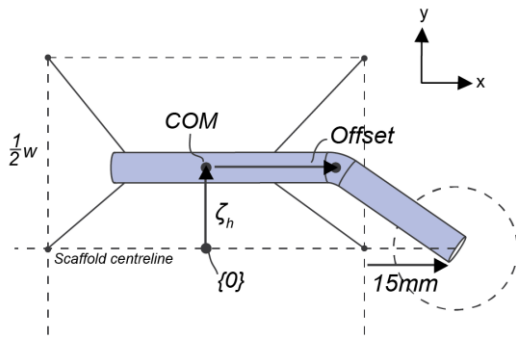


Figure 4.13 – The curvature in the overtube is defined by the angle required for the tip to reach a point 15mm in front of the scaffold from a chosen homing pose ζ_h .

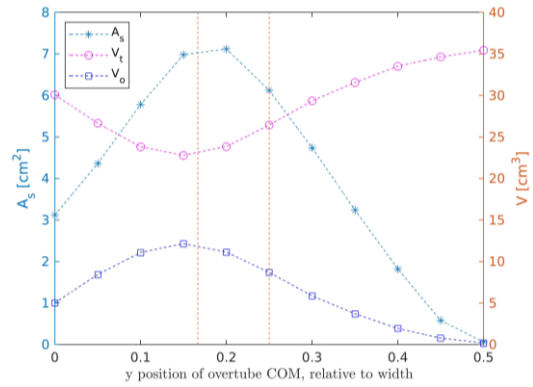


Figure 4.14 - The workspace for curvatures determined by $y_{com} = [0, 0.05, \dots, 0.5]w$. The vertical lines indicate the y_{com} for the geometric centre and at $y_{com} = w/4$.

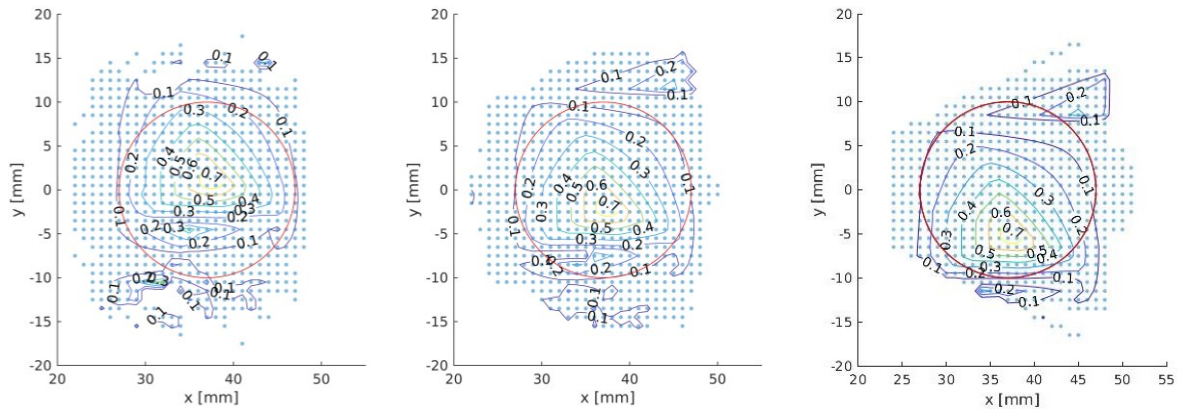


Figure 4.15 – The workspace of both instruments when determining the curvature with y_{com} at $0.3w$, $0.4w$ and $0.5w$ (left to right)

¹⁵ The other axes and rotations could also be used; however, this creates too many variables to explore. An optimization technique for this and the cable entry-points is discussed in Chapter 7.

4.3.5 Scaffold parameters and manufacturing

The final values of the scaffold parameters and the resulting scaffold dimensions are shown in Table 4.3 and Table 4.4, respectively. The workspace of the system is shown in Figure 4.16. The instrument workspace is 28.8 cm³ in total, with a 9.8 cm³ overlap and 6.6 cm² overlap at the tissue surface.

b	c	d	e	g_i	k_i	θ_{min}	θ_{max}	α_1	α_2	β
24mm	6.5mm	5.0mm	4.6mm	15mm	25.7mm	20deg	89deg	16.5deg	17.7deg	28.6deg

Table 4.3 – Parameters of the final scaffold design.

	Undeployed	Deployed
Width	30mm	66mm
Height	18mm	39.6mm
Length	72.9mm	61mm
Circumference	83.2mm	162.2mm

Table 4.4 – The dimensions of the scaffold when deployed and undeployed.

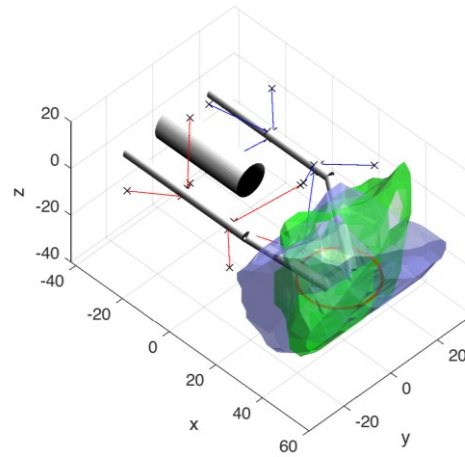


Figure 4.16 – The workspace of the left (green) and right (blue) instrument. A 20mm red circle is used to simulate a lesion.

The deployed and undeployed scaffold are shown in Figure 4.17. The scaffold is made of stainless steel (LaserForm 17-4PH) using Direct Metal Printing (Prox DMP 100, 3D Systems, USA). The choice of material is made to provide a robust platform for benchmarking and multiple *ex vivo* and *in vivo* studies. The scaffold includes slots to guide the Bowden cables containing the CDPM actuation cables. The PTFE inner sleeve, which is used to reduce friction, is extended longer than the Bowden cable to prevent friction at the attachment point. The scaffold is deployed by changing length a . The change in length is achieved by rotating threaded rods in the scaffold. Two pieces of the scaffold are moved towards each other as the M3 threaded rod is constrained on one side and has a nut on the other. Rotating a flexible piano wire rod through a PTFE Bowden provides the rotation of the threaded rod in the scaffold.

An earlier iteration of the scaffold (Appendix A.2) used a spring-loaded actuation mechanism controlled by a cable guided through a steel Bowden cable. A pre-clinical *in vivo* trial of the system led to a more robust mechanism. The trial also led to the bullet shape and current dimensions of the scaffold.

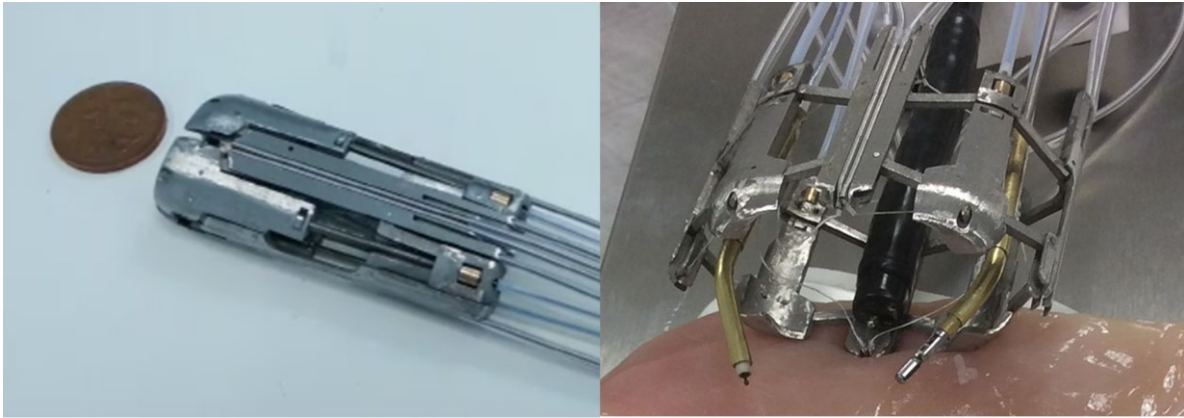


Figure 4.17 – The scaffold undeployed (left) and deployed (right).

4.4 Bench-testing

The original idea behind the use of a CDPM for flexible endoscopy was based on the high payload capacity of CDPMs. The original CYCLOPS [34] concept already showed that high forces could be achieved. However, the cables were guided directly from the motors to the scaffold, without conduit cables. Also, the system used a different size and shape of both scaffold and overtube. These changes influence the payload capacity and the positional accuracy of the end-effector, and therefore both aspects are evaluated experimentally in the following sections.

4.4.1 Force exertion

The payloads were evaluated with both a straight and a curved overtube, in order to evaluate the effect of the overtube shape. It was expected that lower forces would be found for the curved overtube, as end-effector forces are affected by the stiffness around the X-axis. The tip of the overtube was clamped and mounted on top of a 6 DoF Loadcell (Nano17, ATI Industrial Automation, Inc., USA). A 16-bit DAQ (NI USB-6259, National Instruments, USA) was used to read the forces. A

modified curved overtube with straight angles was used for the clamping of the tip. The setup for the straight and curved overtube is shown in Figure 4.18. Forces were measured while moving the overtube in both directions along the 3 axes: x^+ , x^- , y^+ , y^- , z^+ , z^- . Forces were evaluated for the overtube placed at the geometric centre of the entry points (homing position), as well as at the

	Straight		Curved
	Homing	Boundary	Homing
x^+	21.31N	46.39N	19.08N
x^-	20.99N	41.01N	24.30N
y^+	7.50N	24.86N	3.47N
y^-	18.46N	26.33N	17.82N
z^+	8.98N	16.59N	5.29N
z^-	9.79N	13.37N	7.65N

Table 4.5 - The measured forces at the tip of a straight and curved overtube.

boundary of the workspace. At the boundary the overtube was moved inwards, i.e. towards the centre of the workspace. Table 4.5 shows the maximum forces at each situation. Figure 4.19 shows the end-effector force and the cable tension for the straight overtube at the boundary for an x^+ motion.

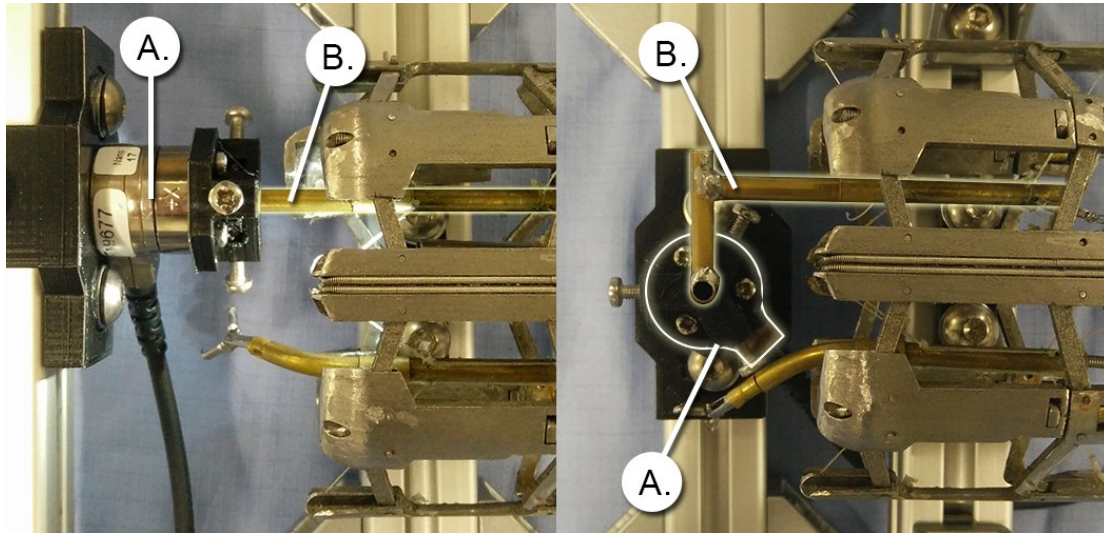


Figure 4.18 – The setup used for measuring the forces with the loadcell (A) and the clamped overtube (B). The images show the clamping method for the straight overtube (left) and overtube with straight angles representing the curved (right). ©2018 IEEE.

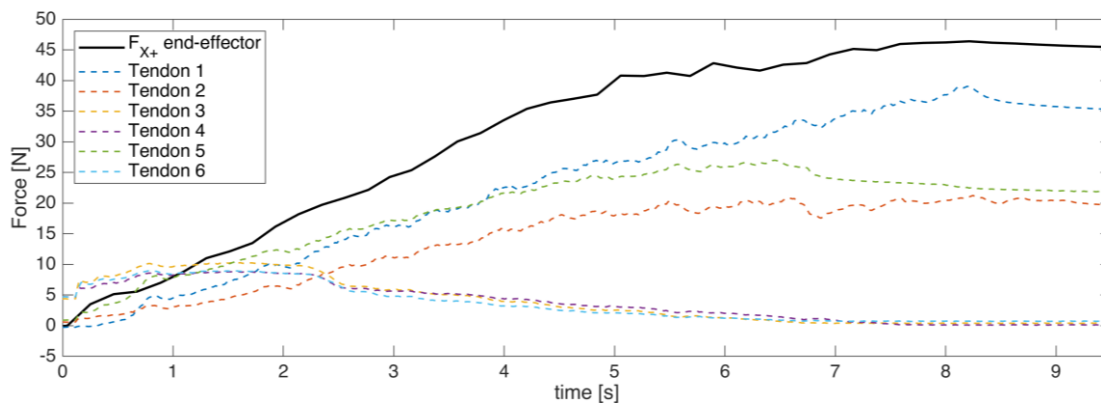


Figure 4.19 – Each of the cable forces and the measured end-effector force using the Nano17. The data shown is for a straight overtube with a motion from the workspace boundary into the x^+ direction. ©2018 IEEE.

The results again show high payloads for the CYCLOPS system, now modified for flexible endoscopy. Slightly lower forces are measured for the curved overtube; however, these still exceed the clinical force requirements for ESD. Even for NOTES, the order of magnitude is sufficient for the manipulation of almost all internal organs. The high forces are an important finding as these are important for further development. Unlike many other flexible endoscopic systems, the payload is not a problem, and offers flexibility in the design of future CDPM mechanisms. For instance, much

lower cable tensions could be used for ESD, leading to thinner scaffold structures made of more compliant materials than the current steel.

All the cable tensions are lower than the maximum end-effector force, which illustrates the efficiency in force transmission. It should be noted that given the cables' maximum rated loads of 13kgf (130N), and how these compare to the maximum measured tensions, it is evident that much higher forces can be achieved. The maximum forces are limited by the control system, as the inverse kinematics are based on the joint space (motor position) rather than the real end-effector position. In reality, the end-effector position will not change because it is rigidly attached to the loadcell. However, the feed-forward control system assumes the end-effector is displaced. Normally once the end-effector pose lies outside of the boundary, the cables responsible for pulling towards the boundary start to release to satisfy the inverse kinematics. This also happens when the theoretical (or desired) end-effector pose lies outside the boundary while the end-effector is clamped to the loadcell. As a result, once the theoretical pose lies outside of the workspace boundaries, the cables start to release and this leads to a reduction of end-effector forces. If the real end-effector position would be used in the control loop this would likely lead to (even) higher forces during the benchmarking experiment. However, as the forces are already sufficiently high for current clinical requirements, this is not necessary.

4.4.2 Control Accuracy

The accuracy of the control is illustrated by a user study involving six engineers and one clinician. Each participant performed a tracing task of an elliptical shape placed at the centre of the scaffold. The curved overtube was modified to straight angles to enable the placement of a pen as the tip. The ellipse had principle axes of 20mm and 15mm. To remove bias related to visualisation, a high definition 3D endoscope was used (EndoEye Flex 2D, Olympus, Japan). The results of the participants are shown in . As a comparison, the participant who performed the task best in terms of error deviation also performed the same task on the da Vinci robot.

shows the results of the tasks. The digitized images were analysed using the open-source scientific image analysis software ImageJ. The length of the drawn line is compared with the circumference of the ellipse (55.3mm). The area between the reference ellipse and the path is taken as a metric for the error. By dividing this length by the overall circumferential length traced (thus without the portion not traced), the average error deviation is calculated.

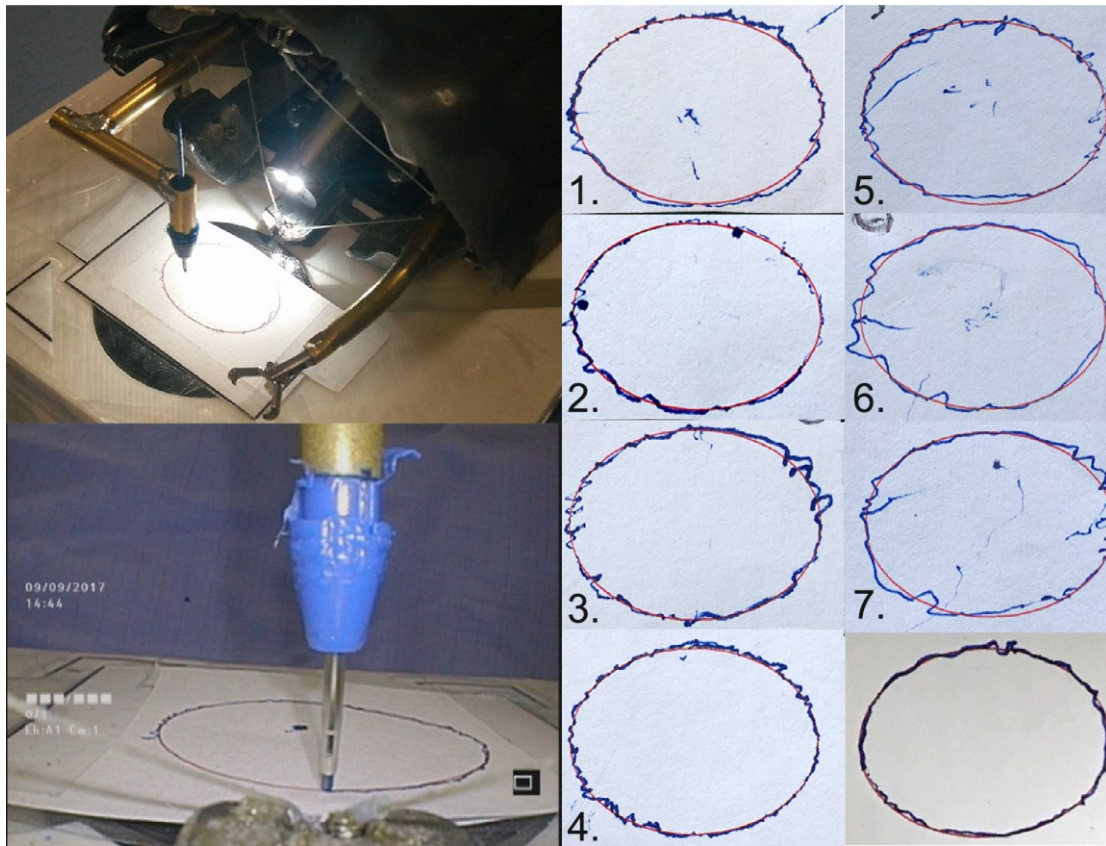


Figure 4.20 – Left: The setup for the tracing task. Right: The results of the 7 users. The bottom-right task is performed by participant 4 on the da Vinci robot. ©2018 IEEE.

	$\mu \pm \sigma$	Range	Da Vinci (Subject 4)	CYCLOPS (Subject 4)
Area Error	$12.69 \pm 1.55\text{mm}^2$	$7.27 - 16.3\text{mm}^2$	6.43mm^2	7.27mm^2
Average mm error deviation	$0.217 \pm 0.06\text{mm}$	$0.133 - 0.302\text{mm}$	0.117mm	0.133mm
Total length drawn	$76.3 \pm 6.7\text{mm}$	$59.3 - 77.9\text{mm}$	59.5mm	64.5mm
Ratio drawn line to circumference	$122.3 \pm 12.1\%$	$107.0 - 140.6\%$	107.4%	116.4%
Elliptical circumference not covered	$2.14 \pm 1.55\%$	$0 - 4.97\%$	0.67%	0.63%
Time to perform the task	$80.0 \pm 21.9\text{sec}$	$43 - 104\text{sec}$	70sec	93sec

Table 4.6 – The results of the ellipse tracing task ($n = 7$). Values are the same as [304].

The metrics show high accuracy for the task. Looking at the tracings, one can see jitter in some users. The jitter seems more frequent at locations with a lower tension factor (as shown in Figure 4.15; note that the system's y-axis is parallel to the long axis of the ellipse). Subject 4 showed that the same task could be performed marginally better with the da Vinci than the CYCLOPS (0.117mm versus 0.133mm average error deviation, respectively). While only evaluated for a single user, the results can be used to place the demonstrated results and used metrics into perspective. In that perspective, and taking into account that the da Vinci is a multimillion-dollar system with a large

development team, the results obtained show that there is promise in further development of the system.

4.5 Pre-clinical validation

Pre-clinical evaluation was performed on porcine tissue. The scaffold was mounted on a gastroscope (13801 PKS video gastroscope, Karl Storz), and two conventional flexible instruments were placed in the overtube. The left instrument was a grasper (FG-44NR-1, Olympus, Japan) and the right instrument was a Dualknife (KD650L, Olympus, Japan). A flexible needle was inserted into the biopsy channel for the mucosal injection. The *ex vivo* and *in vivo* trials were performed by an endoscopist experienced in ESD.

4.5.1 *Ex vivo* validation

Ex vivo ESD was performed on both chicken skin and porcine stomach. The undeployed scaffold was inserted into the stomach and deployed. After deployment, the stomach was closed using sutures to enable insufflation of the stomach. ESD was performed on the mucosa, as shown in Figure 4.21. A lesion of approximately 26x30mm was dissected, which approximates the workspace presented above.

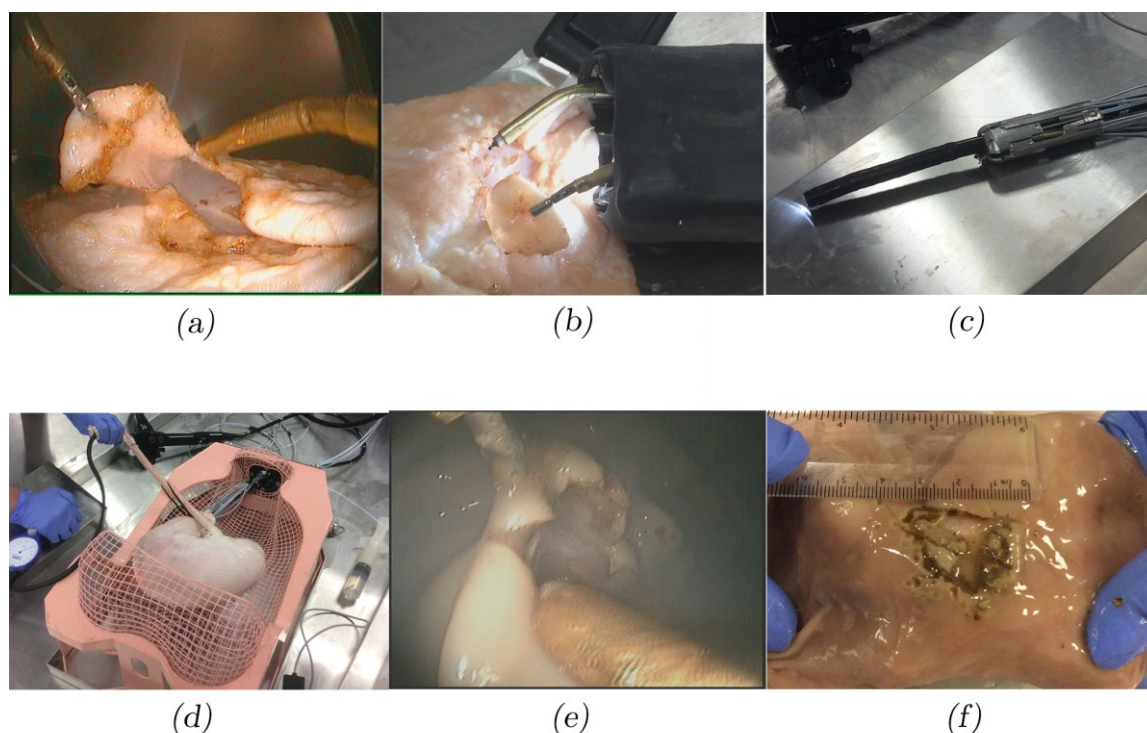


Figure 4.21 – (a,b) ESD performed on chicken skin. (c) The endoscope with the undeployed scaffold on it before insertion into the porcine stomach. (d) The insufflated stomach with the scaffold inserted. (e) ESD performed in the stomach. (f) The dissected mucosa of the stomach.

4.5.2 *In vivo validation*

The system was tested in two *in vivo* porcine studies. The first study was carried out with an older version of the scaffold based on spring-deployment (Appendix A.1). The study revealed difficulties in deployment and navigation, preventing the performance of ESD. The unsuccessful deployment was related to the deployment actuation mechanism and the fact the scaffold was outward-deploying. An attempt to perform the ESD when partly deployed (Figure 4.22) was unsuccessful due to the unknown scaffold parameters leading to a broken cable. The study led to an improved second design with smaller dimensions and a new deployment mechanism. The breakage of cable can be partly prevented by use of a tension control routine, which was implemented in Chapter 5.



Figure 4.22 – The first animal trial with the scaffold partly deployed, showing a clear view of the gastrointestinal tract and the setup. ©2018 IEEE.

The second trial was performed on a 60 kg pig. The scaffold was successfully inserted into the anus and navigated through two flexures to a depth of 52cm. Further navigation was prevented due to faeces. The silicone outer shell was shown to cause somewhat more resistance than the previously used latex, and required lubrication. The scope-and-scaffold was retracted to a previous section of the rectum, where the system was deployed. Pneumorectum was maintained. Marking and injection

of the mucosa was successfully performed (Figure 4.23). During the circumferential dissection of the simulated lesion, a perforation was detected. As a result, the colonic pressure dropped, occluding visualisation of the lesion (Figure 4.23f) and preventing further ESD. The scaffold was inserted into another section of the bowel, assisted by a laparotomy. However, the scaffold was too large for deployment in this section and the resulting workspace was too small to perform a full ESD.

While a full ESD was not performed, the trial indicated directions for future developments. Two important points of feedback were the occurrence of tissue perforation and the size-to-workspace relationship of the scaffold. Tissue perforation is the most important aspect to prevent in further developments of this technology; as such, this should be explored further. A possible explanation is the thickness of the colon wall, which is notoriously thin in humans and may be even thinner in pigs. Another factor that may have caused the perforation is the combination of the type of knife used and the large angle of incidence as result of the overtube curvature. ESD is often performed at a shallow angle to better visualise the underlying submucosa. As indicated by Yoshida et al., the choice of diathermy instrument can cause perforation in specific situations [305]. At a large angle of incidence, the short-tip dualknife might be more prone to perforations than for instance an insulated tip knife, possibly with a shorter blade than is conventionally used. The appropriate combination of blade and angle of incidence should be evaluated separately.

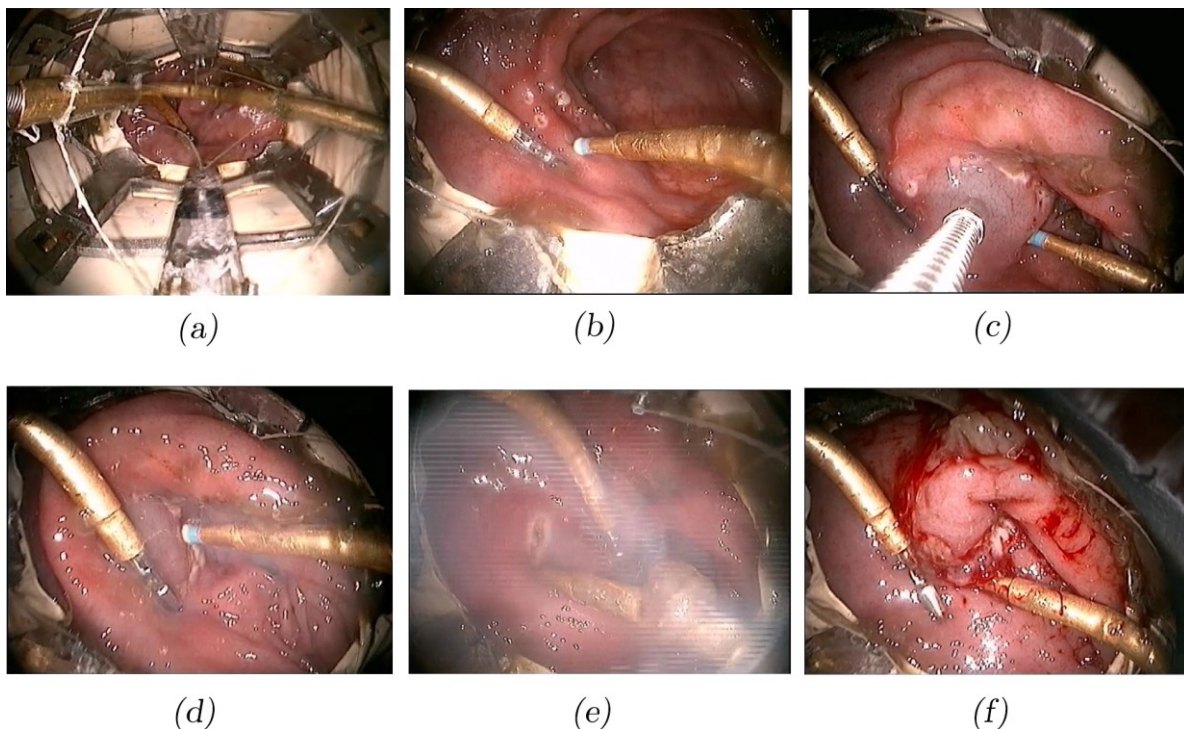


Figure 4.23 – The second animal trial. (a) The scaffold fully deployed. (b) The marking of the lesion. (c) The flexible needle is inserted into the endoscope's working channel, and shown here while injecting underneath the mucosa of the marked lesion. (d) Circumferential dissection of the marked lesion. (e) The dissection just before perforation of the bowel. (f) The bowel collapses inwards due to the loss of pressure.

4.6 Discussion

Current endoscopic techniques display limited dexterity and low payload capacities, and the improvements they offer for ESD are therefore limited. The current chapter evaluated whether a CDPM can be used to provide high payload capacity and dexterity for flexible endoscopy. The ESD CYCLOPS displayed unprecedentedly high forces and high accuracy. The system also showed initial feasibility *during ex vivo* and *in vivo* porcine tests.

The workspace of the instruments is highly dependent on the thickness of the scaffold and the circumference of the colon. The latter also became apparent during the *in vivo* test, in which the workspace was not large enough to perform ESD when the scaffold did not fully deploy. An increase in workspace is required to enable removal of non-polypoid lesions of all sizes. The method currently used to assess the optimal configuration is based on evaluation of the effects of specific design choices, rather than a full parametric workspace optimization. Further workspace optimisation is discussed in Chapter 7. One of the possible approaches enlarges the workspace of the instruments by the addition of an active joint in the overtube. Such a joint, placed serially, will inevitably influence the force exertion capability of the end-effector. However, looking at the systems discussed in Chapter 3, it is noticeable that the low force capacity is often attributable to a proximal elbow joint. By placing the serial joint at a relatively distal point on the overtube, this effect can be minimized. Additional precautions can be taken by creating a joint which can lock into preset positions, or which can be stiffened.

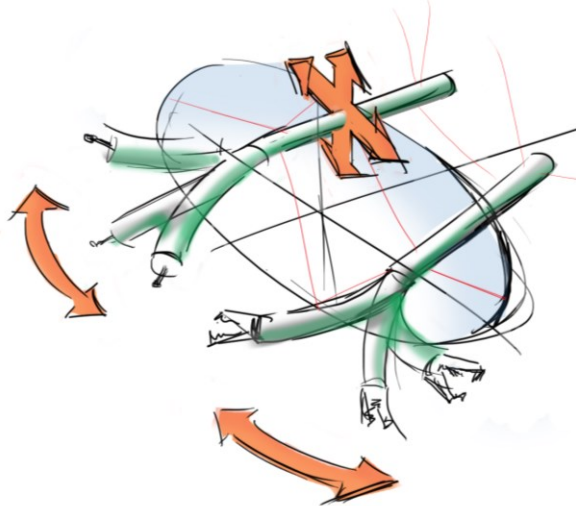


Figure 4.24 - The addition of a serial link should contribute to an increase of workspace.

The current scaffold design is characterized by a relatively high complexity, with multiple links and moving parts. The number of movable parts is often a concern with regard to the robustness of mechanisms, and in further developments, attempts should be made to minimize the number of parts. As previously mentioned, the use of an inflatable scaffold is one promising direction for future development. The current study highlighted that the shape of such inflatable scaffold should ideally be elliptical to increase the workspace on the tissue surface. The relationship between scaffold thickness and workspace shows that the thickness of the inflatable scaffold should be minimized to allow for an appropriate workspace. The combination of an elliptical shape and thin wall can lead to a decrease in the force-bearing capability of such scaffolds. However, the current study also shows that the cable

forces can be reduced, as the current approach outperforms the force requirements for ESD. These low forces are a clear benefit in the development of the next iteration of scaffolds.

Arguably, the use of multiple CDPMs with high DoFs adds complexity to the system, with each of the 12 cables requiring its own actuators, sensors and transmission mechanism. The efficient force transmission shows that the current motors are much stronger than required in practice. While these motors are essential during development in order to explore the capabilities of the system, an eventual system aimed at commercialisation can probably use much smaller motors than a serial robotic equivalent. Further, especially when considering an inflatable scaffold, the system can be created as a disposable scaffold structure, thereby not requiring post-procedure cleaning and sterilisation. Currently, the cable is guided to the motor units along multiple pulleys and eventually wound around the motor spool. Displacement of the cable from the guided path at this section of the system is by far the most common reason for cable failure. Replacing the mechanism with a belt-driven linear guide will strongly increase the robustness of the system. Another way to further reduce complexity is to lower the number of cables. It may be possible to use fewer cables in future iterations, by looking more specifically at the dexterity required for each individual instrument. The use of springs or other elastic elements is an alternative method to reduce the number of motors, similar to the mechanisms used in [97].

In conclusion, the current study has demonstrated clear benefits of the use of CDPMs in flexible endoscopy. The study was also important in evaluating further directions for development of the system for further clinical translation. Special focus will be placed on steps required for the continuation of the scaffold development with an inflatable scaffold.

Chapter 5

Cable-driven parallel mechanisms with force-sensing capabilities

The current chapter discusses the ability of CDPMs to measure the forces acting on the surgical instruments. Rigid parallel architectures are often used in the development of loadcells, and the same properties can be used for CDPMs. The use of a CDPM to sense forces can be applied in minimally invasive surgery (MIS) to provide haptic feedback and offer safe tissue interactions. As mentioned in Chapter 1, the absence of haptic feedback is one of the shortcomings of current surgical robotic systems. This chapter will first discuss the available technology and development used to provide haptic feedback in MIS. This is followed by a discussion of the CYCLOPS Data Acquisition System (CDAQS), which is capable of providing haptic feedback thanks to the CDPM configuration. The CDAQS has been benchmarked for force estimation and tested with surgical trainees.

5.1 Haptic feedback in minimally invasive surgery

Haptic feedback is defined as the sense of touch related to either tactile or kinaesthetic sensing. Tactile sensing is the sense of temperature, vibrations and texture, provided through mechanoreceptors and thermoreceptors in the skin. Kinaesthetic sensing is the sensing of forces, which is achieved through proprioception and mechanoreceptors in the muscles, tendons and joints, and is often referred to as *force feedback*. Both tactile and kinaesthetic feedback are important for

haptic palpation. Palpation is the examination of a specific part of the body or organ by hand in order to understand tissue pathology and tissue structures for the purposes of screening, diagnosis and surgery. For soft tissue, tissue stiffness is often an indication for disease pathology, such as when palpation is used to detect breast and prostate cancer [306].

In open surgery, palpation is used to detect the disease and margins for adequate resection. However, the transition from open to laparoscopic surgery has led to a loss of tactile and force feedback. This is caused by the interaction of the laparoscopic instrument with the trocar, leading to friction and the scaling and mirroring of forces through the pivoting around the fulcrum point [307]. Additionally, a transmission mechanism is used for the actuation of graspers, leading to additional loss of grasping force feedback. One method used in MIS to restore haptic feedback to the surgeon is hand-assisted laparoscopic surgery (HALS), in which an additional incision is made for the surgeon to insert his/her hand through and handle the tissue. One advantage of HALS over conventional laparoscopic surgery is the ability to palpate tissue, e.g. when performing liver resection [308]. However, for HALS a large incision is needed to insert the hand and it takes a large portion of the intra-abdominal workspace.

The development of Robot-Assisted Minimally Invasive Surgery (RMIS) has led to new technologies for the restoration of haptic feedback. However, it remains limited in RMIS, with the most widely used commercial system, the da Vinci®, providing no haptic feedback at all. Force measurement and estimation is predominantly based on the use of existing sensors or the addition of sensors at different locations on the surgical instruments, as seen in Figure 5.1 [309]. Generally, the closer the sensor is placed to the distal end of the instrument, the more accurate the force measurements are. Transenterix' Senhance system provides haptic feedback during RMIS using sensors placed at the base of the robotic instruments. However, such use of sensors at the base of the instrument encounters similar issues of friction and hysteresis caused by the trocar in conventional laparoscopic surgery [309]. Unfortunately, we could not find a technical study of the Senhance system demonstrating that the system is able to provide accurate force sensing despite the presence of friction between instruments and the trocar, a fulcrum point acting as a lever for forces, and tissue elasticity at the port as a possible source of error. Another method to estimate tip forces is to use sensors at the joint space of the actuators; this is referred to as *indirect force sensing* due a force transmission mechanism in between the sensors and the tip. The fact that measurement occurs before the transmission mechanism is also considered to be one of the limitations of this method, introducing error due to friction and hysteresis [307]. Tadano et al. estimated the forces at the tip of a cable-driven laparoscopic robotic instrument actuated by means of pneumatic pistons rather than DC motors [310]. They used a neural network to compensate for the friction in the cable transmission

and to estimate forces at the instrument tip using the pneumatic pressure measured at the actuators. Similarly, the tip forces can also be estimated through measurement of the motor currents. Sang et al. developed a force estimation method for the da Vinci system using motor currents and dynamics, which achieved a force accuracy of 0.1N [311]. Another group suggested the use of a parallel structure to provide tip dexterity and force estimation at the tip of a rigid laparoscopic instrument [312]. The design achieved high accuracy along axial and bending axes. The authors have developed a 15mm diameter version of the system, and suggest that a 10mm diameter version should be possible in future developments. In addition to this design's relatively large size, its need for a dedicated force-sensing instrument may constitute a limitation preventing its use for a wider range of applications in MIS in which safe tissue interaction is beneficial. Another group developed a parallel structure for force sensing and control of two instruments, such as a grasper and diathermy [313]. The system estimates the forces by using strain gauges near the actuation motors. However, the system's 38mm shaft is incredibly large by MIS standards; possible applications include Transanal Endoscopic Microsurgery (TEMS) with a 40mm retractor port.

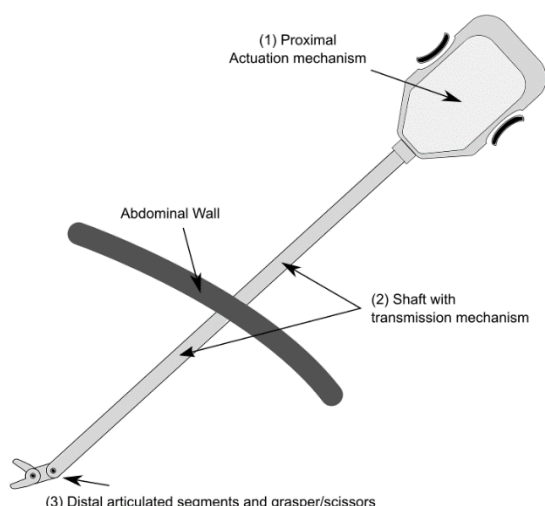


Figure 5.1 - Different locations at which force sensors are placed to measure forces at the instrument tip.



Figure 5.2 – Using a parallel structure to enable accurate force sensing at the proximal end of the instrument [312] ©2018 IEEE.

The placement of strain gauges has been used to measure strains along the instrument shaft of laparoscopic instruments. A modular sleeve has been developed for conventional 5mm instruments to measure the 2DoF bending moments along the instrument shaft [314]. Strain gauges have also been implemented in the EndoPAR system for training neural networks for autonomous tasks [129]. One of the main limitations of the use of strain gauges along the shaft is the sensitivity for changes in temperature changing the resistance, and thereby the calibration of a system [309]. Placing sensors

at the distal end of the instrument is challenging due to the stringent clinical requirements in terms of size, robustness and sterilization of instruments [315].

Different types of technologies such as optical, capacitance and piezoelectric sensing have been developed to sense forces in MIS; their limitations are summarized in [309][316]. Such sensors are often used for tactile sensing and the measurement of grasping forces. One notable development is the DLR MiroSurge robotic platform, which uses strain gauges at the instrument tip to provide force measurements in 6 DoF (Figure 5.3) [32]. The strain gauges are integrated into a miniature Stewart-Gough platform at the tip of the 10mm wristed surgical instrument. The DLR MiroSurge technology seems very promising, combining lightweight robotic arms with haptic sensing technology, and is designed to be sterilisable. Medtronic showed interest in the system a few years ago and further development of the system is likely happening behind the scenes.

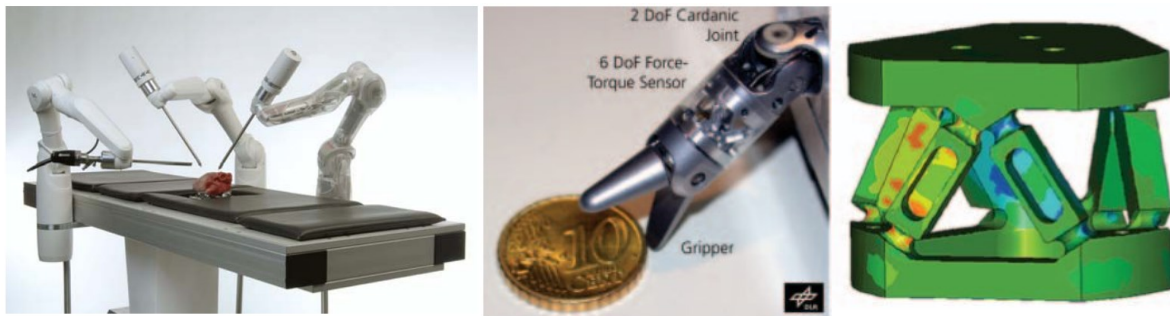


Figure 5.3 – The DLR MiroSurge system. The centre image shows the articulated end-effector mounted on a Stewart-Gough platform (Right). Each of the links of the Stewart Platform has a strain gauge used to sense forces in 6 DoF at the instrument tip. Image sources: [32][317].

The use of a parallel Stewart-Gough platform is common in 6 DoF force/torque sensors, as is discussed by [318][319]. CPDMs, being a tendon-based version of such platform, have many of the same kinematics as conventional Stewart-Gough platforms, and therefore can potentially be used for force sensing. The CYCLOPS da Vinci Instrument (CYCLOPS dVI) was developed by MRes student Kiyoteru Miyashita. The system is a modified da Vinci instrument that is combined with the CDPM (Figure 5.4) [320]. It involves the placement of a 4-cable planar CDPM on a rigid (not yet deployable) structure. The development of the CYCLOPS dVI for the purpose of force sensing originates from earlier work on the microCYCLOPS and neuroCYCLOPS, in which force-sensing capabilities can be beneficial from a safety perspective when dealing with sensitive brain tissue. The microCYCLOPS and neuroCYCLOPS are discussed in Appendix A.3.

The CYCLOPS dVI was developed for the endoscopic scanning of tissue surfaces, and is intended to eventually be able to safely follow a surface contour based on force-sensing. The work showed that the CDPM could detect forces as low as 0.2N at the tip of the instrument. A crucial aspect of the high force sensitivity is the efficient force transmission from the end-effector to the

joint space. As mentioned in Chapter 2, this efficiency has to do with the inherent properties of parallel mechanisms, and the fact that forces are spread over all the cables. The tension of all the cables can be used to estimate end-effector forces, as will be discussed in greater detail later in this chapter. However, in practice, the tension in the cables is not measured at the distal side but at the proximal side, outside the body. Therefore, the transmission of cable forces from the end-effector to the proximal loadcells introduces errors in the tension measurement due to friction. The CYCLOPS dVI is designed to lower the friction by introducing straight pathways and minimizing the number of contact points, such as pulleys. A more extensive discussion on the CYCLOPS dVI is presented in Appendix A.4 and [320].

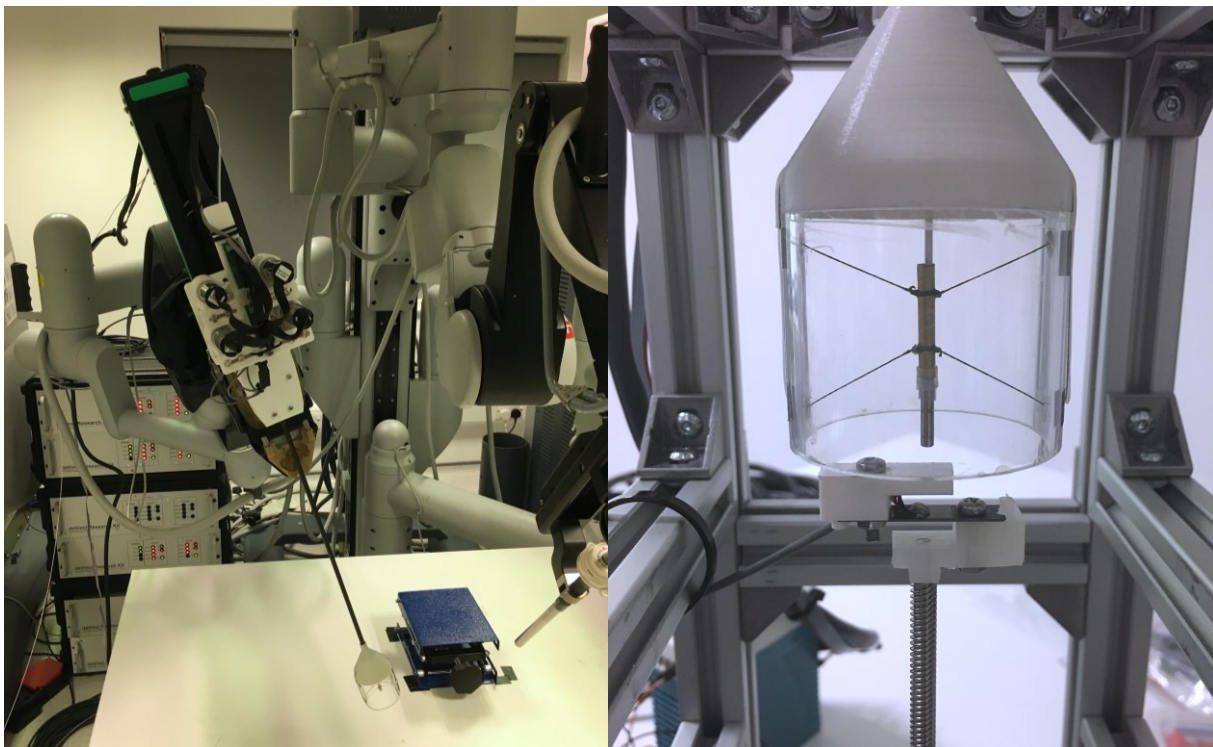


Figure 5.4 – The CYCLOPS dVI, in which the CDPM is used integrated into a surgical instrument mounted on the da Vinci robot. Image source: [320]. Left: The system mounted on the da Vinci Robot. Right: The end-effector with endoscopic probe, controlled with a planar CDPM.

The reduction of friction in the transmission mechanism can be also applied in the designs of other mechanisms, such as the SIMPLE system (Chapter 6) and microCYCLOPS. The CYCLOPS dVI has also not been explored for spatial CDPMs (e.g. 5DoF, such as the ESD CYCLOPS), which are more common. Therefore, this chapter aims to develop a general understanding of the force sensing capabilities of CDPMs, using the CYCLOPS Data Acquisition System (CDAQS). To the authors' knowledge, the CDAQS and the CYCLOPS dVI are the first CDPMs whose end-effector force sensing capacities have been explored– not just in surgery, but in any context.

5.2 The CDAQS system

The CDAQS (Figure 5.5) is a scaled-up CDPM used for development purposes, e.g. developing the control system and evaluating the force sensitivity of the system. The CDAQS uses an aluminium 40x40x53cm frame to which motor units are attached. The motor units (Figure 5.5c) consist of a 9mm diameter cable spool, a loadcell (LCL-020, Omega Engineering, Inc., USA) and a brushless DC motor (2232S024BX4 22F 25:1, Faulhaber GmbH, Germany). The cables are guided over the loadcell pulley and through a short PTFE tube, and from there to the end-effector. Due to the straight pathway and the use of PTFE tubing, friction is minimized.

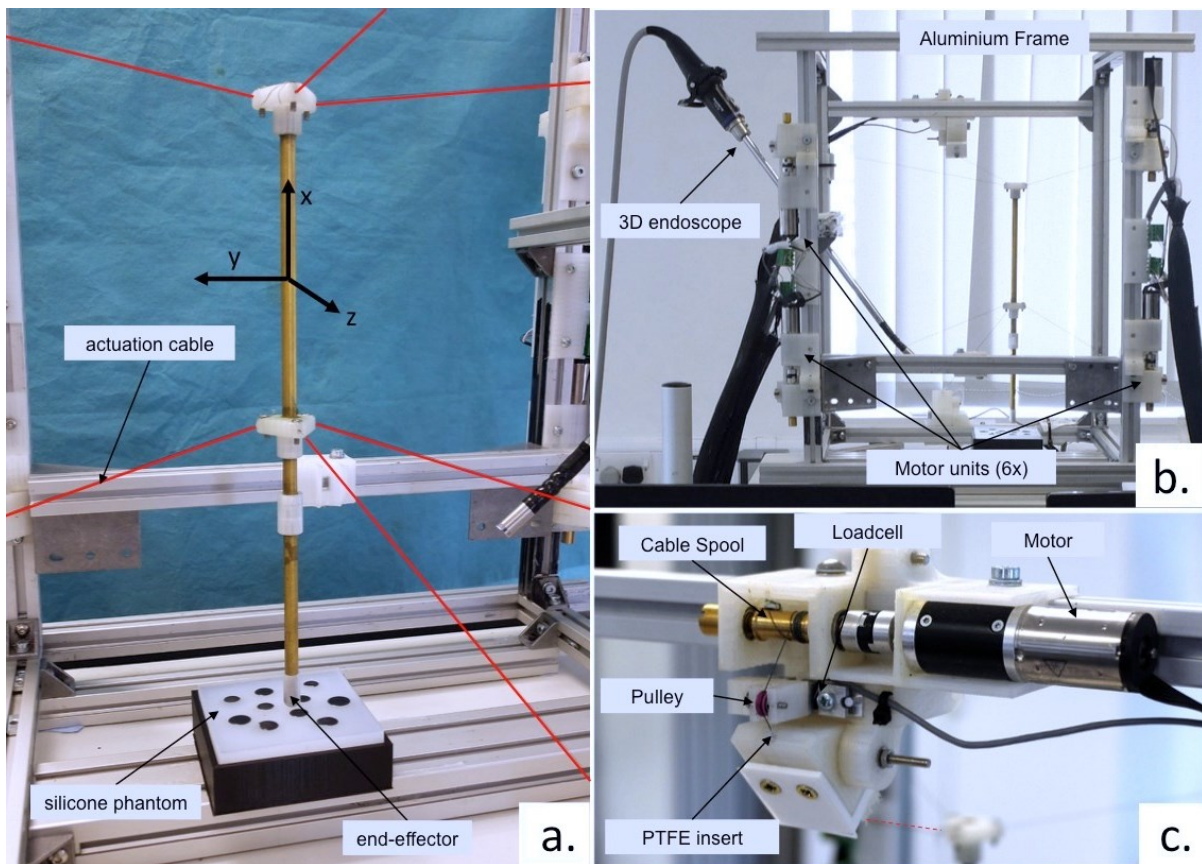


Figure 5.5 – **(a)** The CDAQS system with 6 actuation cables to provide 5 DoF. **(b)** The aluminium frame used for mounting of the motors and the endoscope. **(c)** One of the motor units, showing the cable pathway from the cable spool to the end-effector. Image source: [321].

Like the ESD CYCLOPS, 6 cables are used to control 5 DoF. The system is summarized in Table 5.1. The system parameters are calibrated using an optical tracking rig (Optitrack Prime 13 Cameras, NaturalPoint, Inc., USA). A holder affixed to the aluminium frame determines the homing position of the probe at the beginning of the control routine. The position of this holder is found by using optical markers. The coordinates of the homing position, entry points and attachment points of the CDAQS are found in Appendix A.5.

End-effector	Probe Length	300mm
	Tip Diameter	8mm
	Controllable DoF	5
Cables	Number of Cables	6
	Material	Spectra (UHMW PE)
	Diameter	0.19mm
	Maximum load	13kgf
	Stiffness	3.1207 kNm
	Spool Diameter	9mm
Frame	Frame size	40x40x53cm
	Workspace	14.6701 dm ³
Motion Scaling	X,Y,Z	0.8

Table 5.1 – The dimensions and properties of the CDAQS system. Table is adopted from [321].

5.2.1 System architecture

In contrast to the ESD CYCLOPS, the CDAQS was developed to use high frequency communication using the EtherCAT interface. The earlier CAN interface presented limitations in terms of communication frequencies when using multiple motors, whereas EtherCAT is well suited for such applications. The PC used runs on Ubuntu 14.04 and is patched with a soft real-time kernel (real-time kernel patch 3.10.108), and acts as the master device. The communication is uses a 1Gbit Ethernet cable, connecting the Linux PC with the daisy-chained slave controllers (MC 5004 P ET, Faulhaber GmbH & Co. KG, Germany). The EtherCAT is configured for 1KHz communication frequency. The loadcells measuring the tension in the cables are connected to a digitizer (Instrunet i100, GW Instruments, Inc., USA). As the digitizer is not compatible with Linux, a single-board computer (LathePanda, Shanghai, China) running Windows 10 is used to collect the data and send the tensions to the Linux PC over a UDP connection. The single-board computer (SBC), digitizer and the slave controllers are all placed together into a box. The loadcells are calibrated by placing the motor units in a position in which the pulley points upwards. A specific lightweight mount is placed on top of the pulleys of the loadcells and place calibrated weights on top of it. As the cable angle is predefined by the design of the motor unit, the weight is converted to its respective cable tension.

5.2.2 Control system

A new control system was implemented for the CDAQS. The control routine is similar to [322]. The higher control frequencies can be used to accurately control the cable tensions, and thus a tension control system was implemented. Figure 5.6 shows the schematics of the control system.

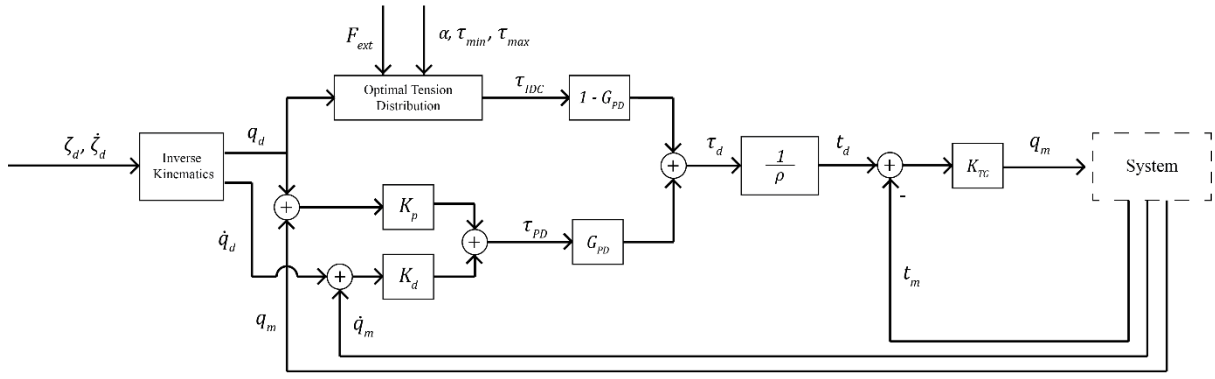


Figure 5.6 – Schematics of the control architecture implemented in the CDAQS system. Image source: [321].

The Inverse Kinematics (IK) is used to translate a desired pose and velocity from the task space to the motor joint space (See Chapter 2). The controller comprises a PD controller, based on measured and desired joint position q_i and velocity \dot{q}_i , and an additional controller to obtain the optimal tension distribution (OTD). The value of both the OTD and the PD controller on the final system input is weighed by $G_{PD} \in [0,1]$:

$$\tau_D = \tau_{PD}G_{PD} + \tau_{IDC}(1 - G_{PD}) \quad (5.1)$$

In which τ_{IDC} and τ_{PD} are the calculated motor torques from both controllers in mNm. The desired τ_D is converted to the desired cable tension by taking the spool radius ρ into account. The error on the desired cable tension on the measured cable tension \vec{t}_m is multiplied by a gain K_{TG} to get the final desired motor angle q_D , making the entire equation:

$$q = \left(\frac{\tau_D}{\rho} - \vec{t}_m \right) K_{TG} \quad (5.2)$$

The PD controller is calculated as:

$$\tau_{PD} = (q_d - q_m)K_P + (\dot{q}_d - \dot{q}_m)K_D \quad (5.3)$$

The optimal tension distribution is important to keep the cable tension between t_{\min} and t_{\max} , the tensions at which cable slackness and failure, respectively, are prevented. The force equilibrium equation 2.3 is modified with $\vec{t} = \rho\tau$ to obtain the OTD. The value $\alpha \in [0,1]$ is used to fine-tune the range of cable tensions, giving the following optimization problem:

$$\begin{aligned} \tau_{IDC} &= \operatorname{argmin}(\|A\rho\tau - \vec{w}\|_2) \\ \text{s.t. } \tau_{\min} &\leq \tau_i \leq \tau_{\min} + (\tau_{\max} - \tau_{\min})\alpha \end{aligned} \quad (5.4)$$

In which A is the structure matrix of the cable-driven parallel mechanism at a certain desired pose ζ_d , also found as the transposed Jacobian: $A = J^T$. The vector \vec{w} is the external wrench vector

acting on the end-effector. The solution for the optimal tension distribution τ_{IDC} is solved online using a bounded-variable least squares method [323], implemented for C++.

5.2.3 Force estimator

The end-effector forces can be estimated using the force equilibrium equations (eq. 2.3):

$$\sum_{i=1}^n \vec{F}_i(\zeta, t_i) + \vec{F}_{ext} + \vec{F}_g + \mathbf{C} \dot{\mathbf{X}} = \mathbf{M} \ddot{\mathbf{X}} \quad (5.5)$$

In which \vec{F}_g and \vec{F}_{ext} are the gravitational and external forces acting on the end-effector. $\vec{F}_i(\zeta, t_i)$ is the force vector for cable i , depending on the end-effector pose ζ and the tension in the cable t_i . Matrices \mathbf{C} and \mathbf{M} are the damping matrix and mass matrix. CDPMs are known to have low inertial effects due to their low end-effector weight. As we are interested in operating the system at low accelerations, the inertial component of equation (5.5) can be omitted (i.e. $\mathbf{M} \ddot{\mathbf{X}} = 0$). Also, the damping of the end-effector is a result of drag, which is typically low for a cylindrical object at this scale moving in air. To elaborate on this, the drag equation ($F_D = \frac{1}{2} \rho C_D A \dot{x}^2$) can be used to estimate the effect on the end-effector while moving with a velocity \dot{x} . In this equation the ρ , C_D and A stand for the mass density of air, the drag coefficient related to the cylindrical geometry and the reference area of this geometry, respectively. The 8mm diameter probe with 300mm length, moving in air at room temperature, will experience a force of $F_D = 6.8 \times 10^{-4} \dot{x}^2$ and $F_D = 2.5 \times 10^{-5} \dot{x}^2$ for a sideways and downwards motion respectively. Velocities of 38m/s and 200m/s are required for drag forces of 1N. Hence, at this scale it is safe to also omit the damping matrix \mathbf{C} . Note that any damping in the cables is a component of the force vectors $\vec{F}_i(\zeta, t_i)$ and thus is not part of the matrix \mathbf{C} . The damping will be partly reflected in both the measured cable tension and the end-effector pose. The estimation of the forces on the end-effector thus becomes:

$$\vec{F}_{ext} = -\vec{F}_g - \sum_{i=1}^n \vec{F}_i(\zeta, t_i) \quad (5.6)$$

The cable force vectors are dependent on the cable direction vectors u_i , which are the first 3 rows of the structure matrix $A^T(\zeta)$ (eq. 2.3). By defining a new matrix \mathbf{U} containing the first 3 rows of the structure matrix, the cable forces can be written as $\sum_{i=1}^n \vec{F}_i(\zeta, t_i) = \mathbf{U} \mathbf{t}_m$ with tension vector $\mathbf{t}_m = [t_1, \dots, t_n]$. An unweighted moving average is used to filter out noise on the measured cable tensions t_i . As the cable tension is read with relatively low frequency, the moving average is applied to 10 previous cable measurements.

5.3 Benchmarking the CDAQS system for force sensing

In order to assess its ability to estimate the end-effector forces, the CDAQS system was benchmarked, first by exerting a force directly on a loadcell, and subsequently by exerting a force on an elastic surface, simulating soft tissue properties. Different controller settings were used in the benchmarking, which are referred to as CS1 and CS2, which represent a gain G_{PD} of 1.0 and 0.2, respectively. These values are chosen as these represent the two extremes of the controller. Values of G_{PD} that are close to 0 lead to less responsiveness of the system as the position is pre-dominantly controlled by the OTD. The lower responsiveness is caused by the errors on the position of the joint space not taken into account by the OTD (in contrast to the PD-controller). In addition to the gains G_{PD} of 1.0 and 0.2, for the force estimation experiments directly on the loadcell also the intermediate value of $G_{PD} = 0.5$ is used, which is denoted as CS1.5.

5.3.1 Direct measurement on loadcell

A force-benchmarking study was conducted by applying a force directly on a loadcell (Nano43, ATI Industrial Automation, Inc. USA). The end-effector moves in a downward motion (x^-) against the loadcell with a linear motion commanded to move at 0.1mm/s over a 3mm distance. Figure 5.7 shows the comparison between the measured and the estimated forces, F_{meas} and F_{est} respectively. The ratio between the maximum of both the measured and estimated forces is compared to assess the accuracy of the estimation: $r = \frac{F_{est,max}}{F_{meas,max}}$. The maximum forces measured by the loadcell are also important to assess the effect of different controller settings. Both values are shown in Table 5.2.

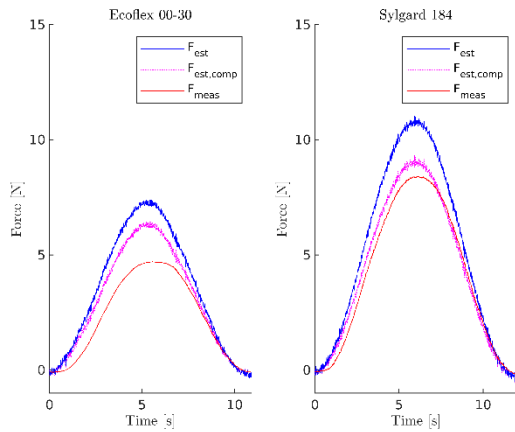


Figure 5.7 – The end-effector force estimation compared to a ground truth loadcell, here shown for control setting CS2. $F_{est,comp}$ represents the force estimation when the pose that is tracked by an a tracker systemImage source: [321].

	$F_{meas,max}$	$F_{est,max}$	$r = \frac{F_{est,max}}{F_{meas,max}}$
CS1	12.43 N	16.77 N	1.35
CS1.5	8.32 N	11.16 N	1.34
CS2	4.37 N	6.04 N	1.38

Table 5.2 – The comparison between ground truth measurement and the force estimation for different control settings.

The results show that the accuracy of the force estimation r remains constant for all control settings. The effect of this parameter on the force estimation was assessed, and it was demonstrated

that except for the reduction of noise of the force estimation, the accuracy of the system remained approximately the same.

The results show that the controller setting has a strong influence on the force exerted on the loadcell. The explanation for this is that the optimal tension distribution requires a lower torque τ_{IDC} than τ_{PD} , as shown in Figure 5.8. To make comparison easier, the torque values are converted to their respective control tensions F_{IDC} than F_{PD} by dividing the torque by the spool radius $\rho = 4.5\text{mm}$. The figure shows that for a CS1.5, the PD-controller remains dominant for determining the overall measured tensions \vec{t}_m . Hence, when changing the contribution of each controller with gain G_{PD} , the tension and thus the forces exerted on the loadcell will change. This is seen in Table 5.2, in which a lower G_{PD} gain (i.e. CS2) leads to lower forces exerted on the loadcell, and vice versa for a high gain G_{PD} .

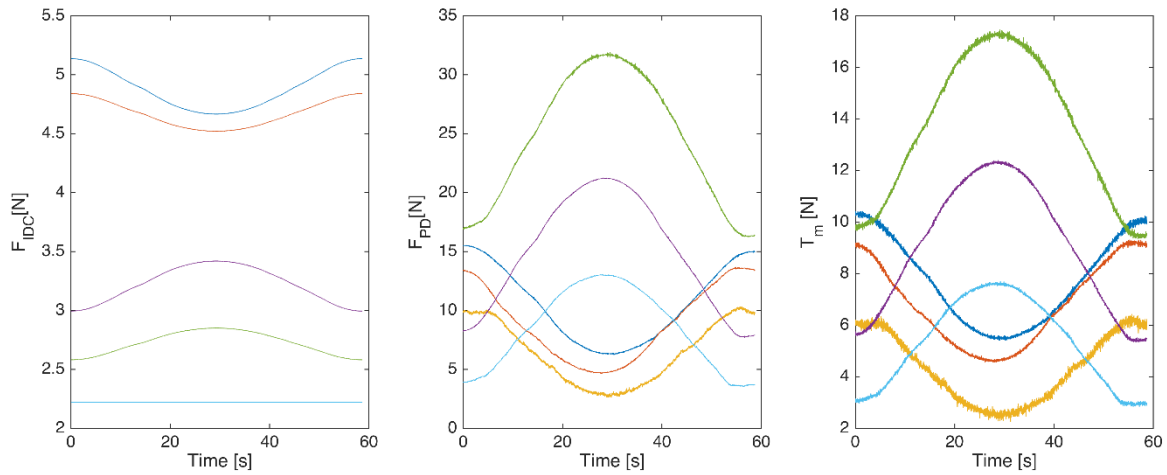


Figure 5.8 – The controller values for each motor while exerted forces on the loadcell, here shown for control setting CS1.5.

5.3.2 Estimation on plain silicone phantoms

Deformation of the surface with which the probe is in contact may affect the force estimation. In addition to the previously used loadcell, two plain silicone phantoms of 80x80x20mm are placed on top of the loadcell, which allows the measurement of all indentation forces on the phantoms. The silicones used are Ecoflex 00-30 (Smooth-on, Inc., Macungie, USA), and Sylgard 184 (Dow Silicones Deutschland GmbH, Germany). The probe is placed in the centre of the phantom and makes a downward motion to deform the silicone material. Each motion consisted of a 12mm linear motion in the downward X direction. Figure 5.9 shows the maximum values found for the system when probing the soft surface at different velocities.

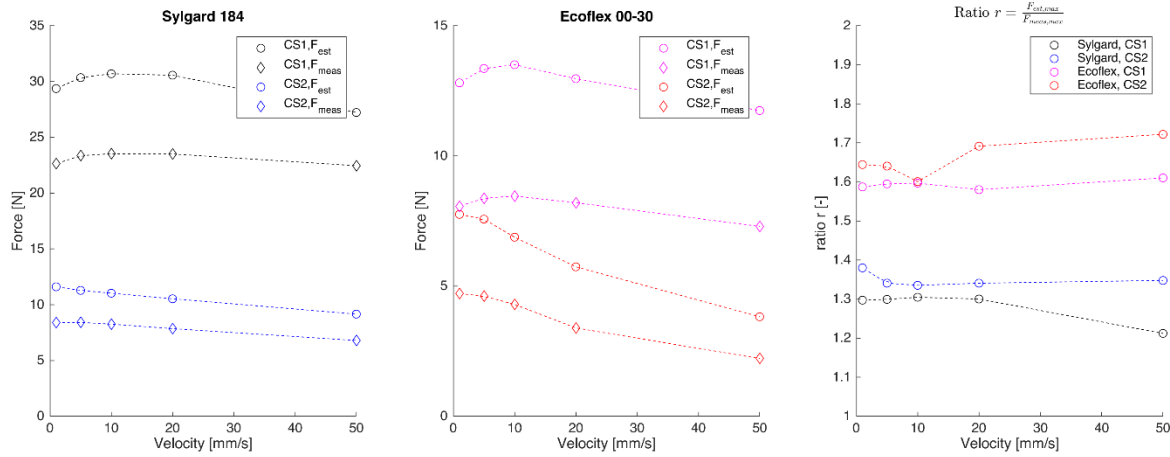


Figure 5.9 - The measured and estimated forces for the hard and soft silicone phantoms (Sylgard and Ecoflex, respectively). The accuracy of the estimation is visible in the ratio between the measured and the estimated forces.

The graphs show that in all cases, the estimated force is higher than the measured ground-truth force. The velocity has a slight influence on the measured and the estimated force, showing a decrease in maximum forces at higher velocities. The estimation accuracy r remains relatively stable for each specific combination of silicone phantom and control settings. Both the estimated and the ground-truth forces decrease slightly for higher velocity in each of the silicone phantoms, which is related to smaller indentation depths at higher velocities. This is verified by looking at the measured displacement of the end-effector, shown in Figure 5.10. For CS2 the silicone deforms less than for CS1, which is in line with the lower end-effector forces, both measured and estimated. The stiffness k_{max} can be calculated by taking the ratio between the measured deformation and the measured or estimated forces, $k_{max} = \frac{F_{max}}{d_{max}}$. As shown in Figure 5.11 any effects of velocity are cancelled out. Notice, however, that the stiffness for the harder Sylgard phantom is different depending on the control setting. The difference suggests that part of the end-effector forces are exerted in a lateral rather than axial direction.

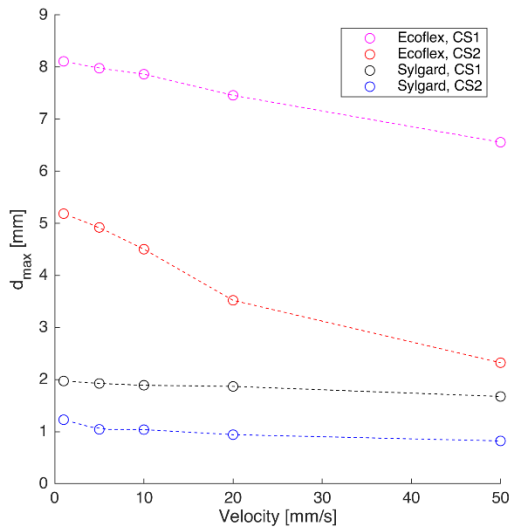


Figure 5.10 – The measured displacement of the end-effector for commanded velocities.

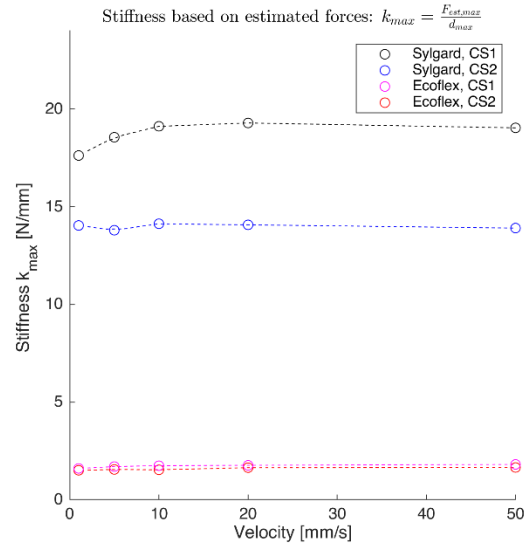


Figure 5.11 – The estimated stiffness based on the measured displacement and the estimated forces.

5.3.2.1 Repeated force measurements

The force measurements on the plain silicone phantoms were repeated 10 consecutive times to evaluate the consistency in the force measurements. Figure 5.12 shows a plot of repeated measurements, of which Figure 5.13 shows the force estimation maximum mean values including the range of $[-2\sigma, 2\sigma]$, with σ being the standard deviation over 10 datapoints at each measurement ($n = 10$). Figure 5.13 shows the range of the mean and standard deviations for all control values and for both the measured and estimated forces, in all cases showing a low standard deviation when comparing the measurement maximum forces for both controller settings and silicone materials. The variations in the mean are explained by the differences on the position, as earlier discussed using Figure 5.10.

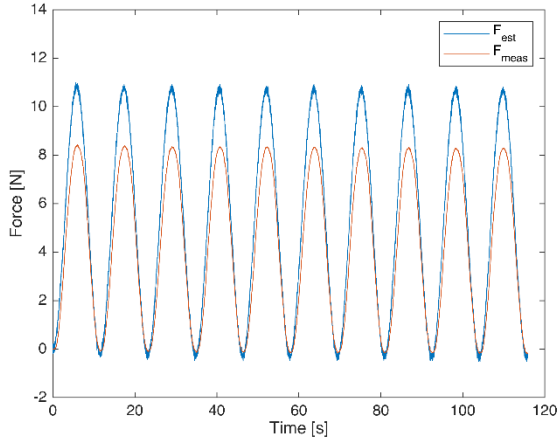


Figure 5.12 – The consecutive repeated ($n = 10$) force estimation and measurement for CS2 at 1mm/s on the Sylgard phantom.

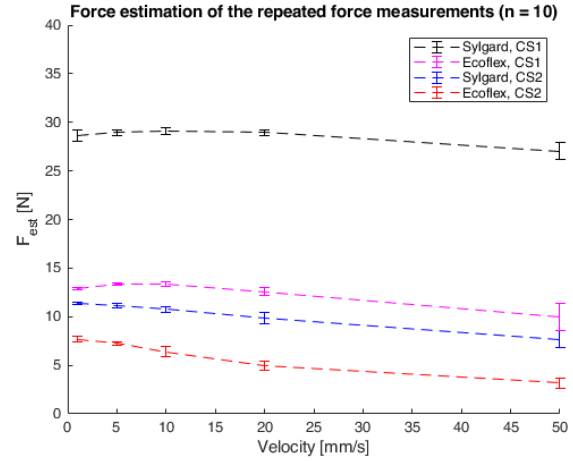


Figure 5.13 - The force estimation of F_{est} with the mean and range of $[-2\sigma, 2\sigma]$ at different velocities ($n = 10$).

		F_{est}		F_{meas}	
		μ	σ	μ	σ
Sylgard 184	CS1	[27.06 - 29.15]N	[0.15 - 0.41]N	[21.27 - 22.20]N	[0.14 - 0.28]N
	CS2	[7.67 - 11.37]N	[0.05 - 0.43]N	[6.87 - 8.45]N	[0.04 - 0.19]N
Ecoflex 00-30	CS1	[9.95 - 13.36]N	[0.04 - 0.69]N	[7.12 - 8.35]N	[0.03 - 0.24]N
	CS2	[3.16 - 7.68]N	[0.10 - 0.28]N	[2.94 - 4.72]N	[0.02 - 0.26]N

Table 5.3 - The range of means and standard deviations found for F_{est} and F_{meas} for each of the velocities [1,5,10,20,50] mm/s.

5.3.2.2 Indentation depth

All previous measurements were conducted for a same indentation depth of 12mm reference motion along the X-axis. To assess whether the depth, and thus also the force magnitude, influences the force estimation, additional experiments were performed in which the indentation depth was incrementally increased. Figure 5.14 shows the estimated and measured forces exerted by the probe on the ecoflex phantom when the IDC controller is used. The ratio between the measured and the estimated forces r is shown in Figure 5.16. Note that the maximum indentation depth for each condition is limited to the saturation force of the ground truth loadcell. For indentations performed on the harder Sylgard phantom with control settings CS1, the maximum indentation depth before reaching the saturation force lies around 12mm. It is clear from the figure that for small indentations, in particular for softer tissue, the force estimation deviates considerably. Looking closer at the initial indentations (Figure 5.17), it is clear that the system is oversensitive for small indentations. This is best explained by the initial cable tensions, which inevitably introduce some friction for each cable. For the same pretension in the cables, the friction (and other sources of noise) will have a proportionally larger effect on the estimation for the low forces compared to higher forces. This is

also related to the indentation depth as the graph illustrates. Low cable tensions will lead to lower friction and higher sensitivity for the estimation of small forces. As mentioned in Chapter 2 (eq. 2.5) stiffness of the end-effector is also related to the cable tension, with lower stiffness achieved by lower cable tensions. Thus, a possible method to decrease friction without influencing the end-effector position is by implementing a stiffness regulation into the control routine. Another way to improve force estimation is by integrating a cable friction model into the controller [324].

Cable slackness occurs at large indentation depths, indicated by the encircled points in Figure 5.16. As can be seen in Figure 5.15, this occurs for cable 3 at the 17th indentation, representative for an indentation input of 34mm depth. Despite the slackness, the force estimation does not seem to be affected by the slackness, as can be seen in both Figure 5.14 and Figure 5.16. While this seems counter-intuitive, the equations (5.6) do not seem to be affected as long as the system pose does not suddenly change drastically. Such a drastic change can happen when the end-effector slips on the surface which it is exerting force on, which the compressed silicone prevents. While this might be a concern, especially when considering handling slippery tissue surfaces with the current system, the slackness only occurs at relatively high forces. While such high forces might exceed the requirements for surgery, the reduction of the pre-tension might also influence the point at which slackness occurs.

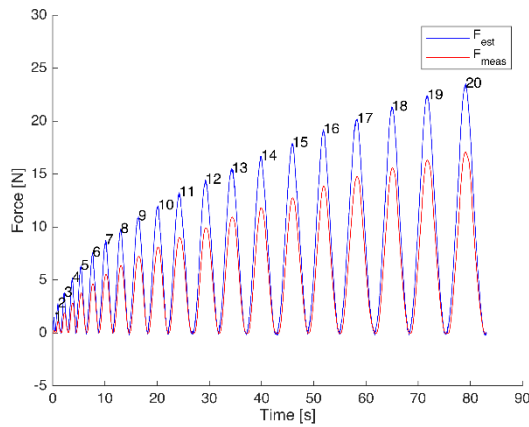


Figure 5.14 – The controller with control settings CS2 on the Ecoflex 00-30 phantom at different indentation depths. Each indentation is a 2mm increment increase of the previous, hence the 20th is an indentation input of 40mm depth.

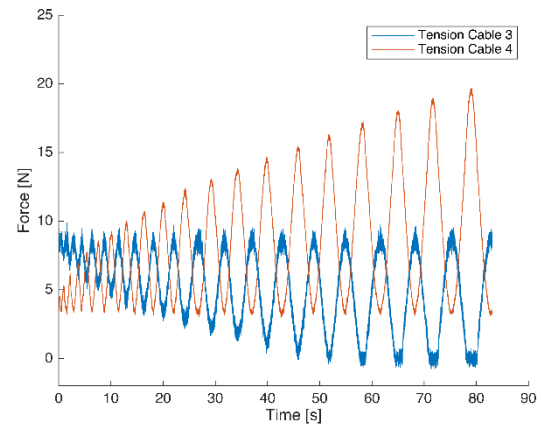


Figure 5.15 – The cable tension during indentations (see Figure 5.14) of cables 3 and 4. Cable 3 has the lowest tension overall, displaying slackness at around the 17th indentation. Cable 4 has the highest measured tensions, which remains below the total estimated force.

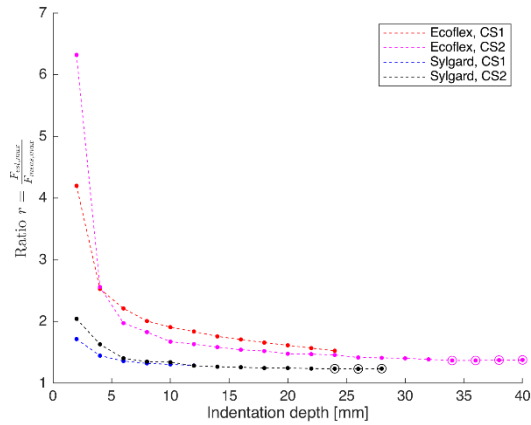


Figure 5.16 – The ratio between the estimated and measured forces. The encircled data points represent indentation depths where at least one cable shows slackness.

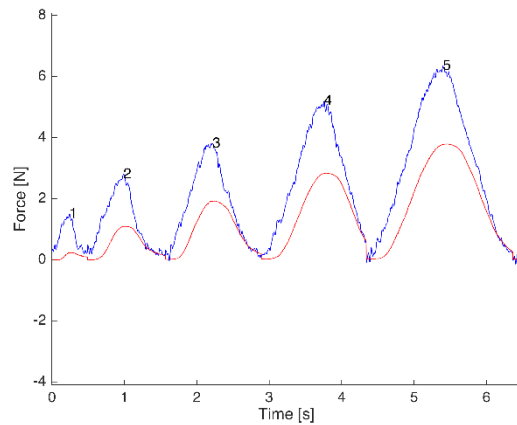


Figure 5.17 – The first indentation steps of the IDC controller on ecoflex.

5.4 Palpation study

22 surgeons in training, with at least 2 years of core surgical training in the British National Healthcare System (i.e. level ST3 or higher), performed a palpation study with the CDAQS system. The palpation study was performed on soft silicone phantoms with harder silicone nodules embedded below the surface, to simulate disease pathology such as a tumour. The phantoms can be seen in Figure 5.18. Ten black dots were marked on the phantom's surface, of which only five dots covered a hidden harder nodule at approximately 2mm below the surface. The number of hidden nodules was unknown to the participants. Ecoflex 00-30 and Sylgard 184 were used as the soft and hard silicone materials, respectively. The stiffness map of the phantoms was evaluated through an autonomous task, as shown in chapter 6.

The aim of the study was to evaluate whether haptic feedback provided by the CDAQS system could be used to improve the detection of simulated tumours. As tissue stiffness can also be partly estimated through visual cues, the study was designed to evaluate whether the addition of haptic feedback to visual cues would improve performance. Additionally, the ability to differentiate between tissue stiffness without any visual clue was assessed, referred to as *blind palpation study*. The user study was split into three parts: (1) a blind palpation study, (2) a visual-haptic comparison study and (3) the blind palpation study repeated to assess improvement in haptic detection. All three parts were performed successively within a timeframe of less than 30 minutes.

The nodule detection rate, task completion time and maximum indentation forces were collected during each part of the study. The nodule detection rate is defined as the percentage of nodules correctly detected by the participant.

The test setup is shown in Figure 5.18. The Geomagic Touch (3D systems, USA) and the endoscope (Endoeye Flex 3D, Olympus, Japan) were used for control and visualisation in the study. The haptic forces were only given along the x-axis, and master to slave motion scaling of factor 0.8 was used. A clutch function was included to set up the position of the haptic device, at the beginning of the study, in the centre of its own workspace with the slave end-effector placed above the phantom. An initial pilot study showed that the haptic rendering could be jumpy when the CS1 control settings were used, which was most likely caused by a combination of high motion responsiveness of the controller combined with low frequency reading of the forces. Therefore, a more intuitive haptic sensation was found for the IDC settings.

The participants were informed about the study through a participant information sheet and were asked to sign a consent form before participating in the study. The average age of the 32 ± 1.9 years, with 18 out of the 22 being male. The Joint Research Compliance Office at Imperial College London approved the study (ICREC reference number 18IC4524). The study was performed in collaboration with PhD student Arianna Saracino [321].

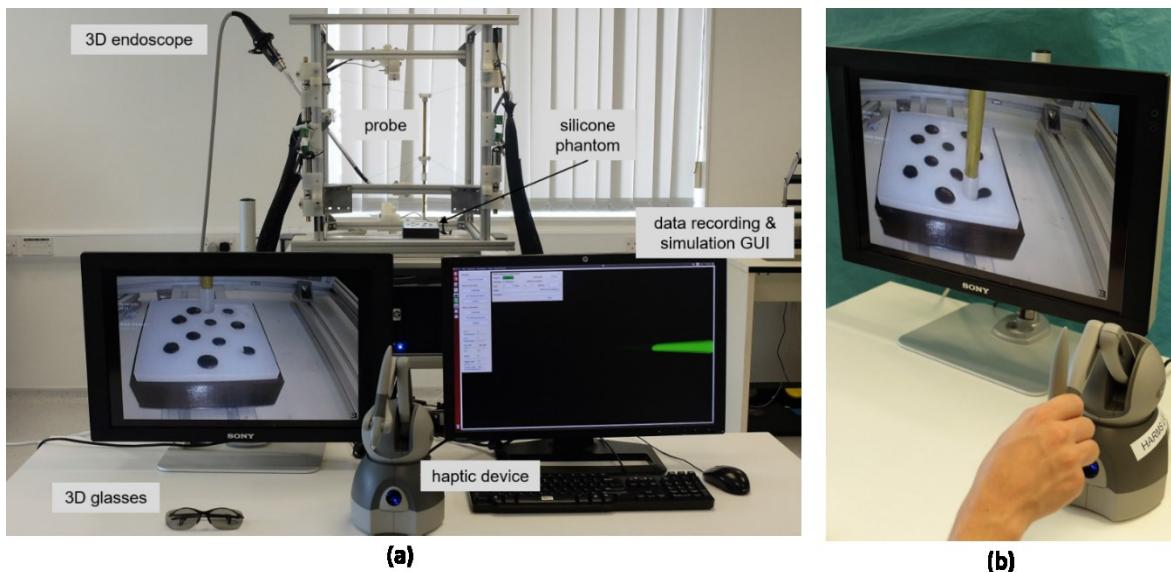


Figure 5.18 – (a) The experimental setup for the palpation user study. Covering the aluminium frame during the user study prevents direct vision of the probe. (b) The haptic device in an upright position. A silicone phantom and the probe are shown in the display. Image source: [321].

5.4.1 Blind palpation study

In the blind palpation study, the participant manually operated the haptic device to perform indentation of the silicone phantom. The haptic device was virtually constrained to only allow motion along the x-axis (indentation). To examine a specific point in the phantom, the examiner moved the phantom to place the point directly below the probe, after which the participant could start palpation. Before moving to a next point on the phantom, the participant indicated whether they

believed that the palpated point had a harder nodule embedded below the surface. The participant could at any point ask for a *reference palpation*, which involved palpation of the soft surrounding silicone as a reference for other palpation points. Each participant first palpated 10 points as training, in which the examiner confirmed or disconfirmed the presence of a nodule. After the training, the study was performed. Again, ten points were palpated but without feedback from the examiner. During the study, the endoscope was switched off, and the robot was covered with a sheet so that the participant could not see the end-effector while they performed the task.

5.4.2 Visual-Haptic comparison study

In the visual-haptic comparison study, the endoscope was used for visualisation. In contrast to the blind study, the participants now used the haptic device to move the probe along all three Cartesian coordinates (x, y, z), while the phantom was kept in place. The study consisted of 2 parts: (1) the palpation task with only visual feedback and (2) the palpation task with both visual and haptic feedback.

During each task, the participants would start with a reference palpation of the white soft silicone of the phantom followed by palpation of the first point in the bottom right corner of the phantom. From here, the participant could use the probe to palpate the remaining 9 points in any order. Each task (visual-only and visual-haptic) involved the palpation of two phantoms; a third phantom was used for training. Training was performed at the beginning of each task, and involved the palpation of all 10 points with feedback from the examiner. After each task, the participant filled out a NASA-TLX form, and upon completion of both tasks the participant filled out a questionnaire to provide a subjective comparison (Appendix A.6). To prevent bias, participants started with either the visual-only task or the visual-haptic task, depending on what task the previous participant had started with (i.e. the first participant of the study could decide which task to start with, after which the first task was alternated for all following participants).

5.4.3 Results

The results of the blind palpation study are summarized in Table 5.4. The blind palpation study shows a statistical significant difference between the indentation forces of the first and second trial. The difference is related to an increase of forces in the trial after the comparison study. The mean of the nodule detection rate did increase, but the difference was not statistically significant.

The quantitative metrics of the comparison study showed a statistically significant increase of nodule detection rate and decrease of maximum indentation forces when haptic feedback was included. No significant difference in the completion time has been seen.

		Trial 1	Trial 2	Statistics
Nodule detection rate [%]		70.9 ± 16.01	77.27 ± 22.51	Z=-1.16, p=0.25
$F_{indent,max}$	Soft	3.38 ± 1.11	3.78 ± 1.07	t(18)=-3.05, p=0.0069
	Hard	3.25 ± 1.14	3.79 ± 1.29	t(18)=-3.29, p=0.0041

Table 5.4 – The results of the blind palpation study. The first and second trials are compared statistically, using the Wilcoxon Signed-rank for the nodule detection rate and the repeated-measures t-test for the maximum indentation forces. Normality of the distribution of the forces has been confirmed with the Shapiro-Wilk test.

		Visual-only task	Visual-Haptic task	Statistics
Nodule detection rate [%]		76.09 ± 19.15	94.35 ± 9.1	Z=-4.5, p<0.0001
$F_{indent,max}$ [N]		4.82 ± 0.81	4.13 ± 1.02	t(21)=4.34, p= 0.0003
Completion time [s]		75.95 ± 28.5	77.36 ± 33.46	t(20)=-0.25, p=0.8

Table 5.5 – The quantitative results of the visual-haptic comparison study. The first and second trials are compared statistically, using the Wilcoxon Signed-rank test for the nodule detection rate and the repeated-measures t-test for the maximum indentation forces and completion time. Normality of the distribution of the forces and the completion time was confirmed using the Shapiro-Wilk test.

5.5 Discussion

This chapter discussed the use of CDPMs for force sensing, based on an earlier study [320]. The CDAQS was developed by the author of this thesis to enable development of a general CDPM system for the evaluation of force sensing during a palpation study. The benchmarking of the system showed that the system could be used to differentiate between forces measured on soft and hard silicone.

The absolute accuracy still deviated considerably from the ground-truth measurement. Two factors are the most likely reasons for the error in the absolute accuracy: the modelling errors caused by the use of the desired rather than the real pose, and measurement errors on the cable tensions. In the force estimation equation (5.6), the accuracy of the cable tension vector $\vec{F}_i(\zeta, t_i)$ is influenced by errors on both the pose ζ and on the tension t_i , and this will affect the final force estimation F_{est} . Using the tracked pose $\zeta_{tracked}$ showed that a large portion of the effect was due to the modelling errors. This is shown in Figure 5.7, in which $F_{est,comp}$ represents the force estimation when the end-effector pose is tracked. In minimally invasive surgery, accurate pose tracking is more challenging. One way to achieve pose tracking of the instruments is by using the endoscope itself, which can provide either a mono or a stereo view, for tracking the instruments (e.g. tracking a pattern placed on the instruments such as in [325]). Another method is to integrate additional sensors, such as an inertial measurement unit, to improve sensing. Pittiglio et al. also developed a pose estimator for a planar cable-driven parallel robot [326]. It is not clear which method is the best for minimally invasive surgery, and further developments can be focused on implementation of position tracking to achieve more accurate force estimation. Another way to improve force estimation is by increasing

the accuracy of the tension measurement. The force estimator assumes zero friction and no cable elasticity – both assumptions which do not represent the real situation. Additionally, the current CDAQS system uses 3D-printed parts in the motor units, which are relatively compliant and can be an additional source of error. Modelling both the friction and elasticity will improve the estimation of the real pose and real cable tension, and thereby increase the absolute accuracy of the system. Future developments should aim at further examining the force estimation along other DoF.

Nevertheless, the force estimation is robust independent of the indentation velocity and slackness, and also the variance on the force estimation is small for repeated indentations illustrating the consistency of the measurement. These are important properties with regard to the use of the device to provide haptic feedback in a less controlled environment such as MIS. The simulation of a palpation task for surgery was used to evaluate the haptic feedback rendering to users. The blind palpation had a high detection rate, showing the haptic feedback could indeed be used to differentiate simulated tissue stiffness. The comparison study showed that the haptic feedback had a positive effect on both the nodule detection rate and the decrease of forces. These results illustrate that implementing force feedback can have a positive effect on the use of CDPMs in minimally invasive surgery. The translation of these findings to minimally invasive surgery requires additional development, which is done for the SIMPLE system in the following chapter. In the current chapter we have discussed the first use of CDPMs for force sensing and that this can be used for providing haptic feedback, illustrating a unique opportunity for MIS.

Chapter 6

SIMPLE: a CDPM for safe autonomous surgical tasks

This chapter discusses the use of CDPMs for safe autonomous surgical tasks. Section 6.1 presents background information about the clinical need for autonomous systems, the current applications of autonomy and the role of force sensing in autonomous tasks. Section 6.2 explores the positional accuracy of the CDAQS during autonomous motions and includes the assessment of the most appropriate control parameters and the robustness of positional accuracy in terms of proximity to singularities. The findings obtained using the CDAQS demonstrate high repeatability and positional accuracy, indicating the feasibility of CDPMs for autonomous motions. It is demonstrated that the position of a force acting on the end-effector can be estimated, which can lead to discrimination between expected forces when handling tissue at the tip, resulting in unexpected collisions with potentially vulnerable tissues.

Following the description of the experiments with the CDAQS, section 6.3 presents a prototype designed to realise the benefits demonstrated by the experiments for the patient using a single-port access method: **Single-Incision MicroPort LaparoEndoscopy (SIMPLE)**. An important part of the system is its assembly before surgery, for which a method is presented in section 6.4. Section 6.5 is used for validation of the force sensitivity of the system and evaluation on the performance of autonomous raster scans on silicone phantoms with the aim of reconstructing the underlying

structures. The design choices involved in the creation of the SIMPLE prototype and its applications in MIS are discussed in section 6.6. Another advantage of the SIMPLE system that is not discussed in this chapter is its ability to optimize the instrument workspace for patient- and procedure-specific requirements. The workspace optimisation of the SIMPLE system is discussed in chapter 7.

6.1 Autonomy in Surgery

6.1.1 *Clinical need for autonomy*

An important clinical reason why we seek to create autonomous surgical robotics is because this may help standardize the quality of surgical procedures. Currently, the quality of surgical procedures is highly dependent on the experience of the surgeon, causing large variations in surgical quality [327]. Surgical robotic systems, in contrast, can be kept up to date with the latest surgical techniques, and their interconnectivity can enable each system to learn from other systems located in hospitals worldwide.

Another reason to pursue this technology is that the workload of surgeons could be reduced through partial automation of common tasks such as knot tying and suturing. The development of intraoperative sensing technology, such as miniaturized ultrasound probes and optical biopsies, can be used for diagnosis or more accurate delineation of a lesion. However, the size of these devices is often minimal, requiring scanning techniques such as a raster scan to cover larger tissue surfaces. Accuracy and appropriate contact forces are of paramount importance in such tasks and are thus almost impossible for surgeons to perform through tele-manipulation. A scanning task performed autonomously, may provide the accuracy and consistency required to increase surgical or diagnostic efficacy.

One specific application of autonomous surgical robots is in remote military or space missions. Both military and spacefaring organisations have contributed to the development of (non-autonomous) surgical robotics. However, the limited connectivity and/or large delays in communication technology that characterise military and spacefaring settings can render the effective performance of tele-operated procedures impossible – hence the need for (semi-)autonomous technology [31]. However, autonomy can also be a useful attribute for surgical robotics systems located in the same physical operating theatre as the surgeon in charge, as it can help manage the increased complexity of the technology. Technological developments in minimally invasive surgery are focusing on miniaturization, which often adds new control challenges for the surgeon; these challenges might be overcome through the development of systems capable of performing autonomous tasks. For instance, one novel development in flexible endoscopy is the use of a (tethered) capsule controlled by an external magnet. While the technology has benefits in terms

of the prevention of buckling and stress on tissues, the magnetic system is not intuitive for manual control [328]. Even when the magnet is robotically controlled, important manoeuvres such as retroflexion are difficult to perform through teleoperation, leading Slawinski et al. to successfully develop an algorithm for autonomous retroflexion [329].

6.1.2 Levels of Autonomy

The term “surgical *robotics*” suggests a high level of autonomy, however, most surgical robotic systems are better characterised as master-slave teleoperated systems. These systems are fully dependent on input from the surgeon, who closes the control loop by interpreting the environment, making decisions and consequently using the master device to manipulate the surgical instruments on the slave side of the system. Systems that do not provide any other functionality in addition to this basic master-slave interaction can be classified as having no autonomy. However, autonomy in robotics is not a binary scale and robotic systems can be described as having different *levels* or *degrees* of autonomy.

In robotics in general, systems are classified according to the role of the human operator: *direct control*, *shared control* and *supervisory control*. Direct control means that the user makes all decisions and is fully responsible for every motion and action of the robot. With shared control, the robot provides additional interpretation of the environment and provides feedback to the user, who can then act accordingly. Supervisory control means that the robot has full autonomy for a specific task or subtask, and the human operator’s role is limited to preventing errors and giving high-level commands. Another more comprehensive classification for automated systems was presented by Beer et al. [330]. This classification uses a 10-level scale and considers the role of the human and robot in three aspects of the task: *sensing*, *planning* and *acting*. The lowest level on the scale represents manual teleoperation. The highest level is full automation, in which the robot is responsible for all three roles, without any human interference. Supervisory control is not classified as the highest level of autonomy because the human still has a controlling role (sensing).

Literature has also been dedicated to autonomy classifications specifically for surgical robotics. An overview of several classifications is given in [331]. One may classify systems according to the role the surgical robot plays in them using the categories of *remote systems*, *passive systems*, *semi-active systems* and *active systems* [332]. Remote systems are the most common type of surgical system due to the widespread use of the da Vinci robot. In this type of system, the surgeon controls the robot from a master console that is mechanically decoupled from the slave robot; mechatronics are used to convey the surgeon’s motion to robot’s motion. As long as a good communication network is guaranteed, the surgeon can perform surgery from thousands of miles away. In contrast, *passive systems* allow the surgeon to position the surgical end-effector, but actively prevent him/her from

manipulating the surgical tool outside a specific area defined by *virtual constraints*. *Semi-active* systems provide continuous feedback to the surgeon, for instance for the guidance of the instruments along a specific pathway. *Active* systems perform a task or subtask fully autonomously after having been configured by the surgeon.

Another 5-level classification for surgical robotics was developed by Yang et al. [333]. This system defines the first level of autonomy as robot assistance, where it is still the surgeon who performs the surgery while the robot gives additional information that enhance the surgeon's performance. Note that on this scale, absence of autonomy is referred to as level zero; teleoperated systems such as the da Vinci fall under this category. At each subsequent level, the system's dependence on the surgeon decreases, as it autonomously performs specific surgical tasks or part of the procedure. In the literature, this is often referred to as semi-autonomy. The highest levels of autonomy (levels 4 and 5) require systems to make complex decisions and perform entire surgeries. In such situations, the surgeon has a supervisory role rather than an executive role.

6.1.3 *Autonomy in surgical robotics*

The positional accuracy of robotics is an important advantage that has led to the introduction of autonomy in early robotic systems. The PROBOT was a system developed for the transurethral resection of the prostate, and autonomous resection was mechanically confined to a conical workspace to ensure safety [28]. The ROBODOC System [334] and the CASPAR system [27] were both developed for bone-cutting for the placement of hip, knee and ankle prostheses. Essentially, the technology is similar to a Computer Numerical Control (CNC) system as used in product manufacturing and performs a pre-programmed task. Strictly speaking, such pre-programmed tasks are more related to automation than autonomy, and after initial preoperative CT scans and co-registration of the frame of reference with the images, the robot does not receive updated feedback about the state of the procedure. Such automation is well suited for orthopaedic surgery because of the controlled environment involving bone, rather than deformable soft tissues. Despite clinical implementation of these systems, the high degree of automation led to safety and liability concerns and eventually to the removal of ROBODOC and CASPAR from clinical practice [335]. The ROBODOC was relaunched as the TSolution One (THINK Surgical) in 2017 [336]. Concerns about the PROBOT are related to surgeons' unease being kept out of the loop and only holding the emergency button [335].

Virtual fixtures are used to guide surgeons along a predefined path or keep the instruments away from crucial anatomies. The use of virtual fixtures is categorized as robotic assistance, which is the first level of autonomy for surgical robotics according to [333]. The first clinical use of virtual fixtures occurred in 1988 in a neurosurgical operation, in which a biopsy needle maintained orientation towards a tumour located in the brain while allowing the surgeon to insert the needle

[24]. The Active Constraint Robot (Acrobot) uses virtual fixtures for bone milling orthopaedic surgery, leading to less concerns about safety by keeping the surgeons into the loop [337]. Another interesting implementation of virtual fixtures in the da Vinci system is the use of dynamically updated constraints enabled by gaze fixation points [338]. An overview of different types of active constraints is given by Bowyer et al. [339].

Imaging modalities play an important role in providing accurate environmental information for autonomous tasks. The abovementioned neurosurgical and orthopaedic systems overlay pre-operative CT or MRI images for guidance during surgery. The presence of bones allows for relatively effective clamping of tissue and helps ensure that the pre-operative images closely correspond to the intraoperative scenario. Co-registration of pre-operative medical images to a clinical setting with soft tissues remains challenging, due to differences caused by tissue deformation [340]. The integration of robotic systems with imaging modalities remains a way to circumvent co-registration issues when dealing with soft tissues. Robotic systems that use energy sources for therapy, such as in radiotherapy (e.g. gamma knife [341] and cyberKnife [342]) or high-intensity focused ultrasound (HIFU) [343], can effectively use intra-operative imaging sources such as X-ray and MRI and therefore are not susceptible to tissue deformation. The integration of advanced sensor technology with accurate mechatronics within the same control loop has also been a point of focus in the development MRI compatible robotic systems [344][345]. These technologies are well-suited for automation or even autonomy using image-guidance, but are limited to specific clinical applications. Furthermore, the use of ionizing radiation in CT and X-ray imaging and the high magnetic fields in (often closed-bore) MRI machines present major limitations for the development and adoption of these robotic systems for intra-operative purposes.

As was briefly mentioned earlier above, acquiring accurate environmental information becomes a greater challenge when dealing with soft tissues, which display high deformation when forces are exerted upon them during an intervention. In path planning for percutaneous interventions, tissue deformation is often modelled, but not updated in real-time, unless integrated within one of the aforementioned imaging modalities (MRI/CT/US). In endoscopy, one way to account for tissue deformation is through 3D reconstruction of the surgical field using conventional (stereo) vision laparoscopes to understand and update the surgical context [346]. However, to do this while performing surgery is highly complex, and most recent studies involving autonomous tasks in surgery are therefore performed in a controlled simulated environment. Hu et al. used a stereovision camera combined with the Raven II system to detect and ablate a simulated tumour [347]. To enable clear 3D segmentation, a high imaging contrast was chosen between the tumour and its background, shown in black and white respectively. Another study by this group used the same imaging approach

for a semi-autonomous path planning of a surface scan [348]. The method combined fluorescence-based imaging to enable more accurate margin detection and, consequently, more accurate resection with possible applications for neurosurgery. The Smart Tissue Autonomous Robot (STAR) has shown that the fluorescence-based imaging can be successfully used for anastomosis of soft tissues in an in-vivo porcine survival study [349]. The system uses a supervised learning algorithm based on near-infrared fluorescence imaging combined with a 3D plenoptic camera to guide the motion of the robotic arm fitted with a surgical instrument. In the experiment in question, a modified suturing instrument with a circular needle was used, and hence conventional bimanual suturing techniques were not required.

Goldman et al. suggested that improved integration of intraoperative data such as tissue stiffness remains an important aspect in enabling safe and reliable teleoperation and low-level autonomous tasks [350]. As discussed in Chapter 5, multiple devices have been developed to enable force sensing in an MIS environment. However, autonomy remains primarily dependent on the use of visual information, and the combination of autonomy and force sensing in a MIS environment is still largely unexplored. The earlier mentioned STAR system used a proximal force sensor to limit the suture tension forces and thereby prevent strictures and stenoses [349]. Mayer et al. [129] used contact forces to train a supervised machine-learning algorithm for autonomous knot tying. The end-effector forces were measured by integrating strain gauges on the instrument shaft. While forces were used to provide the surgeon with haptic feedback while generating training data, the algorithm was trained using only the gripper position data. Outside of surgery, force-based input has been successfully used for the training of autonomous robotic tasks for the purposes of safe human-machine interaction (HRI) and for application in situations when end-effectors are (partly) visually occluded [351]. Similarly, the addition of force-based inputs in MIS can be used for safer autonomous surgical procedures, even when direct endoscopic visualisation of the instruments is absent.

Research into force sensing has primarily focused on its use for autonomous palpation. Goldman et al. developed a control method to create a surface map and tissue impedance map [350]. Nichols et al. trained a supervised machine-learning algorithm using ultrasound elastography data to convert force-position data, acquired from an autonomous robotic palpation, into a stiffness map [352]. An improvement was realized by more accurate boundary detection of lesions in a further study [353]. In all these studies, the palpation data was acquired using a robotic arm or gantry with a loadcell mounted as the end-effector. For minimally invasive surgery, however, intraoperative measurement of forces combined with positional data remains a challenge. Beccani et al. developed a wireless palpation device which was able to create a stiffness map based on measured forces [354]. However, the device is highly dependent on the use of an external magnetic field to localize the position of the

probe. As such fields are highly non-linear, the placement of an external magnet significantly limits the workspace of the system. Campisano et al. developed a soft robotic tactile element (SRTE) which, when placed in an array, can in the future be used for the creation of a stiffness map of an organ surface in a single step [355]. A single SRTE module was able to detect different nodules embedded in a silicone surface; however, these SRTE modules had a size of 30x30mm, and each contained an embedded barometric sensor with dimensions of 5mmx3mmx1.5mm. Significant downscaling of the modules is required before an array of SRTEs can be used for a soft robotic skin which is useful for MIS purposes. An overview of different tactile sensing methods is given in Konstantinova et al. [316]. One of the main challenges in this area relates to the miniaturization of sensors to fit the small access ports used in MIS and the stability of the force measurement when used in a dynamic organ scanning environment. The authors also point out that one of the main limitations of strain gauges and piezoelectric elements relates to sensor inaccuracies caused by changes in temperature.

As yet, there exists no system capable of performing an autonomous palpation task without the need of sensors inside the body. Two criteria for the performance of an autonomous palpation task are accurate control of the instrument position and accurate estimation of instrument forces. As shown in chapter 5, CDPMs can be used to measure forces at the distal tip of an instrument. Also, as demonstrated in an earlier evaluation [326][356], CDPMs are able to achieve submillimetre accuracy in the execution of automated motions. Both positional accuracy and force estimation depend on the amount of friction in the cables, and minimizing friction is therefore of paramount importance in ensuring adequate autonomous motions. To complement earlier work, section 6.2 evaluates the accuracy of the current control system and the repeatability of the system using the CDAQS platform. The study also includes a robustness analysis in terms of accuracy during motion, and an evaluation of aspects that result in the deterioration of positional accuracy. Section 6.3 discusses the SIMPLE system, which is the clinical translation of a low-friction CDPM to single-incision laparoscopic surgery.

6.2 Autonomous tasks using the CDAQS System

A first evaluation of CDPMs performing autonomous tasks was performed using the CDAQS system. The study is important to evaluate the general ability of CDPM mechanisms to perform autonomous tasks, independent of the limitations of specific MIS prototypes. In this section, particular attention is given to the positional accuracy, in addition to the force estimation information provided in Chapter 5. A safety stop was also evaluated, in which the location of the force was taken into account. Such a safety stop can discriminate between forces applied to the tip of the instrument and unexpected forces at another location along the instrument shaft, to ensure safety.

6.2.1 Positional accuracy

The positional accuracy of the system was assessed by placing passive markers on the CDAQS rig for calibration and optical tracking of the instrument position (Figure 6.1). The passive markers were tracked using two cameras (OptiTrack Prime13W, NaturalPoint Inc. USA) connected to a Windows 10 Laptop via an Ethernet connection. Data regarding the positional coordinates of the end-effector and the cable tensions were sent to a Linux PC using the UDP communication protocol.

6.2.1.1 Step response

The accuracy of the controller was evaluated based on a step response task of 10mm along x,y,z axes. The controller is described in Chapter 5. The values of K_{TG} , G_{PD} and α were varied during the experiments. The settling time, steady-state error and rise time were evaluated for each setting. The steady-state error ε was calculated at 3 seconds after the reference input and averaged over the last 500 samples. The settling time t_s was calculated from the initial input signal to the moment at which the response settles within a 2% bandwidth from the final settled value. The rising time t_r was calculated for the slope between 10%-90% of the final value. The results are shown in Table 6.1.

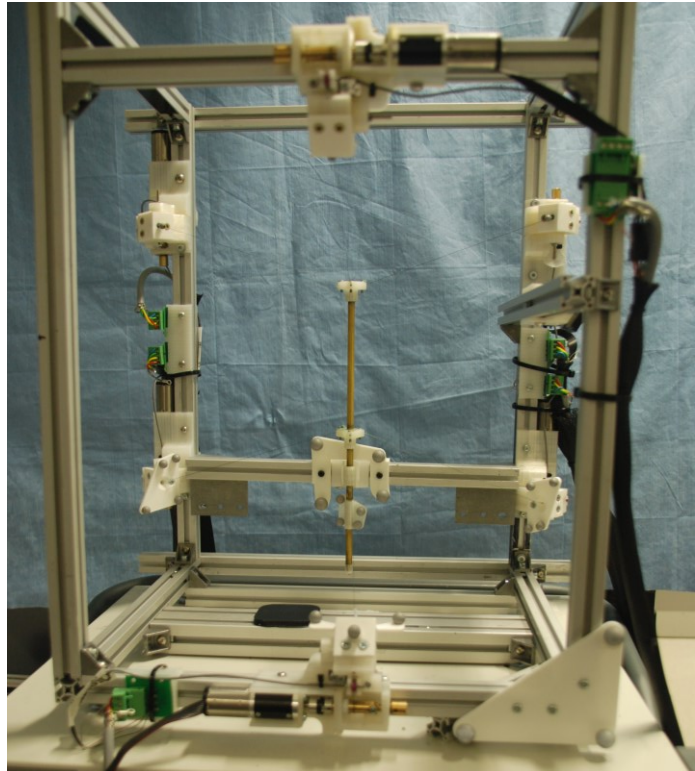


Figure 6.1 - The CDAQS system with markers placed on the ports and end-effectors.

The table shows that for a higher gain G_{PD} (and thus a lower gain $G_{IDC} = 1.0 - G_{PD}$), the rise time and the settling time improve. Also, a high K_{TG} results in a better response time compared to other values. The value of α did not seem to influence the accuracy or settling time strongly. There was no controller value that showed a clear effect on the steady state errors. To evaluate the accuracy further during a discretized motion, the following sections discuss the accuracy of the system during a linear and circular motion.

		X-axis			Y-axis			Z-axis		
		ε [%]	t_r [s]	t_s [s]	ε [%]	t_r [s]	t_s [s]	ε [%]	t_r [s]	t_s [s]
$G_{PD} = 0.2$ $K_{TG} = 300$	$\alpha = 0.0$	15.0	0.70	1.68	1.32	0.42	1.01	-4.78	0.67	1.31
	$\alpha = 0.5$	8.68	0.64	1.98	12.9	0.66	1.10	0.98	0.70	1.51
	$\alpha = 1.0$	-1.81	0.57	1.48	20.3	0.69	1.25	-5.39	0.52	1.85
$\alpha = 1.0$ $K_{TG} = 300$	$G_{PD} = 0.2$	-7.44	0.54	1.36	22.4	0.73	1.32	4.51	0.69	1.27
	$G_{PD} = 0.5$	6.65	0.27	0.81	1.44	0.27	0.52	-6.71	0.29	0.51
	$G_{PD} = 1.0$	6.57	0.14	0.32	-3.61	0.12	0.25	-5.76	0.18	0.29
$G_{PD} = 1.0$ $\alpha = 1.0$	$K_{TG} = 100$	7.11	0.40	0.78	0.20	0.10	0.70	-5.25	0.38	0.76
	$K_{TG} = 200$	6.91	0.20	0.44	0.24	0.16	0.32	-4.51	0.18	0.34
	$K_{TG} = 300$	6.26	0.12	0.33	0.64	0.10	0.23	-4.94	0.14	0.29

Table 6.1 - The step response for different controller settings, with steady state error ε , rise time t_r and settling time t_s .

6.2.1.2 Linear motion

A linear motion was performed in which the end-effector moved from the centre of the scaffold ($X_0 = [0,0,0,0,0,0]$). The motion was defined by a sinusoidal motion along the x,y,z, axis in local coordinates, with an amplitude of 20mm and 0.25 Hz frequency (approximately 5mm/s). Each measurement consisted of 5 consecutive motions. A line defined by the origin of the motion and the most distant point measured was used for calculation of the accuracy of the linear motion. The orthogonal distance from this line to a data point shows the deviation of the straight pathway of the line. The root mean square error (RMSE) and the deviation of the length relative to the given 20mm length $\varepsilon_{\|\vec{x}\|}$ are taken as a metric for the accuracy of the line. The deviation from the orthonormality of the axis vectors relative to the plane defined by other two axes ε_{\angle} is also taken as metric for the accuracy of the motion. The results are displayed in Table 6.2.

	X-axis			Y-axis			Z-axis		
	$\varepsilon_{\ \vec{x}\ }$ [mm]	RMSE [mm]	$\varepsilon_{\angle\vec{x}}$ [deg]	$\varepsilon_{\ \vec{y}\ }$ [mm]	RMSE [mm]	$\varepsilon_{\angle\vec{y}}$ [deg]	$\varepsilon_{\ \vec{z}\ }$ [mm]	RMSE [mm]	$\varepsilon_{\angle\vec{z}}$ [deg]
$G_{PD} = 1.0, \alpha = [\cdot] *$	0.78	0.0726	-0.58	0.44	0.1207	-2.76	0.13	0.1108	-8.61
$G_{PD} = 0.2, \alpha = 0.5$	2.00	0.5418	-1.15	2.33	0.3711	2.62	18.61	0.2511	-9.78
$G_{PD} = 0.2, \alpha = 1.0$	0.78	0.6076	2.39	3.21	0.4860	13.03	18.18	0.3762	-9.96

Table 6.2 - The accuracy of the linear motion, shown in the length of the path and the RMSE for different control modes.

The results show that $G_{PD} = 1.0$ achieves the straightest line with an RMSE between 0.073 and 0.121 mm. The accuracy of the motion is strongly influenced when the IDC controller is used. The orthonormality results show the motions are not completely orthogonal to each other, whereas setting the controller to $G_{PD} = 1$ reaches the best results again.

6.2.1.3 Circular motion

A circular motion with a radius of 20mm was performed along each of the main axes (x,y,z). The circle motion was repeated three times, with a frequency of 0.05 Hz (approximately 6mm/s). The circular motion was fitted to a plane with a principle component analysis (PCA) and the linear least squares method was used to fit a circle to the now 2D data.

The circle around the X-axis for control $G_{PD} = 1.0$ is shown in Figure 6.2. Table 6.3 shows the results for different controller settings. $RMSE_{plane}$ represents the accuracy of the planar fitting of the data and is a measure for accuracy along the off-plane axes. The accuracy on the plane itself is

represented by $RMSE_{circle}$. The error on the radius relative to the commanded 20mm radius ϵ_r and the error of the centre of the fitted circle along the Y-axis and Z-axis (ϵ_y and ϵ_z , respectively) are also included for the accuracy of the fitting. The task was also fitted with an ellipse, as this shape was observed when looking at the data. An ellipse be fitted very accurately, as shown with the $RMSE_{ellipse}$ in the table.

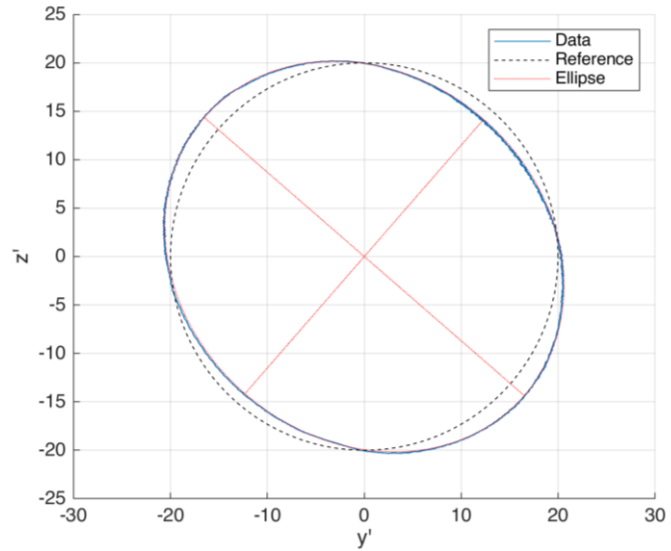


Figure 6.2 – The circular task (blue) shown for three repetitions with controller settings $G_{PD} = 1.0$. The end-effector pathway shows a high repeatability as the three separate circles cannot be distinguished visually. The pathway shows deformation of the circle towards an ellipse. The fitting of the ellipse is so accurate that the ellipse is hidden behind the pathway, making only the axes of the ellipse visible.

Controller Settings	$RMSE_{plane}$ [mm]	ϵ_r [mm]	ϵ_x [mm]	ϵ_y [mm]	$RMSE_{circle}$ [mm]	$RMSE_{ellipse}$ [mm]
$G_{PD} = 1.0, \alpha = [.] *$	0.151	0.39	1.448	0.549	1.099	0.165
$G_{PD} = 0.5, \alpha = 1.0$	0.133	0.10	1.618	0.243	0.782	0.108
$G_{PD} = 0.2, \alpha = 0.5$	0.127	-0.37	1.523	0.329	0.619	0.055
$G_{PD} = 0.2, \alpha = 1.0$	0.131	-0.83	1.533	0.265	0.736	0.032

Table 6.3- Accuracy of the circular motion around the X-axis, starting from centre of scaffold ($X_0 = [0,0,0,0,0,0]$).

Table 6.4 shows the accuracy of the circle when rotated along the other axes. In these experiments the controller setting $G_{PD} = 1$ is used. The table includes a subdivision of the $RMSE_{circle}$ for each of the three circles performed.

	$RMSE_{plane}$ [mm]	ε_r [mm]	ε_x [mm]	ε_y [mm]	$RMSE_{circle}$ [mm]				$RMSE_{ellipse}$ [mm]
					All Circles	1 st circle	2 nd circle	3 rd circle	
X-axis	0.151	0.39	1.448	0.549	1.099	1.104	1.092	1.100	0.165
Y-axis	0.033	-0.21	-0.634	1.745	0.564	0.561	0.564	0.566	0.063
Z-axis	0.096	0.01	-0.528	-1.364	0.554	0.572	0.543	0.546	0.078

Table 6.4 - Accuracy of the circular motion for $G_{PD} = 1.0$ around x,y,z axis.

The results show in all control settings a good fitting to the circle to the plane with a RMSE ranging from 0.127mm to 0.151 mm. The ε_r shows an accurate radial fitting compared to the desired task. However, the circle can be seen as not being completely circular, as found in the $RMSE_{circle}$ and the small but present deviation of the centroid of the data compared to the centroid of the fitted data ($\varepsilon_x, \varepsilon_y$). Noticeable from the circular motion task is the repeatability. The RMSE circle fitting of the entire dataset, which comprises of three repetitions of a single circle pathway, is similar to the RMSE found for each individual circle. This indicates a high repeatability of the system, which is explored further in the following section.

6.2.1.4 Repeatability task

A repeatability test was performed in which the end-effector moved with a step response to an arbitrary position at a distance of 10mm. After approximately 2.5 seconds, which is more than the settling time found in section 6.2.1.1, the probe would move back to its original position and the accuracy of this position compared to the previous was assessed. The task was performed at 100 consecutive but arbitrary points generated by a uniform randomization vector using the Eigen library. The pitch and yaw were kept constant throughout the experiment. Figure 6.3 shows the motion of the end-effector for $G_{PD} = 1$, and the accuracies for different control settings are shown in Table 6.5. The mean and standard deviations of the error were calculated relative to the mean of the entire data set, thus $\mu_\varepsilon = \mu(X - \bar{X})$ and $\sigma_\varepsilon = \sigma(X - \bar{X})$ respectively. The results show a submillimetre repeatability of the system, with the highest accuracy for $G_{PD} = 1$ with 0.174 ± 0.073 mm.

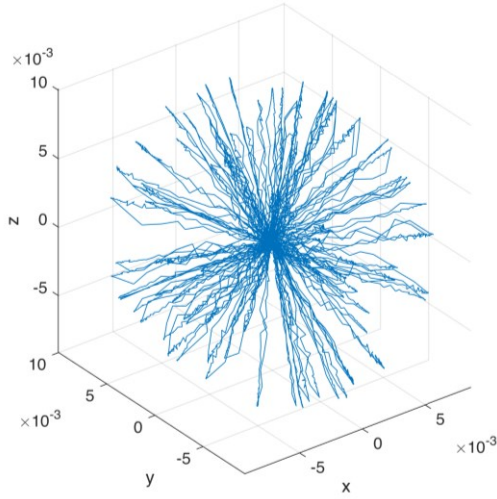


Figure 6.3 – The 3D position of the end-effector during the repeatability task of 100 random motions. All dimensions given are in metre.

Control Settings	μ_ε [mm]	σ_ε [mm]
$G_{PD} = 1.0, \alpha = [.] *$	0.174	0.073
$G_{PD} = 0.5, \alpha = 1.0$	0.350	0.114
$G_{PD} = 0.2, \alpha = 1.0$	0.684	0.150
$G_{PD} = 0.2, \alpha = 0.5$	1.115	0.448

Table 6.5 - The mean and standard deviation of a repeated repositioning task at different control conditions ($n=100$).

6.2.2 Robustness analysis on positional accuracy

The above results show that the system is able to achieve submillimetre accuracy and repeatability, both of which are considered important for automated motions. The current section explores how the positional accuracy of the end-effector is affected by its position in the workspace. The singularities in the workspace, and the proximity of the end-effectors to this, play an important role in the accuracy of the system. The proximity to singularities can be estimated using the tension factor (TF) [55] (see Chapter 2). At singularities some cables will lose tension, and thus the TF reaches an asymptote: $\lim_{t_i \rightarrow 0} TF(t_i) = 0$. The TF is based on the fact that when approaching the singularity, the tension in some cables decreases, while the tension in others increases. Hence, the difference between the highest and the lowest cable tension changes. Such increase in cable tension will also influence other effects such as hysteresis and friction, and hence the accuracy of the system is likely to be affected by proximity to the singularities.

The linear and circular motion tasks have been repeated at points close to the singularity. The linear experiments are performed at increasing x coordinates, at $(\zeta_0 = [c_x, 0, 0, 0, 0])$, with c_x having one of the following values: 0,30,60,70mm. The singularity plane is defined by the top three entry points (indices 4,5 and 6), and are defined by the normalized vectors $u = \frac{\vec{v}_{46}}{\|\vec{v}_{46}\|}$ and $v = \frac{\vec{v}_{56}}{\|\vec{v}_{56}\|}$. At the homing position ($\zeta = [0, 0, 0, 0, 0]$) the end-effector can be moved 69.8mm along the x axis to reach the singularity plane. Hence, the chosen values of c_x represent a relative starting position at approximately [0,43,86,100]% of the total distance from the centre of the workspace to the singularity, which is important when generalizing the current finding to other scaffold sizes.

c_x	X-axis				Y-axis				Z-axis			
	$\varepsilon_{\ \vec{x}\ }$ [mm]	RMSE [mm]	$\varepsilon_{\angle\vec{x}}$ [deg]	TF_{μ} [-]	$\varepsilon_{\ \vec{y}\ }$ [mm]	RMSE [mm]	$\varepsilon_{\angle\vec{y}}$ [deg]	TF_{μ} [-]	$\varepsilon_{\ \vec{z}\ }$ [mm]	RMSE [mm]	$\varepsilon_{\angle\vec{z}}$ [deg]	TF_{μ} [-]
0	-0.79	0.073	-0.58	0.58	0.44	0.121	-2.76	0.56	0.13	0.111	-8.61	0.58
30	-0.51	0.093	-0.16	0.28	0.44	0.119	-3.49	0.32	0.20	0.092	-9.28	0.36
60	-6.64	2.466	2.93	0.04	0.39	0.180	6.58	0.08	-0.14	0.110	-	0.10
70	-9.17	0.693	-3.59	0.01	0.70	0.303	5.50	0.02	0.17	0.190	-	0.03

Table 6.6 - The accuracy of the linear motion in x,y,z direction at different heights c_x in the workspace.

As earlier experiments showed the highest accuracy at $G_{PD} = 1$, this was also used during the robustness analysis experiment. The linear motions are shown in Figure 6.6 and the line fittings are shown in Table 6.6. The figure shows that at motions in the x direction starting from $c_x = 60\text{mm}$ and $c_x = 70\text{mm}$ ‘hit’ the singularity plane, at which the motion suddenly strongly deviates and moves along a pathway aligned with the singularity plane. The Y and Z axis, however, remain straight and approximately the designated 20mm length, seen in the RMSE and ε_l , respectively. These findings are in line with the average tension factor TF_{μ} calculated during each motion. Note also that all motions are slightly pivoted (-11.9°) around the Y axis. The same behaviour is observed in the circular task and is likely related to the calibration method. As is shown in Figure 6.1, a single bracket is used for calibration which may lead to the angle around the Y axis to be insufficiently controlled.

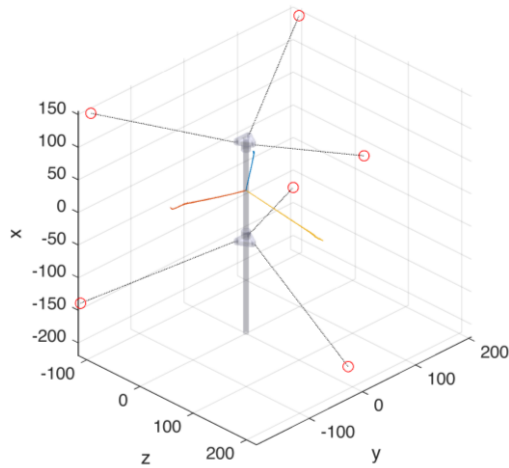


Figure 6.4 – The linear trajectory of the instrument to singularity planes.

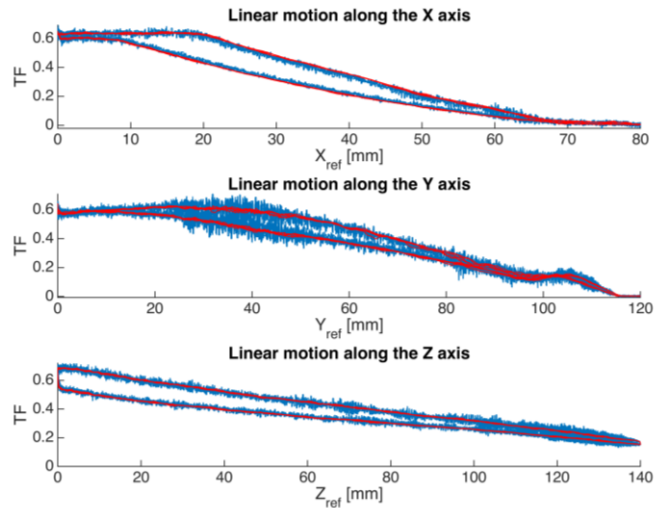


Figure 6.5 – The tension factor as part of the linear motion from the centre of the scaffold to the singularity. Blue: raw data. Red: the moving average over 50 samples.

As a comparison, a motion over the entire workspace was also performed, starting at the origin and moving in x,y,z directions with lengths of 70mm, 120mm and 140 mm, respectively (Figure 6.4). The motion was repeated 5 times. The tension factor as a function of the motion is shown in Figure 6.5; the red line is the moving average over 50 samples. The figure illustrates that the TF decreases steadily when approaching the singularity plane, as expected. The TF also displays the hysteresis in

the system as seen in the difference in the direction of motion, with the motion towards the singularity being lower than away from it.

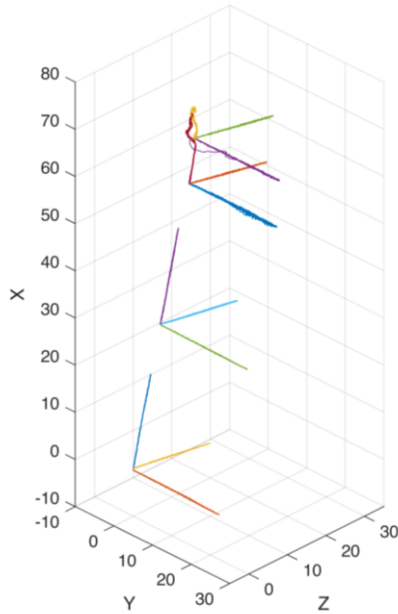


Figure 6.6 - The linear motions at different x starting positions. The singularity plane lies around $x = 70$ and this can be seen in the motion along the x -axis when reaching this plane. All dimensions are in millimetre.

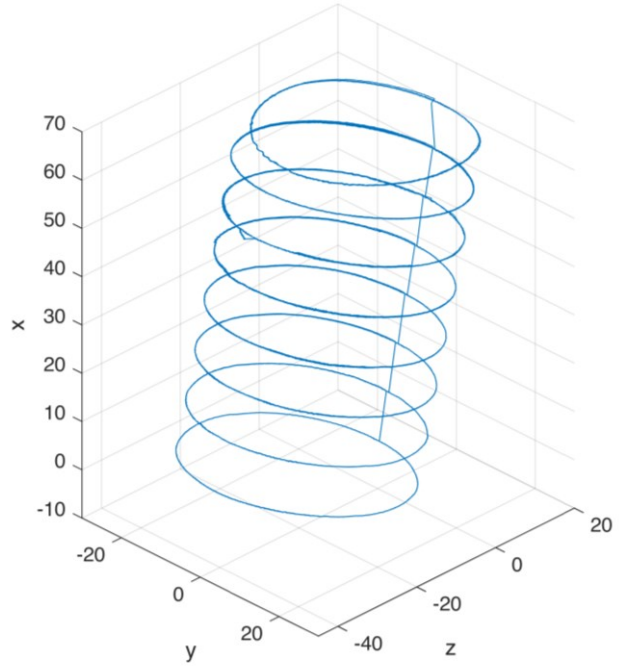


Figure 6.7 – The circular task at different heights c_x in the workspace. The upper-most circle ‘hits’ the singularity plane, shown by the difference in the shape. All dimensions are in millimetre.

The circle motions are performed with a radius of 20mm around the X-axis at incremental starting positions of 10mm along the x -axis. Figure 6.7 and Table 6.7 show the results of the motion. The results show that although proximity to the singularity increases the tension factor, it has a minimal effect on the circle task. However, at the singularity itself ($c_x = 70$), the plane at which the circle is performed shifts and aligns with the singularity plane. The tension factor is calculated from the minimum and maximum cable tensions measured at each instance during the circle task and the mean and standard deviation are taken as a metric for the proximity to the singularity.

The data show that the RMSE of the circle slowly increases when approaching the singularity plane, thus illustrating that the task becomes less circular (Figure 6.7). Even on the singularity plane the system is able to perform a circle task, albeit restricted to the singularity plane itself rather than a plane orthonormal to the X-axis. The change of plane can be seen in the increase in angle $\varepsilon_{\angle \vec{x}}$. As expected, the average TF of each circle task decreases when approaching the singularity plane, and the standard deviation is also slightly reduced. Overall, the tasks only display a strong decline in performance when the singularity plane is reached, showing robustness for autonomous motions within a large section of the workspace.

	$\frac{c_x}{w_x}$	$RMSE_{plane}$ [mm]	$\varepsilon_{\angle \vec{x}}$ [deg]	ε_r [mm]	ε_x [mm]	ε_y [mm]	$RMSE_{circle}$ [mm]	Tension Factor	
								μ [-]	σ [-]
$c_x = 0$	0%	0.150	-	0.38	4.168	2.290	1.098	0.636	0.045
$c_x = 10$	14.3%	0.145	0.49	0.42	3.004	1.717	1.141	0.560	0.035
$c_x = 20$	28.6%	0.140	0.88	0.41	2.195	1.120	1.162	0.436	0.034
$c_x = 30$	42.9%	0.148	1.27	0.37	1.545	0.584	1.197	0.324	0.027
$c_x = 40$	57.1%	0.153	1.71	0.36	0.977	-0.110	1.234	0.222	0.025
$c_x = 50$	71.4%	0.144	2.16	0.43	0.704	-0.384	1.291	0.133	0.020
$c_x = 60$	85.7%	0.149	2.00	0.37	0.249	-0.970	1.217	0.056	0.016
$c_x = 70$	100%	0.228	7.97	-1.37	-8.242	-4.561	1.401	0.017	0.009

Table 6.7 - The tensions factor for each circular motion at different proximities to the singularity plane at $c_x = 70\text{mm}$.

6.2.3 Raster scan

A raster scan was performed on the 80x80mm top surface of the phantoms used during the user study in Chapter 5. The raster scan involved the discretization of the surface in a 35x35 grid along the YZ plane (Figure 5.5), with a spacing of 2mm and a total of 1225 points. A 6mm indentation at 5mm/s was performed at each point and the speed between each point along the YZ plane was 20mm/s. $G_{PD} = 1$ was used as control setting during the raster scan. The raster scan (Figure 6.8) clearly shows where the nodules are, with forces between 5-6.5N compared to forces of 3-4N for the softer surrounding silicone.

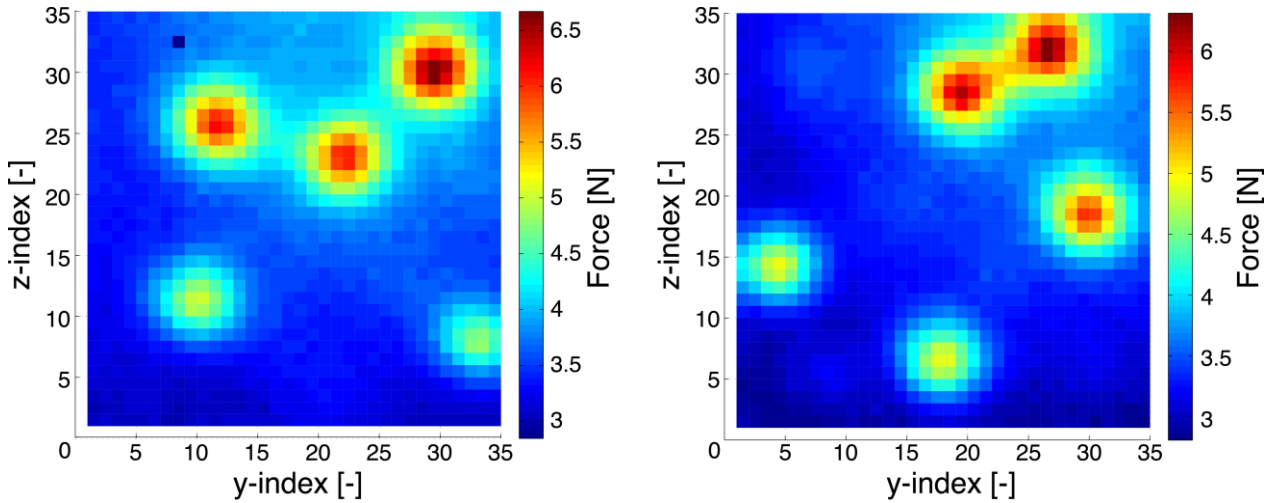


Figure 6.8 – Raster scan on the phantoms used in the user study presented in chapter 5. The color of each pixel represents the estimated force at a specific indentation. The indentation are performed along the x-axis, resulting in a 35x35 grid with a spatial resolution of 2mm on the YZ-plane. Image source: [321].

6.2.4 Overview of autonomous motions with CDAQS

The step response of the different controller settings showed that the controller achieved the highest accuracy and a short settling time for $G_{PD} = 1$. The experiments showed that this control setting also achieved the highest positional accuracy during an autonomous linear and circular task. The repeatability of the system was first demonstrated by performing each circular task three times

and comparing the fitting error of the same circle to each subsection of the dataset. The RMSE shown for each subsection of the data did not deviate strongly from the RMSE of the entire dataset, indicating high repeatability. To confirm the repeatability further, 100 randomized motions confirmed an error of $0.17\text{mm} \pm 0.073\text{mm}$. Again, the repeatability was the highest for $G_{PD} = 1$ and therefore this setting was the most suitable for autonomous motions.

The circular task yielded relatively low accuracy due to the distortion of the circle to an ellipse. This distortion is best explained by inaccuracies in the homing position of the end-effector. The homing position is determined by a 3D-printed bracket at the aluminium frame. However, while this can be used for the initial position, it does not control the initial tension of the cables. As mentioned in Chapter 2, the position is a function of both tension and cable length and is prone to errors for the relatively compliant cables used in the CDAQS. Overall, the results indicate that future developments must focus on the incorporation of cable elasticity and the establishment of a robust calibration routine. One self-calibration routine [70] was tried for a planar version of the system, but this yielded no accurate results, which led to the use of the calibration bracket. However, the experiments show that further improvement of the calibration is important and other calibration routines should be explored [102][103].

Despite limitations of the calibration, the raster scan on silicone phantoms demonstrated the first use of the mechanism for an autonomous scanning task. The results provide a map of the hidden nodules which can be used in MIS to map the stiffness of a tissue surface. The ability to perform a raster scan is further explored in the SIMPLE system, designed as a low-friction system for clinical use.

6.3 The SIMPLE system

SIMPLE is a *Single Incision MicroPort LaparoEndoscopic* surgical robotic system that uses a novel extraluminal access method to control surgical instruments. The key advantage of this access method is its low friction, allowing for end-effector force sensitivity and positional accuracy. The prototype is the clinical translation of the CDAQS system for single-incision laparoscopic surgery. The SIMPLE system enables intra-abdominal force sensing without the addition of sensors within the body. The system is illustrated in Figure 6.9 and consists of 3 main parts: (1) the abdominal external scaffold, (2) abdominal motor units and (3) the transperitoneal arm. A unique aspect of the concept is the use of multiple microports ($<2\text{mm}$), one for each abdominal motor unit, through which actuation cables are inserted into the insufflated abdomen. The resulting direct cable pathway provides low friction to facilitate accurate positioning of a surgical end-effector and high force-sensing capability. The microports can be positioned on the external scaffold in such a manner to ensure a procedure-

appropriate instrument workspace within the pneumoperitoneum (the optimisation method is discussed in Chapter 7). The transperitoneal arm is used to provide additional cable entry points in the abdomen and delivers the instrument overtubes. Vision is provided by an endoscope inserted through the same port as the transperitoneal arm.

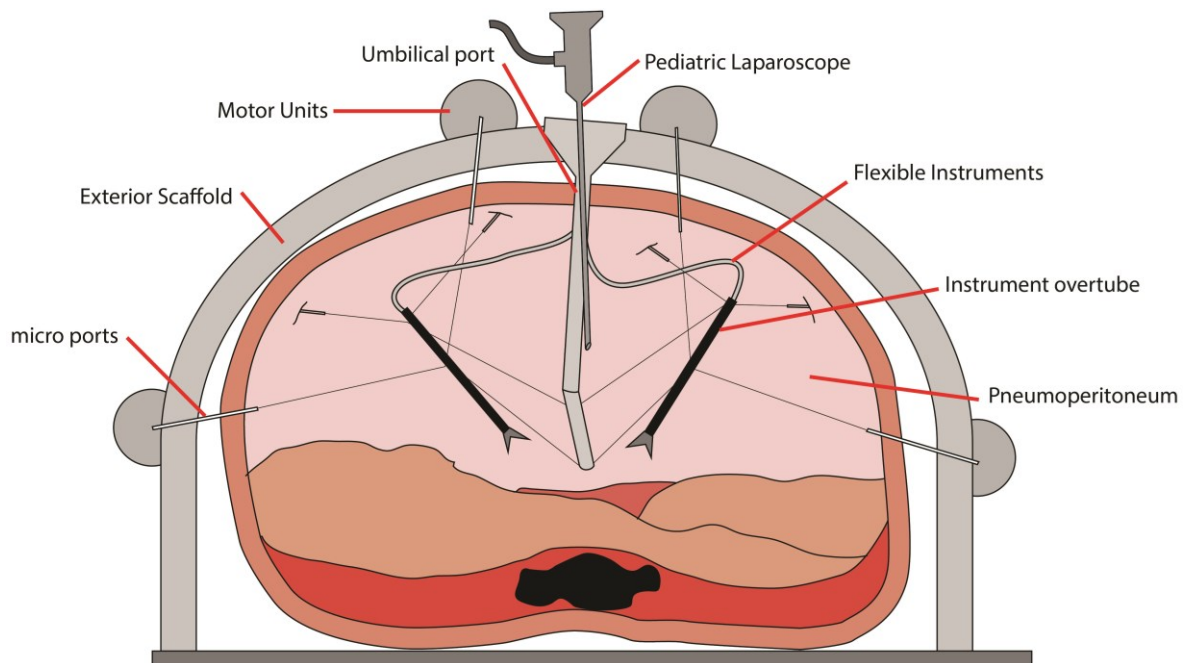


Figure 6.9 – The main concept of SIMPLE.

6.3.1 Prototype

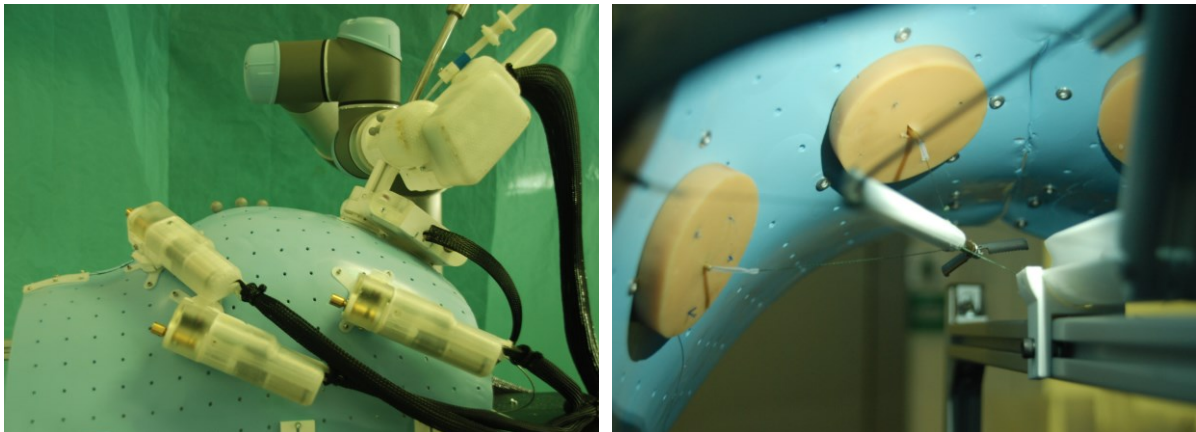


Figure 6.10 - The SIMPLE prototype shown from the outside (left) and from the inside (right).

Images of the prototype are shown in Figure 6.10. The prototype was developed to provide bimanual instrument control. Six cables are used for the actuation of each instrument, of which three are guided through the transperitoneal arm, and the other three inserted via microports (for a bimanual system 6 microports are required). Depending on the cable configuration, the CDPM can provide a maximum of 5 DoF to each instrument. The prototype was created using additive manufacturing methods. The majority of parts are made of PLA (Ultimaker BV, Netherlands) and

Nylon (Markforged Inc, USA), and several parts are made of clear SLA material (GPCL04, Formlabs Inc, USA).

6.3.1.1 Abdominal motor units

The abdominal motor unit shown in Figure 6.11 is similar to the mechatronic design of the CDAQS, consisting of a cable spool, cable pulley, loadcell (LCL-020, OMEGA Engineering, INC. USA) and a motor (2232S024BX4 25:1 22F, Faulhaber GmbH & Co.KG, Germany). The mechatronics are connected to the control box via 2-metre shielded cables; the control box is similar to the one described in Chapter 5, the major difference being the replacement of the Windows-based digitizer by a Linux-based one (USB-DUX Sigma, Incite Technology Ltd., UK). As a result, the single-board Windows computer and the UDP interface could be removed, allowing 1Khz readings of the loadcells. To amplify the loadcell signal, a small PCB board with an INA125U op-amp (Texas Instruments, Inc. USA) was designed and integrated in each motor unit. A 324-ohm transistor was used to set the gain to approximately 189.

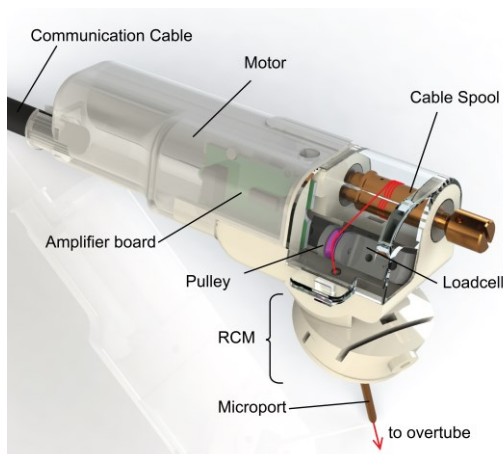


Figure 6.11 –The abdominal motor unit and its components. The cable pathway (red) is guided into the abdomen via a single pulley. The RCM is mounted on the scaffold.

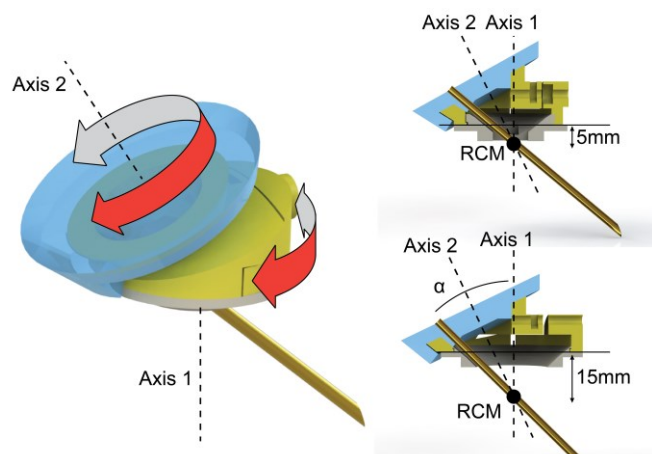


Figure 6.12 – The RCM mechanism adapted from [357]. Rotation around the two axes is used to set the orientation. The images on the right show the cross-section for an RCM at 5mm and 15mm depth.

The motor units have a base that uses a remote centre-of-motion mechanism (RCM), which is designed such that the rotational point of the microport is placed approximately in the centre of the abdominal wall to reduce straining the tissue (Figure 6.12). This RCM mechanism was developed by Song et al. [357] and was chosen for its simplicity and because it could be scaled down to sizes suitable for the SIMPLE system. The depth of the remote centre-of-motion (Figure 6.12, right) is predetermined for the RCM. However, the simplicity of the mechanism makes the use of different bases to cope with variation in patients' skin thickness economically feasible. The design and the range of angles of the needle can be easily adjusted by changing the angles of the axes. The mechanism is used to position the microport shaft at an optimal angle to allow operation with

minimal friction. A PTFE inner tubing is used to further minimize friction. In the current prototype, the RCM mechanism is used in conjunction with a clamping screw to fixate it at a pre-defined angle. It would also be possible to have the mechanism unclamped and enable the cable to re-orientate the passive microport during operation. However, the current motor units are designed to be asymmetrical, meaning that gravity will influence cable behaviour if not clamped.

6.3.1.2 External Scaffold

The external scaffold (Figure 6.13) was created from a 3.2mm thermoplastic sheet (BenePlas Low Temp, Benecare Medical Ltd, UK) already used for the creation of patient-specific splints. The material's low glass-transition temperature around 60 degrees Celsius makes it easy to use hot water to change the otherwise rigid material into a compliant sheet. The sheet material was moulded over a dVRK (da Vinci Research Kit) laparoscopic trainer to obtain the shape of the pneumoperitoneum. The sheet material has a grid of holes, which was used to attach the port bases at fixed locations. A large port was created for the transperitoneal arm and was placed centreline at the approximate location of the umbilicus. On the inside, a 10mm silicone slab was placed at each port to simulate the abdominal wall, as shown in Figure 6.10 (right).

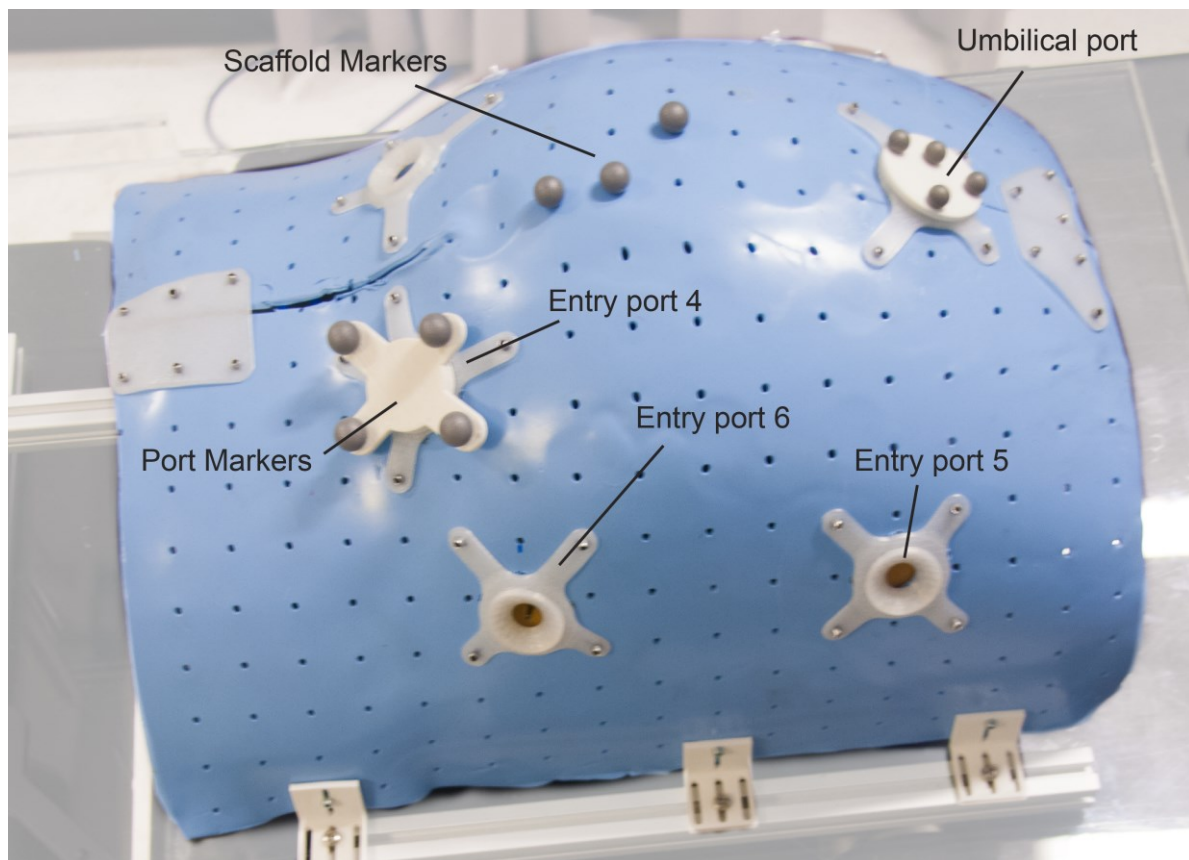


Figure 6.13 – The scaffold made with thermoplastic materials. The position of the scaffold and each of the ports is calibrated using passive optical trackers.

6.3.1.3 Transperitoneal arm

The transperitoneal arm (Figure 6.14) comprises a proximal side containing motors and sensors and a distal shaft which is inserted into the abdomen. The shaft has a diameter of 25mm and accommodates the 10mm endoscope (EndoEye Flex 3D, Olympus, Japan), two flexible instruments and overtubes. The end of the shaft is articulated to control the position of the bottom cable entry points, two per overtube. Two other entry points for actuation cables are placed at the umbilical port and actuated with motors in the lower motor units (Figure 6.16). The flexible instrument shown in Figure 6.10 (right) is created by modifying a laparoscopic grasper to a flexible shaft.

The proximal section of the arm contains four motors for cable actuation and another for the articulation of the shaft. Two further motors are located at the port of the transperitoneal arm to accommodate two additional cables. The endoscope is inserted at the proximal end and is clamped in position. A mounting point is added to the mechanism to enable attachment to the UR5 robotic arm (Universal Robots A/S, Denmark).

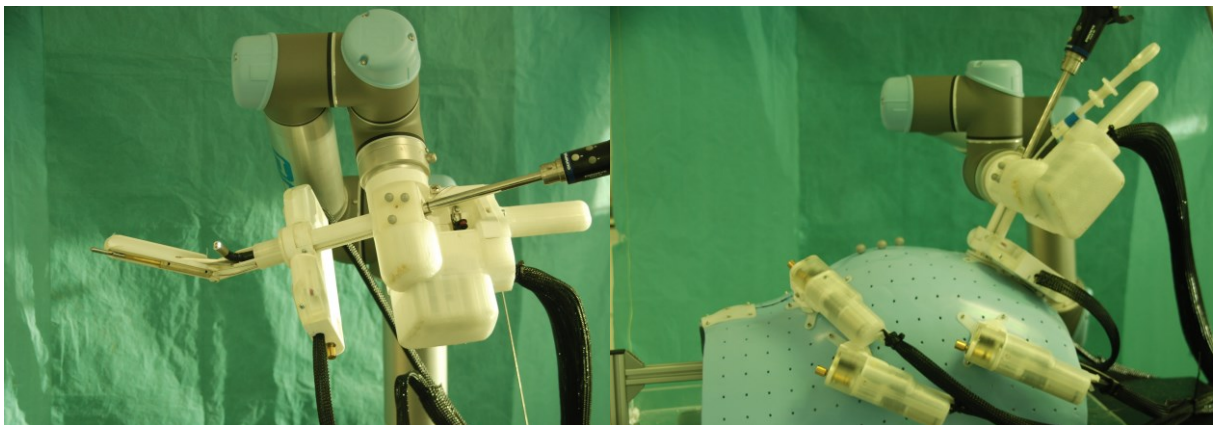


Figure 6.14 - The transperitoneal arm shown attached to the UR5 robot (left) and when placed into the scaffold (right).

6.3.1.4 Cable actuation and transmission

The intra-abdominal cables are actuated using the same motors and loadcells as the abdominal motor units. The cables are guided along straight paths to the cable entry point inside the abdomen, guided by pulleys. At the cable entry points, a PTFE tube is used to enable a sharper bending radius. For each CDPM (i.e. both the left and right instrument), the pathway of the first and second cables passes through the transperitoneal arm, as shown in Figure 6.15. Two pulleys are used to enable measurement of the cable tension and align the cable along the main shaft. PTFE tubing is used in the articulated distal section.

The third cable of each CDPM is positioned at the umbilical entry port; the cable pathway is shown in Figure 6.16. Two pulleys are used to redirect the cable from the cable spool to the entry point in the body. The first pulley is connected to a loadcell to measure the cable tension. The cable

between the first and second pulleys is aligned along the pivoting axis of the motor units, allowing the motor units to be positioned at any desired angle to comply with the abdominal surface. An eyelet is placed at the entry point and PTFE tubing is used to minimize friction at this point.

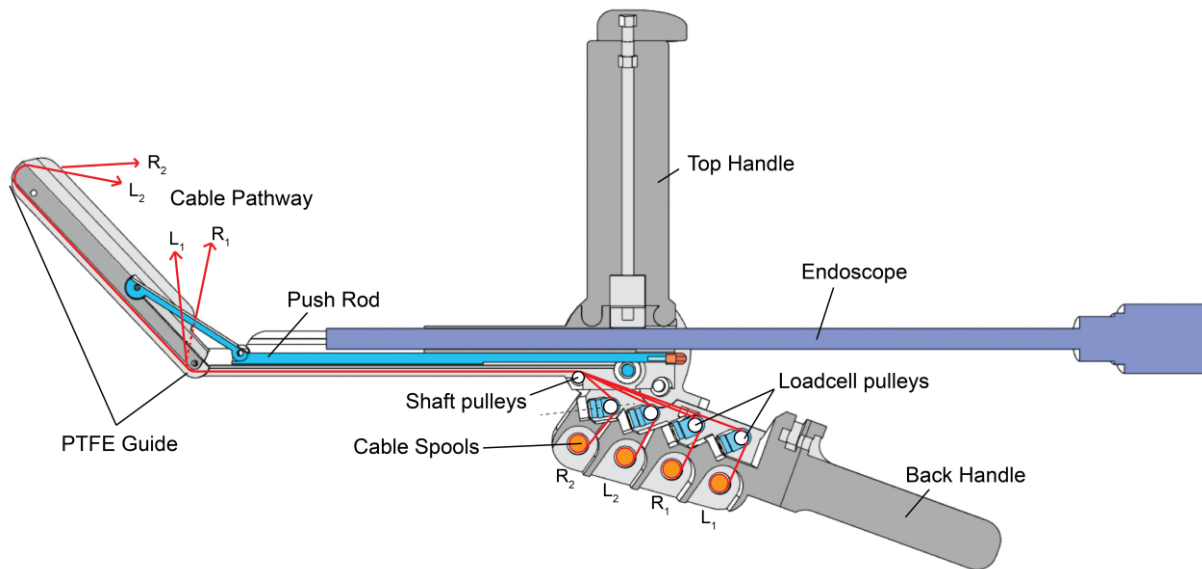


Figure 6.15 - Pathway (in red) for the first and second cables through the transperitoneal arm.

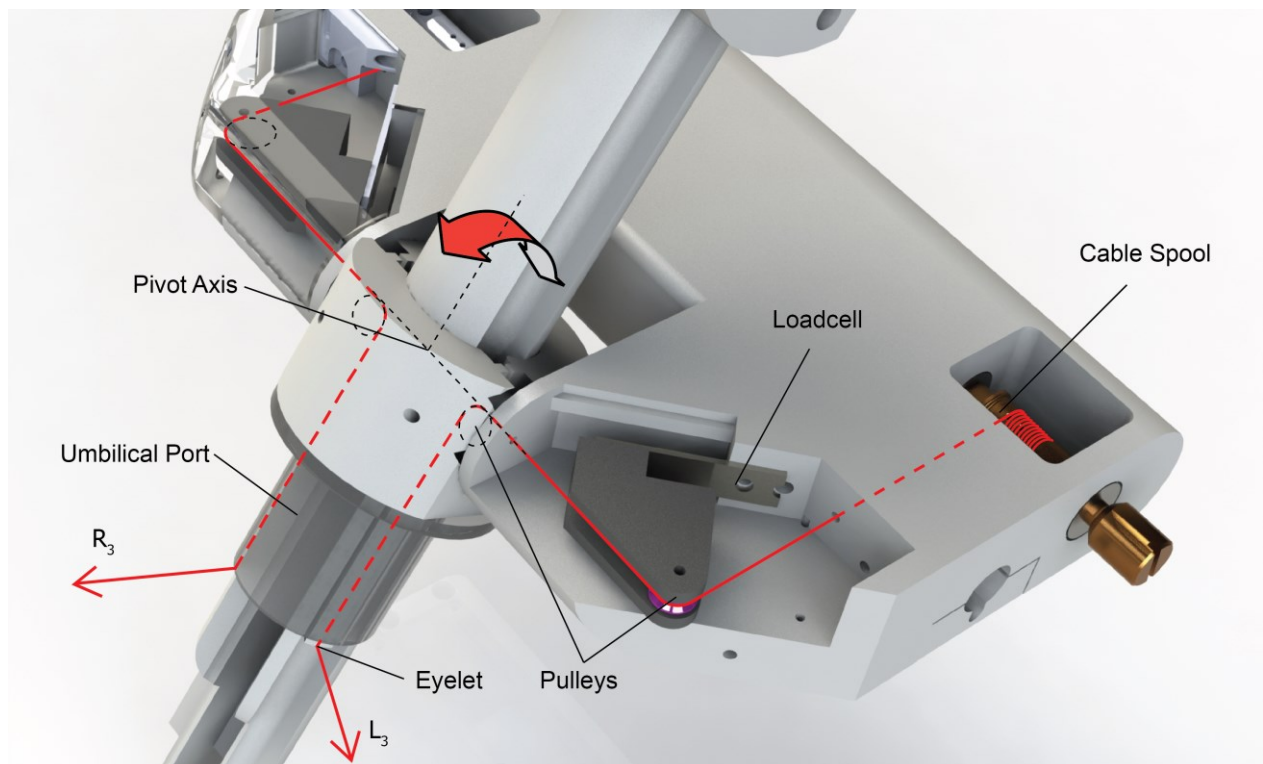


Figure 6.16 – Pathway of cable 3, placed at the entry port of the transperitoneal arm.

6.3.1.5 Actuation of the shaft

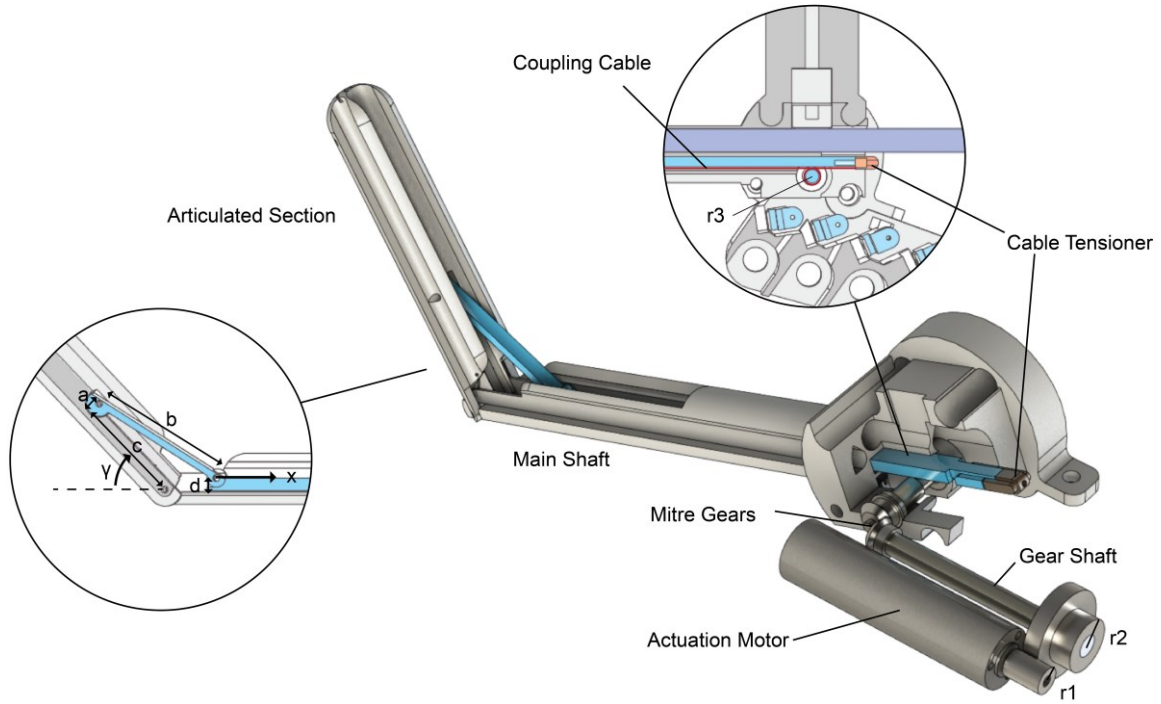


Figure 6.17 - The transmission mechanism for articulation of the tip of the transperitoneal arm.

The articulated section of the shaft is actuated through a link mechanism using a push rod, as shown in Figure 6.17. The angle of the bottom shaft γ can be described as a function of the linear displacement of the pushrod x :

$$x(\gamma) = a \sin(\gamma) + b(\cos(\delta(\gamma)) - 1) + c(1 - \cos(\gamma)) \quad (6.1)$$

$$\delta(\gamma) = \sin^{-1}\left(\frac{a \cos(\gamma) + c \sin(\gamma) - d}{b}\right) \quad (6.2)$$

The push rod is coupled to a capstan with stainless steel cable (7x7 cable, part no. 2018, Carl Stahl Sava Industries, Inc. USA). The steel cable is wound once around the steel capstan and tensioned by a setscrew. The capstan is connected to the motor via a set of mitre gears and a set of spur gears (2232S024BX4 25:1 22F, Faulhaber, Germany). The relationship between the motor angle θ_m and linear translation of the push rod is found as: $\theta_m = \frac{r_2}{r_1 r_3} x$. Given the equations (6.1)-(6.2) and Table 6.8 the required motor angle θ_m can be found for a desired joint angle γ_d . The inverse relationship, the forward kinematics, becomes more cumbersome to solve quickly due to the non-linearities introduced by the geometric functions. One pragmatic solution for the forward kinematics is to find a parametric fitting (Appendix A.7).

Dimension	a	b	c	d	r_1	r_2	r_3
Value	6mm	46.5mm	60mm	6mm	4.80mm	12mm	3.75mm

Table 6.8– Dimensions of the values given in equations (6.1)-(6.2) and Figure 6.17.

The transmission ratio from the motor to the shaft is set such that it is possible to maintain a steady angle γ while the system is in operation. The mechanism acts in the XZ plane; therefore, the 2D static equilibrium equations can be used. Note that the local coordinate frame of the tip is used for these equations.

$$\begin{bmatrix} \Sigma F_x \\ \Sigma F_z \\ \Sigma M_y \end{bmatrix} = \begin{bmatrix} f_{diag} \cos(\beta) - f_{main} \cos(\gamma) \\ 2F_t + f_{diag} \sin(\beta) + f_{main} \sin(\gamma) \\ f_{diag}(c \sin(\beta) + a \cos(\beta)) - \Sigma T_{z,i} x_i \end{bmatrix} = 0 \quad (6.3)$$

In which $T_{z,i}$ is the cable tension in each cable acting at a fixed distance x_i from the pivot point. i represents the indices of the cables used for each instrument. The angle is $\beta(\gamma) = \gamma - \delta(\gamma)$, and with equation (6.2), the system of equations is solvable. The forces in the push rod (f_{main}) and diagonal bar (f_{diag}) are found as a function of angle γ and the cable tensions $F_{t,i}$:

$$f_{main}(F_t, \gamma) = f_{diag}(F_t, \gamma) \frac{\cos(\beta(\gamma))}{\cos(\gamma)} \quad (6.4)$$

$$f_{diag}(F_t, \gamma) = \frac{\Sigma F_{t,i} x_i}{c \sin(\beta(\gamma)) + a \cos(\beta(\gamma))} \quad (6.5)$$

The capstan to cable interface is important to enable for conveyance of the motion. The pretension in the cable is an important aspect in preventing slippage, and can be found with the capstan equation:

$$F_{shaft} = T_{PT} e^{\mu \phi} \quad (6.6)$$

In which T_{PT} represents the cable pretension and μ is the friction coefficient between the capstan and the steel cable. The pretension is realized through the cable tensioner shown in Figure 6.17, which uses a small M2 hex bolt to elongate the actuation shaft and thereby put strain on the cable.

6.4 System Assembly

From a clinical perspective one of the main challenges of the system is the intra-abdominal assembly of the cables. The use of microports with the abdominal motor units prohibits the connection of the cables between the end-effectors and motors before insertion into the body. Intra-abdominal connection of cables can be achieved in two ways, depending on whether the cables are guided from the inside-out or from the outside-in. The former is challenging, as it requires the cables

to be threaded through the peritoneum using tools inside the peritoneal cavity, although it would be easier to connect the cables to the motor units located outside of the body than to the instruments inside it. This method most likely requires an instrument for the puncturing of the abdominal wall from the inside in order to create the microports (Figure 6.18a). Such an instrument would have to be manipulated through the main umbilical port and placing a microport at the desired port position would be a challenging endeavour. Alternatively, introducing the cables from the outside into the abdomen would make port placement easier, but connecting the cables to the overtube is more challenging. A solution for this problem can be found in laparoscopic suturing devices, e.g. in such simple designs as the Capiro OPEN ACCESS suture capturing device (Boston Scientific, MA, USA), which uses a circular needle to insert a barbed suture into the tissue after which the suture is grabbed by the device on the other side. The connection mechanism could possibly be integrated into the overtube; such a mechanism can consist only of a single compliant needle-receiving element. Figure 6.18b illustrates how such a device can be used for SIMPLE.

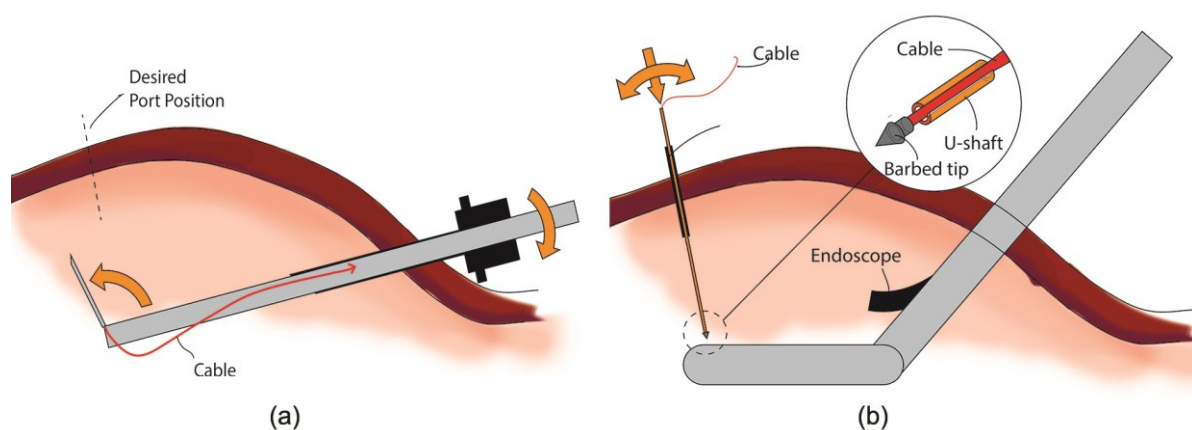


Figure 6.18 – Two different approaches to connect the cables. (a) “inside-out”: a device is used to insert the port in the desired position and couple the cables outside of the body. (b) “Outside-in”: the cable with a barbed-tip is inserted into the microport and manipulated with a U-shaped shaft. A mechanism, such as seen in the Capiro OPEN ACCESS is used to connect the cable to the overtube.

The assembly of the robotic system, then, can be envisioned as comprising the following steps:

1. Insufflation of the abdominal cavity using a Veress Needle.
2. Creation of the umbilical port and insertion of the transperitoneal arm. The overtubes are introduced simultaneously with the arm. The cables that are guided through the transperitoneal arm are already preconnected to the overtubes.
3. Moulding of the scaffold over the insufflated abdomen.
4. Placement of the abdominal motor units on the scaffold and the introduction of microports under endoscopic visualisation of the peritoneum.

5. Assembly of the remaining cables of the abdominal motor units (Figure 6.18).

Note that in these steps, a minor change should be made to the scaffold at the umbilical port to enable placement of the scaffold after the transperitoneal arm is placed. The position of the abdominal ports, as well as the main port, can be determined in advance based on the specific workspace requirements for a procedure or based on pre-operative data and simulated insufflation of the peritoneum [358]. The port positioning is further explored in Chapter 7.

6.5 Validation

6.5.1 Feasibility of Intra-abdominal cable assembly

To demonstrate the initial feasibility of the cable assembly method, the Capio OPEN ACCESS suture capturing device was placed into the scaffold and affixed to the transperitoneal arm at the position of one of the overtubes. The barbed suture was placed at the end of an actuation cable and placed into a long hollow brass U-shaped shaft with a 1.25mm diameter. The shaft was used to insert the barbed-tipped cable into the simulated abdominal cavity and manipulate the barbed tip into the capture device. After the tip was inserted and connected, the U-shape of the shaft – being open along the entire longitudinal axis - allowed it to be removed from the microport through which it was inserted while leaving the actuation cable in place. Figure 6.19 shows stills from the video of the connection task, in which it took 59 seconds to connect two cables. The video shows the second time that the task was performed, after a first quick trial, which illustrates the feasibility of the assembly method under 2D laparoscopic visualisation. It should be noted, however, that the video is only used to indicate that such an approach is feasible; the connection itself, while solid, was not evaluated in terms of maximum tension forces. Before integrating this method in SIMPLE, a more thorough evaluation of alternative connection methods should be conducted. At the present stage, such evaluation was outside the scope of the study.

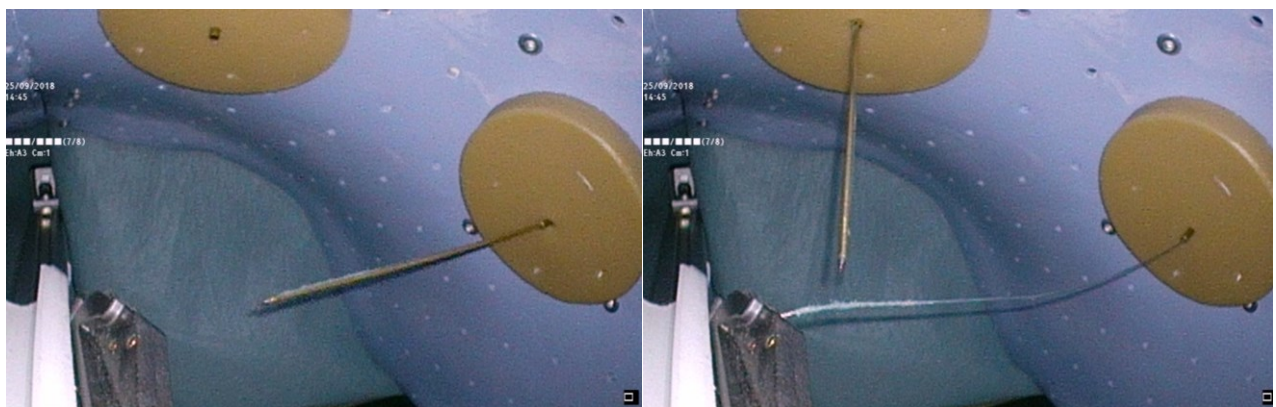


Figure 6.19 – Stills of the video assembly method using the brass insertion tool. The video shows the second attempt to connect two cables, which took 59 seconds at the second attempt.

6.5.2 Benchmarking

A benchmarking study was conducted to evaluate the accuracy of the force estimation of the system. A 3D printed pillar was placed within the scaffold, against which the instrument then exerted forces. The pillar, similar to the one shown in Figure 6.21, was mounted on a 6 DoF loadcell (Nano43, ATI Industrial Automation, Inc., USA). The force measurements were conducted in the positive X direction, and both negative and positive Y directions. The unbiased force readings are shown in Figure 6.20.

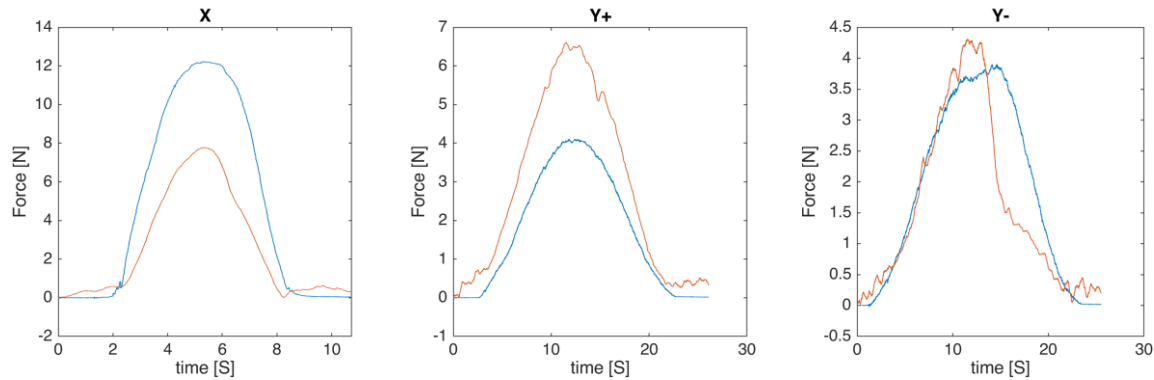


Figure 6.20 – The force estimation (red) compared to the ground truth measurements (blue), for motions in the X+, Y+ and Y- directions, respectively.

The figure shows that along the X direction the estimated forces are lower than the forces measured with the loadcell, but an overestimation for forces in the Y+ direction. The most likely reason for the difference compared to the CDAQS system (Chapter 5) is related to calibration, which is discussed at the end of this chapter. Similar behaviour is seen at a range of linear velocities, as well as a similar ratio between the maximum measured and estimated forces $= \frac{\max(F_{est})}{\max(F_m)}$, as shown in Table 6.9. While compared to the ground truth measurements the results show relatively high inaccuracies, the system can detect relative force differences and thereby enable the creation of a relative stiffness map, which are also independent of the end-effector velocity.

	x^+	y^+	y^-
0.1mm/s	0.63	1.65	1.09
0.5mm/s	0.64	1.61	1.10
1.0mm/s	0.64	1.61	1.08
5.0mm/s	0.58	1.59	1.22

Table 6.9 - The ratio for the maximum measured and estimated forces $r = \frac{\max(F_{est})}{\max(F_m)}$ at different linear velocities.

6.5.3 Raster scanning

A raster scan was performed on silicone samples of 25x25mm. Each sample was mounted on a base made of PLA and placed within the instrument workspace, perpendicular to the tool axis (Figure 6.21). During scanning, $G_{PD} = 1$ was used as control setting, in line with the findings in section 6.2.

The staircase raster scan was used to evaluate the force estimation accuracy of the system compared to a ground-truth loadcell measurement. The phantom was made of PLA and ecoflex 00-20 silicone rubber, in which the PLA was used for the hard ‘steps’ and the silicone to level the top surface (Figure 6.22). The bottom right step (step 1) was not covered with any silicone, whereas for each downward step - in a clockwise direction - a 2mm layer of silicone was added. The comparison between the ground-truth and the estimation is shown in Table 6.10 and Figure 6.23. The metrics in the table were calculated using only the inner 8x8 data points of each step. This was done to exclude measurements which are affected by the size and shape of the instrument’s tip (5mm diameter round tip) and the slipping of the instrument near the edge of the step. The 8x8 grid leaves a border of 5 samples between each quadrant, and 2 on the edge.

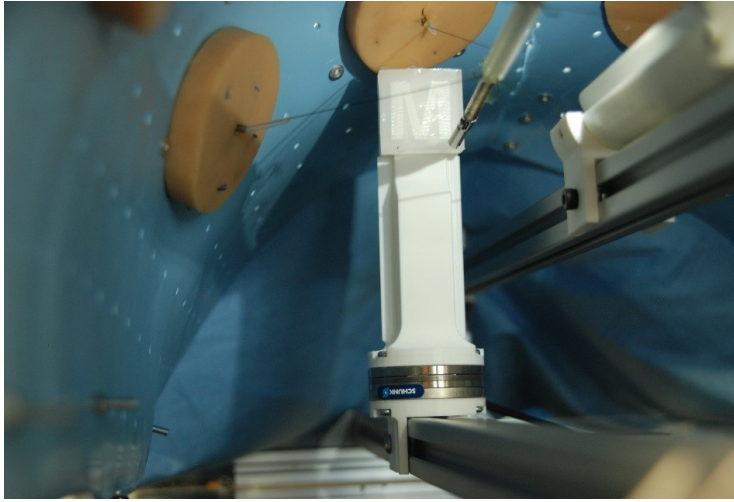


Figure 6.21 – The setup used for the raster scan. A loadcell is used at the base of the pillar for measuring the ground-truth forces.

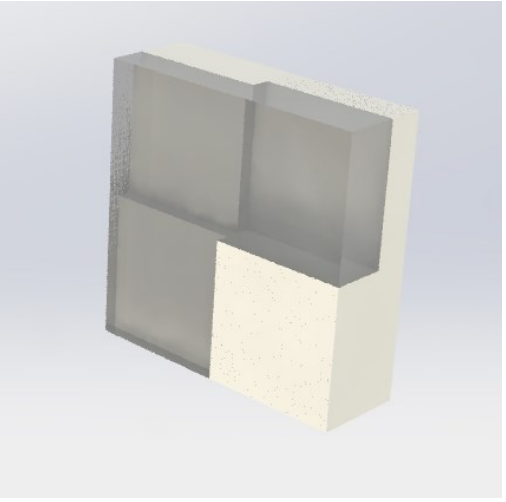


Figure 6.22 - Silicone/PLA phantom used for the staircase experiments.

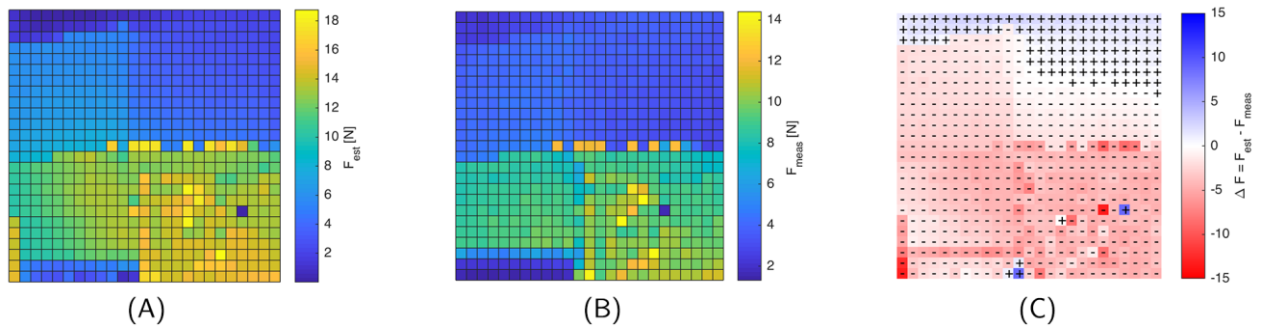


Figure 6.23 – Comparison between the loadcell measurements (A) and the force estimation (B) of the same raster scan. The difference between both force maps is shown in (C) and is calculated as $\Delta F = F_{est} - F_{meas}$. The force map is 25x25 pixels for the raster scan with a 1mm resolution.

The result shows an overall underestimation of the tip forces compared to the ground truth measurement, which is consistent with the findings for force estimation along the x-axis in section

6.5.2 . When looking at the difference between the measured and the estimated forces, it becomes clear that the difference is smaller for the steps with more silicone. However, this gradient is also seen within the stairs themselves, hinting that the source of the inaccuracy lies with the calibration or errors in the entry port positions.

	F_{est}	F_{meas}	$Diff(F)$
Step 1	9.78 ± 1.72	14.02 ± 2.31	-4.23 ± 2.32
Step 2	8.58 ± 1.28	12.09 ± 0.98	-3.50 ± 1.22
Step 3	4.14 ± 0.36	5.84 ± 0.97	-1.70 ± 0.66
Step 4	3.41 ± 0.22	3.30 ± 0.46	0.10 ± 0.61
Entire Phantom	6.12 ± 3.03	8.39 ± 4.85	-2.27 ± 2.40

Table 6.10 - The average value for each step (inner 8x8 samples) and the difference between the measured and estimated value.

The same scan was performed on other shapes, including the six letters of the acronym ‘SIMPLE’. The position of the phantom was kept constant for all measurements. As with the abovementioned staircase phantom, a combination of PLA and silicone material was used. The overall dimensions of the phantoms and the result for each of the letters is shown in Figure 6.24. The images showed some degree of deformation compared to the reference image. To quantify the deformation, it was assumed that it could be described as a shear and scale affine transformation between the reference image and the measured image:

$$\begin{bmatrix} x_m \\ y_m \end{bmatrix} = \begin{bmatrix} c_1 & \lambda \\ 0 & c_2 \end{bmatrix} \begin{bmatrix} x_{ref} \\ y_{ref} \end{bmatrix} \quad (6.7)$$

In which c_1 and c_2 are responsible for the scaling of the axes x and y, respectively, and λ determines the shear between both images. The equation can be written more compactly as: $\vec{x}_m = M\vec{x}_{ref}$. For each letter, a number of reference points are selected from the CAD model, and the coordinates of the same points are manually selected in the image. The most suitable fit between both reference points is found by numerically solving the following minimization problem over n coordinate points:

$$c = \underset{c}{\operatorname{argmin}} \left(\frac{1}{n} \sum_{i=1}^n \| M\vec{x}_{ref,i} - \vec{x}_{m,i} \|_2 \right) \quad (6.8)$$

The solution c gives the shear and scaling to achieve the best fit: $c = [c_1 \quad c_2 \quad \lambda]^T$. The accuracy of the fit was assessed by deforming a reference image with the calculated shear and scaling factors and overlaying the image with a normalized image of the measurement. The reference image created at a higher resolution (300x300px), after which it was cropped and scaled down to the 25x25px format. The binary image with a threshold of 0.5 was used to compare with the normalized force image retrieved with the SIMPLE system. For each letter, the values are given in Table 6.11.

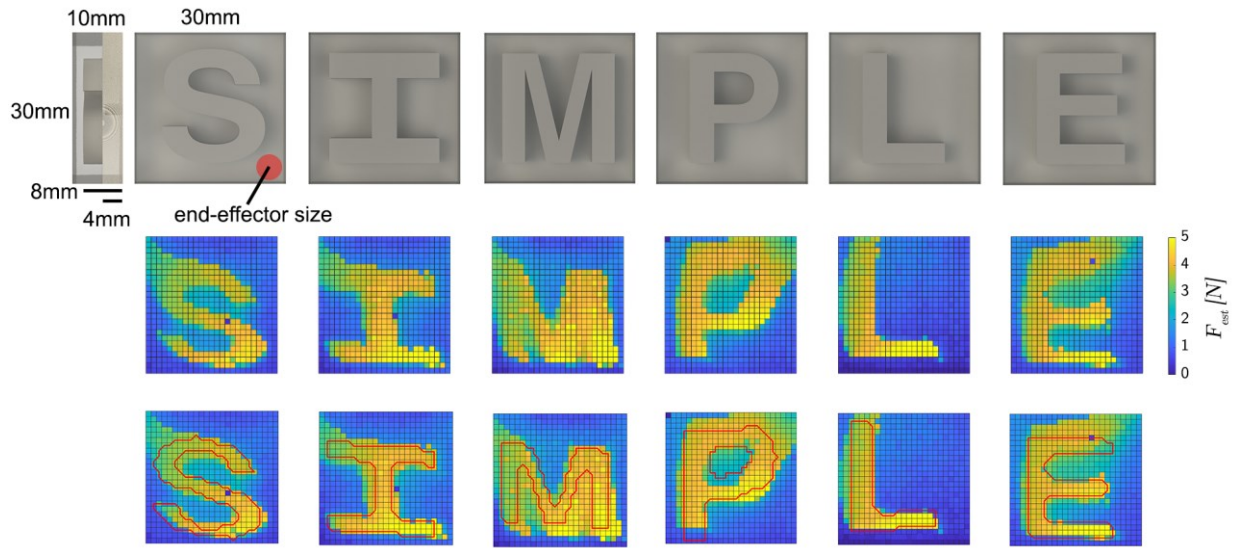


Figure 6.24 - The raster scan performed on each letter. The top row shows the CAD model used to create the phantoms, the middle row shows the force images as collected with the system. The bottom row shows the fitting of affine transformation of the contours of the letters to points in the dataset. The parameters for the affine transformation are shown in Table 6.11.

	"S"	"I"	"M"	"P"	"L"	"E"
c_1 [%]	97%	95%	93%	101%	104%	98%
c_2 [%]	85%	78%	70%	103%	99%	89%
$\phi = \tan^{-1}(\lambda)$ [deg]	7.4	4.2	3.9	-4.0	-2.4	1.8
RMSE[mm]	1.29	1.14	2.72	1.50	0.36	1.57

Table 6.11 - The fitted parameters for affine transformation of the reference image to the force map, as described in eq.(6.7) and (6.8). c_1 and c_2 represent scaling on the x and y-axis, respectively.

The first three letters show relatively consistent distortion with positive angles ϕ , and downscaling on the y-axis (c_2). The relatively high fitting error (RMSE) of the letter M is explained by the narrow space between each leg of the letter being smaller than the size of the 5mm end-effector. The P and L show minor scaling on the y-axis. The letter L has the best fitting.

6.6 Discussion

This chapter evaluated the use of CDPMs for autonomous motions. Autonomy was explored based on the results of Chapter 5, in which forces at the tip of the instrument could be estimated and successfully used for haptic feedback in a palpation task. The current chapter is based on the premise that a surgical system that has the ability to sense end-effector forces can use this to safely perform autonomous surgical tasks. As eloquently put in [359]: *"Perhaps the most significant challenge of automating any clinical task is to be able to anticipate, detect, and respond to all possible failure modes"*.

The CDAQS' positional accuracy was evaluated during the performance of an autonomous tasks, showing high repeatability. The positional accuracy of the system during a line and circle task was

submillimetre; however, it also showed deviations from the original track. The positional accuracy of the system can be further improved by focusing on improvement of the calibration routine. The positional accuracy was robust against the effects of singularities in the workspace, only demonstrating clear deterioration of the autonomous task directly at the singularity plane.

The SIMPLE system was presented in this chapter as a system which can be used for autonomous tasks. SIMPLE uses a novel and patented approach (GB 1806943.5) for the deployment of a CDPM in the abdomen. The system uses direct cable pathways provided by microports to reduce friction and create a large workspace in the abdomen. The microports can be considered to be scarless due to their small needle-sized dimensions. Another innovation of the system is a mouldable scaffold used to position the motor units over the insufflated abdomen. The resulting system cannot only measure forces at the end-effector, but has a small footprint in the surgical theatre. A single robotic arm is used to hold and manipulate the transperitoneal arm. If further reduction of surgical footprint and costs is required, the robotic arm can be replaced by a static clamp to maintain the position of the transperitoneal arm. A method for assembly was shown in section 6.5.1, and an initial feasibility study showed that two cables could be connected within a minute. However, as formulated in [360]: *“Future surgical robots will be mounted on the operating table directly and will be reconfigurable with ease by nontechnical personnel.”*. The assembly of the system can be seen as adding complexity to the procedure, and additional attention should therefore be devoted to making this as simple as possible. Fast disassembly of the system is another important aspect for clinical use, as emergency situations may require conversion to open surgery. In such situations, either the cables can be cut or the abdominal motor units should fully release the cables by unwinding their spools. Releasing the cables enables removal of the microports, followed by the scaffold in its entirety and the transperitoneal arm. However, the time required for this disassembly is of vital importance and should receive specific attention in further developments.

SIMPLE was evaluated using an autonomous raster scanning task. The system was able to identify the hidden shapes in the silicone during a basic autonomous palpation task. The force estimation, however, underperformed in comparison to the CDAQS system in Chapter 5. One possible reason for this is error in the entry port positions. The entry points are found using markers placed on the outside of the scaffold, which are calculated to the remote centre of motion of the abdominal motor units. Small errors in the measurement of the port position will lead to an increased error in the port position due to the leverage effect. Such errors in the internal parameters of the system will also affect the positional accuracy and lead to the deformation seen in the raster scan images. However, the deformation of this error is not consistent for all images, hinting that calibration also plays a role. The measurement of port positions can be improved in future work by

looking at techniques developed for stereotactic surgery, such as in orthopaedics and neurosurgery. Another aspect that can be a source of error on both the autonomous task and the force estimation is friction. While we assume that the friction is low, it may still have a substantial effect on the force measurements and end-effector position. Experimental validation of the friction is required to understand its contribution to errors with regard to both aspects. Ways of reducing friction include more accurate manufacturing methods and the embedding of friction compensation in the control routine. Friction compensation can be realized using the same methods as mentioned in the discussion of Chapter 5, such as the use of friction models [361] [324].

The current system is still in a very early stage and can be improved considerably in future developments. The transperitoneal arm should receive additional attention. The diameter (now 25mm) can be reduced by replacing the endoscope with a camera integrated into the shaft. The shaft of the current prototype is made out of 3D-printed plastic material and can be further reduced in diameter by using stronger materials and more robust manufacturing methods. The scaffold of the SIMPLE system showed an initial mouldable proof of concept, and the optimal material for surgery should be further evaluated. Part of this evaluation should consider the patients' body position. The supine position¹⁶ is commonly used in laparoscopic surgery; however, for several surgeries, the patient is positioned differently to let gravity retract the bowel and thus provide workspace. For example, the Trendelenburg position is used for lower abdominal surgery; the bed is placed at an angle so that the head of the patient is lower than the legs, causing the intestines to move downwards, providing workspace for surgery. Similarly, the reverse Trendelenburg position is used for upper abdominal surgery. To provide workspace and retraction of the intestines in laparoscopic surgery on the kidneys, the patient is typically laid on the side opposite to the kidney undergoing surgery. Another approach specific to kidney surgery is the retroperitoneal approach, in which laparoscopic instruments are inserted from the back. It should also be noted that the position of the patient also has an effect on the *total* intra-abdominal workspace provided by the insufflation [362]. The SIMPLE system is expected to function well in these situations, as the scaffold is body-mounted and mouldable, meaning that it can be adapted to the specific requirements of each surgery. The workspace and port placements of the abdominal motor units for the supine position are analysed in Chapter 7.

¹⁶ In the supine position the patient lays on his/her back and the surgical bed is kept horizontal.

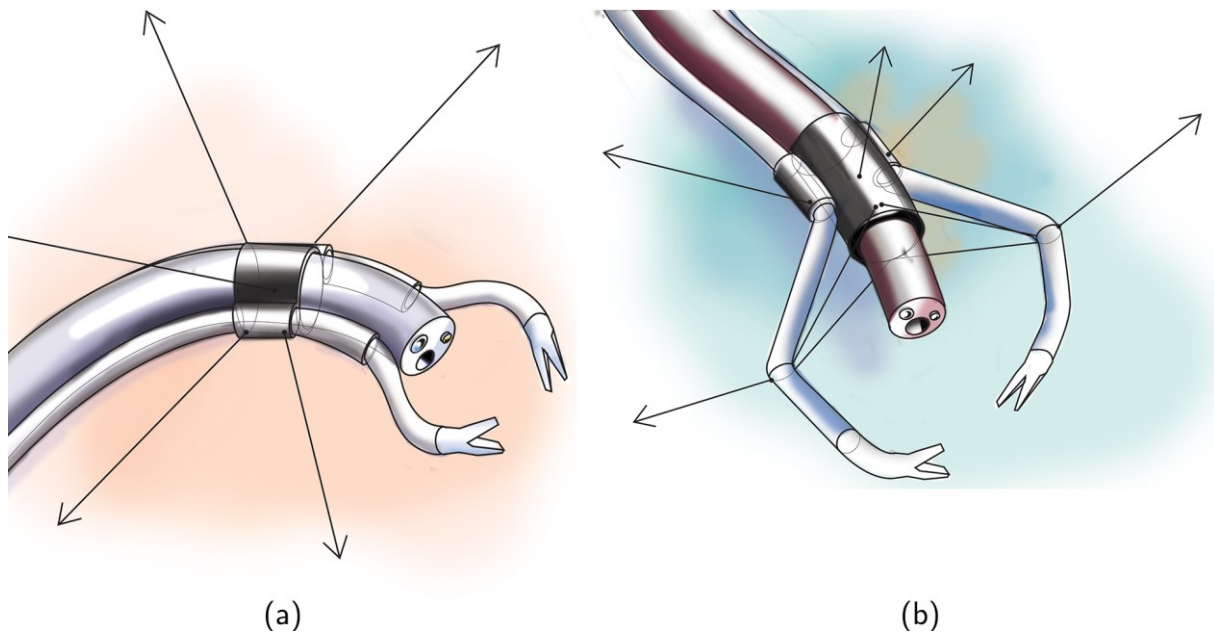


Figure 6.25 – Possible configurations for using SIMPLE in NOTES: (a) Endoscope stabilisation. (b) A combination of endoscope stabilisation with additional cable-driven elbow joints to provide high forces and sufficient stiffness during manipulation.

The SIMPLE system does not have to be controlled autonomously; furthermore, as demonstrated in Chapter 5, CDPMs can be used for manual palpation tasks, and may contribute to the safer performance of surgical tasks by granting the surgeon improved contextual awareness during surgery. As discussed in Chapter 3, many single-port systems allow still limited payloads and, based on the results from the ESD CYCLOPS in Chapter 4, it is safe to expect that the SIMPLE system has a high payload capacity as well. The high payloads will be an advantage compared to other systems for performing single-port surgery. SIMPLE can also be used in other locations than the abdomen. A possible extension would be thoracoscopic surgery in which a lung is deflated to provide workspace for the instruments. In addition to single-port surgery, the SIMPLE approach can potentially also be used in combination with other access methods seen in MIS. The transvaginal NOTES approach (vNOTES) is, in many cases, performed using straight and rigid laparoscopic instruments. Like the rigid instruments used in vNOTES, the current rigid transperitoneal arm can be used in transvaginal approaches. For other NOTES procedures that require flexible endoscopes (e.g. transgastric), the rigid transperitoneal arm cannot be used. A flexible version of the transperitoneal arm would introduce additional cable friction and would likely not provide enough rigidity to constitute a stable base against forces in the cables. However, the transperitoneal arm is not necessarily required in all cases, and a system that only uses abdominal motor units is still an option for NOTES. One important technical challenge encountered in NOTES is endoscope stability [20] [289]. A CDPM can be used to stabilize and control the position of the endoscope (Figure 6.25a).

Another challenge for flexible (and rigid single-port) systems, as discussed in Chapter 3, is the low stiffness of elbow joints. Cables can be used to provide a stiff base for elbow joints from which surgery can be performed (Figure 6.25b).

An alternative approach is to use a cable-suspended CDPM specifically for tissue manipulation (Figure 6.26). An overtube is not necessarily required in this case, and a clip can be used as the end-effector. Such a device could, for instance, be used for gallbladder manipulation during cholecystectomies. Once the clip is attached to tissue, the angle of the clip becomes trivial and therefore a two- or three-cable suspended CDPM would provide substantial manoeuvrability of the tissue. Another

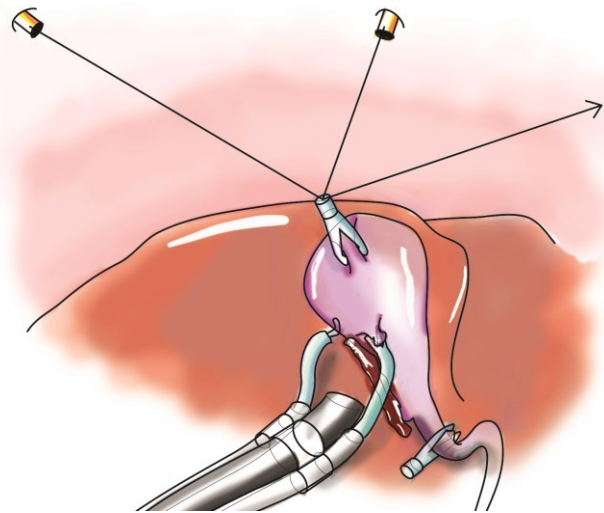


Figure 6.26 – An example of a cable-suspended CDPM used for tissue retraction.

application for a suspended CDPM for tissue retraction could be in gastric ESD. As seen in Chapter 4 (Figure 4.2), a hybrid percutaneous technique already exists for a tissue retraction in the stomach and in this context a suspended CDPM would provide improved control for retraction of the mucosa. The bladder is another hollow organ which can be accessed with a percutaneous approach, as used for drainage (e.g. for percutaneous suprapubic cystostomy). Similarly, in neurosurgery, multiple thin electrodes are used for deep brain stimulation (DBS) and stereoelectroencephalography (SEEG), and the same concept can be used when the thin probes are replaced by microports to provide access for cables into the (lateral) ventricles. However, there is no evidence on the potential clinical advantages of this approach for bladder or neurosurgery, as further investigations are required.

In conclusion, this chapter evaluated the use of CDPMs for autonomous tasks and introduced the SIMPLE system. SIMPLE's novel access method can be used to provide haptic feedback, instrument dexterity and sufficiently high payloads in single-port surgery. The fact that the approach requires cable assembly and disassembly adds complexity, and this needs to be simplified in future developments. The access method can potentially be used in other MIS applications, which needs to be explored further.

Chapter 7

Workspace optimisation for surgical applications

The prototypes discussed in the previous chapters – the ESD CYCLOPS, CDAQS and SIMPLE – illustrate the workspace versatility that can be achieved by changing the cable configurations. An early-stage form of workspace optimization was demonstrated before with the ESD CYCLOPS (section 4.3), which was based on piecewise changing of a single parameter. However, by taking all parameters simultaneously into account an optimal solution is found. Similarly, the SIMPLE system was designed for use within the abdominal cavity, and can potentially be used for a wide range of applications targeting different organs depending on the specific procedure. The workspace of the instruments was not explored in earlier chapters, as it is highly dependent on the position of the abdominal motor units and the transperitoneal arm. In this chapter, patient-specific data are used to demonstrate how the system can be customised to specific requirements. The use of optimization algorithms is also discussed, to make systems procedure- or patient-specific, using the ESD CYCLOPS and SIMPLE as case studies.

7.1 Optimization Algorithm

As mentioned in earlier chapters, the workspace of a CDPM is directly related to the configuration of the workspace. However, no algebraic description for this relation exists, and thus the workspace of a configuration is found through a discretized search over the possible workspace

of the end-effector. The absence of an algebraic description is also reflected in the objective function of an optimization routine, leaving out many gradient-based optimization methods. Additionally, to assess the feasibility of a queried pose, the optimal tension distribution must be calculated, making each iteration computationally expensive. Additionally, the workspaces of CDPMs are not necessarily convex (e.g [56]), and thus any optimization method must deal with non-convexity and discontinuities.

The particle swarm optimization (PSO) method is a derivative-free method that can be used for high dimensional global optimization problems [363]. PSO uses a population of particles that mimic the swarm behaviour seen in animals and insects. For each iteration, each particle moves along the n-dimensional problem space at a given velocity which is determined by the particle's own best position, as well as the overall best position in the swarm. PSO has been used for multiple optimization routines in robotics, including workspace optimization for CDPMs [364][365]. In this chapter we therefore use a hybrid PSO [366] combined with a particle filter optimization (PFO) [367] to solve the optimization problem (Appendix A.8). The hybrid PSO is a conventional PSO adapted to have linear upper and lower bounds.

The initial optimization framework for the ESD CYCLOPS was developed by MSc student, Yi Wei Pang who was supervised by us during his Masters thesis [368] and is based on the C++ *simpsolib* library developed by Tomás Arredondo¹⁷. The framework is used for the optimization of the ESD CYCLOPS for a theoretical and simulated task space. The optimization algorithm was developed further and implemented for optimization of the SIMPLE system. The novelty of the method discussed in this chapter lies in the use of procedures-specific and patient-specific data for the optimization of CDPMs.

7.2 Case study: procedure-specific optimization of the ESD CYCLOPS

The algorithm was used to find configurations of the ESD CYCLOPS with an improved workspace for performing ESD. The objective function was defined as the maximization of the feasible points of a desired task space within the systems workspace. The design vector, containing the parameters optimized for, was defined as such (Figure 7.1):

$$V_{dv} = [\vec{\theta}, \vec{p_v}, \vec{b_v}, L_{tool}, \xi_y, \xi_z, a_L]$$

¹⁷ Tomas V. Arredondo is an Assistant Professor at the Universidad Tecnica Federico Santa Maria, Chile. *Simpsolib* v1.7.1. is available at <http://profesores.elo.utfsm.cl/~tarredondo/code/simgalib/1-7-1/>

in which $\vec{\theta}$ represents the row vector of the cross-sectional angle of the cable ($\theta = [\theta_1, \dots, \theta_n]$). \vec{p}_v represents the x position along the length of the overtube, $\mathbb{R}^{n \times 1}$. \vec{b}_v represent the x position along the length of the overtube. In order to minimize the dimensions of the design vector, the front and back cables are clustered in their x position, i.e. $\vec{b}_v = [x_{front} \ x_{back}]$. The scaffold cross-section is defined as an ellipse, consisting of a circle for each instrument. L_{tool} is the length of the overtube. When optimizing for a curvature, ξ_y, ξ_z and a_L are used as the angles and bending point along the overtube, respectively.

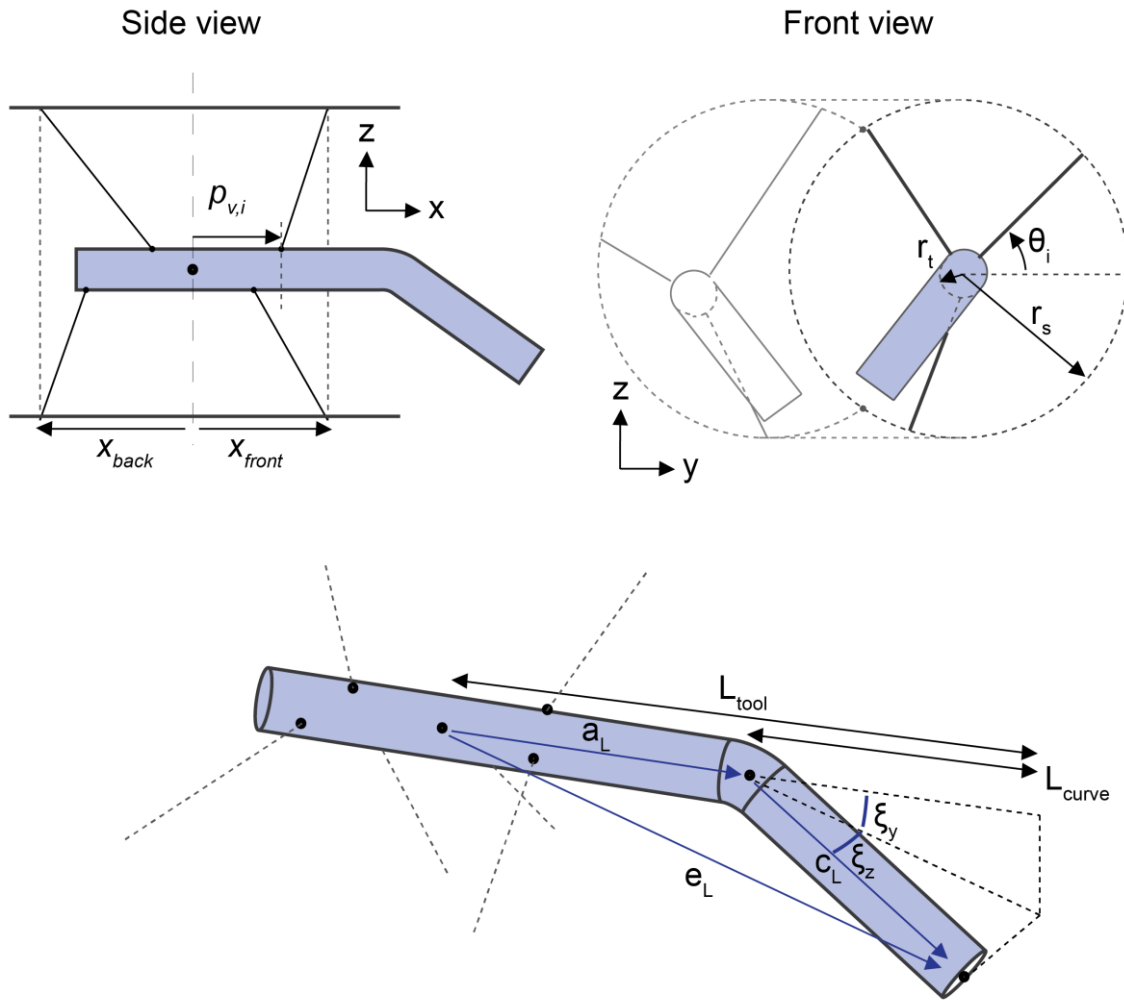


Figure 7.1 – The definition of the dimensions for the design vector.

The size of the design vector is $15 + 3(n - 6) + 3c$, where n is the number of cables. The value of $c \in \{0,1\}$ represents the presence of a curvature in the tool. For a 6-cable ESD CYCLOPS, with a single curvature, the total size of the design vector is therefore 18. The objective function is shown in Figure 7.2. The objective function is evaluated for each individual particle in the swarm population for a single iteration of the PSO algorithm.

Two conditions are included in the objective function to prevent specific configurations. The crossing of cables between any cable i and any other cable j can occur when the x-coordinate of the attachment point is $p_{i,x} < p_{j,x}$ while the entry points is $b_{i,x} > b_{j,x}$. This definition does not mean that cable interference necessarily occurs, however, using this condition allows for the exclusion of cable configurations in which interference is more likely. A second condition only allows systems with a larger distance between the cable entry points than the largest distance between the cable attachment points (i.e. the cables are visually configured in an 'X' shape). The choice was made to include these configurations, as they are known to generally have a high stability. If the conditions are satisfied, the objective function returns the tension factor of the workspace, which is

always positive. If the conditions are not satisfied, a negative number is returned. Finding a global optimum cannot be guaranteed for non-convex optimization problems, leading to local optima to be found. Therefore, the algorithm was repeated in multiple runs, of which the highest value was selected as optimum.

7.2.1 Workspace optimization using a theoretical task space

The system was optimized using a theoretical task space. In this theoretical task, an oblate (or flat) spheroidal task space was defined starting 5mm in front of the bottom part of the scaffold. The diameter in the XY plane represents the size of the lesion, whereas the height of the workspace along the Z-axis represents the lifting of the instruments. The optimization was run for lesions of $d_l = [20,30,40]mm$ diameter. The height of the lesion set at 15mm for all lesion dimensions. For the grasper, an external force of -2.26N was used to simulate the force requirements at the tip of the instrument for the provision of tissue traction [300]. The population was set to 500 particles, and 30 PSO iterations. The maximum value was selected after 5 runs.

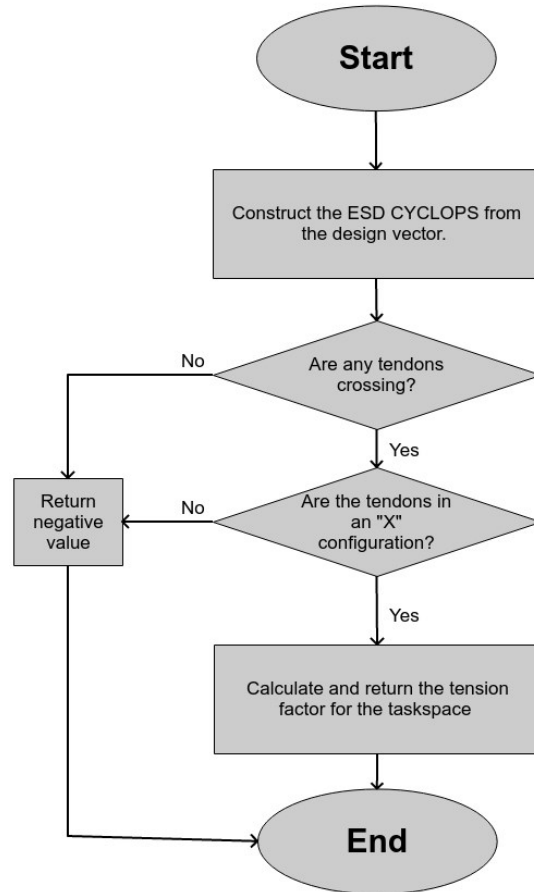
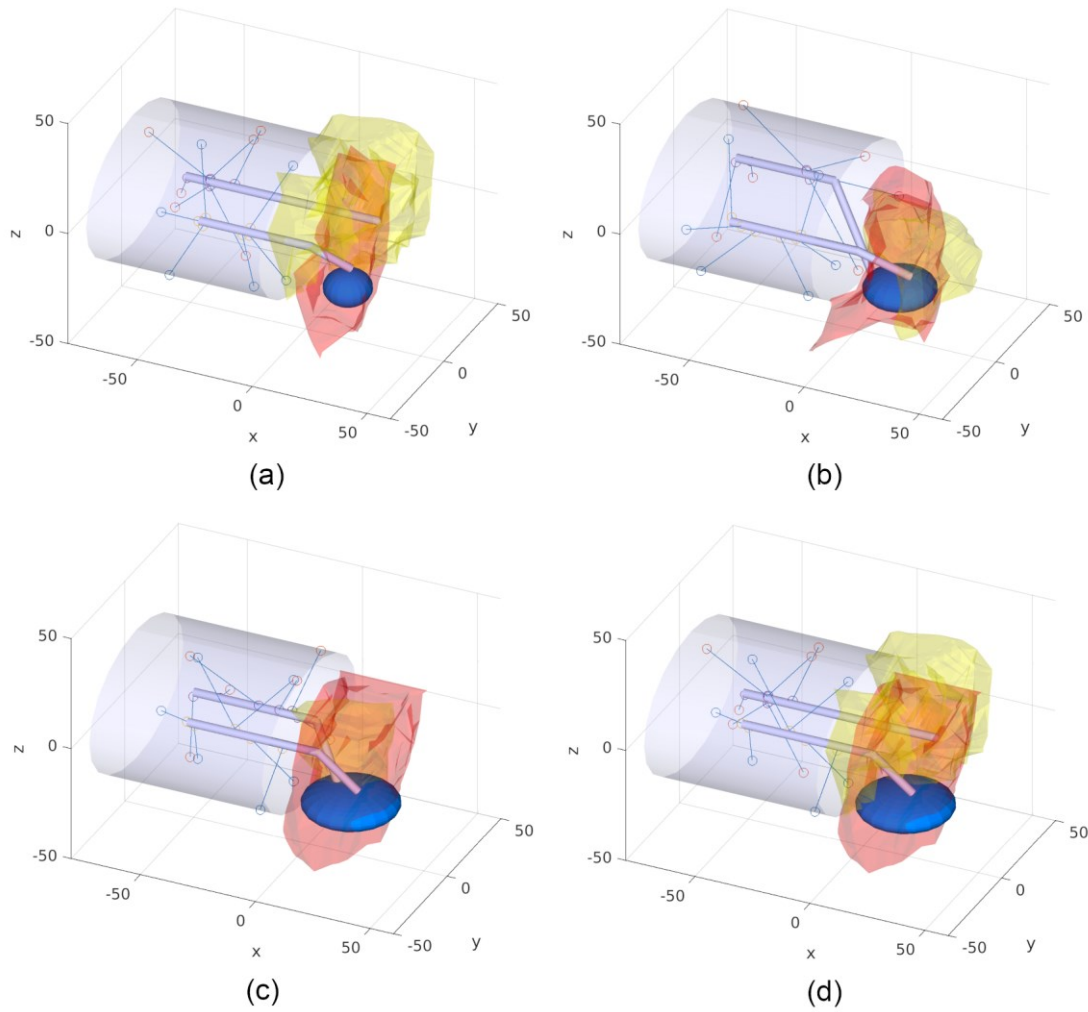


Figure 7.2 – The objective function used for the optimization of the ESD CYCLOPS.



*Figure 7.3 – The optimized systems with the theoretical ESD task space shown in blue. The workspace of the left and right instruments are yellow and red, respectively. In all cases, an outer circumference equal to a 70mm diameter colon was used. All dimensions in the figures are in millimetres. The percentage of the task space reached and the workspace volumes are shown in Table 7.1. **(a)**, **(b)** and **(c)** are the systems found for optimization for a 20mm, 30mm, and 40mm lesion. **(d)** is the combined system using the left instrument of configuration (a) and the right instrument of configuration (c).*

The results are shown in Figure 7.3 and Table 7.1. The results for the configuration of the ESD CYCLOPS as used in Chapter 4 were calculated for the same theoretical task space and used for comparison with the optimized system. The 4th column combines the solution with the largest workspace volume of the left instrument and the right instrument, which were found for the optimization of the 20mm and 40mm lesion, respectively. The optimization results show an improvement in terms of percentage of task space and total workspace and instrument overlap when compared to the ESD CYCLOPS. The diathermy instrument shows the best results, with 100% of the lesion reached for 20mm lesions, and up to 72% for the 40mm lesion. The combined system shows the largest total and overlapping workspace. The system could also reach a large portion of the 40mm simulated lesion.

	Lesion size	Left Instrument (Grasper)		Right Instrument (Diathermy)		Combined Workspace	
		Task space [%]	Workspace Volume	Task space [%]	Workspace Volume	Overlap	Total
Optimized	20mm	92.3%	63.6 cm ³	100%	27.6 cm ³	9.68 cm ³	81.5 cm ³
	30mm	81.2%	21.4 cm ³	90.3%	22.7 cm ³	6.19 cm ³	37.9 cm ³
	40mm	13.6%	13.51 cm ³	73.0%	47.9 cm ³	7.26 cm ³	54.2 cm ³
Combined	40mm	64.0%	63.6 cm ³	73.0%	47.9 cm ³	17.8 cm ³	93.7 cm ³
ESD CYCLOPS	20mm	49.4%	10.3 cm ³	49.4%	10.3 cm ³	4.0 cm ³	16.5 cm ³

Table 7.1 – The optimized systems for 20,30 and 40mm lesions. As a comparison, the 20mm lesion is included of the ESD CYCLOPS, as configured in chapter 4. For each instrument, the combined system uses the configuration from the optimization which has the largest workspace volume, and therefore uses the left instrument configuration found for 20mm optimization and the right instrument configuration for 40mm optimization.

It is important to note that, in the combined solution, the cable configurations for both instruments lead to a large workspace. The left instrument (Figure 7.4a) uses a centralized point on the scaffold that is actuated by 4 cables. Characteristic of the configuration is that both front and back cables are connected at this point along the shaft. This is different than the classical CYCLOPS design, combining only the front and back cables at separate points along the x axis of the overtube. The two other cables are used to provide rotation around the y axis (pitch angle). The cables are configured to be very suitable for the provision of torsion around the y axis to counter downwards forces at the instrument tip, which is a result of the inclusion of this force at the instrument tip. However, looking at the configuration, it is evident that the system cannot exert forces in the opposite direction, which may become a problem if the surgeon wants to exert a downward force on the tissue. For low force requirements in the downward direction, moving the attachment point of the top left cable further left along the overtube may solve this problem.

One way to solve such solutions from an optimization perspective is by defining both a zero wrench task space and a wrench-feasible workspace, which are weighted to provide the final result of the objective function. Note that this will result in additional computational time, but this becomes practical for task spaces with a small set of datapoints, such as the 441 points used during optimization. Further research should be dedicated to establishing the best method to combine the force-closure and wrench-feasible workspace for optimization.

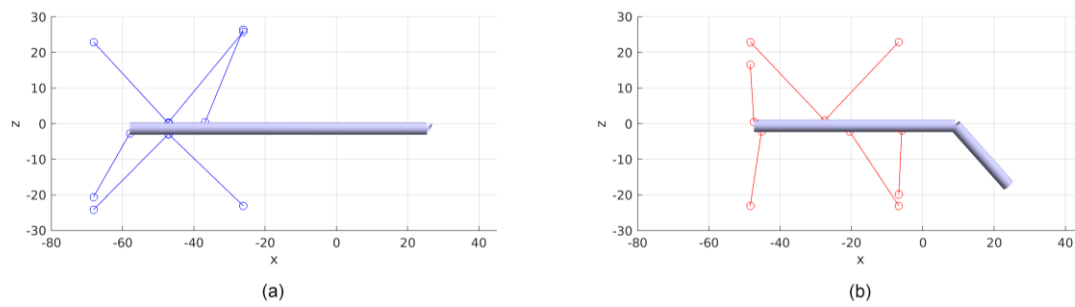


Figure 7.4 – Side view of the **(a)** left and **(b)** right cable configurations of the combined optimized system (Figure 7.3d). All dimensions are in millimetres.

7.2.2 Workspace optimization using a surgical task space

In order to further understand the task space requirements for ESD, the task space data were recorded during a simulated procedure in which an endoscopist performed an ESD on animal tissue. The recorded data were then used in the optimization routine. A task space acquired during a simulated ESD procedure is a better representation of the real scenario and therefore leads to better workspace and force requirements. An ESD CYCLOPS which is optimized with these requirements will likely be more intuitive to control and more suitable for performing ESD

7.2.2.1 Collecting the task space

A rig, shown in Figure 7.5, was developed to track the task space used for the optimization problem. The rig was used to record the position and the forces of an ESD task performed in an open surgical fashion in which an endoscope is used for visualisation. The open surgical setting was chosen because it reflects the ideal situation for control of the instruments in terms of dexterity and efficiency of movements. To keep the task relevant for the ESD CYCLOPS, the master side including the visualisation, haptic handles and foot pedal were maintained.

The rig used an optical tracking system with 4 cameras (Optitrack Prime 13, NaturalPoint, Inc., USA) to track the 6DoF positions of two modified instruments within the aluminium structure. The instruments were customized to mimic both the overtube and the haptic controller handles of the ESD CYCLOPS (Figure 7.6). The same endoscopic grasper (FG-44NR-1, Olympus, Japan) and diathermy instruments (DualKnife KD-650L, Olympus, Japan) were placed in the left and right handle, respectively. The left instrument, being the tissue grasper, had a 6DoF loadcell embedded in the handle to measure forces during ESD. The button of the left instrument was used to open and close the grasper, which was actuated by the motor unit (Figure 7.7) and the electrocautery was activated using a foot pedal connected to the Erbe system (VIO 200D, Erbe Elektromedizin GmbH, Germany). This is exactly the same as the ESD CYCLOPS.

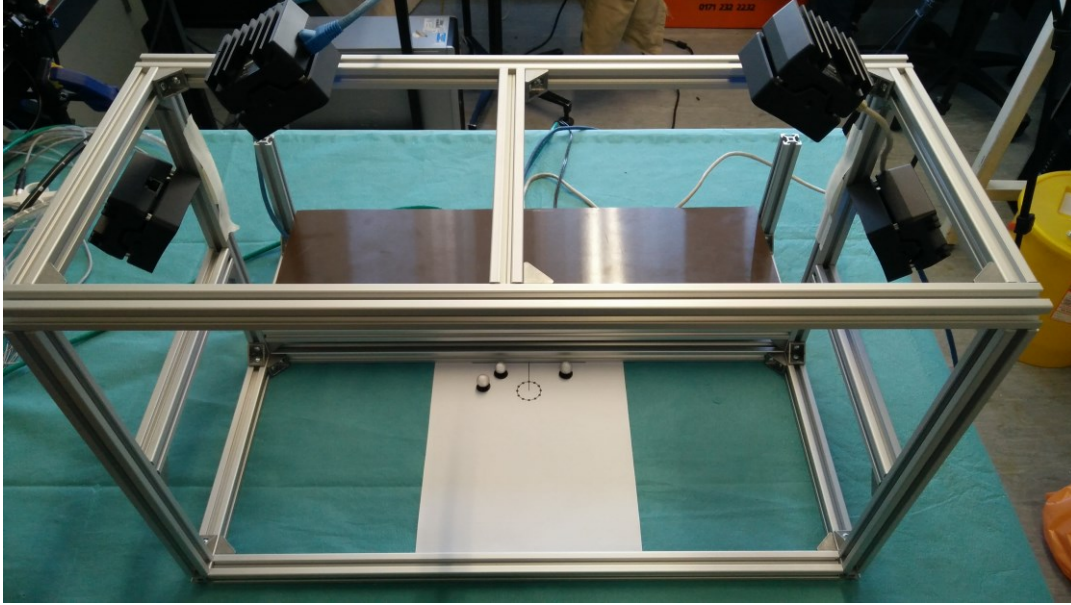


Figure 7.5 – The aluminium rig used for the collection of the task space. A dummy task space is shown in the figure; this was used for early validation of the algorithm before proceeding to the data collection during an ESD with ex vivo tissue.

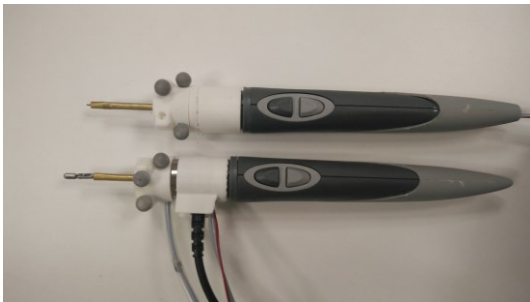


Figure 7.6 – The modified instruments used for data collection. The top instrument was used for diathermy cutting, and the bottom instrument for grasping.

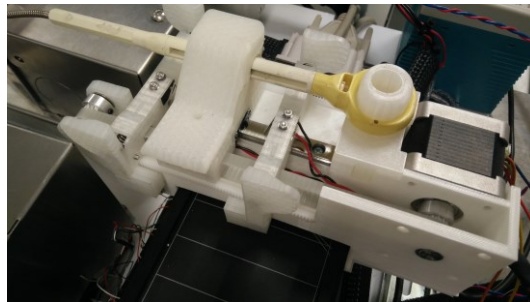


Figure 7.7 – The motor unit used for the CYCLOPS system was used for actuation of the grasper.

7.2.2.2 Recorded Data

An endoscopist trained in ESD used the rig to perform a simulated procedure on ex vivo chicken thigh with skin (Figure 7.8). A 20mm diameter lesion was drawn with a pen on the skin, after which the endoscopist performed the task according to the conventional approach: marking of the lesion with the diathermy instrument, followed by circumferential cutting and submucosal dissection of the lesion (Figure 4.1b). The pointcloud of the tip's 3D positions during the procedure is shown in Figure 7.10. The yaw and pitch angles and the forces are shown in Figure 7.11 and Figure 7.9, respectively.

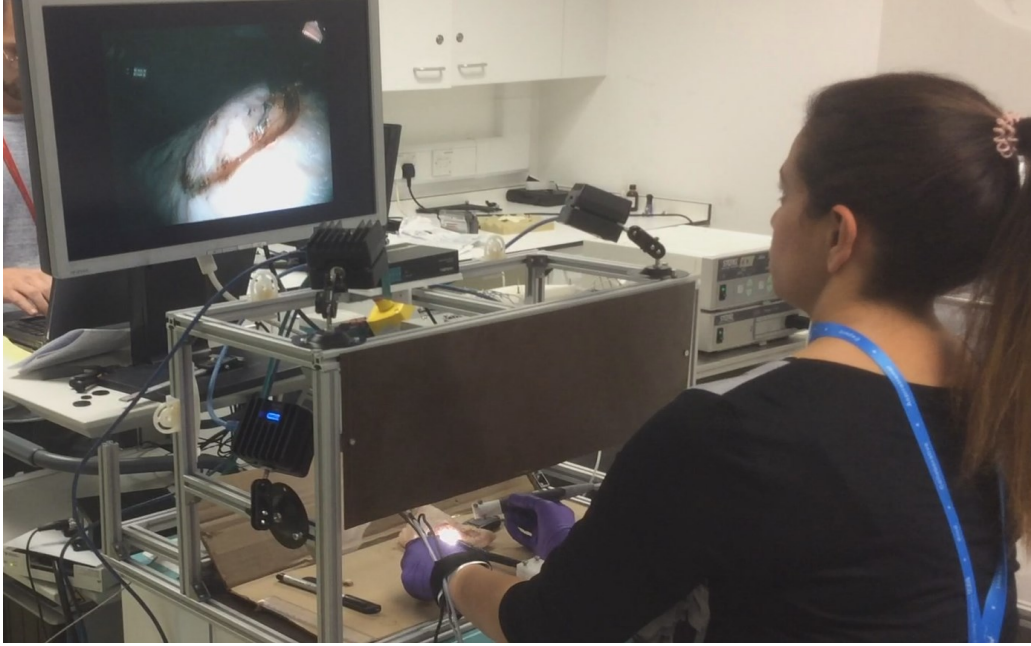


Figure 7.8 – The data collection of the ESD task on ex vivo chicken tissue.

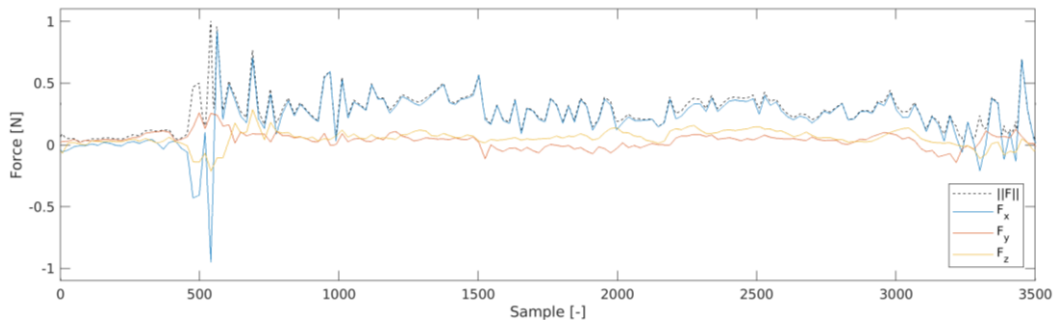


Figure 7.9 – The forces at the tip of the grasper (left instrument) along the x, y, z axes.

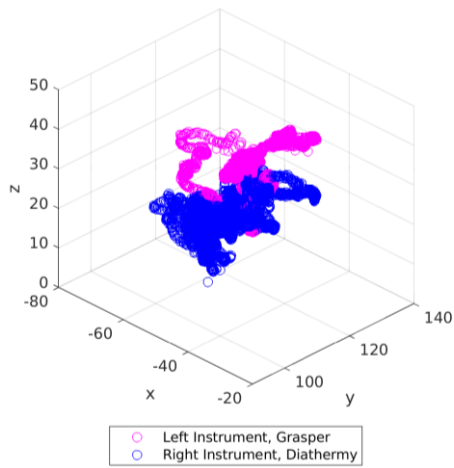


Figure 7.10 – The 3D pointcloud of each of the instruments during the simulated ESD task. All dimensions are in millimetre.

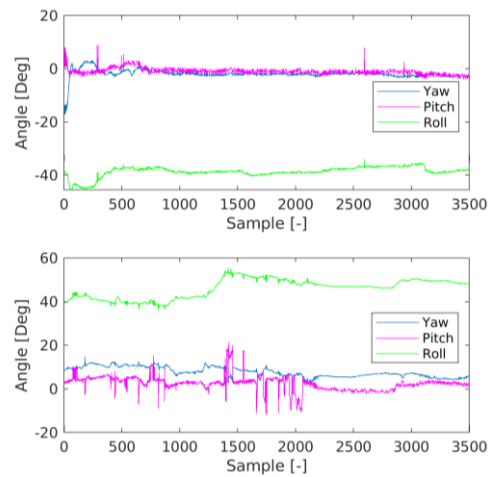


Figure 7.11 – The yaw, pitch and roll of the instruments (**top:** left instrument, **bottom:** right instrument).

7.2.2.3 Optimization results

The left and right instruments were optimized using the positions, angles and forces found that are shown in previous section. Figure 7.12 shows the optimized task space for overtubes with both a

single curvature and a double curvature. The volume of the task-scape and the percentage of the task space within the system workspace are shown in Table 7.2.

Colon Diameter	Tool Curvature	Left instrument		Right Instrument	
		Task space [%]	Workspace Volume	Task space [%]	Workspace Volume
70mm	Single	100%	2.59 cm ³	94.13%	9.44 cm ³
	Double	100%	5.28 cm ³	96.52%	4.65 cm ³
60mm	Double	89.7%	7.34 cm ³	98.84%	7.51 cm ³

Table 7.2 – The size of the workspace and the percentage of the task space for the optimized configurations shown in Figure 7.12.

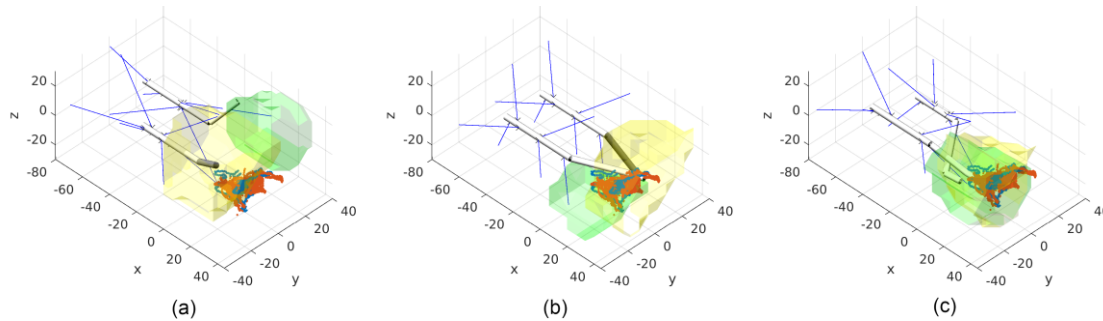


Figure 7.12 – The systems optimized using the recorded task space. The workspaces without external forces of the left and right instrument are indicated in green and yellow, respectively. The percentages of the task space and the workspace volume are shown in Table 7.2. All dimensions are in millimetres. **(a)** The configuration found for single-curved instruments and a scaffold designed for a 70mm diameter colon. **(b)** The configuration found for a 70mm diameter colon with double-curved instruments. **(c)** The double curvature optimized configuration for a 60mm diameter colon.

7.2.3 Discussion ESD CYCLOPS optimization

The optimization of the ESD CYCLOPS was performed using a theoretical task space and using a second task space which was recorded during a simulated ESD procedure. In comparison to the ESD CYCLOPS developed in Chapter 4, the theoretical task space showed improvements in terms of percentage of feasible points of the task, instrument overlap and total workspace. The optimization algorithm is still prone to local optima, as we showed by combining two solutions of the instrument configurations with the largest workspace. The combined system showed that an increased portion of the large 40mm lesion could be reached.

When the workspace of the ESD CYCLOPS is optimized using the recorded task space, the system was able to reach the majority of the points in the task space. The system that was optimized using a single curvature overtubes shows an upward-angled tip section, which contrasts with the downward angles which are used in the ESD CYCLOPS and were found for the systems optimized to the theoretical task space. Optimization of the ESD CYCLOPS using a recorded task space may lead to a more intuitive control of the system for ESD procedures due to the fact that it is optimized to a task space based on unconstrained hand motions. However, it should also be noted that using a single

dataset for optimization can lead to overfitting of the data. Overfitting to specific force requirements is illustrated with the single curvature configuration of the left instrument placed at an arbitrary point along the task space (Figure 7.13). As the cables can only pull, the position of the instrument can only be in equilibrium with an external force. Such a system will not have the flexibility to cope with the large variety of motions required to perform ESD on different lesion sizes and positions. The left instrument of the combined system, discussed above in relation to Figure 7.4, will also function only with an external force at the tip. The zero-wrench and wrench-feasible workspace can be combined to prevent overfitting of the system to a specific external force. For optimization the combination of both workspaces need to be expressed in a single numerical value, which requires the weighing of both the zero-wrench and wrench-feasible workspace. The best trade-off between both workspaces is open to further investigation.

Overfitting of the system's configuration to the recorded dataset can be further prevented by collecting a larger dataset of simulated ESD procedures that is representative for the sizes and different types of lesions found in the population. Furthermore, the data should be collected from procedures performed by multiple users in order to account for the variety of motions and techniques used by endoscopists. An alternative approach is to collect endoscopist-specific datasets for the optimization of the system's workspace,

leading to a tailored system in which instrument handling is likely even more intuitive than in a system optimized using an inter-endoscopist dataset. Such endoscopist-specific optimization will require a scaffold which can be adjusted easily to specific needs, which may be possible using a manufacturing technique for single-use inflatable scaffolds [292]. Another important consideration is whether realising endoscopist-specific systems is desirable from the perspective of standardized surgical training and potential legal and regulatory matters.

Nevertheless, the method presented in this chapter has been proven feasible for the collection of a task space dataset during a simulated surgical procedure and the optimization of the system to this dataset. Further developments should include a stability analysis and evaluation of the intuitiveness of the configurations found. As intuitive control is based on many factors, the most appropriate method is the rapid prototyping of a physical model of the cable configuration and

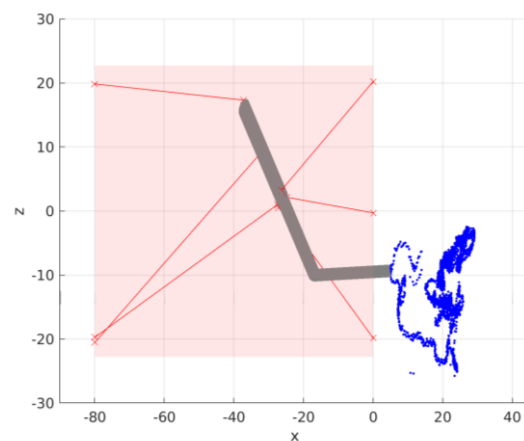


Figure 7.13 – The left instrument (grasper) of the single curvature configuration placed at a specific position of the recorded task space.

coupling of the system to the current motor units. It should be noted that for the eventual implementation of an optimized configuration in the ESD CYCLOPS prototype, any limitations caused by the scaffold structure itself should be taken into account. For example, the current scaffold uses rigid links that only permit the placement of cable entry points at specific positions on these links. An inflatable scaffold structure is less limited to specific positions at which cable entry points can be placed; its design offers more flexibility, making it easier to place the cables in an optimal configuration. This is yet another advantage of an inflatable system. The physical limitations of such a scaffold should also be considered in the optimization process, once a more final scaffold design has been settled on.

Another consideration is the overtube design; ideally, the overtube would be packaged within the undeployed scaffold for the introduction and navigation of the endoscope in the GI tract. In this light, the double curvature overtube may prove to be disadvantageous for compact packaging into a small undeployed scaffold. However, a mechanism can be used to introduce the curvature in the overtube after the scaffold is deployed, thereby allowing the overtube to be compactly packaged in the undeployed scaffold. The benefit of a double curvature is that it most likely enables further reduction of the scaffold diameter. Another possible benefit, looking back at the bowel perforation that occurred in the *in vivo* studies discussed in Chapter 4, is that the instrument angle is less acute in relation to the tissue surface.

The current optimization process uses fixed scaffold dimensions and size. However, the optimization routine could be developed further to enable variation in scaffold size and shape. Another way to expand optimisation possibilities would be to add an articulated link at the end of the overtube, as mentioned in the discussion of Chapter 4. Despite that further improvements for the optimization method are possible, the results shows that a next-generation ESD CYCLOPS can be developed with a larger workspace and optimal design.

7.3 Case Study: Patient-specific optimization of the SIMPLE system

A second case study was used to optimize the SIMPLE system. The use of microports and an articulated transperitoneal arm give this system a unique level of reconfigurability. Like in laparoscopic surgery, port placement determines the workspace of the instruments, and should be configured for the specific needs of the procedure. Surgeries are often preceded by the collection of CT (or MRI) images of the patient for diagnosis and pre-operative planning. These data can be used as a basis to create patient- and procedure-specific SIMPLE systems. However, the SIMPLE system is mounted *after* the abdominal cavity is insufflated, while CT-scans of the abdomen are taken without

any insufflation. This discrepancy can be overcome by using computer models that are based on pre-operative images to simulate the shape and size of the abdomen after insufflation.

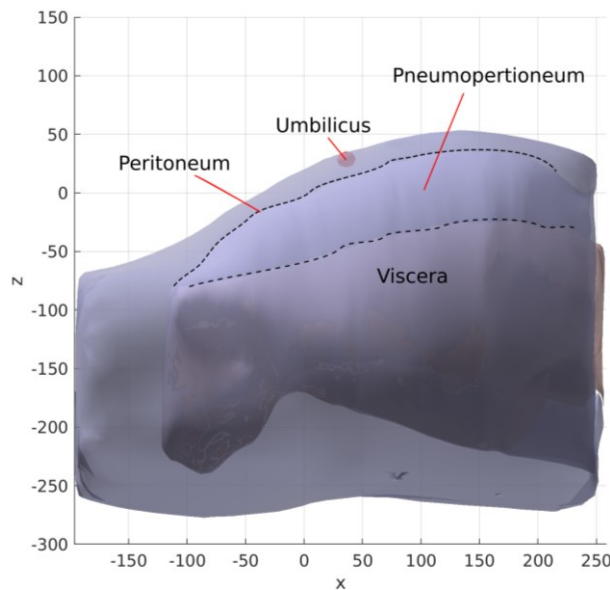


Figure 7.14 – The STL files obtained from the pneumoperitoneal simulation study.

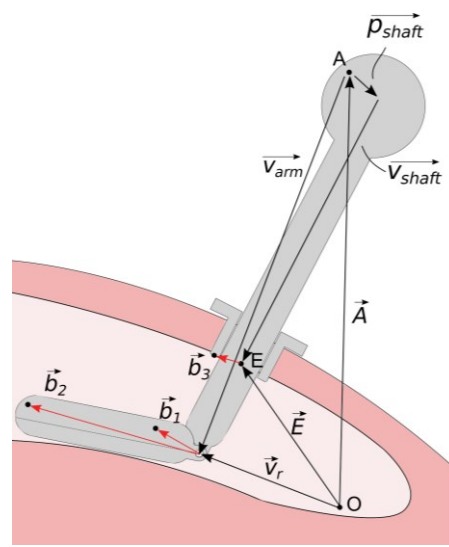


Figure 7.15 – Schematics used for the calculation of the cable entry points on the transperitoneal arm.

One development at the Department of Surgery and Cancer has focused on providing a fast and accurate simulation model for pre- and intra-operative planning. Part of this simulation framework includes the simulation of a pneumoperitoneum for the patient in a supine position [358]. The CT or MRI images of the patient are semi-autonomously segmented to 3D models and inserted into the simulation framework. The researchers have validated the simulation with an *in vivo* porcine study, in which the simulation was compared to the pneumoperitoneum obtained via CT scans of the pig. The difference between the simulated insufflation and the ground-truth measurement at 16mmHg pressure showed a mean Hausdorff distance of 5.3mm. The Hausdorff distance represents the distance between each point in one dataset and the nearest point in the other dataset. A feasibility study with the simulation of the pneumoperitoneum was performed on a human, in which specific landmarks on the outer abdominal wall were measured after pneumoperitoneum and compared to the simulated pneumoperitoneum. The approach was demonstrated to be feasible, and a larger study should be performed to accurately evaluate its feasibility across multiple patients. The 3D model of the insufflated pneumoperitoneum for the patient scan is shown in Figure 7.14, and was used for the optimization of the SIMPLE system. Similar accuracies were found in another study on the modelling of the pneumoperitoneum [369][370].

7.3.1 Design vector and Objective function

The schematics and dimensions used for the optimization the SIMPLE system are shown in Figure 7.15. The cable entry points of the system are positioned on the parametrized abdominal surface $z = P_{ab}(x, y)$, and we can thus fully determine the 3D coordinates of the microports based on $b_{x,i}$ and $b_{y,i}$, i.e. $i \in \{4,5,6\}$:

$$b_{z,i} = P_{ab}(b_{x,i}, b_{y,i}) \quad (7.1)$$

With regard to the entry points on the transperitoneal arm ($i \in \{1,2,3\}$), the angles α, β and γ determine the orientation of the arm, while θ represents the angle between the main shaft and the articulated section of the shaft (see section 6.3). The transperitoneal arm is constrained by the entry point in the body \vec{E} and the viscera defined by polynomial $z = P_{vis}(x, y)$. The attachment point \vec{A} of the transperitoneal arm to the robotic arm (or static clamp) holding the SIMPLE system can be found by:

$$\vec{A} = -R(\alpha, \beta, \gamma) + \begin{bmatrix} 0 \\ 0 \\ c_2 \end{bmatrix} \vec{E} - R(\alpha, \beta, \gamma) P_{shaft}, \quad (7.2)$$

in which c_2 represents the portion of the shaft of the transperitoneal arm along the vector v_{shaft} which is outside the body. The rotation point of the main shaft to the articulated shaft, V_r , depends on the position of the local coordinate V_{arm} and the position \vec{A} :

$$V_r = \vec{A} + R(\alpha, \beta, \gamma) V_{arm}, \quad (7.3)$$

and is constrained by a position along the surface of the viscera:

$$V_{r,z} = h_{offset} + P_{vis}(V_{r,x}, V_{r,y}), \quad (7.4)$$

The offset h_{offset} is determined by the distance from the outside of the shaft to the pivot point V_r . The equations (7.2)-(7.4) can be solved using the linear least-squares method to obtain the unknowns \vec{A} , c_2 and V_r (Appendix A.9), and hence the entry points inside the body can be found as a function of α, β, γ and θ . Having determined the 3D coordinates of V_r , the cable entry points B_i for $i = 1,2,3$, can be calculated:

$$\begin{aligned} b_{i,g} &= V_r + R(\alpha, \beta, \gamma) R_\theta b_{i,l} \quad i = 1,2 \\ b_{3,g} &= \vec{E} + R(\alpha, \beta, \gamma) b_{3,l} \end{aligned} \quad (7.5)$$

In which R_θ is the rotation matrix around the local Y axis: $R_\theta = R(0, \theta, 0)$. The equations (7.1)-(7.5) show that all entry points can be calculated based on the angles α, β, γ and θ and six coordinates $(b_{x,i}, b_{y,i} \forall i = 4,5,6)$. The attachment points in vector $\vec{p}_v \in \mathbb{R}^{6 \times 1}$ are the positions

along the local x axis of the overtube. The total design vector for the optimisation of the system becomes:

$$V_{dv} = [\vec{p}_v, \vec{b}_{v,ab}, \alpha, \beta, \gamma, \theta, L_{tool}], \quad (7.6)$$

in which \vec{p}_v is the row vector containing all elements along the length of the overtube and $\vec{b}_{v,ab}$ contains the x and y positions of the abdominal entry points.

The objective function is shown in Figure 7.17. In contrast to earlier optimization, the *Task Space (TS) Tension Factor* TF_{TS} is used in the objective function:

$$TF_{TS} = \sum_{i=1}^k TF_i(\zeta_i, w_i) \quad (7.7)$$

Where k vectors in 3D Cartesian coordinates are points in the task space, i.e. $TS \in \mathbb{R}^{3 \times k}$. For unfeasible points, the tension factor is set to zero. The TF_{TS} is always positive due to the cable tension being positive for all feasible positions. The objective function also contains numerous conditions that have to be fulfilled to realize acceptable solutions. If these conditions are not fulfilled, a negative value is returned. The earlier in the objective function the condition occurs, the more negative the value is. For a bimanual system, the TF_{TS} of both instruments is summed and returned as value. To incentivise solutions in which both instrument configurations are feasible solutions, the negative values returned from the conditions are larger than the total highest theoretical possible task space tension factor, which is equal to the size of the task space size k .

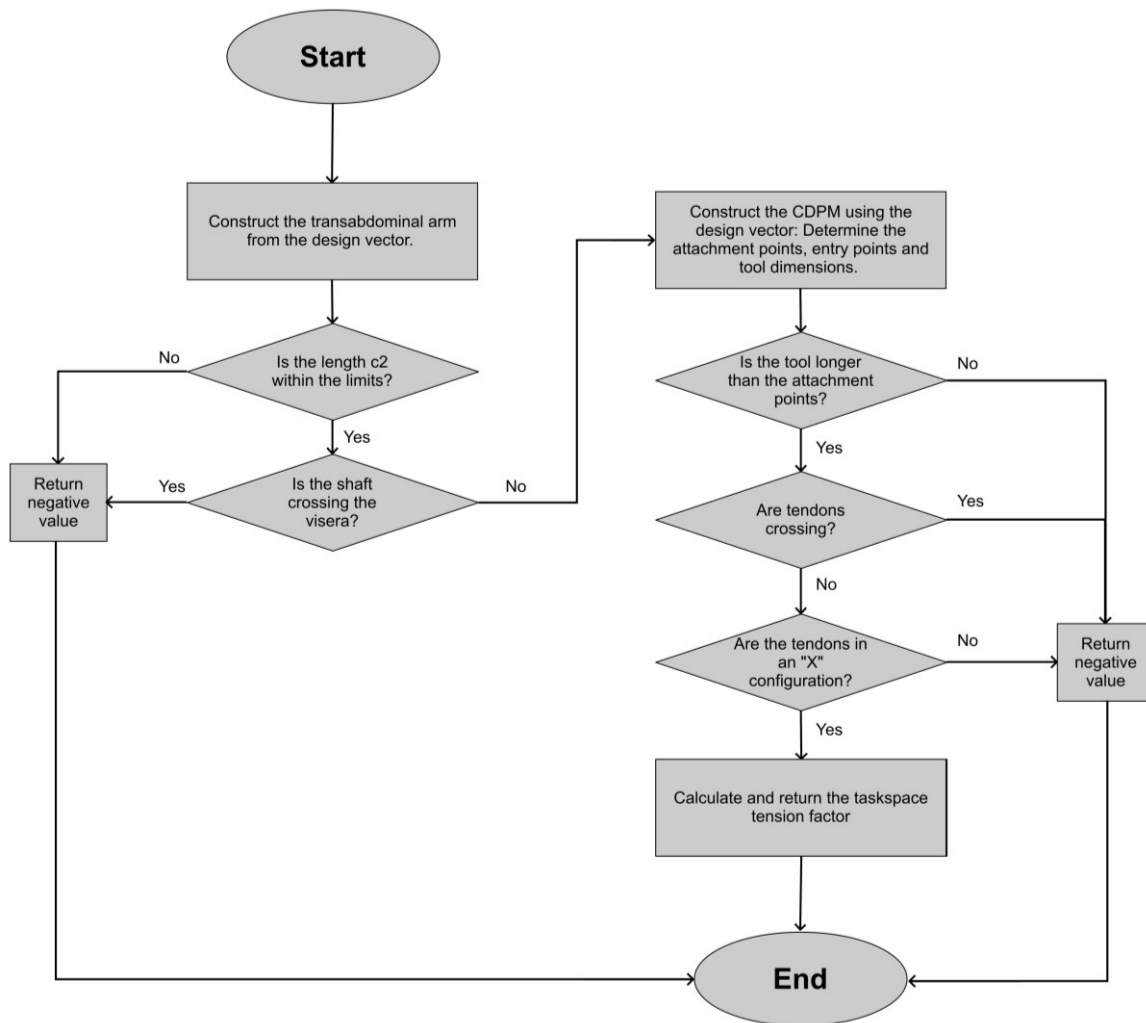


Figure 7.16 – The objective function used for optimization of the SIMPLE system.

7.3.2 Task space definition

The optimisation routine requires the parameterization of the abdominal space into the abdominal polynomial $z = P_{ab}(x, y)$ and the visceral polynomial $z = P_{vis}(x, y)$. A third- degree bivariate polynomial fitting of the abdominal surface is shown in Figure 7.17. The data points that represent the inside surface of the abdominal surface were used. The RMSE of 5.98mm is the accuracy of the surface fitting. Similarly, the top visceral surface can be fitted with a bivariate polynomial. However, to find the transperitoneal position vector \vec{A} algebraically, a 1st degree bivariate polynomial should be used, which represents a plane surface (Figure 7.17). The accuracy of the planar fitting is low, with a RMSE of 17.57mm. A numerical solver for \vec{A} - rather than the algebraic one - can be integrated when an increased accuracy of the fitting is required. Doing so would result in a slowing down of the already cumbersome computation, and as the soft visceral

surface with predominantly the colon and small intestine is rather deformable, its parameterization to a plane is acceptable.

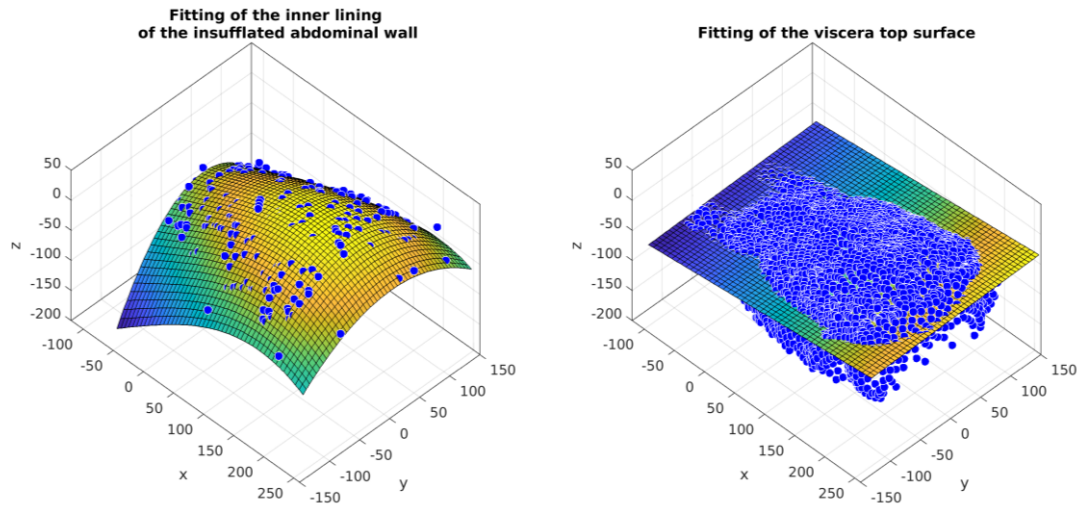


Figure 7.17 – The fitting of the abdominal wall inner surface (left) and the viscera (right). All dimensions are in millimetre.

The task space of the SIMPLE is defined as a spherical workspace placed at different locations in the abdomen. Specific locations inside the body are selected as regions for optimisation. The 3D coordinates are found using the software ITK-SNAP [371]. Figure 7.18 shows the axial and sagittal plane of a selected point for a point on left medial section of the right liver lobe. The coordinates of the anterior liver surface, appendix, the cystic duct of the gallbladder and the left and right renal hilum are found and summarized in Appendix A.10. The parameterized surfaces and the coordinates are shown in Figure 7.19. Spheres of 30mm to 80mm are placed at the landmark to act as a basic task space. The spheres' outer surface, discretized in 441 points, is used for the purposes of the optimisation.

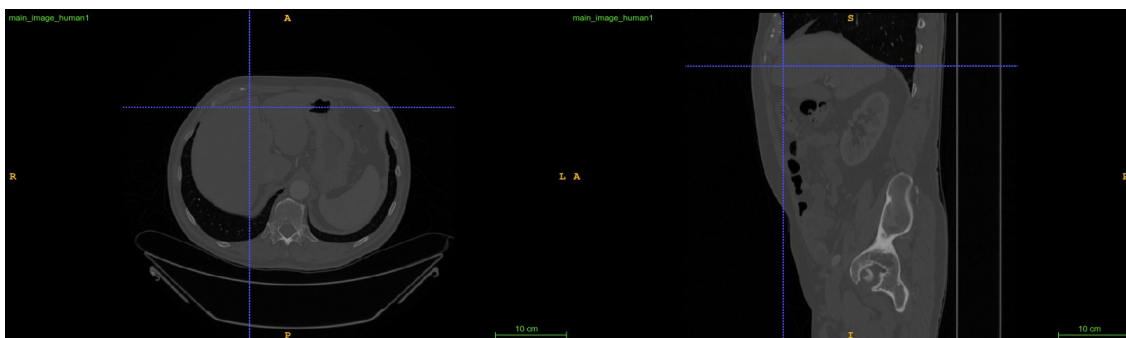


Figure 7.18 – The axial (left) and sagittal planes indicating a point on the right liver lobe, left medial section.

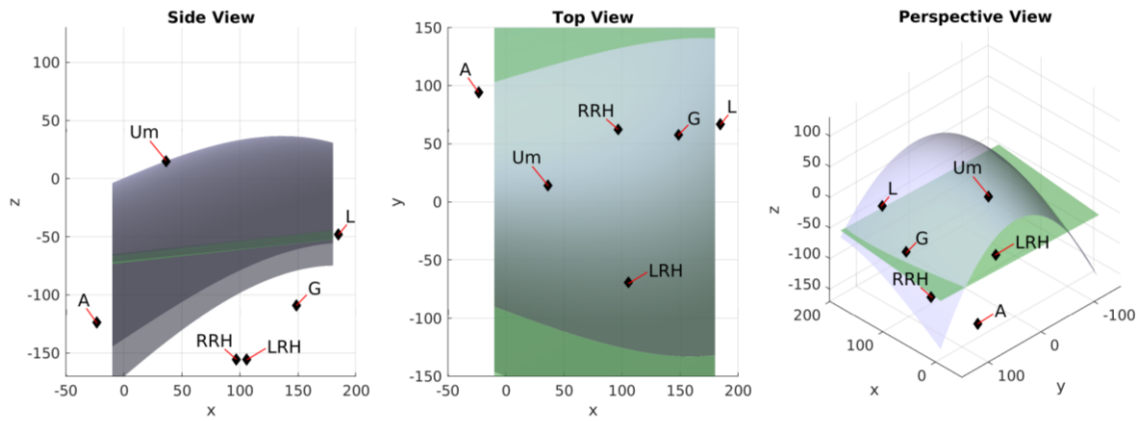


Figure 7.19 – The parameterized surfaces and landmarks Appendix (A), Umbilicus (Um), Right Renal Hilum (RRH), Left Renal Hilum (LRH), the selected point on the liver (L) and the cystic duct of the gallbladder (G). All dimensions are in millimetre.

7.3.3 Manual Configuration

Before proceeding to the optimization algorithm, the system was configured in a manner that seemed feasible for the performance of the task on the liver surface (Figure 7.20). The same method is used for configuring a bimanual system which is shown in Figure 7.21. Table 7.3 shows the percentage of the task space reached for both configuration of the single and double instrument system, the task space tension factor TS_{TF} and the average tension factor over all feasible points in the task space $TF_{TS,\mu}$.

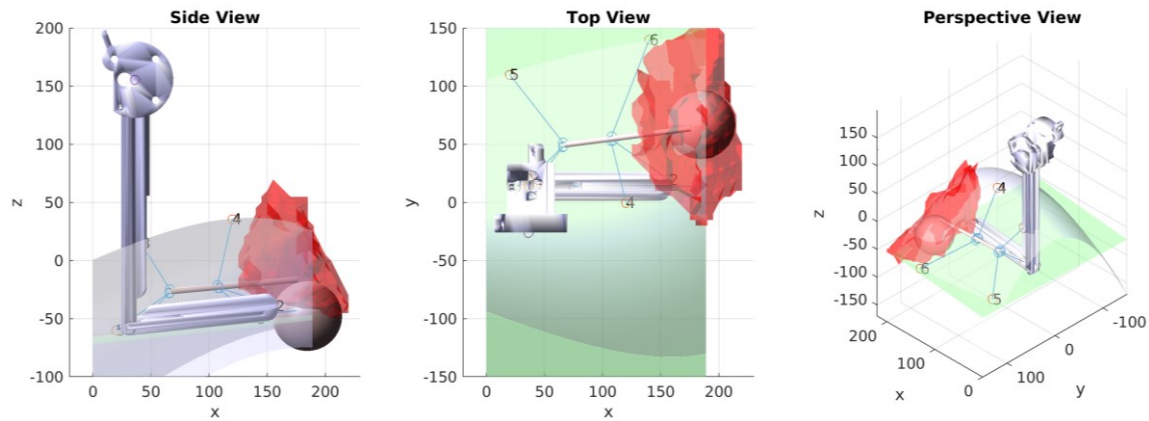


Figure 7.20 – The manual configured system, optimized for the selected point on the surface of the liver. A 60mm sphere is shown in the figure as task space. All dimensions are in millimetre.

The table shows that for the systems that are configured manually the full task space is never reached. Looking at the side view in the figures, one sees that visceral constraints prevent the instruments from reaching the bottom section of the sphere. The bimanual configuration shows that both instruments can only reach a low percentage of the task space, which is explained by the fact that the workspaces of the instruments are linked to each other by the transperitoneal arm. As a

result, the identified solution is a trade-off in the workspace of both instruments. The task space tension factor TF_{TS} and the average tension factor $TS_{TF,\mu}$ are low in both single and double instrument configurations, demonstrating the low quality of the workspace.

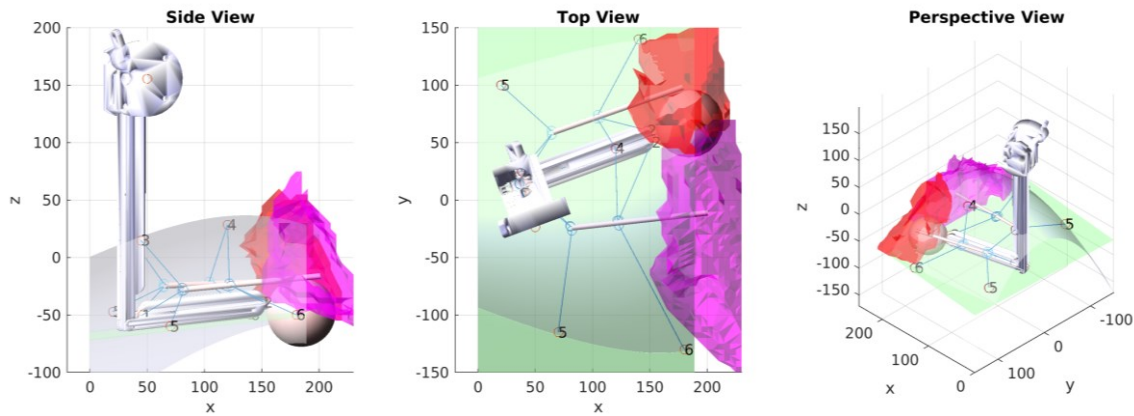


Figure 7.21 – Manual configuration for a bimanual system for the reaching of points on the liver surface. The workspace of the left and right instrument are shown in red and purple, respectively. The peritoneum and the abdominal viscera are shown in light grey and green, respectively. The dimensions are given in millimetre.

		Sphere diameter	Task space [%]	TF_{TS} [-]	$TS_{TF,\mu}$ [-]
Single Instrument	Left	30mm	48%	40.5	0.19
		60mm	45%	40.9	0.21
		80mm	35%	30.7	0.20
Double Instrument	Left	30mm	5%	0.75	0.04
		60mm	29%	20.6	0.16
		80mm	30%	31.6	0.24
	Right	30mm	7%	1.71	0.05
		60mm	11%	5.35	0.10
		80mm	11%	4.53	0.05

Table 7.3 – The results of the manually configured single and double instrument system when targeting a selected point on the liver surface. All dimensions are in millimetre.

7.3.4 Optimized Systems

The anatomical landmark on the liver is the most superficially located point in the viscera and therefore the most suitable for initial optimization. The optimizations for a single instrument and a bimanual system are shown in Figure 7.22, Figure 7.23 and Table 7.4. The single instrument system performs better with the optimization algorithm than when manually configured; it is able to reach the entire 30mm sphere, and large parts of the 60mm sphere. The bimanual system, however, still shows poor results, albeit with a slight improvement when compared to the system which was configured manually. Other optimization runs show similar results, in which the left instrument yields a better result than the right one. It should be noted that finding a feasible configuration for the bimanual system with the optimization routine was only possible when fixating the parameters of the transperitoneal arm (i.e. parameters $\alpha, \beta, \gamma, \theta$). The parameters of the transperitoneal arm were

set to those used in the manually configured bimanual system. This choice was made because the two instruments are mathematical interconnected through the cable entry points on the transperitoneal arm which made optimization impossible, at least with the available computational means. The lesions located deeper in the viscera, such as the selected point on the gallbladder, did not yield any positive results.

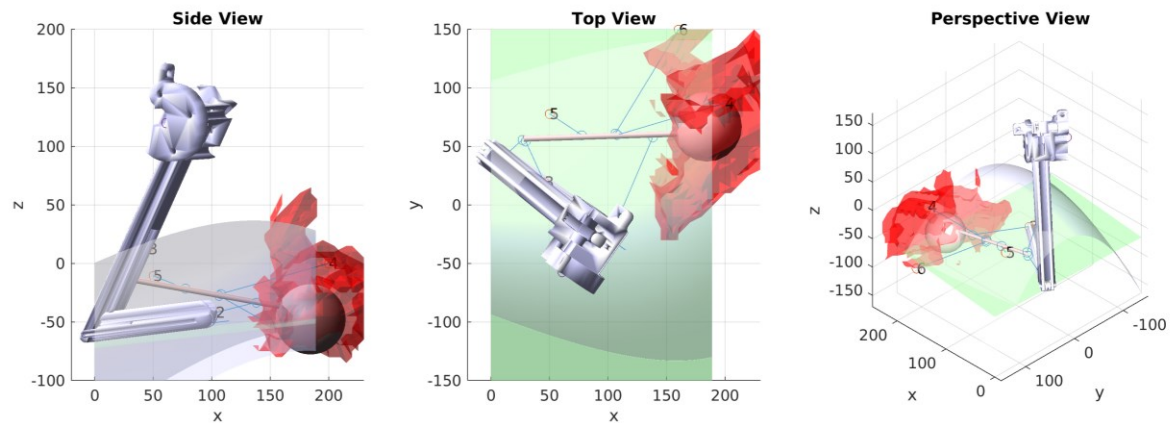


Figure 7.22 – The single-instrument system which was optimized using a task space positioned at the selected point on the liver. All dimensions are in millimetre.

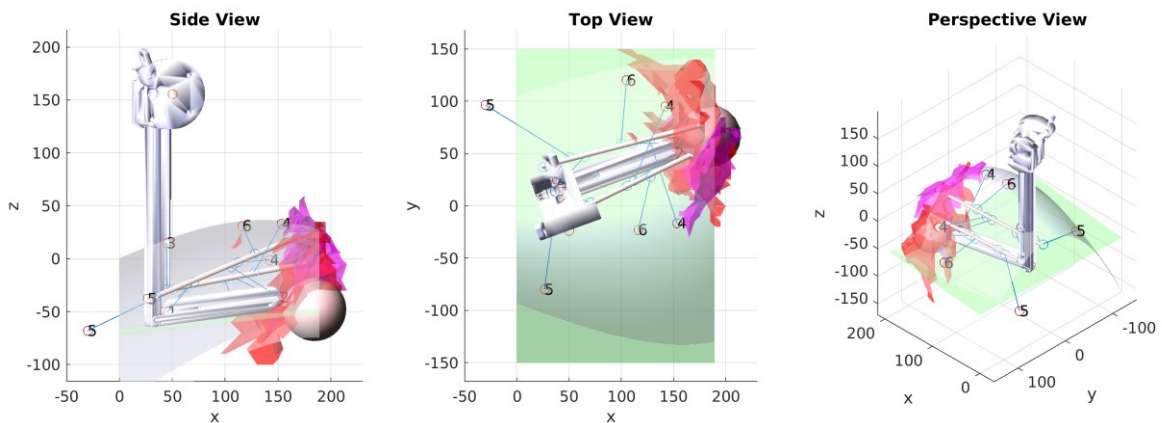


Figure 7.23 – Results found for an optimized bimanual system. All dimensions are in millimetre.

		Sphere diameter	Task space [%]	TS_{TF} [-]	$TS_{TF,\mu}$ [-]
Single Instrument	Left	30mm	100%	138.9	0.32
		60mm	74%	48.8	0.15
		80mm	35%	12.9	0.08
Double Instrument	Left	30mm	45%	83.4	0.42
		60mm	28%	27.3	0.22
		80mm	16%	9.07	0.13
	Right	30mm	2%	0.12	0.02
		60mm	25%	9.71	0.09
		80mm	20%	13.0	0.15

Table 7.4 – The optimized system for a 30mm sphere placed at the selected position on the liver surface. The workspace was evaluated for 30mm, 60mm, and 80mm task spaces.

Other interesting configurations are found when purposefully allowing the overtube to be rotated (i.e. the instrument tip points towards the pivot point of the transperitoneal arm, rather than towards the end of the transperitoneal arm). A configuration for a single instrument is shown in Figure 7.24. The system is able to achieve 79% and 68% of the 60mm and 80mm task space, respectively. Whether such rotating of the overtube is realistic in a physical system design should be further explored; however, it illustrates that the optimization routine can be further expanded to account for alternative configurations.

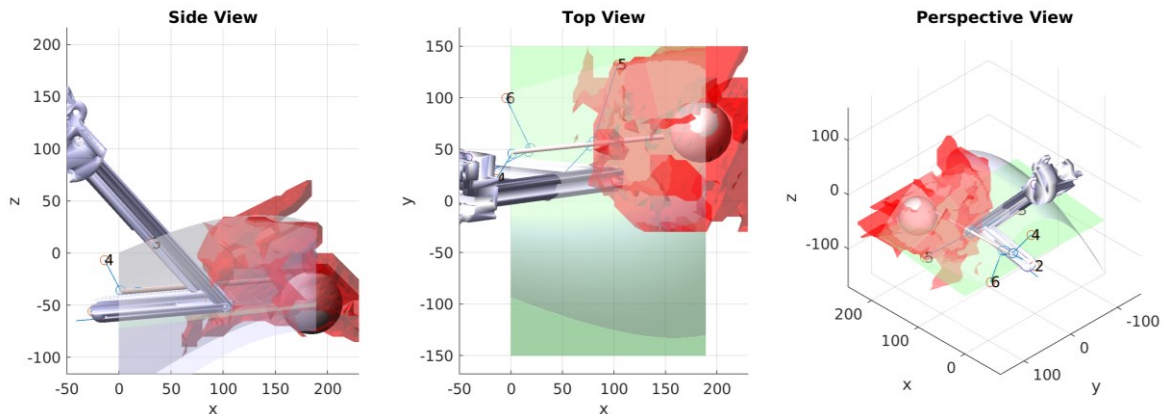


Figure 7.24 – The system in a configuration in which the overtube is reversed. Note that in this case cables 2, 4 and 6 are the rear cable, as opposed to the systems shown in earlier optimizations.

7.3.5 Discussion of the SIMPLE Optimization

The study shows that patient-specific pre-operative data can be used for the optimization of the SIMPLE system. A single-instrument configuration was successfully found for a task space placed at the anterior medial section of the right liver lobe. For other anatomical landmarks, the visceral constraint limits the finding of feasible solutions. However, as the tissue is soft and, in the case of the colon and small intestine, can be manipulated and retracted, the constraint as used in the optimization therefore does not accurately represent the real scenario. As mentioned in Chapter 6, the patient's position and the orientation of the surgical bed are used to let gravity assist with the retraction of the intestines and thereby create workspace for surgery. For instance, for upper abdominal surgery the reversed Trendelenburg position is used for the creation of workspace. Similarly, the patient is placed on one side for surgery on the kidneys. The SIMPLE system's scaffold can accommodate for this, and therefore can be used for determining a more realistic constraint of the viscera. However, the currently used simulation of the pneumoperitoneum is validated for the supine position and does not have gravity incorporated for the retraction of the intestines in other positions. In addition to gravity, the articulation section of the transperitoneal arm can be used as a means of retracting tissue to reach locations deeper in the viscera. Obviously, when the visceral

constraint is removed completely, other solutions are possible (Figure 7.25). However, completely removing the visceral constraint is unrealistic as well, and a soft constraint can therefore most likely be used to allow for some degree of soft tissue deformation to simulate retraction. Finding appropriate parameters to simulate such a soft constraint is a complex matter and will depend on the specific location in the body.

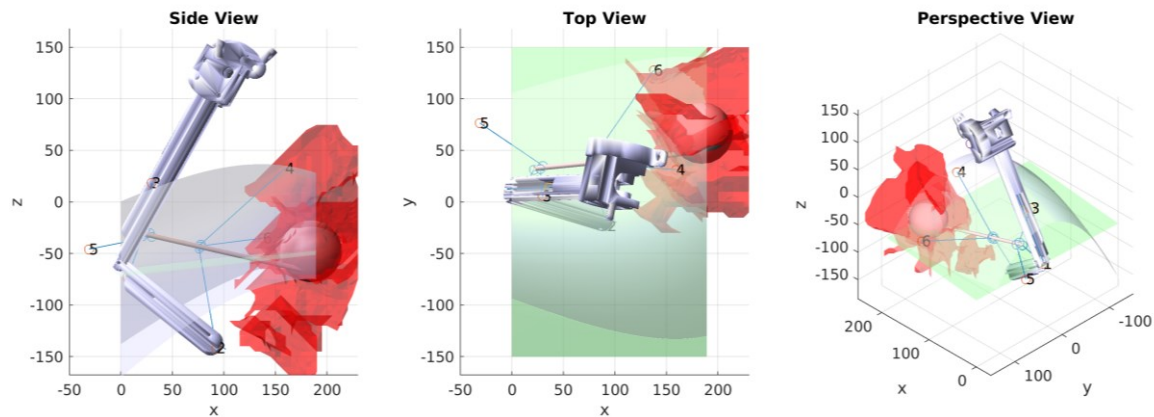


Figure 7.25 – An optimized configuration when the visceral surface constraint is removed.

Additionally, in contrast to the ESD CYCLOPS, the current optimization does not include curved instruments. This can be included to increase the reach of the instruments, but more importantly it can increase the overlap in workspace between both instruments. The optimization results of the bimanual system are mainly poor due to the limited overlap of instrument workspaces and introducing a curvature to the design can be used, similar to the ESD CYCLOPS, to increase instrument overlap and make bimanual surgery with SIMPLE feasible. However, the most suitable approach would likely be to have an articulated instrument tip, rather than a predefined curvature as seen in the ESD CYCLOPS. This is because a predefined overtube will complicate motions for specific manoeuvres, such as found in suturing and knot-tying. Note that such tasks also require rotation around the axis, and so a method for rotation of the instruments, such as demonstrated in [372], should be included in further development and optimization.

Currently the optimization assumes a fixed position, the umbilicus, as the access port for the transperitoneal arm. While an umbilical port is preferred for its 'scarless' nature, other port positions on the abdomen are feasible, and these can be implemented in the optimization algorithm. An alternative approach, as mentioned briefly in Chapter 6, is to use a transvaginal port for the introduction of the transperitoneal arm. Another aspect not explored in the optimization described in this chapter is the possibility of moving the transperitoneal arm to increase the workspace of the instruments; if performed in a well-coordinated manner, this can lead to an overall increase in workspace. Another possible improvement for the optimization is to include the design of the

transperitoneal arm in the optimization routine. Specifically, it is not clear whether the length of the articulated section or the position of the cable entry points is optimal. Although they certainly add complexity and thus computational time to the optimization process, all these considerations should be taken into account in further developments.

Nevertheless, while further improvements are required, the optimization shows that sufficient workspace can be found for a single instrument to reach sections of the liver, which can be used for palpation, as discussed in Chapters 5 and 6. The system is suitable for such specific tasks, but not yet for full bimanual surgery. The use of patient-specific simulated pneumoperitoneum can be used as a basis for optimization. The optimization approach is not limited to the current SIMPLE system, and can also be used for systems that only use abdominal motor units, for example. The accuracy of the positioning of the microports on the abdomen will play an important role in the overall accuracy of the workspace estimation. Hence, an error margin should also be included in the optimization of the cable configurations to a specific task space. The accuracy of this approach should be further evaluated by performing *in vivo* preclinical studies.

7.4 Conclusion

The current chapter discussed the workspace optimization of CDPM mechanisms for Minimally Invasive Surgery. The ESD CYCLOPS was optimized using a theoretical task space and showed an improved workspace in comparison to the prototype discussed in Chapter 4. Additionally, a method was developed to record the forces and locations of instruments during a simulated ESD procedure. The collected data were used for the optimization of the ESD CYCLOPS. Special care should be taken against overfitting by collecting a larger and therefore more representative dataset. Additionally, the SIMPLE system was optimized using a patient-specific model of the pneumoperitoneum. The system could be optimized to cover a section of the liver with the instrument; however, other anatomical landmarks were not feasible with the current model due to the presence of stringent constraints. Appropriate visceral constraint should include the retraction of the intestines, either through gravity or by retraction using the transperitoneal arm. For a bimanual system an articulated tip could be used to increase the overlap in workspace between the two instruments. As the system is still in an early stage of development, alternative configurations or even systems without the transperitoneal arm can benefit from the current optimization method. Overall, both case-studies demonstrate that optimization can be used to develop procedure- and possibly patient-specific CDPM systems.

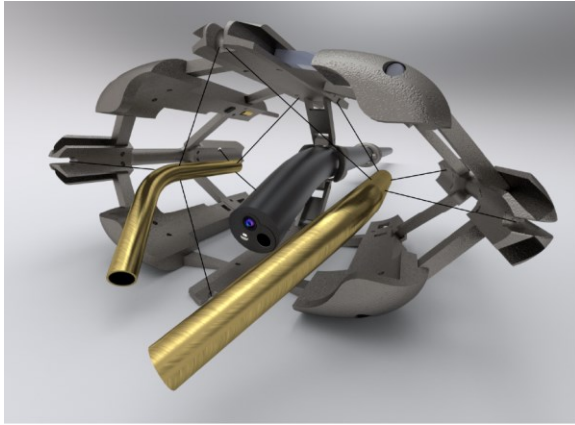
Chapter 8

Research Synthesis and Discussion

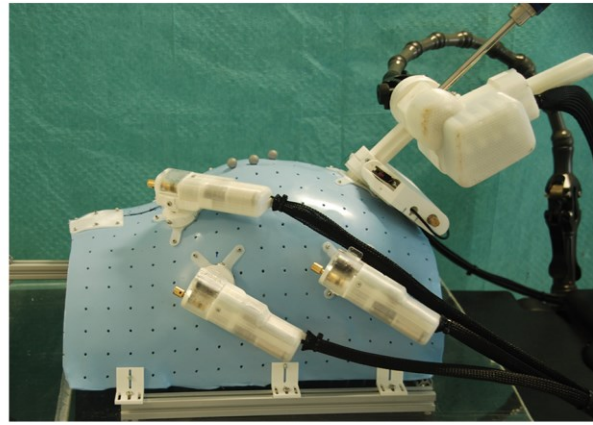
This chapter synthesizes the research project and places the developed prototypes into the larger context of MIS. This thesis has extensively discussed the ESD CYCLOPS and SIMPLE systems. The CYCLOPS dVI - briefly introduced in Chapter 5 and in Appendix A.4 – is another system that adopts an alternative approach in employing CDPMs in MIS. The microCYCLOPS and neuroCYCLOPS systems, both developed by the author of this thesis, also did not receive a great deal attention in this thesis, but are presented in Appendix A.3. Each prototype has its own clinical and technical advantages for MIS, and this can be used to create a development framework to identify new clinical applications for CDPMs, as demonstrated in section 8.1 below. The achievements of this thesis and opportunities for further developments are discussed in section 8.2. Section 8.3 presents conclusions.

8.1 Development framework for cable-driven parallel mechanisms

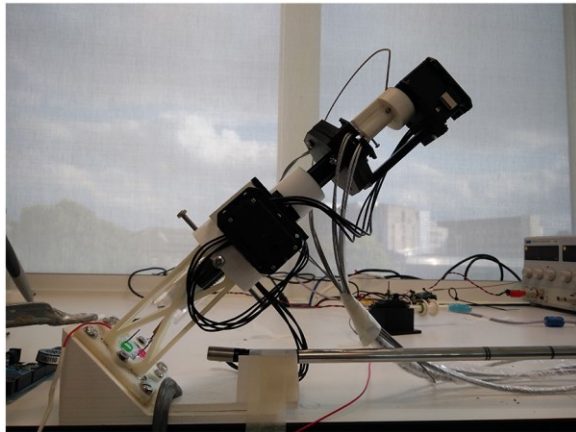
The prototypes developed during this thesis (Figure 8.1) differ not only in terms of size and workspace, but also with regard to the minimally invasive access method they use; this is discussed in the following two sections. These characteristics can be used to create a framework based on which it may be possible to find new opportunities for the current prototypes and develop other prototypes for MIS procedures.



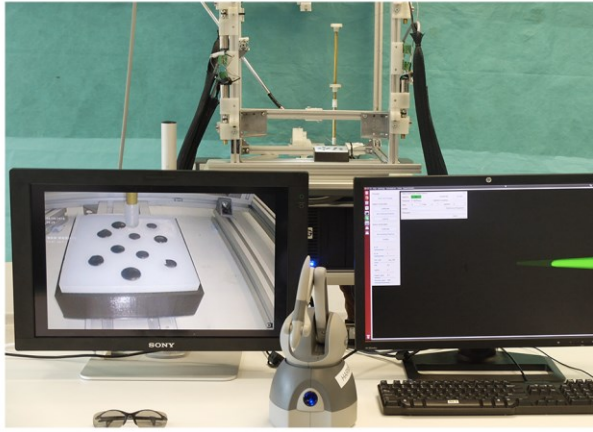
ESD CYCLOPS



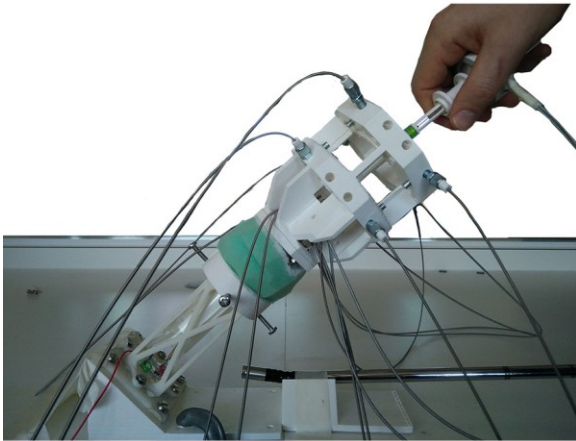
SIMPLE



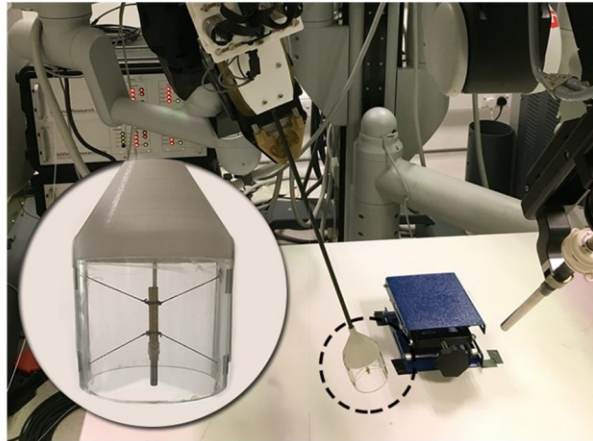
microCYCLOPS



CDAQS



neuroCYCLOPS



CYCLOPS dVI

Figure 8.1 – An overview of the CDPM prototypes.

8.1.1 End-effector Workspace Size

The size of the end-effector workspace varies considerably between the prototypes. The SIMPLE has by far the largest workspace, as the system can be configured to span the entire abdomen. The intra-abdominal workspace is highly dependent on the pressure used for insufflation and the body position of the patient [362]. Similar to laparoscopy, the ports can be placed to accommodate the

workspace in the area of interest. The CYCLOPS dVI has a small workspace due to the use of a small scaffold with a planar CDPM. However, by mounting it on a long rigid shaft and using the da Vinci robot to control its position and orientation, the reach of the CDPM end-effector becomes much larger; the workspace becomes similar to the workspaces seen in laparoscopy [373]. The ESD CYCLOPS is constrained by the dimensions of the gastrointestinal tract and thus has a smaller workspace when compared to the CYCLOPS dVI and SIMPLE. The workspace is even smaller for the neuroCYCLOPS and microCYCLOPS (Appendix A.3). The neuroCYCLOPS and microCYCLOPS are both based on the principle of combining a CDPM with a tubular retractor, meaning that the tubular retractor itself acts as a constraint for the workspace of the instruments. For example, the neuroendoport™, is a tubular retractor used to reach deep-seated lesions in the brain. It has a diameter of 11.5mm which serve as a constraint for the scaffold dimensions. However, the scaffold can move along the longitudinal axis of the tubular retractor which increases the overall workspace of the CDPM. Another aspect which increases the reach of the end-effectors is reorientation of the retractor itself. The aforementioned neuroendoport, for instance, can be pivoted after it has been placed into the brain to extend the reach of the inserted instruments [374].

The workspace optimization methods developed in Chapter 7 can easily be adapted to the constraints of the tubular retractor to optimize the workspace of the neuroCYCLOPS and microCYCLOPS. The workspace of the CYCLOPS dVI is more dependent on the motion of the shaft than the CDPM itself, as mentioned above.

8.1.2 *Minimally invasive access method*

In addition to workspace size, CDPMs also vary with regard to the minimally invasive access methods used to introduce them into the body. The ESD CYCLOPS uses the natural orifice of the anus to gain access and is navigated through the tortuous colon. The scaffold is then deployed to provide a workspace for the performance of an ESD task. The deployment of the scaffold is used to stabilize the endoscope and itself in relation to the colonic tissue.

SIMPLE uses the percutaneous approach to introduce multiple cables into the abdomen, or possibly other parts of the human anatomy, as discussed in Chapter 6. As the name suggests, the transperitoneal arm uses the transperitoneal approach. Another prototype which uses the transperitoneal approach is the CYCLOPS dVI, which is used by the da Vinci robot as an instrument for robotic laparoscopic surgery. The transperitoneal approach can be placed in the larger category of extraluminal access methods, in which a pathway is created from outside the body through the skin to gain access into a lumen. Another extraluminal access method is the retroperitoneal approach used in laparoscopy, in which a space is created behind the peritoneum for surgery (predominantly

on the kidneys and adrenal glands). Spaces that are specifically created provide workspace for MIS are also referred to as *potential spaces* and are used in various forms of surgery, such as video endoscopic inguinal lymphadenectomy, totally extraperitoneal laparoscopic hernioplasty and video-assisted thorascopic surgery (through deflation of a lung). The CYCLOPS dVI could potentially be used for these approaches after the scaffold is made deployable. Other extraluminal approaches are possible for SIMPLE, though any access method should take into account not only the introduction of the transperitoneal arm, but also the placement of the microports.

The neuroendoport, the tubular retractor of the microCYCLOPS and neuroCYCLOPS, is also used for the creation of workspace. The use of tubular retractors is also seen in other minimally invasive surgeries, and therefore the microCYCLOPS and neuroCYCLOPS may potentially be used in a broader range of applications. Tubular retractors are seen in minimally invasive spine surgery for procedures such as microendoscopic lumbar discectomy and resection of spinal tumours [375] [376]. Tubular retractors are also seen in MIS rectal surgery, referred to as Transanal Endoscopic Microsurgery (TEMS) [377]. Non-tubular tissue retractors are also potential candidates for this approach, e.g. laryngoscopes for transoral surgery. A system for transoral surgery (TORS CYCLOPS) is currently being developed by another PhD candidate in the department of Surgery and Cancer, and a patent application was recently filed (Application Number GB1901147.7).

8.1.3 Framework synthesis

As mentioned above, the variety in workspace requirements and access methods of different surgeries have led to the development of different prototypes. The systems can be placed into a grid based on the size and shape of the access route and the workspace required at the region of interest (Table 8.1). In this grid, distinctions are made based on the number of pathways, whether the pathway is straight or tortuous, and the size of the entry point (A_{entry}) relative to the size of the workspace (WS). Note that the size of a workspace is typically defined in terms of volume, while the size of an entry port is given based on surface area. The relative size of the workspace to the access point determines whether a system's scaffold has to be deployable or not; a workspace with the same size as the entry port does not necessarily need a scaffold that is deployable, as is the case for the neuroCYCLOPS and microCYCLOPS. The systems in the bottom row of the grid ($WS > A_{entry}$) require deployment or assembly and are colour-coded yellow or green (see below) in the grid. This thesis also demonstrated the force sensing ability of the CYCLOPS dVI and the SIMPLE system, which is made possible through the use of straight cable pathways; this is indicated with the colour blue. Systems which can sense forces but require deployment are colour-coded green. Systems with tortuous paths may be able to sense forces at the tip, but additional research is required to take the frictional forces into account. For flexible endoscopic robotic systems, end-effector payloads may

constitute a limitation in surgery, as discussed in Chapter 3; on the other hand, CDPM systems that follow tortuous pathways, such as the ESD CYCLOPS, can provide sufficiently high end-effector payloads for flexible endoscopy, as demonstrated in Chapter 4. An advantage of CDPMs in general is that they offer high payloads, as long as the scaffold can provide sufficient counter-force. As CDPMs, all the prototypes shown in the grid share this advantage.

	<i>Single Access Pathway</i>		<i>Multiple Access Pathways</i>	
	Straight	Tortuous	Straight	Tortuous
$WS \approx A_{entry}$	NeuroCYCLOPS microCYCLOPS	TORS CYCLOPS ¹⁸	?	?
$WS > A_{entry}$	CYCLOPS dVI	ESD CYCLOPS	SIMPLE	?

Table 8.1 – The CDPM prototypes categorized according to type of pathway and workspace size (WS) relative to entry port size A_{entry} . The colours indicate systems which can be used for force-sensing (blue), systems that require a scaffold that is deployed/assembled (yellow), or both (green).

The grid can be used to identify new approaches for the introduction of CDPMs into the body for minimally invasive surgery, as indicated by the empty spaces in the grid. For instance, one can imagine a version of the SIMPLE system in which snake-like robots – e.g. concentric tube robots – to create tortuous pathways from microport entrances. This could be a potential method to deploy SIMPLE in areas in which a straight pathway would pass through critical tissue structures. On the other hand, it should be noted that curved microports would add complexity to the assembly of the system, introduce higher frictions between the cables and the ports, and likely lead to a limited payload capacity due to reduced stiffness of the cable conduit. However, whether or not such an approach is useful depends primarily on the specific requirements of the clinical procedure in question.

It is also important to realize that this grid, at the current stage, only represent prototypes using *fully constrained* CDPMs. Similar grids can be made based on other ways of classifying CDPMs (e.g. *hybrid*, *suspended* and *multi-link*); such classification systems were discussed in Chapter 2. Also discussed in Chapter 2 was the fact that fully constrained CDPMs require the scaffold to encapsulate the cable attachment points. The prototypes developed in this thesis use an overtube that extends beyond the scaffold. In contrast, hybrid and suspended CDPMs can reach points outside of their

¹⁸ A PhD student in the department, Ming Zhao, is currently developing the TORS CYCLOPS for flexible transoral laser surgery [356].

scaffold structure and therefore do not necessarily require an extended overtube. For instance, suspended CDPMs can be used for tissue retraction for the ESD CYCLOPS and SIMPLE (Figure 6.26). Another type of CDPM, which was not explored in this thesis, involves the adaption of a planar CDPM to follow a surface. The epicardial planar CDPM [37] can be classified as an example of such a *surface-constrained* CDPM. The epicardial robot is inserted through a single straight pathway and is deployable (i.e. $WS > Entry$); it can thus be placed in the bottom-left box of the grid. Adopting a broader definition of CDPMs would allow for expansion of the grid to include different types of CDPM.

	<i>Single Access Pathway</i>		<i>Multiple Access Pathways</i>	
	Straight	Tortuous	Straight	Tortuous
$WS \approx Entry$	<ul style="list-style-type: none"> • Percutaneous • Transanal • Transparenchymal (neurosurgery) 	<ul style="list-style-type: none"> • Endovascular • Peroral(or transoral) • Transbronchial 	?	?
$WS > Entry$	<ul style="list-style-type: none"> • Transperitoneal (SILS) • Transurethral (rigid) • Transvaginal (vNOTES) 	<ul style="list-style-type: none"> • Transurethral (flexible) • Transvaginal • Transgastric • Transesophageal 	<ul style="list-style-type: none"> • Transperitoneal • Retroperitoneal • Extraperitoneal • Transthoracic • Transocular • Arthroscopy 	?

Table 8.2 – The classification of several minimally invasive access methods using the same principles as the grid presented above in Table 8.1.

A similar grid can be made for the access methods used in MIS (Table 8.2). Note that the table is not exhaustive, and is primarily intended as a method to classify MIS access methods with the objective of identifying new clinical opportunities for the current prototypes and the development of new CDPM prototypes. For instance, when comparing Table 8.2 with Table 8.1, it would appear that the CYCLOPS dVI could perhaps be adapted for transurethral approaches that use rigid endoscopes. While the comparison is useful to identify potential new developments, it does not take clinical requirements into account. A more pragmatic approach would be to identify the limitations encountered during specific minimally invasive surgical procedures, and evaluating whether CDPMs can be used to overcome those limitations.

Generally speaking, this grid can be used to identify potential new developments for cable-driven parallel mechanisms which can lead to improvements for minimally invasive surgical procedures.

8.2 Discussion and future work

The prototypes developed in this thesis have played an important role in identifying several opportunities for the use of CDPMs in MIS. The strengths of CDPMs, discussed in Chapter 2, include deployability and high payloads (up to 46N), both of which were demonstrated over the course of the development of the ESD CYCLOPS. Additionally, the efficient force transmission of CDPMs was taken advantage of to incorporate force sensing into presented prototypes. The CYCLOPS dVI system showed it could measure forces as small as 0.2N at the tip of the end-effector. Essential to this approach was the use of low-friction cable conduits. The CDAQS system was used to verify whether the force sensing capabilities could be used for haptic feedback; these tests demonstrated that haptic feedback led to a higher nodule detection rate during a simulated palpation task performed by surgeons in training. The SIMPLE system was developed for single-port surgery, with low friction being assured through the introduction of microports.

The ESD CYCLOPS has shown success in performing ESD on *ex vivo* animal tissue, with partial ESD performed on *in vivo* in pigs. The two animal trials were important in understanding the next steps to take in the development of the system for ESD in humans. One important factor was the acute angle of the instruments relative to the tissue, which may have contributed to the perforation that occurred during the second trial. Further research should be dedicated to identifying the appropriate instrument angle in order to prevent this. Another important aspect that needs further development is the scaffold. The current prototype uses a scaffold that is based on the principle of a four-bar mechanism for deployment. The approach was practical for the downscaling of the CYCLOPS system to a size which can be used in trials, and was able to withstand sufficiently high enough cable forces. The inflatable prototype that was manually built in-house was too large and fragile to be use in a pre-clinical trail. However, as mentioned in Chapter 4, an inflatable scaffold will be an important factor in the next steps of development. As inflatable balloons are already safely used in endoscopy, the same approach can be used to provide a safer method for deploying the scaffold. Furthermore, it can likely be packaged more compactly, which is an advantage in the navigation through the body. A third benefit of such an approach is that the scaffold can be developed as a disposable part of the system, removing the need to clean the scaffold after usage. A disposable scaffold would also be cheaper to produce, as it eliminates the need to design components to be resistant to mechanical failure as a result of repeated use of the system. An important aspect is the higher patient acceptability of an inflatable, “soft” component, which was an outcome in a meeting with a representative group of colorectal cancer patients. Another important step for further development of the ESD CYCLOPS is a comparative study to assess whether the system provides an advantage when compared to standard ESD techniques.

The workspace of the system was sufficient to perform an initial ESD and the system could remove lesions *ex vivo* that were larger than 20mm diameter. However, lesions much larger than 20mm can still not be dissected with the current prototype, and considering that many lesions smaller than 20mm can be removed safely and efficiently with EMR, the workspace should be further increased before the system is put to use in clinical practice. The workspace optimization method in Chapter 7 yielded good results, indicating that a larger workspace is possible, and preliminary evaluations have already been carried out in a physical system. This chapter also presented a method through which the workspace could be optimized to a task space recorded during a simulated ESD. The initial steps for optimization were shown, but a larger dataset should be collected to overcome issues related to overfitting. Additionally, a single joint can be added to the overtubes to further increase the workspace of the instruments (Figure 4.24). As the high payload of the ESD CYCLOPS exceeds the requirements for ESD, a system with a single joint will most likely lead to a combination of a large workspace and sufficiently high payloads. Whether such a joint is practically feasible and does indeed lead to improved performance during ESD tasks should be explored in further developments.

The SIMPLE system presented a novel approach using microports for the actuation of cables to control a CDPM inside the body. The assembly of the system was identified as one of the most important aspects to be considered for use in surgery, and a feasibility study using a preliminary setup was demonstrated. The system could sense forces and could be used to create a force map of phantoms containing plastic letters hidden in silicone. A deformation related to positional accuracy was found in the force maps. As the deformation was not consistent for all letters, it likely relates to the calibration of the end-effector position before use. The workspace analysis performed in Chapter 7 showed that a selected landmark on the liver could be reached with a single-instrument system, and thus such a system could be used for autonomous palpation of the liver surface. In a bimanual system, the combination of straight instruments and the dependence of both CDPMs on the position of the transperitoneal arm lead to limited overlap of instruments, and therefore no satisfactory solution has yet been identified for bimanual surgery. The overlap between instruments can be increased by the addition of one or more curvatures in the overtube, similar to how it has been used for the ESD CYCLOPS. Similarly, the use of a single predefined or articulated curvature in a bimanual SIMPLE system should be explored. The use of the system with different operational positions of the patient should also be explored in further developments. The scaffold itself currently uses a thermoplastic material which becomes compliant at relatively low temperatures; this characteristic is used to mould the scaffold over the insufflated abdomen. Other mechanisms for scaffolds, such as the use of granular jamming materials and suction to the abdomen, should be explored further. The

microports used in SIMPLE can also be applied for other purposes, such as endoscope and instrument stabilization in NOTES, or for tissue retraction. Further exploration is needed to determine whether such an approach can solve some of the issues in NOTES.

The CDAQS system was developed for research purposes, and not intended for use in surgery. The system was used for the development of the new control routine and mechatronics. Additionally, a new method for calculation of the optimal tension distribution was proposed. The method was able to solve the optimal tension distribution in real-time for a six-cable system, and can also be used for more cables. However, this method has not been systematically compared with other methods that can be used for calculation of the optimal tension distribution; this will be addressed in the future. Also, the CDAQS can be used to develop and validate other improvements to the control routine. One such improvement that should receive significant attention is the calibration of the system. An accurate calibration routine is important to achieve high positional accuracy during autonomous tasks and to ensure that the manual control of the CDPM remains intuitive. As most systems are deployable, calibration should be efficient and accurate. Another possible improvement for the control routine and the force estimation is the compensation for or estimation of friction in the cables. Also, embedding the elasticity of the cables in the control routine will likely lead to more accurate pose estimation, and can be further used to improve the accuracy of force estimation and positional control. Both friction and elasticity should be embedded into the control routine, and they both affect the calibration of the end-effectors, which will be specifically beneficial for systems with relatively high cable friction, such as the ESD CYCLOPS. It should also be noted that in addition to the fact that such improvements to the control system are feasible, the results presented in this thesis were achieved with relatively simple control routines, meaning that even better results are possible with further development.

In Chapter 2 several technical limitations of CDPMs are described (Table 2.1). Two technical limitations, the computationally expensive forward kinematics and the actuation redundancy, are inherent to CDPMs and therefore did not receive specific attention. Nevertheless, these two technical limitations are not critical for the use of CDPMs in MIS. The computationally expensive forward kinematics is less critical as in normal control the inverse kinematics is more important than the forward kinematics. In contrast to serial mechanisms, parallel mechanisms have inverse kinematics that are computationally inexpensive which, due to the more frequent use of the IK, leads to a comparative advantage in overall. For the limitation of actuation redundancy, CDPMs require more actuators than degrees of freedom. The ESD CYCLOPS and SIMPLE only have a single actuation redundancy, which has limited consequences for the system in overall. In addition, the efficient force transmission enables the actuators to be smaller when compared to serial mechanisms with equal

payloads. The other limitations mentioned in Chapter 2 have been addressed during the thesis. The most important of these limitations is the need for an encapsulating scaffold structure. The prototypes show three different MIS access methods which can be used to provide the CDPM's scaffold. The cable slackness is addressed by developing a tension control routine, which is implemented in the CDAQS and SIMPLE system. Another limitation is the possible collision of cables; the prototypes prevent this by using cable configurations in which cable collision is unlikely (i.e. the 'X' configuration) and, when using two CDPMs, keeping them physically separated. However, cable crossing can be used to increase the workspace and overlap of two instruments. The interference between two cables may potentially be modelled and embedded into the control routine to prevent unexpected motions of the end-effectors.

The economic aspects of CDPMs have not received attention during the thesis. However, as mentioned in Chapter 2, many CDPMs are developed for the potential to reduce costs. The use of smaller actuators directly reduces hardware costs. Additionally, when compared to the slave manipulator of the da Vinci system the developed prototypes do not require large support structures, saving additional hardware costs. Further hardware costs are saved by using conventional endoscopes for visualisation. Developments of the ESD CYCLOPS are focused on creating an inflatable scaffold for single-use, saving costs on cleaning and sterilisation services. Other potential cost-saving aspects of the ESD CYCLOPS are reduced procedure time, reduced complications (and thus follow-up treatment) and training time. However, these aspects should be explored further in future comparative and clinical studies. Additionally, the concept behind the ESD CYCLOPS is applicable for a wider range of gastrointestinal surgeries than ESD and the development of a more versatile system (e.g. using articulated sections) can lead to the increase of its value. The economic value of the SIMPLE system is too early to estimate at present stage. The palpation task can provide an improved positive margin during dissection and therefore lead to more curative treatment. However, on the bigger scale the focus on safe automation can prove to be a unique advantage to standardise surgical (sub-)tasks and reduce complications. Further development and research will be needed to understand the full potential of the technology.

8.3 Conclusion

This thesis explored the use of cable-driven parallel mechanisms for minimally invasive robotic surgery. Chapters 2 and 3 were important in identifying opportunities for CDPMs in single-port and flexible endoscopic surgical systems. Low payloads, limited end-effector dexterity and lack of haptic feedback are common problems with many of the robotic systems that have been developed for single-port and flexible endoscopic robotic surgery. CDPMs can be used to overcome these limitations, which this thesis illustrates with the development of several CDPM prototypes. The high

force capability of these prototypes was demonstrated for flexible endoscopy, with end-effector forces up to 46N. The high forces are due to the efficient transmission of forces from the cables to the end-effector. The efficient force transmission is also used for the sensing of contact forces in endomicroscopy, displaying sensitivity to forces as small as 0.2N. The efficient force transmission was employed to provide haptic feedback to surgeons in training, demonstrating an increased nodule detection rate during a palpation task. The prototypes also demonstrated that CDPMs can be used for several minimally invasive access methods, including transanal, percutaneous and transparenchymal approaches. This final chapter has been dedicated to identifying future courses of development. The current research is, to the author's knowledge, the first attempt at developing a general framework of CDPMs for MIS. As the research shows, CDPMs have the potential to realise unique advantages with a positive impact on MIS.

Appendices

A.1 Dimensions cable entry points of the ESD CYCLOPS

The cable entry points of the ESD CYCLOPS scaffold are:

$$B = \begin{bmatrix} -22 & -22 & 22 & 22 & -22 & 22 \\ 4.1 & 4.1 & 0.7 & 0.7 & 0 & 0 \\ 0 & 0 & 0 & 0 & 1.8 & 0 \end{bmatrix} + \begin{bmatrix} -22 & -22 & 22 & 22 & -22 & 22 \\ 0 & 0 & 0 & 0 & w/2 - t & w/2 - t \\ h/2 - t & -h/2 + t & h/2 - t & -h/2 + t & 0 & 0 \end{bmatrix}$$

In which h , w and t are defined in Chapter 4, equations (4.1).

A.2 First generation scaffold of the ESD CYCLOPS

The first generation ESD CYCLOPS scaffold is shown in Figure A.2.1. The scaffold is larger than later version and uses an outward-folding, rather than inward-folding, four-bar mechanism. This scaffold was used for the first porcine animal trial, as discussed in Chapter 4.

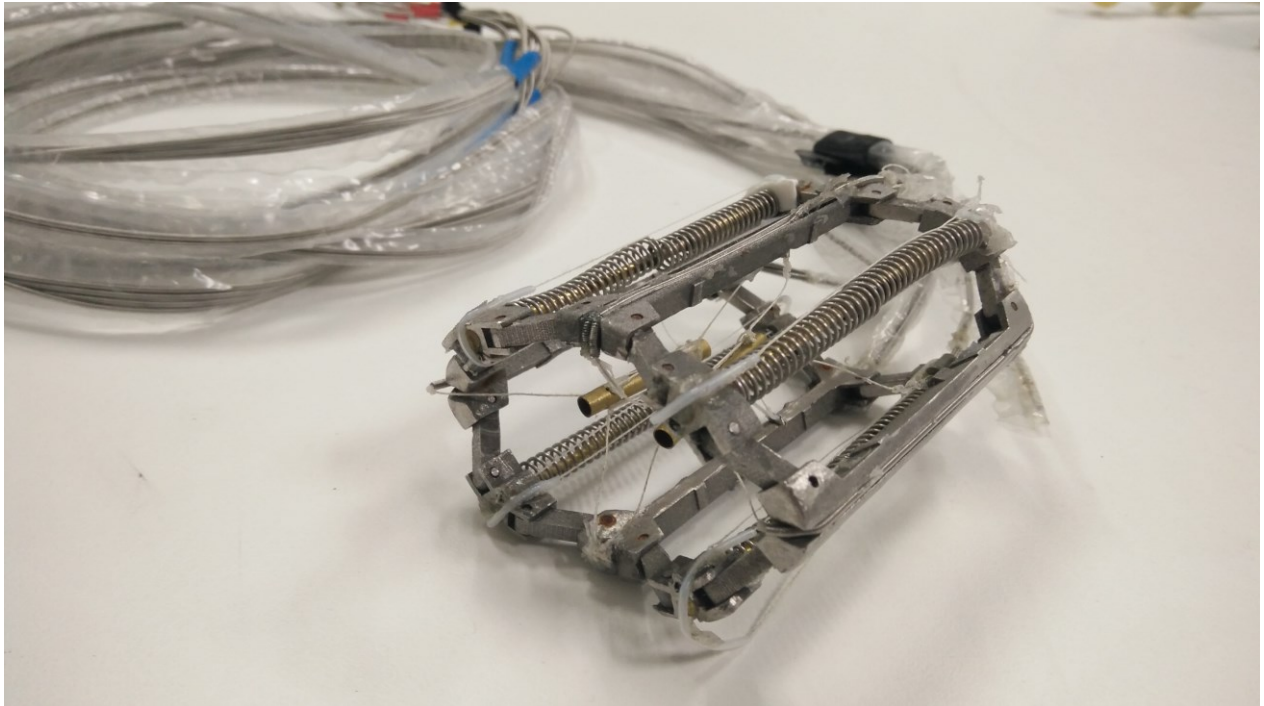


Figure A.2.1 - A first version of the ESD CYCLOPS scaffold.

A.3 neuroCYCLOPS and microCYCLOPS

The neuroCYCLOPS and microCYCLOPS are two iterations of the CYCLOPS system for neurosurgery and are shown in Figure A.3.1 and Figure A.3.2, respectively.

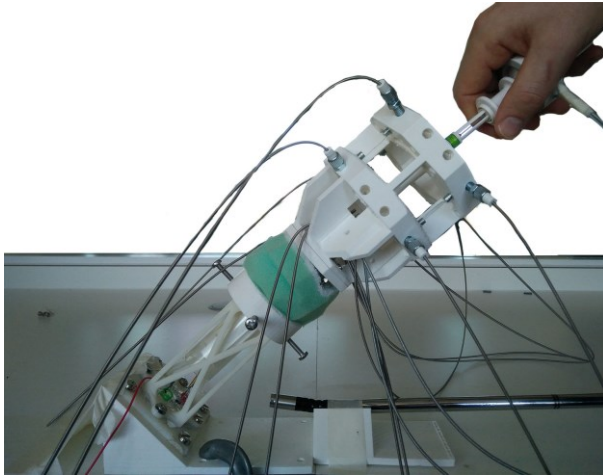


Figure A.3.1 - The neuroCYCLOPS

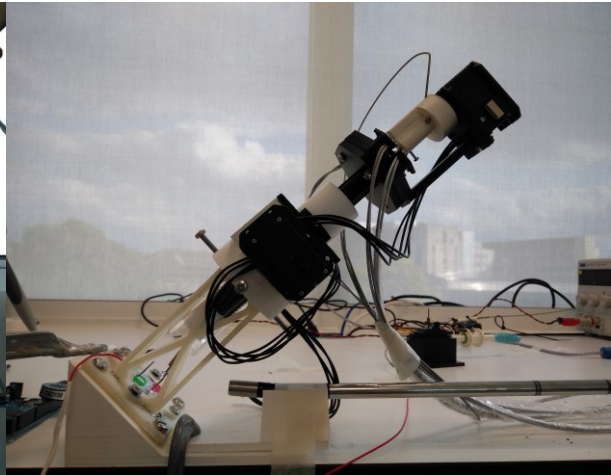


Figure A.3.2 - The microCYCLOPS

Both systems have been developed in earlier stage of this PhD, and are important to discuss briefly for their alternative minimally invasive access method. The core principle behind the access method is the use of a tubular tissue retractor to create a pathway and workspace inside the body. In case of the neuroCYCLOPS and microCYCLOPS, the tissue retractor is a neurosurgical brain dilator [374] which is used to gain access and remove deep-seated tumours (Figure A.3.3). As the brain dilator creates a pathway through paranchymal brain tissue, this access method is referred to as the transparachymal approach. The smallest brain dilators is the neuroendoport™, which creates a 11.5mm pathway for neuroendoscopic visualisation.

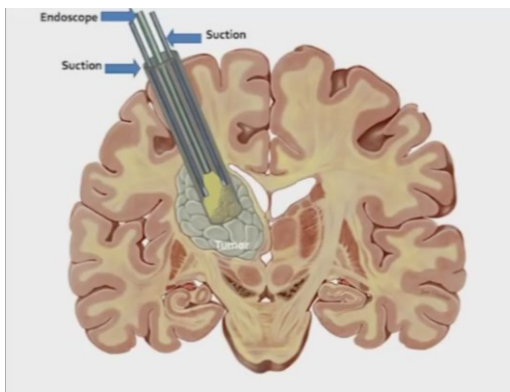


Figure A.3.3 - The neuroendoport used for reaching deep-seated brain tumours.

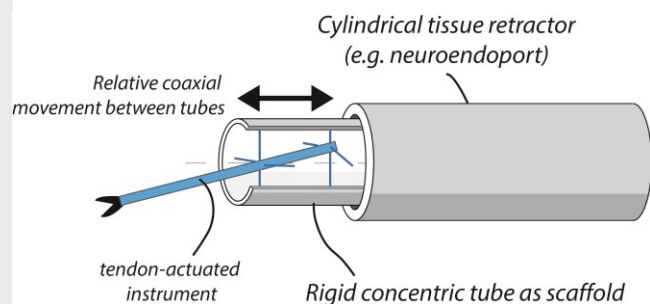


Figure A.3.4 - The CDPM principle adapted for the use with a cylindrical tissue retractor.

To resect tumours multiple long and slender instruments are inserted into the narrow pathway, and typically, an assistant is required to hold and manipulate the tubular device during resection. The CDPM can be used to increase instrument dexterity and to provide a stable platform for dissection and aspiration of tumours. Figure A.3.4 illustrates the way the CDPM is adapted for the

neuroCYCLOPS and microCYCLOPS to be used in junction with a tubular retraction device. The difference between both prototypes is the control method, which is manual in the neuroCYCLOPS and robotic in the microCYCLOPS. The principle of the manual neuroCYCLOPS is shown in Figure A.3.5. The motion of the master CDPM is duplicated by the way the cables are routed (Figure A.3.5b). The instrument is controlled in 6DoF, of which 5DoF are provided by the CDPM and an additional rotational DoF (roll) is provided by a pulley mechanism attached to the flexible instrument's shaft (Figure A.3.5a). The current prototype has a 18mm outer diameter, and further scaling down is required to fit the system in the neuroendoport. The systems provided a larger workspace when compared to the use of long slender instruments inside the neuroendoport. A pilot study, in which the neuroCYCLOPS was compared to long slender instruments in a peg-transfer task, demonstrated the neuroCYCLOPS lead to a reduction of undesired clashes with surrounding structures and therefore can be used to improve accuracy in control during neurosurgical removal of deep-seated lesions.

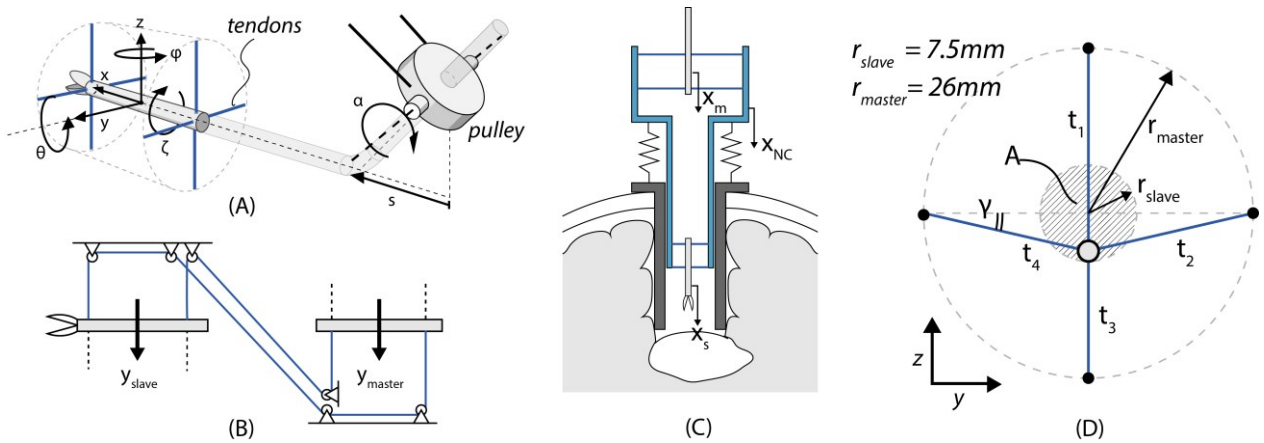


Figure A.3.5 - The principle of the manual control used for the neuroCYCLOPS.

The microCYCLOPS showed similar results, but friction in the Bowden cables resulted in less controllability when compared to the neuroCYCLOPS. A second generation of the microCYCLOPS has been developed (Figure A.3.6) in which the Bowden cables were replaced by direct pulley-pathways which resulted in a low friction in the actuation mechanism. The prototype has not been finished yet as further improvements on the control systems were required. However, the focus on low force transmission eventually led to the development of the CYCLOPS dVI. The aim of the microCYCLOPS 2.0 is the use of safe automated scanning to classify brain tissue with optical biopsies (e.g. hyperspectral imaging) followed by dissection of the tissue (e.g. using cavitron ultrasound surgical aspiration).



Figure A.3.6 - A second generation of the microCYCLOPS. The Bowden cables are replaced by direct cable pathways.

A.4 CYCLOPS da Vinci Instrument

The CYCLOPS da Vinci Instrument (CYCLOPS dVI, shown in Figure A.4.1) has been developed for the accurate control of contact forces between an endomicroscopy probe and tissue. Endomicroscopy can provide direct *in vivo* information about tissue pathology and has the potential to be used in surgery for detecting disease margins and subsequent accurate dissection. To ensure diseased tissue is dissected with positive margins a large area of the lesion should be visualised. However, endomicroscopy is currently based on a single probe which can only visualise a small surface area. Automation can provide a solution to this by using a scanning routine to create a map of a tissue surface. However, the quality of the endomicroscopy image highly depends on the contact forces between the tissue and the probe; it should be sufficient to ensure proper contact but when too high this degrades image quality and deforms the tissue. The CYCLOPS dVI has been developed to accurately estimate the contact forces by using a CDPM structure. It uses a four-cable planar CDPM to control its overtube, which contains the endomicroscopy probe.

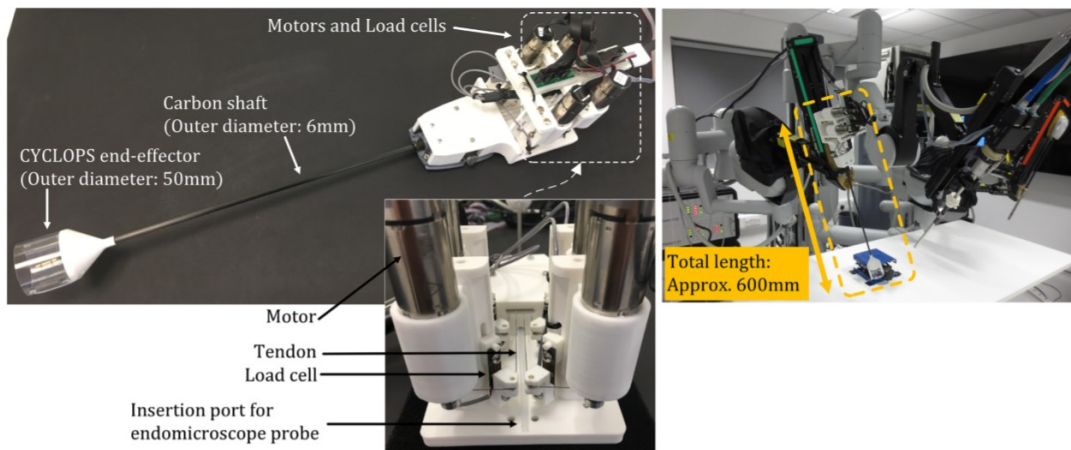


Figure A.4.1 - The prototype of the CYCLOPS dVI. The different parts are shown left. The right image shows the instrument mounted on the da Vinci system. Image source: [320].

The force sensitivity of the probe was evaluated on bovine liver tissue and compared to a ground-truth loadcell (Figure A.4.2). The experiments showed that contact forces as small as 0.2N could be sensed. However, an evaluation with experts in which the relationship between contact forces and quality of endomicroscopy images was assessed, showed that a 0.05N contact force yielded the highest quality images. The found contact force lies below the 0.2N minimal threshold of the CYCLOPS dVI, however to ensure high quality images were collected the probe was indented into the tissue up to 0.2N from which it acquires images while stepping backwards with submillimetre accuracy. The mechanism can therefore perform a safe scanning routine and acquire high quality endomicroscopy images. As adequate contact forces depends on tissue properties such as stiffness,

this can vary depending on the type of tissue and disease pathology. To ensure that high quality images are acquired independent of the scanned tissue, the routine should be combined with image analysis algorithms to assess image quality. However, the system showed that a basic autonomous scanning routine could be embedded and that high sensitivity can be measured with a CDPM. The force sensitivity can be used to provide haptic feedback to the surgeon, which has been explored with the CDAQS system in Chapter 5. Additionally, this approach can lead to further surface mapping, as explored by the SIMPLE system in Chapter 6.

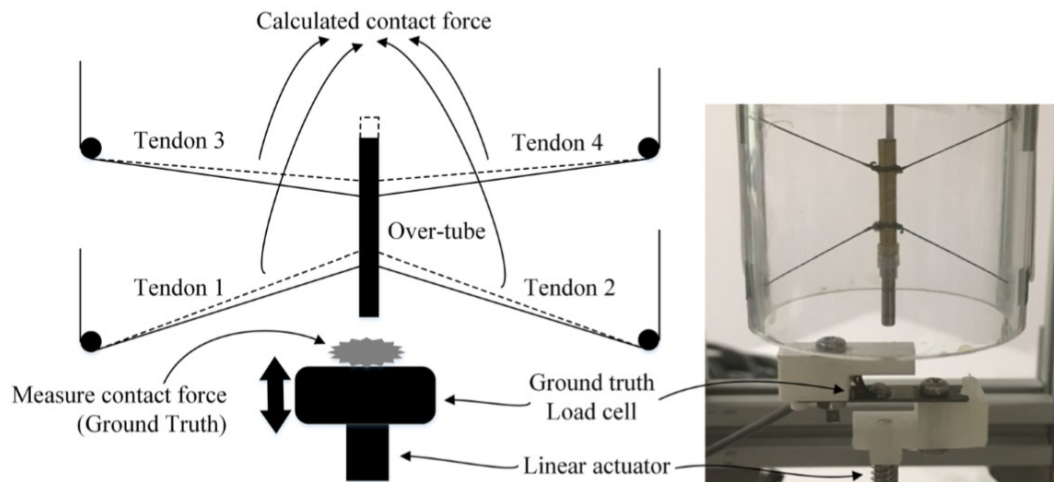


Figure A.4.2 - The planar CDPM used to control the endomicroscopy probe. The setup shown is used for comparison with the ground-truth loadcell. Image source: [320].

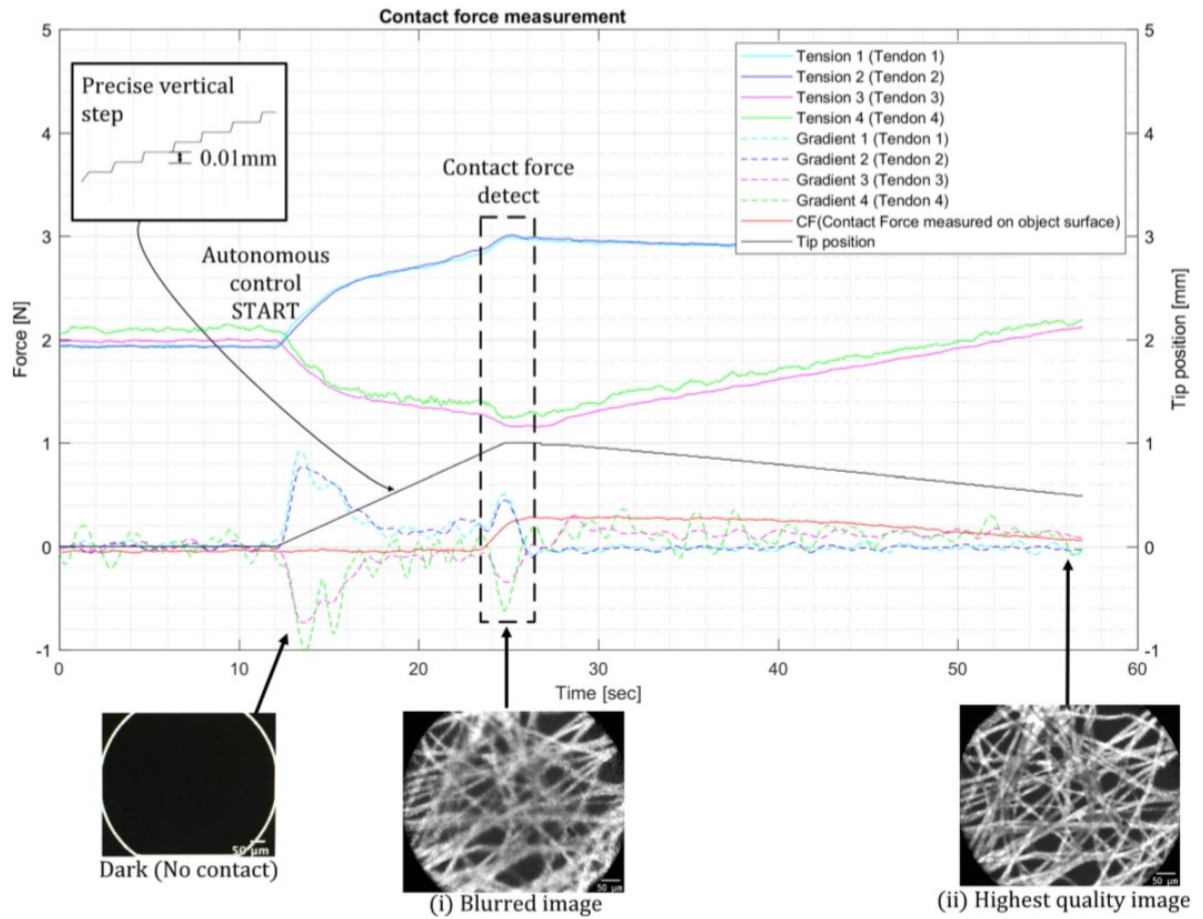


Figure A.5.3 - A single indentation performed by the CYCLOPS dVI. The endomicroscopy probe approaches the tissue surface until a contact force is detected (red). Then, the probe is slowly retracted while acquiring images. Image source: [320].

A.5 Cable coordinates of the CDAQS system

The entry points of the CDAQS are in millimetre:

	<i>Cable 1</i>	<i>Cable 2</i>	<i>Cable 3</i>	<i>Cable 4</i>	<i>Cable 5</i>	<i>Cable 6</i>
<i>X</i>	-126.8	-173.9	-137.4	142.6	140.8	154.7
<i>Y</i>	205.0	-22.1	-199.1	203.3	3.3	-190.4
<i>Z</i>	-116.3	214.1	-111.6	-103.7	218.5	-101.0

The cable attachment points of the probe in local coordinates are (in millimetre):

	<i>Cable 1</i>	<i>Cable 2</i>	<i>Cable 3</i>	<i>Cable 4</i>	<i>Cable 5</i>	<i>Cable 6</i>
<i>X</i>	-76.5	-76.5	-76.5	76.5	76.5	76.5
<i>Y</i>	14.3	0	-14.3	14.3	0.0	-14.3
<i>Z</i>	-8.3	16.5	-8.3	-8.3	16.5	-8.3

A.6 The results of the subjective evaluation of the palpation study

During the palpation user study discussed in Chapter 5 both quantitative and qualitative data was collected [321]. The qualitative data is shown in this section.

A NASA-TLX questionnaire was used to assess the subjective workload during the user study. The participants filled in the form after each task of the comparison study, which was either the visual-only or the visual-haptic palpation task. The results are shown in Figure A.6.1. Higher scores corresponded to a higher workload. The Wilcoxon signed-rank test was used for comparison between the overall workload showing statistical significance ($Z=3.36$, $p=0.0008$). The individual factors showed a significant difference for physical demand ($Z=2.55$, $p=0.011$), performance ($Z=1.97$, $p=0.049$), effort ($Z=3.05$, $p=0.002$) and frustration ($Z=2.68$, $p=0.0074$). In all cases the difference was due to a decreased workload for the combined visual-haptic task.

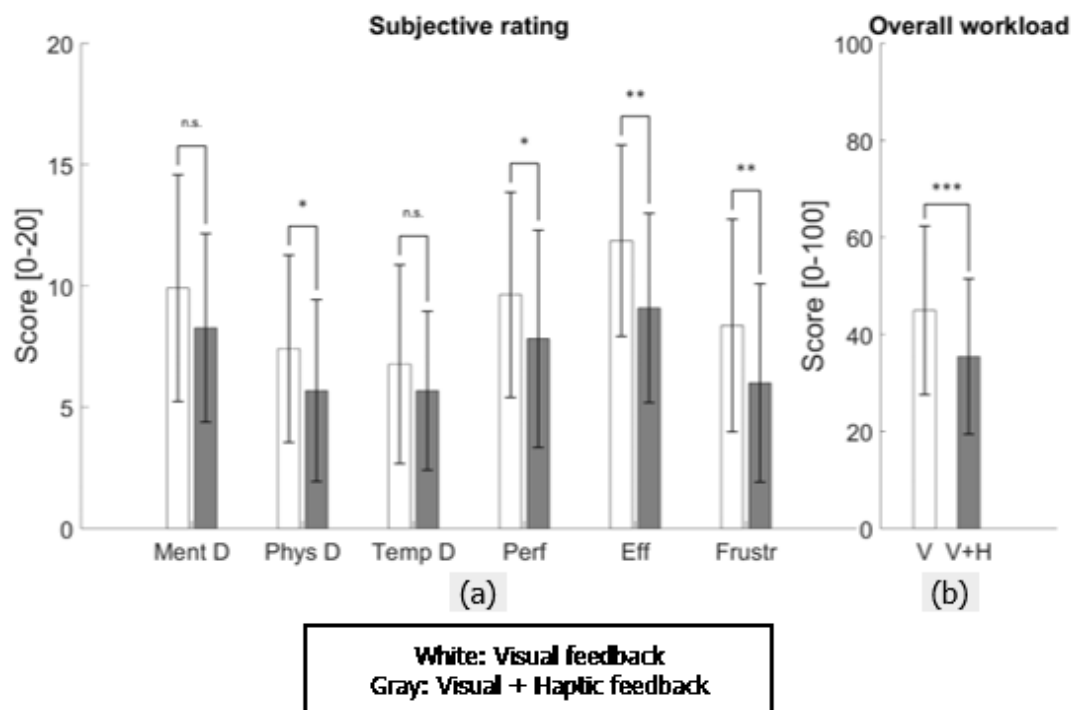


Figure A.6.1 - NASA-TLX results. (a) Single factors: (Mental Demand, Physical Demand, Temporal Demand, Performance, Effort, Frustration). (b) Overall workload: a higher score stands for a higher perceived workload. Image source: [321]

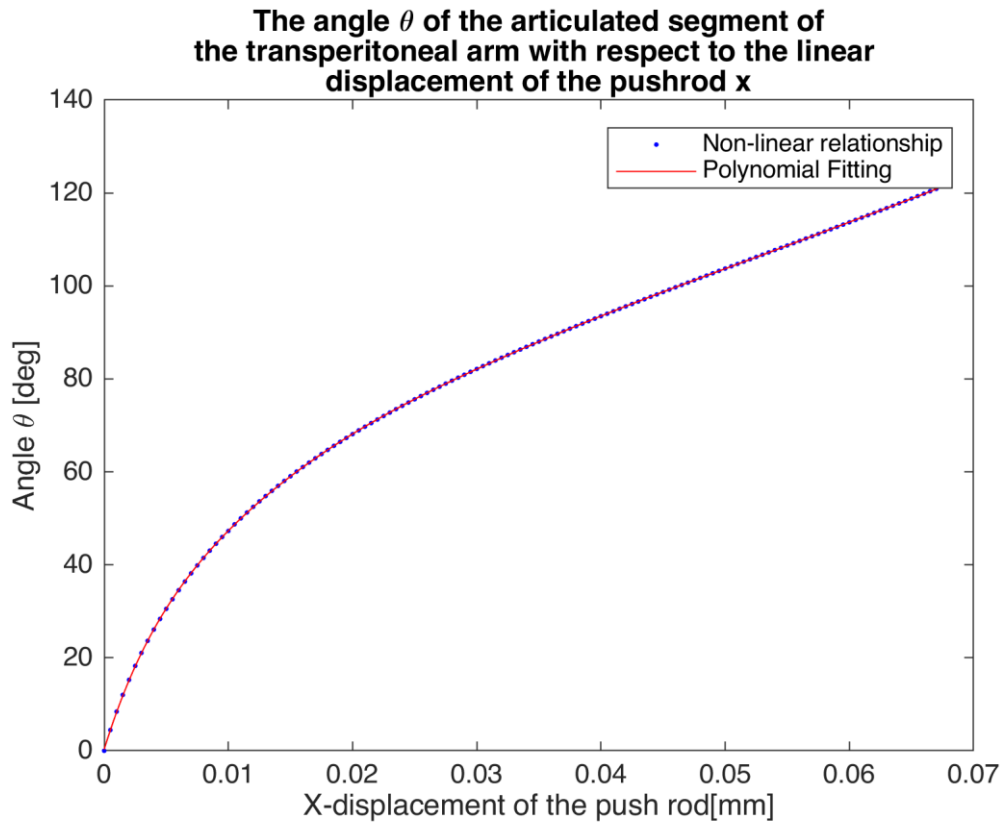
Additionally, a questionnaire with a Likert scale was presented to the participants at the end of the comparison study. The results are shown in Table A.6.1. These qualitative results refer to the comparison between Visual-only and Visual-Haptics experimental conditions.

Question #	SD [%]	D [%]	N [%]	A [%]	SA [%]
1. I was feeling more comfortable using the system with force feedback	/	10	10	62	19
2. The task was easier to perform with force feedback than without force feedback	/	5	14	48	33
3. The task with force feedback was less stressful than without force feedback	/	14	33	38	14
4. Overall, I would choose to have force feedback than not having force feedback	/	10	5	48	38

Table A.6.1 - The results from the questionnaire, using a Likert scale. The questionnaire was held after participants had finished the comparison study (visual-only vs visual-haptic). SD: strongly disagree, D: disagree, N: neutral, A: agree, SA: strongly agree. [321]

A.7 Parametric fitting of the forward kinematics of the transperitoneal shaft

In chapter 6 the non-linear equations (6.1) and (6.2) can be fitted parametrically to describe the angle θ as a function of the position of the linear position of the push rod x . The figure below shows the relationship and its parametric fitting.



The following 9th order polynomial is used:

$$\theta(x) = p_1x^9 + p_2x^8 + p_3x^7 + p_4x^6 + p_5x^5 + p_6x^4 + p_7x^3 + p_8x^2 + p_9x + p_{10}$$

The fitted parameters for the equation in radians are shown in the table below. The RMSE of the fitting is 0.04 radians.

p_1	p_2	p_3	p_4	p_5	p_6	p_7	p_8	p_9	p_{10}
4.07e+14	-1.366e+14	1.96e+13	-1.57e+12	7.741e+10	-2.447e+09	5.083e+07	-7.248e+05	8683	0.2815

A.8 Algorithm structure used for workspace optimisation

The pseudocode below shows the combined Particle Swarm Optimisation (PSO) and Particle Filter Optimisation (PFO) algorithm used for the workspace optimisation in Chapter 7. Multiple *runs* are used to find the optimal solution, in which this routine below is repeated to find other optima. The best value found during all these runs is used as the selected optimum.

Optimization algorithm used to find the optimal parameter configuration for the ESD CYCLOPS for a given task space. The pseudocode represents a single run of the algorithm.

Input: Task space, parameter upper and lower bounds, ESD CYCLOPS constants

Output: Design vector parameters

- 1 Initialize particle swarm by sampling the parameter space uniformly
- 2 Evaluate the objective function for each particle

Particle Swarm search loop

- 3 **for** $i < \text{number of PSO iterations}$ **do**
- 4 Update particle velocities and positions
- 5 Evaluate objective function for each particle
- 6 **if** no better position is found **then**
- 7 Perform pattern search poll step for best particle
- 8 **if** poll step succeeds **then**
- 9 Increase pattern search mesh size
- 10 **else**
- 11 Decrease pattern search mesh size
- 12 **end if**
- 13 **end if**
- 14 Perform simulated annealing based random resampling
- 15 **end for**

Particle Filter Optimization loop

- 16 Initialize particle swarm for PFO by sampling from previous population
- 17 **for** $i < \text{number of PFO iterations}$ **do**
- 18 Update particle velocities and positions
- 19 Evaluate objective function for each particle
- 20 Update weights of particles based on value of the objective function
- 21 Resample particles based on weights
- 22 **end for**
- 23 **Return** best position and value of the objective function

A.9 Linear-least squares method for calculation of the robot-mounting point of the transperitoneal arm

The equations (7.2)- (7.4) in Chapter 7, can be rewritten in the general algebraic form of $Ax = b$:

$$\begin{bmatrix} r_{13} & 1 & 0 & 0 & 0 & 0 & 0 \\ r_{23} & 0 & 1 & 0 & 0 & 0 & 0 \\ r_{33} & 0 & 0 & 1 & 0 & 0 & 0 \\ 0 & 1 & 0 & 0 & -1 & 0 & 0 \\ 0 & 0 & 1 & 0 & 0 & -1 & 0 \\ 0 & 0 & 0 & 1 & 0 & 0 & -1 \\ 0 & 0 & 0 & 0 & -P_{10} & -P_{01} & 1 \end{bmatrix} \begin{bmatrix} c_2 \\ A_x \\ A_y \\ A_z \\ V_{r,x} \\ V_{r,y} \\ V_{r,z} \end{bmatrix} = \begin{bmatrix} E_x - e_x^T R P_{shaft} \\ E_y - e_y^T R P_{shaft} \\ E_z - e_z^T R P_{shaft} \\ -e_x^T R V_{arm} \\ -e_y^T R V_{arm} \\ -e_z^T R V_{arm} \\ h_{offset} + P_{00} \end{bmatrix}$$

The values r_{13}, r_{23} and r_{33} represent the ij th element of the rotation vector $R(\alpha, \beta, \gamma)$. The first order polynomial is used for obtaining the algebraic description of viscera, $P_{vis}(x, y) = P_{00} + P_{10}x + P_{01}y$. The first order polynomial represents a plane in 3D space, and it is a simplification from the more complex outer surface of the viscera. While higher order polynomials would get a better fitting to the visceral surface, it would also lead to additional variables in the above equation (e.g. $V_{r,x}^2, V_{r,y}^2$ and $V_{r,x}V_{r,y}$ for a second order polynomial). With more variables the above equation will not have a closed-form solution, requiring numerical solutions to find all variables. Such a numerical solution becomes cumbersome when many iterations are required, which is the case during the optimization routine. By taking the first order polynomial as an assumption, the variables can be solved algebraically using a linear least-squares.

A.10 Anatomical Landmarks selected using CT-images

The landmarks used in chapter 7 are found in the table A.10.1 and the figures A.10.1-A.10.5.

	<i>X-axis</i>	<i>Y-axis</i>	<i>Z-axis</i>
Umbilicus, after pneumoperitoneum of 16mmHg	36.10	14.17	28.70
Liver, Left medial section	184.4	66.87	-47.72
Gallbladder (Cystic Duct)	148.4	57.75	-108.8
Appendix	-23.60	94.23	-123.4
Left Renal Hilum	105.4	-69.04	-155.3
Right Renal Hilum	96.40	62.31	-155.3

Table A.10.1 - 3D coordinates (in millimetre) of points found using the CT images. The global origin provided by the CT scanner is used. The coordinates are found by highlighting the anatomical position in the ITK Snap software, as shown for each point in Figures A.10.1.-A.10.5. The umbilicus coordinate is found after simulated inflation of 16mmHg using software developed at the Department of Surgery and Cancer, Imperial College London[358].

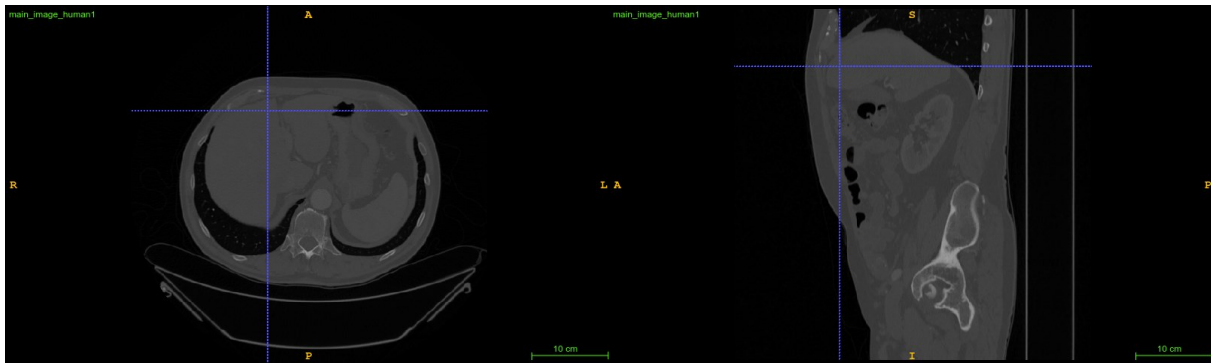


Figure A.10.1 - The axial (left) and sagittal plane indicating a point on the right liver lobe, left medial section.

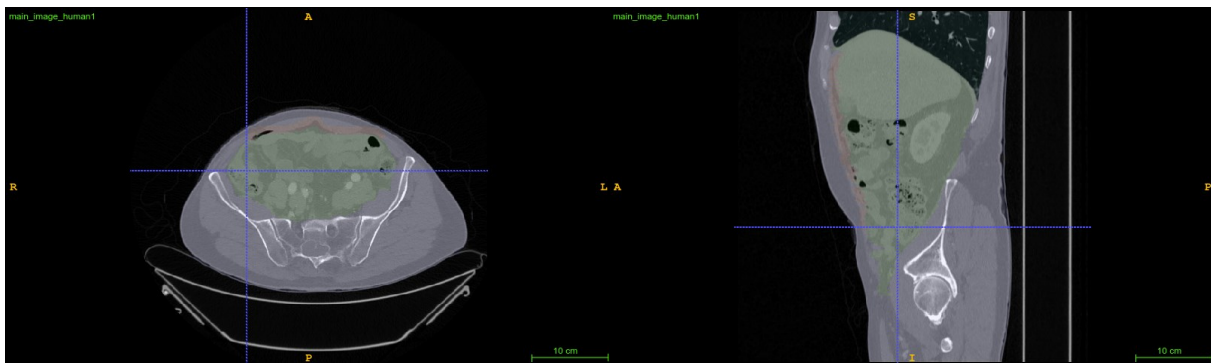


Figure A.10.2 - The axial (left) and sagittal plane indicating the appendix.

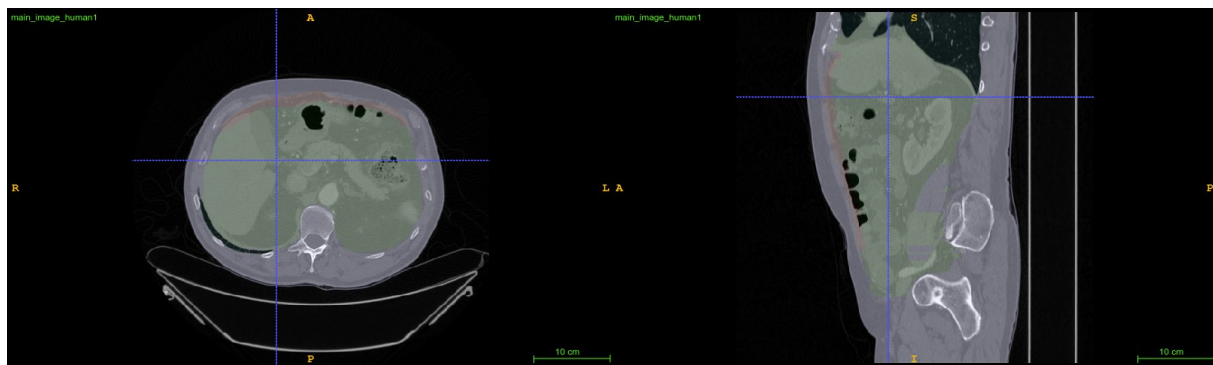


Figure A.10.3 - The axial (left) and sagittal plane indicating the cystic duct of the gallbladder.

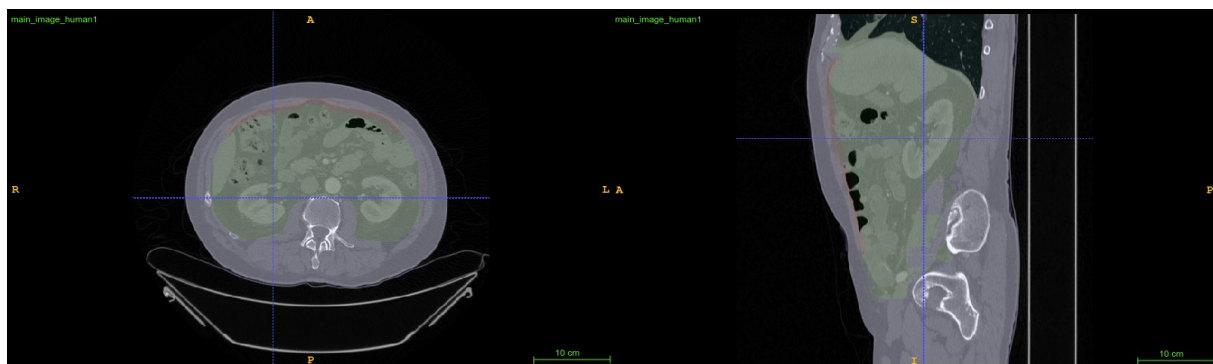


Figure A.10.4 - The axial (left) and sagittal plane indicating the right renal hilum.

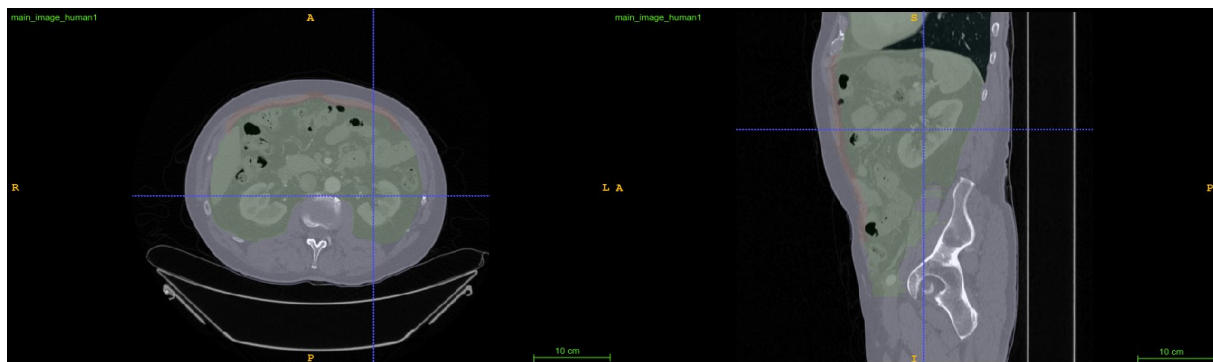


Figure A.10.5 - The axial (left) and sagittal plane indicating the left renal hilum.

References

- [1] A. C. S. van Heel, "A new method of transporting optical images without aberrations," *Nature*, vol. 173, no. 4392, p. 39, 1954.
- [2] H. H. Hopkins and N. S. Kapany, "A flexible fibrescope, using static scanning," *Nature*, vol. 173, no. 4392, p. 39, 1954.
- [3] S. D. S. Peter and G. W. Holcomb III, "History of Minimally Invasive Surgery," *Atlas Pediatr. Laparosc. Thoracoscopy*, p. 1, 2008.
- [4] G. S. Litynski, "Kurt Semm and the fight against skepticism: endoscopic hemostasis, laparoscopic appendectomy, and Semm's impact on the 'laparoscopic revolution,'" *JSL J. Soc. Laparoendosc. Surg.*, vol. 2, no. 3, p. 309, 1998.
- [5] B. I. Hirschowitz, "A personal history of the fiberscope," *Gastroenterology*, vol. 76, no. 4, pp. 864–869, 1979.
- [6] J. Wallén, *The history of the industrial robot*. Linköping University Electronic Press, 2008.
- [7] C. C. L. or Open Resection Study Group and others, "Laparoscopic surgery versus open surgery for colon cancer: short-term outcomes of a randomised trial," *Lancet Oncol.*, vol. 6, no. 7, pp. 477–484, 2005.
- [8] D. I. Watson, R. J. Baigrie, and G. G. Jamieson, "A learning curve for laparoscopic fundoplication. Definable, avoidable, or a waste of time?," *Ann. Surg.*, vol. 224, no. 2, p. 198, 1996.
- [9] D. C. Miller, J. T. Wei, R. L. Dunn, and B. K. Hollenbeck, "Trends in the diffusion of laparoscopic nephrectomy," *JAMA*, vol. 295, no. 21, pp. 2476–2482, 2006.
- [10] K. Ahmed, T. T. Wang, V. M. Patel, K. Nagpal, J. Clark, M. Ali, S. Deeba, H. Ashrafian, A. Darzi, T. Athanasiou, and others, "The role of single-incision laparoscopic surgery in abdominal and pelvic surgery: a systematic review," *Surg. Endosc.*, vol. 25, no. 2, pp. 378–396, 2011.
- [11] A. Arezzo, R. Passera, A. Bullano, Y. Mintz, A. Kedar, L. Boni, E. Cassinotti, R. Rosati, U. F. Romario, M. Sorrentino, and others, "Multi-port versus single-port cholecystectomy: results of a multi-centre, randomised controlled trial (MUSIC trial)," *Surg. Endosc.*, vol. 31, no. 7, pp. 2872–2880, 2017.
- [12] H.-J. Li, L. Huang, T.-J. Li, J. Su, L.-R. Peng, and W. Liu, "Short-term outcomes of single-incision

- versus conventional laparoscopic surgery for colorectal diseases: meta-analysis of randomized and prospective evidence," *J. Gastrointest. Surg.*, vol. 21, no. 11, pp. 1931–1945, 2017.
- [13] L. Yang, J. Gao, L. Zeng, Z. Weng, and S. Luo, "Systematic review and meta-analysis of single-port versus conventional laparoscopic hysterectomy," *Int. J. Gynecol. Obstet.*, vol. 133, no. 1, pp. 9–16, 2016.
- [14] X. Fan, T. Lin, K. Xu, Z. Yin, H. Huang, W. Dong, and J. Huang, "Laparoendoscopic single-site nephrectomy compared with conventional laparoscopic nephrectomy: a systematic review and meta-analysis of comparative studies," *Eur. Urol.*, vol. 62, no. 4, pp. 601–612, 2012.
- [15] A. N. Kalloo, V. K. Singh, S. B. Jagannath, H. Niiyama, S. L. Hill, C. A. Vaughn, C. A. Magee, and S. V Kantsevov, "Flexible transgastric peritoneoscopy: a novel approach to diagnostic and therapeutic interventions in the peritoneal cavity," *Gastrointest. Endosc.*, vol. 60, no. 1, pp. 114–117, 2004.
- [16] D. A. Tsin, "Culdolaparoscopy: a preliminary report," *JSLS J. Soc. Laparoendosc. Surg.*, vol. 5, no. 1, p. 69, 2001.
- [17] D. A. Tsin, R. J. Sequeria, and G. Giannikas, "Culdolaparoscopic cholecystectomy during vaginal hysterectomy," *JSLS J. Soc. Laparoendosc. Surg.*, vol. 7, no. 2, p. 171, 2003.
- [18] D. A. Tsin, L. T. Colombero, D. Mahmood, J. Padouvas, and P. Manolas, "Operative culdolaparoscopy: a new approach combining operative culdoscopy and minilaparoscopy," *J. Am. Assoc. Gynecol. Laparosc.*, vol. 8, no. 3, pp. 438–441, 2001.
- [19] E. Della Flora, T. G. Wilson, I. J. Martin, N. A. O’rourke, and G. J. Maddern, "A review of natural orifice transluminal endoscopic surgery (NOTES) for intra-abdominal surgery: experimental models, techniques, and applicability to the clinical setting," *Ann. Surg.*, vol. 247, no. 4, pp. 583–602, 2008.
- [20] D. Rattner and A. Kalloo, "ASGE/SAGES working group on natural orifice transluminal endoscopic surgery," *Surg. Endosc. Other Interv. Tech.*, vol. 20, no. 2, pp. 329–333, 2006.
- [21] D. W. Rattner, R. Hawes, S. Schwaitzberg, M. Kochman, and L. Swanstrom, "The Second SAGES/ASGE White Paper on natural orifice transluminal endoscopic surgery: 5 years of progress," *Surg. Endosc.*, vol. 25, no. 8, pp. 2441–2448, 2011.
- [22] S. D. Schwaitzberg, K. Roberts, J. R. Romanelli, D. J. Desilets, D. Earle, S. Horgan, L. Swanstrom, E. Hungness, N. Soper, M. L. Kochman, and others, "The NOVEL trial: natural orifice versus laparoscopic cholecystectomy—a prospective, randomized evaluation," *Surg. Endosc.*, vol. 32,

- no. 5, pp. 2505–2516, 2018.
- [23] J. F. Baekelandt, P. A. De Mulder, I. Le Roy, C. Mathieu, A. Laenen, P. Enzlin, S. Weyers, B. W. J. Mol, and J. J. A. Bosteels, “Hysterectomy by Transvaginal Natural Orifice Transluminal Endoscopic Surgery versus laparoscopy as a day-care procedure: a randomised controlled trial,” *BJOG An Int. J. Obstet. Gynaecol.*, vol. 126, no. 1, pp. 105–113, 2019.
 - [24] Y. S. Kwoh, J. Hou, E. A. Jonckheere, and S. Hayati, “A robot with improved absolute positioning accuracy for CT guided stereotactic brain surgery,” *IEEE Trans. Biomed. Eng.*, vol. 35, no. 2, pp. 153–160, 1988.
 - [25] S. Lavallee, J. Troccaz, L. Gaborit, P. Cinquin, A.-L. Benabid, and D. Hoffmann, “Image guided operating robot: a clinical application in stereotactic neurosurgery,” in *Robotics and Automation, 1992. Proceedings., 1992 IEEE International Conference on*, 1992, pp. 618–624.
 - [26] M. Jakopcic, S. J. Harris, F. y Baena, P. Gomes, and B. L. Davies, “The Acrobot® system for total knee replacement,” *Ind. Robot An Int. J.*, vol. 30, no. 1, pp. 61–66, 2003.
 - [27] W. Siebert, S. Mai, R. Kober, and P. F. Heeckt, “Technique and first clinical results of robot-assisted total knee replacement,” *Knee*, vol. 9, no. 3, pp. 173–180, 2002.
 - [28] S. J. Harris, F. Arambula-Cosio, Q. Mei, R. D. Hibberd, B. L. Davies, J. E. A. Wickham, M. S. Nathan, and B. Kundu, “The Probot—an active robot for prostate resection,” *Proc. Inst. Mech. Eng. Part H J. Eng. Med.*, vol. 211, no. 4, pp. 317–325, 1997.
 - [29] M. J. H. Lum, D. C. W. Friedman, G. Sankaranarayanan, H. King, K. Fodero, R. Leuschke, B. Hannaford, J. Rosen, and M. N. Sinanan, “The RAVEN: Design and validation of a telesurgery system,” *Int. J. Rob. Res.*, vol. 28, no. 9, pp. 1183–1197, 2009.
 - [30] B. Hannaford, J. Rosen, D. W. Friedman, H. King, P. Roan, L. Cheng, D. Glozman, J. Ma, S. N. Kosari, and L. White, “Raven-II: an open platform for surgical robotics research,” *IEEE Trans. Biomed. Eng.*, vol. 60, no. 4, pp. 954–959, 2013.
 - [31] T. Haidegger and Z. Benyo, “Surgical robotic support for long duration space missions,” *Acta Astronaut.*, vol. 63, no. 7–10, pp. 996–1005, 2008.
 - [32] U. Hagn, R. Konietzschke, A. Tobergte, M. Nickl, S. Jörg, B. Kübler, G. Passig, M. Gröger, F. Fröhlich, U. Seibold, and others, “DLR MiroSurge: a versatile system for research in endoscopic telesurgery,” *Int. J. Comput. Assist. Radiol. Surg.*, vol. 5, no. 2, pp. 183–193, 2010.
 - [33] V. Vitiello, “Emerging Robotic Platforms for Minimally Invasive Surgery,” *Biomed. Eng. IEEE*

Rev., vol. 6, pp. 111–126, 2013.

- [34] G. P. Mylonas, V. Vitiello, T. P. Cundy, A. Darzi, and G.-Z. Yang, “CYCLOPS: A versatile robotic tool for bimanual single-access and natural-orifice endoscopic surgery,” *2014 IEEE Int. Conf. Robot. Autom.*, pp. 2436–2442, 2014.
- [35] P. Berkelman, E. Boidard, P. Cinquin, and J. Troccaz, “LER: The light endoscope robot,” in *Intelligent Robots and Systems, 2003.(IROS 2003). Proceedings. 2003 IEEE/RSJ International Conference on*, 2003, vol. 3, pp. 2835–2840.
- [36] I. Bricault, E. Jauniaux, N. Zemiti, C. Fouard, E. Taillant, F. Dorandeu, P. Cinquin, I. Bricault, E. Jauniaux, N. Zemiti, C. Fouard, E. Taillant, and L. P. R. A. Light, “LPR : A Light Puncture Robot for CT and MRI Interventions,” 2008.
- [37] A. D. Costanza, N. A. Wood, M. J. Passineau, R. J. Moraca, S. H. Bailey, T. Yoshizumi, and C. N. Riviere, “A parallel wire robot for epicardial interventions,” in *Engineering in Medicine and Biology Society (EMBC), 2014 36th Annual International Conference of the IEEE*, 2014, pp. 6155–6158.
- [38] P. Berkelman, P. Cinquin, J. Troccaz, J. Ayoubi, C. Letoublon, and F. Bouchard, “A compact, compliant laparoscopic endoscope manipulator,” in *Proceedings 2002 IEEE International Conference on Robotics and Automation (Cat. No. 02CH37292)*, 2002, vol. 2, pp. 1870–1875.
- [39] J. Albus, R. Bostelman, and N. Dagalakis, “The NIST robocrane,” *J. Robot. Syst.*, vol. 10, no. 5, pp. 709–724, 1993.
- [40] N. G. Dagalakis, J. S. Albus, B.-L. Wang, J. Unger, and J. D. Lee, “Stiffness study of a parallel link robot crane for shipbuilding applications,” *J. Offshore Mech. Arct. Eng.*, vol. 111, no. 3, pp. 183–193, 1989.
- [41] M. Nahon, G. Gilardi, and C. Lambert, “Dynamics/control of a radio telescope receiver supported by a tethered aerostat,” *J. Guid. Control. Dyn.*, vol. 25, no. 6, pp. 1107–1115, 2002.
- [42] F. Takemura, M. Enomoto, T. Tanaka, K. Denou, Y. Kobayashi, and S. Tadokoro, “Development of the balloon-cable driven robot for information collection from sky and proposal of the search strategy at a major disaster,” in *Advanced Intelligent Mechatronics. Proceedings, 2005 IEEE/ASME International Conference on*, 2005, pp. 658–663.
- [43] R. Verhoeven, “Analysis of the workspace of tendon-based Stewart platforms,” Universität Duisburg-Essen, Fakultät für Ingenieurwissenschaften~..., 2004.

- [44] D. Lau, D. Oetomo, and S. K. Halgamuge, "Generalized modeling of multilink cable-driven manipulators with arbitrary routing using the cable-routing matrix," *IEEE Trans. Robot.*, vol. 29, no. 5, pp. 1102–1113, 2013.
- [45] S. Rezazadeh and S. Behzadipour, "Workspace analysis of multibody cable-driven mechanisms," *J. Mech. Robot.*, vol. 3, no. 2, p. 21005, 2011.
- [46] S. Behzadipour, R. Dekker, A. Khajepour, and E. Chan, "DeltaBot: A new cable-based ultra high speed robot," in *ASME 2003 International Mechanical Engineering Congress and Exposition*, 2003, pp. 533–537.
- [47] D. T. M. Lau, "Modelling and analysis of anthropomorphic cable-driven robots," The University of Melbourne, 2014.
- [48] D. B. Roppenecker, a Meining, G. Horst, H. Ulbrich, and T. C. Lueth, "Interdisciplinary development of a Single - Port Robot," pp. 612–617, 2012.
- [49] S. Behzadipour and A. Khajepour, "Stiffness of cable-based parallel manipulators with application to stability analysis," *J. Mech. Des.*, vol. 128, no. 1, pp. 303–310, 2006.
- [50] A. Fattah and S. K. Agrawal, "On the design of cable-suspended planar parallel robots," *J. Mech. Des.*, vol. 127, no. 5, pp. 1021–1028, 2005.
- [51] A. M. Hay and J. A. Snyman, "Optimization of a planar tendon-driven parallel manipulator for a maximal dextrous workspace," *Eng. Optim.*, vol. 37, no. 3, pp. 217–236, 2005.
- [52] C. M. Gosselin, I. Ebert-Uphoff, P. Lafourcade, M. Llibre, and C. Reboulet, "Design of a Parallel Wire-Driven Manipulator for Wind Tunnels."
- [53] S. Fang, D. Franitza, M. Torlo, F. Bekes, and M. Hiller, "Motion control of a tendon-based parallel manipulator using optimal tension distribution," *IEEE/ASME Trans. Mechatronics*, vol. 9, no. 3, pp. 561–568, 2004.
- [54] A. Moradi, "Stiffness analysis of cable-driven parallel robots," Queen's University, 2013.
- [55] C. B. Pham, S. H. Yeo, G. Yang, and I.-M. Chen, "Workspace analysis of fully restrained cable-driven manipulators," *Rob. Auton. Syst.*, vol. 57, no. 9, pp. 901–912, 2009.
- [56] J. A. Snyman and A. M. Hay, "The chord method for the determination of non-convex workspaces of planar parallel platforms," in *Advances in Robot Kinematics*, Springer, 2000, pp. 285–294.

- [57] C. Gosselin, "Cable-driven parallel mechanisms: state of the art and perspectives," *Mech. Eng. Rev.*, vol. 1, no. 1, pp. DSM0004--DSM0004, 2014.
- [58] S. Qian, B. Zi, W.-W. Shang, and Q.-S. Xu, "A review on cable-driven parallel robots," *Chinese J. Mech. Eng.*, vol. 31, no. 1, p. 66, 2018.
- [59] X. Tang and R. Yao, "Dimensional design on the six-cable driven parallel manipulator of FAST," *J. Mech. Des.*, vol. 133, no. 11, p. 111012, 2011.
- [60] P. Dewdney, M. Nahon, and B. Veidt, "The large adaptive reflector: A giant radio telescope with an aero twist," *Can. Aeronaut. Sp. J.*, vol. 48, no. 4, pp. 239–250, 2002.
- [61] A. Pott, H. Mütterich, W. Kraus, V. Schmidt, P. Miermeister, and A. Verl, "IPAnema: a family of cable-driven parallel robots for industrial applications," in *Cable-Driven Parallel Robots*, Springer, 2013, pp. 119–134.
- [62] S. Kawamura, W. Choe, S. Tanaka, and S. R. Pandian, "Development of an ultrahigh speed robot FALCON using wire drive system," *Proc. - IEEE Int. Conf. Robot. Autom.*, vol. 1, pp. 215–220, 1995.
- [63] A. Pott, C. Meyer, and A. Verl, "Large-scale assembly of solar power plants with parallel cable robots," in *Robotics (ISR), 2010 41st International Symposium on and 2010 6th German Conference on Robotics (ROBOTIK)*, 2010, pp. 1–6.
- [64] K. Maeda, S. Tadokoro, T. Takamori, M. Hiller, and R. Verhoeven, "On design of a redundant wire-driven parallel robot WARP manipulator," in *Robotics and Automation, 1999. Proceedings. 1999 IEEE International Conference on*, 1999, vol. 2, pp. 895–900.
- [65] R. Bostelman, A. Jacoff, F. Proctor, T. Kramer, and A. Wavering, "Cable-based reconfigurable machines for large scale manufacturing," in *Proceedings of the 2000 Japan-USA Symposium on Flexible Automation*, 2000, pp. 23–26.
- [66] P. Bosscher, R. L. Williams II, L. S. Bryson, and D. Castro-Lacouture, "Cable-suspended robotic contour crafting system," *Autom. Constr.*, vol. 17, no. 1, pp. 45–55, 2007.
- [67] E. Barnett and C. Gosselin, "Large-scale 3D printing with a cable-suspended robot," *Addit. Manuf.*, vol. 7, pp. 27–44, 2015.
- [68] R. R. Thompson and M. S. Blackstone, "Three-dimensional moving camera assembly with an informational cover housing," US6873355B1, 2005.
- [69] J. Rodnunsky, "System and method for moving objects within three-dimensional space,"

US8638989B2, 2004.

- [70] P. H. Borgstrom, B. L. Jordan, B. J. Borgstrom, M. J. Stealey, G. S. Sukhatme, M. A. Batalin, and W. J. Kaiser, "Nims-pl: A cable-driven robot with self-calibration capabilities," *IEEE Trans. Robot.*, vol. 25, no. 5, pp. 1005–1015, 2009.
- [71] B. L. Jordan, M. A. Batalin, and W. J. Kaiser, "NIMS RD: A rapidly deployable cable based robot," in *Robotics and Automation, 2007 IEEE International Conference on*, 2007, pp. 144–150.
- [72] C. Melchiorri and G. Vassura, "Development and application of wire-actuated haptic interfaces," *J. Robot. Syst.*, vol. 18, no. 12, pp. 755–768, 2001.
- [73] M. Sato, "Development of string-based force display: SPIDAR," in *8th international conference on virtual systems and multimedia*, 2002.
- [74] M. Hirose, K. Hirota, T. Ogi, H. Yano, N. Takehi, M. Saito, and M. Nakashige, "HapticGEAR: the development of a wearable force display system for immersive projection displays," in *Virtual Reality, 2001. Proceedings. IEEE*, 2001, pp. 123–129.
- [75] J. v Zitzewitz, G. Rauter, R. Steiner, A. Brunschweiler, and R. Riener, "A versatile wire robot concept as a haptic interface for sport simulation," in *Robotics and Automation, 2009. ICRA'09. IEEE International Conference on*, 2009, pp. 313–318.
- [76] N. Tarrin, S. Coquillart, S. Hasegawa, L. Bouguila, and M. Sato, "The stringed haptic workbench: a new haptic workbench solution," in *Computer graphics forum*, 2003, vol. 22, no. 3, pp. 583–589.
- [77] D. Surdilovic and R. Bernhardt, "STRING-MAN: a new wire robot for gait rehabilitation," in *Robotics and Automation, 2004. Proceedings. ICRA'04. 2004 IEEE International Conference on*, 2004, vol. 2, pp. 2031–2036.
- [78] G. Rosati, P. Gallina, S. Masiero, and A. Rossi, "Design of a new 5 dof wire-based robot for rehabilitation," in *Rehabilitation Robotics, 2005. ICORR 2005. 9th International Conference on*, 2005, pp. 430–433.
- [79] D. Mayhew, B. Bachrach, W. Z. Rymer, and R. F. Beer, "Development of the MACARM-a novel cable robot for upper limb neurorehabilitation," in *Rehabilitation Robotics, 2005. ICORR 2005. 9th International Conference on*, 2005, pp. 299–302.
- [80] Y. Mao and S. K. Agrawal, "Design of a cable-driven arm exoskeleton (CAREX) for neural

- rehabilitation," *IEEE Trans. Robot.*, vol. 28, no. 4, pp. 922–931, 2012.
- [81] J. Merlet and D. Daney, "A portable, modular parallel wire crane for rescue operations," in *Robotics and Automation (ICRA), 2010 IEEE International Conference on*, 2010, pp. 2834–2839.
 - [82] S. Tadokoro, R. Verhoeven, M. Hiller, and T. Takamori, "A portable parallel manipulator for search and rescue at large-scale urban earthquakes and an identification algorithm for the installation in unstructured environments," in *Intelligent Robots and Systems, 1999. IROS'99. Proceedings. 1999 IEEE/RSJ International Conference on*, 1999, vol. 2, pp. 1222–1227.
 - [83] E. Kljuno and R. L. Williams, "Vehicle simulation system: controls and virtual-reality-based dynamics simulation," *J. Intell. Robot. Syst.*, vol. 52, no. 1, pp. 79–99, 2008.
 - [84] P. Miermeister, M. Lächele, R. Boss, C. Masone, C. Schenk, J. Tesch, M. Kerger, H. Teufel, A. Pott, and H. H. Bühlhoff, "The cablerobot simulator large scale motion platform based on cable robot technology," in *Intelligent Robots and Systems (IROS), 2016 IEEE/RSJ International Conference on*, 2016, pp. 3024–3029.
 - [85] M. Karkoub, M.-G. Her, C. C. Peng, C. C. Huang, and M. I. Ho, "Design and control of a cable-controlled haptic motion simulator," *Robotica*, vol. 30, no. 5, pp. 709–719, 2012.
 - [86] X. Wang, Y. Hu, and Q. Lin, "Workspace analysis and verification of cable-driven parallel mechanism for wind tunnel test," *Proc. Inst. Mech. Eng. Part G J. Aerosp. Eng.*, vol. 231, no. 6, pp. 1012–1021, 2017.
 - [87] M.-D. Otis, M. Mokhtari, C. du Tremblay, D. Laurendeau, F.-M. De Rainville, and C. M. Gosselin, "Hybrid control with multi-contact interactions for 6dof haptic foot platform on a cable-driven locomotion interface," 2008.
 - [88] Jrienstra, "A Skycam HD camera at Stanford Cardinals Stadium," *Wikimedia Commons*, 2009. [Online]. Available: https://commons.wikimedia.org/wiki/File:Sky_Cam_at_Stanford.jpg.
 - [89] J.-D. Deschênes, P. Lambert, S. Perreault, N. Martel-Brisson, N. Zoso, A. Zaccarin, P. Hébert, S. Bouchard, and C. M. Gosselin, "A cable-driven parallel mechanism for capturing object appearance from multiple viewpoints," in *3-D Digital Imaging and Modeling, 2007. 3DIM'07. Sixth International Conference on*, 2007, pp. 367–374.
 - [90] N509FZ, "Scale model of FAST at the Five-Year Achievements Exhibition," *Wikimedia Commons*, 2017. [Online]. Available: [https://commons.wikimedia.org/wiki/File:Scale_model_of_FAST_at_the_Five-Year_Achievements_Exhibition_\(20171015151703\).jpg](https://commons.wikimedia.org/wiki/File:Scale_model_of_FAST_at_the_Five-Year_Achievements_Exhibition_(20171015151703).jpg).

- [91] K. H. J. Voss, V. van der Wijk, and J. L. Herder, "A cable-driven parallel mechanism for the interaction with hemispherical surfaces," in *New Trends in Mechanism and Machine Science*, Springer, 2013, pp. 409–417.
- [92] A. Vilchis, J. Troccaz, P. Cinquin, K. Masuda, and F. Pellissier, "A new robot architecture for tele-echography," *IEEE Trans. Robot. Autom.*, vol. 19, no. 5, pp. 922–926, 2003.
- [93] X. Jin, D. I. Jun, X. Jin, J. Seon, A. Pott, S. Park, J.-O. Park, and S. Y. Ko, "Upper limb rehabilitation using a planar cable-driven parallel robot with various rehabilitation strategies," in *Cable-Driven Parallel Robots*, Springer, 2015, pp. 307–321.
- [94] A. Alamdari and V. Krovi, "Robotic physical exercise and system (ROPES): A cable-driven robotic rehabilitation system for lower-extremity motor therapy," in *ASME 2015 International Design Engineering Technical Conferences and Computers and Information in Engineering Conference*, 2015, p. V05AT08A032--V05AT08A032.
- [95] W. Y. Ho, W. Kraus, A. Mangold, and A. Pott, "Haptic interaction with a cable-driven parallel robot using admittance control," in *Cable-Driven Parallel Robots*, Springer, 2015, pp. 201–212.
- [96] Y. Mao, X. Jin, G. G. Dutta, J. P. Scholz, and S. K. Agrawal, "Human movement training with a cable driven ARm EXoskeleton (CAREX)," *IEEE Trans. Neural Syst. Rehabil. Eng.*, vol. 23, no. 1, pp. 84–92, 2015.
- [97] H. Liu, C. Gosselin, and T. Lalibert , "A spatial spring-loaded cable-loop-driven parallel mechanism," in *ASME 2011 International Design Engineering Technical Conferences and Computers and Information in Engineering Conference*, 2011, pp. 1301–1308.
- [98] H. Liu, "Conceptual design, static and dynamic analysis of novel cable-loop-driven parallel mechanisms," 2012.
- [99] H. Liu, C. Gosselin, and T. Lalibert , "Two-Degree-of-Freedom Decoupled Non-Redundant Cable-Loop-Driven Parallel Mechanism," in *ASME 2012 International Design Engineering Technical Conferences and Computers and Information in Engineering Conference*, 2012, pp. 781–790.
- [100] Y. Wischnitzer, N. Shvalb, and M. Shoham, "Wire-driven parallel robot: Permitting collisions between wires," *Int. J. Rob. Res.*, vol. 27, no. 9, pp. 1007–1026, 2008.
- [101] D. Q. Nguyen and M. Gouttefarde, "On the improvement of cable collision detection algorithms," in *Cable-Driven Parallel Robots*, Springer, 2015, pp. 29–40.

- [102] P. Miermeister and A. Pott, "Auto calibration method for cable-driven parallel robots using force sensors," in *Latest Advances in Robot Kinematics*, Springer, 2012, pp. 269–276.
- [103] J. A. D. Sandretto, D. Daney, M. Gouttefarde, and C. Baradat, "Calibration of a fully-constrained parallel cable-driven robot," INRIA, 2012.
- [104] R. J. Caverly and J. R. Forbes, "Flexible cable-driven parallel manipulator control: Maintaining positive cable tensions," *IEEE Trans. Control Syst. Technol.*, vol. 26, no. 5, pp. 1874–1883, 2018.
- [105] M. A. Khosravi and H. D. Taghirad, "Dynamic modeling and control of parallel robots with elastic cables: singular perturbation approach," *IEEE Trans. Robot.*, vol. 30, no. 3, pp. 694–704, 2014.
- [106] P. Miermeister, W. Kraus, T. Lan, and A. Pott, "An elastic cable model for cable-driven parallel robots including hysteresis effects," in *Cable-Driven Parallel Robots*, Springer, 2015, pp. 17–28.
- [107] J. E. Kennedy, "High-intensity focused ultrasound in the treatment of solid tumours," *Nat. Rev. cancer*, vol. 5, no. 4, p. 321, 2005.
- [108] G. Kósa, M. Shoham, and M. Zaaroor, "Propulsion method for swimming microrobots," *IEEE Trans. Robot.*, vol. 23, no. 1, pp. 137–150, 2007.
- [109] J. D. Raman, D. J. Scott, and J. A. Cadeddu, "Role of magnetic anchors during laparoendoscopic single site surgery and NOTES," *J. Endourol.*, vol. 23, no. 5, pp. 781–786, 2009.
- [110] A. De Donno, L. Zorn, P. Zanne, F. Nageotte, and M. de Mathelin, "Introducing STRAS: a new flexible robotic system for minimally invasive surgery," in *Robotics and Automation (ICRA), 2013 IEEE International Conference on*, 2013, pp. 1213–1220.
- [111] C. E. D'iaz, R. Fernández, M. Armada, and F. de J. Garcia Gutierrez, "State of the art in robots used in minimally invasive surgeries. Natural Orifice Transluminal Surgery (NOTES) as a particular case," *Ind. Robot An Int. J.*, vol. 42, no. 6, pp. 508–532, 2015.
- [112] J. Zhao, B. Feng, M.-H. Zheng, and K. Xu, "Surgical robots for SPL and NOTES: a review," *Minim. Invasive Ther. Allied Technol.*, vol. 24, no. 1, pp. 8–17, 2015.
- [113] N. Simaan, R. M. Yasin, and L. Wang, "Medical technologies and challenges of robot-assisted minimally invasive intervention and diagnostics," *Annu. Rev. Control. Robot. Auton. Syst.*, vol. 1, pp. 465–490, 2018.

- [114] B. P. M. Yeung and T. Gourlay, "A technical review of flexible endoscopic multitasking platforms," *Int. J. Surg.*, vol. 10, no. 7, pp. 345–354, 2012.
- [115] B. P. M. Yeung and P. W. Y. Chiu, "Application of robotics in gastrointestinal endoscopy: A review," *World J. Gastroenterol.*, vol. 22, no. 5, p. 1811, 2016.
- [116] H. M. Le, T. N. Do, and S. J. Phee, "A survey on actuators-driven surgical robots," *Sensors Actuators A Phys.*, vol. 247, pp. 323–354, 2016.
- [117] N. Simaan, R. H. Taylor, and H. Choset, "Intelligent Surgical Robots with Situational Awareness," *Mech. Eng. Mag. Sel. Artic.*, vol. 137, no. 09, pp. S3–S6, 2015.
- [118] E. A. Arkenbout, P. W. J. Henselmans, F. J. W. Geurts, and P. Breedveld, "A state of the art review and categorization of multi-branched instruments for NOTES and SILS," *Surg. Endosc.*, vol. 29, no. 6, pp. 1281–1296, 2015.
- [119] M. O. Schurr, A. Arezzo, B. Neisius, H. Rininsland, H.-U. Hilzinger, J. Dorn, K. Roth, and G. F. Buess, "Trocara and instrument positioning system TISKA," *Surg. Endosc.*, vol. 13, no. 5, pp. 528–531, 1999.
- [120] G. F. Buess, A. Arezzo, M. O. Schurr, F. Ulmer, H. Fisher, L. Gumb, T. Testa, and C. Nobman, "A new remote-controlled endoscope positioning system for endoscopic solo surgery," *Surg. Endosc.*, vol. 14, no. 4, pp. 395–399, 2000.
- [121] H. Rininsland, "ARTEMIS. A telemanipulator for cardiac surgery," *Eur. J. Cardio-Thoracic Surg.*, vol. 16, no. Supplement_2, pp. S106–S111, 1999.
- [122] M. M. Dalvand and B. Shirinzadeh, "Motion control analysis of a parallel robot assisted minimally invasive surgery/microsurgery system (PRAMiSS)," *Robot. Comput. Integr. Manuf.*, vol. 29, no. 2, pp. 318–327, 2013.
- [123] C.-H. Kuo, J. S. Dai, and P. Dasgupta, "Kinematic design considerations for minimally invasive surgical robots: an overview," *Int. J. Med. Robot. Comput. Assist. Surg.*, vol. 8, no. 2, pp. 127–145, 2012.
- [124] U. Kim, D.-H. Lee, Y. B. Kim, D.-Y. Seok, J. So, and H. R. Choi, "S-surge: Novel portable surgical robot with multi-axis force-sensing capability for minimally invasive surgery," *IEEE/ASME Trans. Mechatronics*, vol. 22, no. 4, pp. 1717–1727, 2017.
- [125] J. Li, Y. Xing, K. Liang, and S. Wang, "Kinematic design of a novel spatial remote center-of-motion mechanism for minimally invasive surgical robot," *J. Med. Device.*, vol. 9, no. 1, p. 011001, 2015.

11003, 2015.

- [126] M. J. H. Lum, J. Rosen, M. N. Sinanan, and B. Hannaford, "Optimization of a spherical mechanism for a minimally invasive surgical robot: theoretical and experimental approaches," *IEEE Trans. Biomed. Eng.*, vol. 53, no. 7, pp. 1440–1445, 2006.
- [127] R. C. O. Locke and R. V Patel, "Optimal remote center-of-motion location for robotics-assisted minimally-invasive surgery," in *Robotics and Automation, 2007 IEEE International Conference on*, 2007, pp. 1900–1905.
- [128] D. Cagle, P. E. G. Kilroy, K. S. Koenig, J. S. Gee, W. Grout, and M. P. Schaller, "Table adapters for mounting robotic arms to a surgical table," US20180078439A1, 2018.
- [129] H. Mayer, F. Gomez, D. Wierstra, I. Nagy, A. Knoll, and J. Schmidhuber, "A system for robotic heart surgery that learns to tie knots using recurrent neural networks," *Adv. Robot.*, vol. 22, no. 13–14, pp. 1521–1537, 2008.
- [130] L. J. M. van den Bedem, *Realization of a Demonstrator Slave for Robotic Minimally Invasive Surgery*. Citeseer, 2010.
- [131] T. Frede, A. Hammady, J. Klein, D. Teber, N. Inaki, M. Waseda, G. Buess, and J. Rassweiler, "The Radius Surgical System—a new device for complex minimally invasive procedures in urology?," *Eur. Urol.*, vol. 51, no. 4, pp. 1015–1022, 2007.
- [132] K. Ikuta, T. Hasegawa, and S. Daifu, "Hyper redundant miniature manipulator" Hyper Finger" for remote minimally invasive surgery in deep area," in *Robotics and Automation, 2003. Proceedings. ICRA'03. IEEE International Conference on*, 2003, vol. 1, pp. 1098–1102.
- [133] F. Jelinek, E. A. Arkenbout, P. W. J. Henselmans, R. Pessers, and P. Breedveld, "Classification of joints used in steerable instruments for minimally invasive surgery—A review of the state of the art," *J. Med. Device.*, vol. 9, no. 1, p. 10801, 2015.
- [134] J. H. Kaouk, R. K. Goel, G.-P. Haber, S. Crouzet, and R. J. Stein, "Robotic single-port transumbilical surgery in humans: initial report," *BJU Int.*, vol. 103, no. 3, pp. 366–369, 2009.
- [135] M. M. Desai, M. Aron, A. Berger, D. Canes, R. Stein, G.-P. Haber, K. Kamoi, S. Crouzet, R. Sotelo, and I. S. Gill, "Transvesical robotic radical prostatectomy," *BJU Int.*, vol. 102, no. 11, pp. 1666–1669, 2008.
- [136] J. Baekelandt, "Robotic vaginally assisted NOTES hysterectomy: the first case series demonstrating a new surgical technique," *Gynecol. Surg.*, vol. 13, no. 1, pp. 57–62, 2016.

- [137] G.-P. Haber, M. A. White, R. Autorino, P. F. Escobar, M. D. Kroh, S. Chalikonda, R. Khanna, S. Forest, B. Yang, F. Altunrende, and others, "Novel robotic da Vinci instruments for laparoendoscopic single-site surgery," *Urology*, vol. 76, no. 6, pp. 1279–1282, 2010.
- [138] L. Morelli, S. Guadagni, G. Di Franco, M. Palmeri, G. Di Candio, and F. Mosca, "Da Vinci single site surgical platform in clinical practice: a systematic review," *Int. J. Med. Robot. Comput. Assist. Surg.*, vol. 12, no. 4, pp. 724–734, 2016.
- [139] P. Berkelman and J. Ma, "A compact modular teleoperated robotic system for laparoscopic surgery," *Int. J. Rob. Res.*, vol. 28, no. 9, pp. 1198–1215, 2009.
- [140] O. J. Isaac-Lowry, S. Okamoto, S. A. Pedram, R. Woo, and P. Berkelman, "Compact teleoperated laparoendoscopic single-site robotic surgical system: Kinematics, control, and operation," *Int. J. Med. Robot. Comput. Assist. Surg.*, vol. 13, no. 4, p. e1811, 2017.
- [141] H. Choi, H.-S. Kwak, Y.-A. Lim, and H.-J. Kim, "Surgical robot for single-incision laparoscopic surgery," *IEEE Trans. Biomed. Eng.*, vol. 61, no. 9, pp. 2458–2466, 2014.
- [142] J. H. Kaouk, G.-P. Haber, R. Autorino, S. Crouzet, A. Ouzzane, V. Flamand, and A. Villers, "A novel robotic system for single-port urologic surgery: first clinical investigation," *Eur. Urol.*, vol. 66, no. 6, pp. 1033–1043, 2014.
- [143] S. Can, A. Fiolka, H. Mayer, A. Knoll, A. Schneider, D. Wilhelm, A. Meining, and H. Feussner, "The mechatronic support system 'HVSPS' and the way to NOTES," *Minim. invasive Ther. allied Technol.*, vol. 17, no. 6, pp. 341–345, 2008.
- [144] F. C. Holsinger, "A flexible, single-arm robotic surgical system for tonsillar resection of the tonsil and lateral pharyngeal wall: Next-generation robotic head and neck surgery," *Laryngoscope*, vol. 126, no. 4, pp. 864–869, 2016.
- [145] S. Can, C. Staub, A. Knoll, A. Fiolka, A. Schneider, and H. Feussner, "Design, development and evaluation of a highly versatile robot platform for minimally invasive single-port surgery," in *Biomedical Robotics and Biomechatronics (BioRob), 2012 4th IEEE RAS & EMBS International Conference on*, 2012, pp. 817–822.
- [146] J. Shang, K. Leibrandt, P. Giataganas, V. Vitiello, C. A. Seneci, P. Wisanuvej, J. Liu, G. Gras, J. Clark, A. Darzi, and others, "A Single-Port Robotic System for Transanal Microsurgery—Design and Validation," *IEEE Robot. Autom. Lett.*, vol. 2, no. 3, pp. 1510–1517, 2017.
- [147] "TransEnterix Announces Global SurgiBot System Agreement." [Online]. Available: <https://www.businesswire.com/news/home/20171218005245/en/TransEnterix-Announces->

Global-SurgiBot-System-Agreement. [Accessed: 15-Jun-2018].

- [148] A. D. Pryor, J. R. Tushar, and L. R. DiBernardo, "Single-port cholecystectomy with the TransEnterix SPIDER: simple and safe," *Surg. Endosc.*, vol. 24, no. 4, pp. 917–923, 2010.
- [149] J. Li, X. Li, J. Wang, Y. Xing, S. Wang, and X. Ren, "Design and evaluation of a variable stiffness manual operating platform for laparoendoscopic single site surgery (LESS)," *Int. J. Med. Robot. Comput. Assist. Surg.*, vol. 13, no. 4, p. e1797, 2017.
- [150] J. Zhao, X. Zheng, M. Zheng, A. J. Shih, and K. Xu, "An endoscopic continuum testbed for finalizing system characteristics of a surgical robot for NOTES procedures," in *Advanced Intelligent Mechatronics (AIM), 2013 IEEE/ASME International Conference on*, 2013, pp. 63–70.
- [151] K. Xu, R. E. Goldman, J. Ding, P. K. Allen, D. L. Fowler, and N. Simaan, "System design of an insertable robotic effector platform for single port access (SPA) surgery," in *Intelligent Robots and Systems, 2009. IROS 2009. IEEE/RSJ International Conference on*, 2009, pp. 5546–5552.
- [152] K. Xu, J. Zhao, M. Fu, and others, "Development of the SJTU unfoldable robotic system (SURS) for single port laparoscopy," *IEEE/ASME Trans. Mechatronics*, vol. 20, no. 5, pp. 2133–2145, 2015.
- [153] J. Shang, C. J. Payne, J. Clark, D. P. Noonan, K.-W. Kwok, A. Darzi, and G.-Z. Yang, "Design of a multitasking robotic platform with flexible arms and articulated head for minimally invasive surgery," in *Intelligent Robots and Systems (IROS), 2012 IEEE/RSJ International Conference on*, 2012, pp. 1988–1993.
- [154] S. M. Seung, H. S. Choi, W. Y. Kim, S. Y. Ko, J. O. Park, and S. H. Park, "Development of manipulator including exchange-type multi-articulated end-effector for single port surgical robot," in *Robotics and Biomimetics (ROBIO), 2011 IEEE International Conference on*, 2011, pp. 425–430.
- [155] K. Hongo, S. Kobayashi, Y. Kakizawa, J. Koyama, T. Goto, H. Okudera, K. Kan, M. G. Fujie, H. Iseki, and K. Takakura, "NeuRobot: telecontrolled micromanipulator system for minimally invasive microneurosurgery—preliminary results," *Neurosurgery*, vol. 51, no. 4, pp. 985–988, 2002.
- [156] S. Seung, P. Liu, S. Park, J.-O. Park, and S. Y. Ko, "Single-port robotic manipulator system for brain tumor removal surgery: SiromanS," *Mechatronics*, vol. 26, pp. 16–28, 2015.
- [157] J. Shang, D. P. Noonan, C. Payne, J. Clark, M. H. Sodergren, A. Darzi, and G.-Z. Yang, "An

- articulated universal joint based flexible access robot for minimally invasive surgery,” in *2011 IEEE international conference on robotics and automation*, 2011, pp. 1147–1152.
- [158] M. Piccigallo, U. Scarfogliero, C. Quaglia, G. Petroni, P. Valdastrì, A. Menciassi, and P. Dario, “Design of a novel bimanual robotic system for single-port laparoscopy,” *IEEE/ASME Trans. Mechatronics*, vol. 15, no. 6, pp. 871–878, 2010.
 - [159] M. Reichenbach, T. Frederick, L. Cubrich, W. Bircher, N. Bills, M. Morien, S. Farritor, and D. Oleynikov, “Telesurgery With Miniature Robots to Leverage Surgical Expertise in Distributed Expeditionary Environments,” *Mil. Med.*, vol. 182, no. suppl_1, pp. 316–321, 2017.
 - [160] L. P. Cubrich, “Design of a Flexible Control Platform and Miniature in vivo Robots for Laparo-Endoscopic Single-Site Surgeries,” University of Nebraska-Lincoln, 2016.
 - [161] T. D. Wortman, J. M. Mondry, S. M. Farritor, and D. Oleynikov, “Single-site colectomy with miniature in vivo robotic platform,” *IEEE Trans. Biomed. Eng.*, vol. 60, no. 4, pp. 926–929, 2013.
 - [162] B. Cheon, E. Gezgin, D. K. Ji, M. Tomikawa, M. Hashizume, H.-J. Kim, and J. Hong, “A single port laparoscopic surgery robot with high force transmission and a large workspace,” *Surg. Endosc.*, vol. 28, no. 9, pp. 2719–2729, 2014.
 - [163] M. Hwang, U.-J. Yang, D. Kong, D. G. Chung, J. Lim, D.-H. Lee, D. H. Kim, D. Shin, T. Jang, J.-W. Kim, and others, “A single port surgical robot system with novel elbow joint mechanism for high force transmission,” *Int. J. Med. Robot. Comput. Assist. Surg.*, vol. 13, no. 4, p. e1808, 2017.
 - [164] Y. Sekiguchi, Y. Kobayashi, Y. Tomono, H. Watanabe, K. Toyoda, K. Konishi, M. Tomikawa, S. Ieiri, K. Tanoue, M. Hashizume, and others, “Development of a tool manipulator driven by a flexible shaft for single port endoscopic surgery,” in *Biomedical Robotics and Biomechatronics (BioRob), 2010 3rd IEEE RAS and EMBS International Conference on*, 2010, pp. 120–125.
 - [165] C. Ishii and K. Kobayashi, “Development of a new bending mechanism and its application to robotic forceps manipulator,” in *Robotics and Automation, 2007 IEEE International Conference on*, 2007, pp. 238–243.
 - [166] Y. Sekiguchi, Y. Kobayashi, H. Watanabe, Y. Tomono, T. Noguchi, Y. Takahashi, K. Toyoda, M. Uemura, S. Ieiri, T. Ohdaira, and others, “In vivo experiments of a surgical robot with vision field control for single port endoscopic surgery,” in *Engineering in Medicine and Biology Society, EMBC, 2011 Annual International Conference of the IEEE*, 2011, pp. 7045–7048.

- [167] W.-H. Shin and D.-S. Kwon, "Surgical robot system for single-port surgery with novel joint mechanism," *IEEE Trans. Biomed. Eng.*, vol. 60, no. 4, pp. 937–944, 2013.
- [168] M. B. Hong and Y.-H. Jo, "Design of a novel 4-DOF wrist-type surgical instrument with enhanced rigidity and dexterity," *IEEE/ASME Trans. Mechatronics*, vol. 19, no. 2, pp. 500–511, 2014.
- [169] J.-P. Merlet, "Optimal design for the micro parallel robot MIPS," in *Robotics and Automation, 2002. Proceedings. ICRA'02. IEEE International Conference on*, 2002, vol. 2, pp. 1149–1154.
- [170] C. Reboulet and S. Durand-Leguay, "Optimal design of redundant parallel mechanism for endoscopic surgery," in *Intelligent Robots and Systems, 1999. IROS'99. Proceedings. 1999 IEEE/RSJ International Conference on*, 1999, vol. 3, pp. 1432–1437.
- [171] S. Matich, C. Neupert, A. Kirschniak, H. F. Schlaak, and P. P. Pott, "A new single-port robotic system based on a parallel kinematic structure," in *Intelligent Robots and Systems (IROS), 2015 IEEE/RSJ International Conference on*, 2015, pp. 236–241.
- [172] H. Lee, Y. Choi, and B.-J. Yi, "Stackable 4-BAR manipulators for single port access surgery," *IEEE/ASME Trans. Mechatronics*, vol. 17, no. 1, pp. 157–166, 2012.
- [173] G. O. Spaun, B. Zheng, and L. L. Swanström, "A multitasking platform for natural orifice transluminal endoscopic surgery (NOTES): a benchtop comparison of a new device for flexible endoscopic surgery and a standard dual-channel endoscope," *Surg. Endosc.*, vol. 23, no. 12, p. 2720, 2009.
- [174] K. Ikeda, K. Sumiyama, H. Tajiri, K. Yasuda, and S. Kitano, "Evaluation of a new multitasking platform for endoscopic full-thickness resection," *Gastrointest. Endosc.*, vol. 73, no. 1, pp. 117–122, 2011.
- [175] K.-H. Fuchs and W. Breithaupt, "Transgastric small bowel resection with the new multitasking platform EndoSAMURAI™ for natural orifice transluminal endoscopic surgery," *Surg. Endosc.*, vol. 26, no. 8, pp. 2281–2287, 2012.
- [176] H. Neuhaus, G. Costamagna, J. Devière, P. Fockens, T. Ponchon, and T. Rösch, "Endoscopic submucosal dissection (ESD) of early neoplastic gastric lesions using a new double-channel endoscope (the" R-scope")," *Endoscopy*, vol. 38, no. 10, pp. 1016–1023, 2006.
- [177] J. A. Astudillo, E. Sporn, S. Bachman, B. Miedema, and K. Thaler, "Transgastric cholecystectomy using a prototype endoscope with 2 deflecting working channels (with video)," *Gastrointest. Endosc.*, vol. 69, no. 2, pp. 297–302, 2009.

- [178] G. O. Spaun, B. Zheng, D. V. Martinec, M. A. Cassera, C. M. Dunst, and L. L. Swanström, "Bimanual coordination in natural orifice transluminal endoscopic surgery: comparing the conventional dual-channel endoscope, the R-Scope, and a novel direct-drive system," *Gastrointest. Endosc.*, vol. 69, no. 6, pp. e39–e45, 2009.
- [179] B. Dallemagne and J. Marescaux, "The ANUBIS™ project," *Minim. Invasive Ther. Allied Technol.*, vol. 19, no. 5, pp. 257–261, 2010.
- [180] L. Zorn, F. Nageotte, P. Zanne, A. Legner, B. Dallemagne, J. Marescaux, and M. de Mathelin, "A novel telemanipulated robotic assistant for surgical endoscopy: preclinical application to ESD," *IEEE Trans. Biomed. Eng.*, vol. 65, no. 4, pp. 797–808, 2018.
- [181] M. T. Moyer, R. S. Haluck, J. Gopal, E. M. Pauli, and A. Mathew, "Transgastric organ resection solely with the prototype R-scope and the self-approximating transluminal access technique," *Gastrointest. Endosc.*, vol. 72, no. 1, pp. 170–176, 2010.
- [182] T. Kobayashi, S. Lemoine, A. Sugawara, T. Tsuchida, T. Gotoda, I. Oda, H. Ueda, and T. Kakizoe, "A flexible endoscopic surgical system: first report on a conceptual design of the system validated by experiments," *Jpn. J. Clin. Oncol.*, vol. 35, no. 11, pp. 667–671, 2005.
- [183] A. Degani, H. Choset, B. Zubiate, T. Ota, and M. Zenati, "Highly Articulated Robotic Probe for Minimally Invasive Surgery.," *Conf. Proc. IEEE Eng. Med. Biol. Soc.*, vol. 2006, no. 1642343, pp. 4167–4172, Jan. 2006.
- [184] T. Ota, A. Degani, D. Schwartzman, B. Zubiate, J. McGarvey, H. Choset, and M. A. Zenati, "A highly articulated robotic surgical system for minimally invasive surgery," *Ann. Thorac. Surg.*, vol. 87, no. 4, pp. 1253–1256, 2009.
- [185] P. J. Johnson, C. M. R. Serrano, M. Castro, R. Kuenzler, H. Choset, S. Tully, and U. Duvvuri, "Demonstration of transoral surgery in cadaveric specimens with the medrobotics flex system," *Laryngoscope*, vol. 123, no. 5, pp. 1168–1172, 2013.
- [186] M. Remacle, V. M. N. Prasad, G. Lawson, L. Plisson, V. Bachy, and S. der Vorst, "Transoral robotic surgery (TORS) with the Medrobotics Flex™ System: first surgical application on humans," *Eur. Arch. Oto-Rhino-Laryngology*, vol. 272, no. 6, pp. 1451–1455, 2015.
- [187] S. J. Bardaro and L. Swanström, "Development of advanced endoscopes for natural orifice transluminal endoscopic surgery," *Minim. Invasive Ther. Allied Technol.*, vol. 15, no. 6, pp. 378–383, 2006.
- [188] L. L. Swanstrom, R. Kozarek, P. J. Pasricha, S. Gross, D. Birkett, P.-O. Park, V. Saadat, R. Ewers,

- and P. Swain, "Development of a new access device for transgastric surgery," *J. Gastrointest. Surg.*, vol. 9, no. 8, pp. 1129–1137, 2005.
- [189] L. Swanström, P. Swain, and P. Denk, "Development and validation of a new generation of flexible endoscope for NOTES," *Surg. Innov.*, vol. 16, no. 2, pp. 104–110, 2009.
- [190] J. C. Espinós, R. Turró, A. Mata, M. Cruz, M. Da Costa, V. Villa, J. N. Buchwald, and J. Turró, "Early experience with the Incisionless Operating Platform™(IOP) for the treatment of obesity," *Obes. Surg.*, vol. 23, no. 9, pp. 1375–1383, 2013.
- [191] C. C. Thompson, M. Ryou, N. J. Soper, E. S. Hungess, R. I. Rothstein, and L. L. Swanstrom, "Evaluation of a manually driven, multitasking platform for complex endoluminal and natural orifice transluminal endoscopic surgery applications (with video).," *Gastrointest. Endosc.*, vol. 70, no. 1, pp. 121–5, Jul. 2009.
- [192] R. I. Rothstein and L. L. Swanstrom, "Use of the direct drive endoscopic system (DDES) for in-vivo mucosal resection in a porcine model," *Gastrointest. Endosc.*, vol. 67, no. 5, p. AB146, 2008.
- [193] D. J. Abbott, C. Becke, R. I. Rothstein, and W. J. Peine, "Design of an endoluminal NOTES robotic system," in *Intelligent Robots and Systems, 2007. IROS 2007. IEEE/RSJ International Conference on*, 2007, pp. 410–416.
- [194] S. J. Phee, S. C. Low, Z. L. Sun, K. Y. Ho, W. M. Huang, and Z. M. Thant, "Robotic system for no-scar gastrointestinal surgery," *Int. J. Med. Robot. Comput. Assist. Surg.*, vol. 4, no. 1, pp. 15–22, 2008.
- [195] S. J. Phee, S. C. Low, V. A. Huynh, A. P. Kencana, Z. L. Sun, and K. Yang, "Master and slave transluminal endoscopic robot (MASTER) for natural orifice transluminal endoscopic surgery," in *Engineering in Medicine and Biology Society, 2009. EMBC 2009. Annual International Conference of the IEEE*, 2009, pp. 1192–1195.
- [196] M. F. Traeger, D. B. Roppenecker, M. R. Leininger, F. Schnoes, and T. C. Lueth, "Design of a spine-inspired kinematic for the guidance of flexible instruments in minimally invasive surgery," in *Intelligent Robots and Systems (IROS 2014), 2014 IEEE/RSJ International Conference on*, 2014, pp. 1322–1327.
- [197] H. Feussner, V. Becker, M. Bauer, M. Kranzfelder, R. Schirren, T. Lüth, A. Meining, and D. Wilhelm, "Developments in flexible endoscopic surgery: a review," *Clin. Exp. Gastroenterol.*, vol. 8, p. 31, 2015.

- [198] C. C. Y. Poon, H. Yang, K. C. Lau, W. Xu, Y. Yam, J. Y. W. Lau, and P. W. Y. Chiu, "A bio-inspired flexible robot with hybrid actuation mechanisms for endoscopic surgery," in *The Hamlyn Symposium on Medical Robotics*, 2014, p. 81.
- [199] K. C. Lau, E. Y. Y. Leung, P. W. Y. Chiu, Y. Yam, J. Y. W. Lau, and C. C. Y. Poon, "A flexible surgical robotic system for removal of early-stage gastrointestinal cancers by endoscopic submucosal dissection," *IEEE Trans. Ind. Informatics*, vol. 12, no. 6, pp. 2365–2374, 2016.
- [200] B. Bardou, F. Nageotte, P. Zanne, and M. de Mathelin, "Design of a robotized flexible endoscope for natural orifice transluminal endoscopic surgery," in *Computational Surgery and Dual Training*, Springer, 2010, pp. 155–170.
- [201] N. Suzuki, A. Hattori, K. Tanoue, S. Ieiri, K. Konishi, M. Tomikawa, H. Kenmotsu, and M. Hashizume, "Scorpion shaped endoscopic surgical robot for NOTES and SPS with augmented reality functions," in *International Workshop on Medical Imaging and Virtual Reality*, 2010, pp. 541–550.
- [202] K. S. Roh, S. Yoon, Y. Do Kwon, Y. Shim, and Y.-J. Kim, "Single-Port surgical robot system with flexible surgical instruments," in *International Conference on Intelligent Robotics and Applications*, 2015, pp. 447–459.
- [203] Y.-J. Kim, S. Cheng, S. Kim, and K. Iagnemma, "A Stiffness-Adjustable Hyperredundant Manipulator Using a Variable Neutral-Line Mechanism for Minimally Invasive Surgery," *IEEE Trans. Robot.*, vol. 30, no. 2, pp. 382–395, Apr. 2014.
- [204] J. Ahn, M. Hwang, D. Baek, H. Kim, and D.-S. Kwon, "Comparison of Master-Slave Mapping Strategies for Efficient Robotic Endoscopy," in *The Hamlyn Symposium on Medical Robotics*, 2018.
- [205] "KAIST K-Flex System." [Online]. Available: <http://robot.kaist.ac.kr/2018/07/02/k-flex-developed-by-our-laboratory-was-selected-as-the-best-surgical-robot-of-the-year/>. [Accessed: 17-Dec-2018].
- [206] D. P. Noonan, V. Vitiello, J. Shang, C. J. Payne, and G.-Z. Yang, "A modular, mechatronic joint design for a flexible access platform for MIS," in *Intelligent Robots and Systems (IROS), 2011 IEEE/RSJ International Conference on*, 2011, pp. 949–954.
- [207] P. Berthet-Rayne, G. Gras, K. Leibrandt, P. Wisanuvej, A. Schmitz, C. A. Seneci, and G.-Z. Yang, "The i 2 Snake Robotic Platform for Endoscopic Surgery," *Ann. Biomed. Eng.*, pp. 1–13, 2018.
- [208] A. C. Lehman, N. A. Wood, S. Farritor, M. R. Goede, and D. Oleynikov, "Dexterous miniature

- robot for advanced minimally invasive surgery,” *Surg. Endosc.*, vol. 25, no. 1, pp. 119–123, 2011.
- [209] A. C. Lehman, J. Dumpert, N. A. Wood, L. Redden, A. Q. Visty, S. Farritor, B. Varnell, and D. Oleynikov, “Natural orifice cholecystectomy using a miniature robot,” *Surg. Endosc.*, vol. 23, no. 2, pp. 260–266, 2009.
- [210] K. Harada, E. Susilo, A. Menciassi, and P. Dario, “Wireless reconfigurable modules for robotic endoluminal surgery,” in *Robotics and Automation, 2009. ICRA’09. IEEE International Conference on*, 2009, pp. 2699–2704.
- [211] S. Tognarelli, M. Salerno, G. Tortora, C. Quaglia, P. Dario, and A. Menciassi, “An endoluminal robotic platform for Minimally Invasive Surgery,” in *Biomedical Robotics and Biomechatronics (BioRob), 2012 4th IEEE RAS & EMBS International Conference on*, 2012, pp. 7–12.
- [212] G. Tortora, M. Salerno, T. Ranzani, S. Tognarelli, P. Dario, and A. Menciassi, “A modular magnetic platform for natural orifice transluminal endoscopic surgery,” in *2013 35th Annual International Conference of the IEEE Engineering in Medicine and Biology Society (EMBC)*, 2013, pp. 6265–6268.
- [213] K. Harada, D. Oetomo, E. Susilo, A. Menciassi, D. Daney, J.-P. Merlet, and P. Dario, “A reconfigurable modular robotic endoluminal surgical system: vision and preliminary results,” *Robotica*, vol. 28, no. 2, pp. 171–183, 2010.
- [214] Y. Saito, K. Sumiyama, and P. W. Chiu, “Robot assisted tumor resection devices,” *Expert Rev. Med. Devices*, vol. 14, no. 8, pp. 657–662, 2017.
- [215] S. V Kantsevoy, M. Bitner, and G. Piskun, “New endoscopic platform for endoluminal enbloc tissue resection in the gastrointestinal tract (with videos),” *Surg. Endosc.*, vol. 30, no. 7, pp. 3145–3151, 2016.
- [216] D. W. Schölvinck, O. Goto, J. J. Bergman, N. Yahagi, and B. L. A. M. Weusten, “The efficacy of an endoscopic grasp-and-traction device for gastric endoscopic submucosal dissection: an ex vivo comparative study (with video),” *Clin. Endosc.*, vol. 48, no. 3, p. 221, 2015.
- [217] R. Nakadate, S. Nakamura, T. Moriyama, H. Kenmotsu, S. Oguri, J. Arata, M. Uemura, K. Ohuchida, T. Akahoshi, T. Ikeda, and others, “Gastric endoscopic submucosal dissection using novel 2.6-mm articulating devices: an ex vivo comparative and in vivo feasibility study,” *Endoscopy*, vol. 47, no. 9, pp. 820–824, 2015.
- [218] J. Gafford, T. Ranzani, S. Russo, H. Aihara, C. Thompson, R. Wood, and C. Walsh, “Snap-on

- robotic wrist module for enhanced dexterity in endoscopic surgery,” in *Robotics and Automation (ICRA), 2016 IEEE International Conference on*, 2016, pp. 4398–4405.
- [219] J. B. Gafford, R. J. Wood, and C. J. Walsh, “A high-force, high-stroke distal robotic add-on for endoscopy,” in *2017 IEEE International Conference on Robotics and Automation (ICRA)*, 2017, pp. 1117–1124.
- [220] N. Fukami, “What we want for ESD is a second hand! Traction method,” *Gastrointest. Endosc.*, vol. 78, no. 2, pp. 274–276, 2013.
- [221] O. Motohashi, “Two-point fixed endoscopic submucosal dissection in rectal tumor (with video),” *Gastrointest. Endosc.*, vol. 74, no. 5, pp. 1132–1136, 2011.
- [222] O. Motohashi, K. Nishimura, N. Nakayama, Y. Inokuchi, and S. Inoue, “Usefulness of two-point fixed endoscopic submucosal dissection for superficial esophageal neoplasms,” *Esophagus*, vol. 13, no. 2, pp. 182–186, 2016.
- [223] T. Iwasa, R. Nakadate, S. Onogi, Y. Okamoto, J. Arata, S. Oguri, H. Ogino, E. Ihara, K. Ohuchida, T. Akahoshi, and others, “A new robotic-assisted flexible endoscope with single-hand control: endoscopic submucosal dissection in the ex vivo porcine stomach,” *Surg. Endosc.*, vol. 32, no. 7, pp. 3386–3392, 2018.
- [224] A. Jiang, G. Xynogalas, P. Dasgupta, K. Althoefer, and T. Nanayakkara, “Design of a variable stiffness flexible manipulator with composite granular jamming and membrane coupling,” in *Intelligent Robots and Systems (IROS), 2012 IEEE/RSJ International Conference on*, 2012, pp. 2922–2927.
- [225] Y.-J. Kim, S. Cheng, S. Kim, and K. Iagnemma, “A novel layer jamming mechanism with tunable stiffness capability for minimally invasive surgery,” *IEEE Trans. Robot.*, vol. 29, no. 4, pp. 1031–1042, 2013.
- [226] Z. Li, J. Feiling, H. Ren, and H. Yu, “A novel tele-operated flexible robot targeted for minimally invasive robotic surgery,” *Engineering*, vol. 1, no. 1, pp. 73–78, 2015.
- [227] M. Manti, V. Cacucciolo, and M. Cianchetti, “Stiffening in soft robotics: a review of the state of the art,” *IEEE Robot. Autom. Mag.*, vol. 23, no. 3, pp. 93–106, 2016.
- [228] B. Maurin, B. Bayle, O. Piccin, J. Gangloff, M. de Mathelin, C. Dognon, P. Zanne, and A. Gangi, “A patient-mounted robotic platform for CT-scan guided procedures,” *IEEE Trans. Biomed. Eng.*, vol. 55, no. 10, pp. 2417–2425, 2008.

- [229] D. Stoianovici, D. Song, D. Petrisor, D. Ursu, D. Mazilu, M. Mutener, M. Schar, and A. Patriciu, "'MRI Stealth' robot for prostate interventions," *Minim. Invasive Ther. Allied Technol.*, vol. 16, no. 4, pp. 241–248, 2007.
- [230] P. Moreira, G. van de Steeg, T. Krabben, J. Zandman, E. E. G. Hekman, F. van der Heijden, R. Borra, and S. Misra, "The MIRIAM Robot: a novel robotic system for MR-guided needle insertion in the prostate," *J. Med. Robot. Res.*, vol. 2, no. 04, p. 1750006, 2017.
- [231] K. Cleary, A. Melzer, V. Watson, G. Kronreif, and D. Stoianovici, "Interventional robotic systems: Applications and technology state-of-the-art," *Minim. Invasive Ther. Allied Technol.*, vol. 15, no. 2, pp. 101–113, 2006.
- [232] M. M. Arnolli, N. C. Hanumara, M. Franken, D. M. Brouwer, and I. A. M. J. Broeders, "An overview of systems for CT-and MRI-guided percutaneous needle placement in the thorax and abdomen," *Int. J. Med. Robot. Comput. Assist. Surg.*, vol. 11, no. 4, pp. 458–475, 2015.
- [233] P. C. Mozer, A. W. Partin, and D. Stoianovici, "Robotic image-guided needle interventions of the prostate," *Rev Urol*, vol. 11, no. 1, pp. 7–15, 2009.
- [234] H. Rafii-Tari, C. J. Payne, and G.-Z. Yang, "Current and emerging robot-assisted endovascular catheterization technologies: a review," *Ann. Biomed. Eng.*, vol. 42, no. 4, pp. 697–715, 2014.
- [235] A. K. Ghamraoui and J. J. Ricotta, "Current and Future Perspectives in Robotic Endovascular Surgery," *Curr. Surg. Reports*, vol. 6, no. 12, p. 21, 2018.
- [236] P. S. Morgan, T. Carter, S. Davis, A. Sepehri, J. Punt, P. Byrne, A. Moody, and P. Finlay, "The application accuracy of the Pathfinder neurosurgical robot," in *International congress series*, 2003, vol. 1256, pp. 561–567.
- [237] J. Burgner-Kahrs, D. C. Rucker, and H. Choset, "Continuum robots for medical applications: A survey," *IEEE Trans. Robot.*, vol. 31, no. 6, pp. 1261–1280, 2015.
- [238] N. J. van de Berg, D. J. van Gerwen, J. Dankelman, and J. J. van den Dobbelsteen, "Design choices in needle steering—A review," *IEEE/ASME Trans. Mechatronics*, vol. 20, no. 5, pp. 2172–2183, 2015.
- [239] H. B. Gilbert, D. C. Rucker, and R. J. Webster III, "Concentric tube robots: The state of the art and future directions," in *Robotics Research*, Springer, 2016, pp. 253–269.
- [240] A. W. Mahoney, P. L. Anderson, P. J. Swaney, F. Maldonado, and R. J. Webster, "Reconfigurable parallel continuum robots for incisionless surgery," in *Intelligent Robots and*

Systems (IROS), 2016 IEEE/RSJ International Conference on, 2016, pp. 4330–4336.

- [241] A. Kuntz, C. Bowen, C. Baykal, A. W. Mahoney, P. L. Anderson, F. Maldonado, R. J. Webster, and R. Alterovitz, “Kinematic design optimization of a parallel surgical robot to maximize anatomical visibility via motion planning,” in *2018 IEEE International Conference on Robotics and Automation (ICRA)*, 2018, pp. 926–933.
- [242] N. Simaan, R. Taylor, and P. Flint, “High dexterity snake-like robotic slaves for minimally invasive telesurgery of the upper airway,” in *International Conference on Medical Image Computing and Computer-Assisted Intervention*, 2004, pp. 17–24.
- [243] C. B. Black, J. Till, and D. C. Rucker, “Parallel Continuum Robots: Modeling, Analysis, and Actuation-Based Force Sensing,” *IEEE Trans. Robot.*, vol. 34, no. 1, pp. 29–47, 2018.
- [244] H. Das, T. I. M. Ohm, C. Boswell, R. O. B. Steele, and G. Rodriguez, “Robot-assisted microsurgery development at JPL,” *Med.*, p. 85, 2001.
- [245] S. Charles, H. Das, T. Ohm, C. Boswell, G. Rodriguez, R. Steele, and D. Istrate, “Dexterity-enhanced telerobotic microsurgery,” in *Advanced Robotics, 1997. ICAR’97. Proceedings., 8th International Conference on*, 1997, pp. 5–10.
- [246] D.-S. Kwon, K. Y. Woo, S. K. Song, W. S. Kim, and H. S. Cho, “Microsurgical telerobot system,” in *Intelligent Robots and Systems, 1998. Proceedings., 1998 IEEE/RSJ International Conference on*, 1998, vol. 2, pp. 945–950.
- [247] C. Nimsky, J. Rachinger, H. Iro, and R. Fahlbusch, “Adaptation of a hexapod-based robotic system for extended endoscope-assisted transsphenoidal skull base surgery,” *min-Minimally Invasive Neurosurg.*, vol. 47, no. 01, pp. 41–46, 2004.
- [248] M. Wapler, V. Urban, T. Weisener, J. Stallkamp, M. Dürr, and A. Hiller, “A Stewart platform for precision surgery,” *Trans. Inst. Meas. Control*, vol. 25, no. 4, pp. 329–334, 2003.
- [249] W. Wei, R. Goldman, N. Simaan, H. Fine, and S. Chang, “Design and theoretical evaluation of micro-surgical manipulators for orbital manipulation and intraocular dexterity,” in *Robotics and Automation, 2007 IEEE International Conference on*, 2007, pp. 3389–3395.
- [250] M. F. Traeger, D. B. Roppenecker, M. R. Leininger, F. Schnoes, and T. C. Lueth, “Design of a Spine-Inspired Kinematic for the Guidance of Flexible Instruments in Minimally Invasive Surgery,” *2014 IEEE/RSJ Int. Conf. Intell. Robot. Syst. Chicago, Sept. 14-18, 2014*, no. Iros, pp. 1–6, 2014.

- [251] C. C. Thompson, M. Ryou, N. J. Soper, E. S. Hungess, R. I. Rothstein, and L. L. Swanstrom, "Evaluation of a manually driven, multitasking platform for complex endoluminal and natural orifice transluminal endoscopic surgery applications (with video)," *Gastrointest. Endosc.*, vol. 70, no. 1, pp. 121–125, 2009.
- [252] J. Ferlay, M. Colombet, I. Soerjomataram, T. Dyba, G. Randi, M. Bettio, A. Gavin, O. Visser, and F. Bray, "Cancer incidence and mortality patterns in Europe: estimates for 40 countries and 25 major cancers in 2018," *Eur. J. Cancer*, 2018.
- [253] "Cancer Research UK." [Online]. Available: <https://www.cancerresearchuk.org/health-professional/cancer-statistics/statistics-by-cancer-type/bowel-cancer>. [Accessed: 17-Dec-2018].
- [254] "National Cancer Institute." [Online]. Available: <https://seer.cancer.gov/statfacts/>. [Accessed: 17-Dec-2018].
- [255] S. Kiriya, Y. Saito, S. Yamamoto, R. Soetikno, T. Matsuda, T. Nakajima, and H. Kuwano, "Comparison of endoscopic submucosal dissection with laparoscopic-assisted colorectal surgery for early-stage colorectal cancer: a retrospective analysis," *Endoscopy*, vol. 44, no. 11, pp. 1024–1030, 2012.
- [256] A. Facciorusso, M. Antonino, M. Di Maso, M. Barone, and N. Muscatiello, "Non-polypoid colorectal neoplasms: Classification, therapy and follow-up," *World J. Gastroenterol. WJG*, vol. 21, no. 17, p. 5149, 2015.
- [257] N. Yoshida, Y. Naito, N. Yagi, and A. Yanagisawa, "Importance of histological evaluation in endoscopic resection of early colorectal cancer," *World J. Gastrointest. Pathophysiol.*, vol. 3, no. 2, p. 51, 2012.
- [258] J. H. Hwang, V. Konda, B. K. A. Dayyeh, S. S. Chauhan, B. K. Enestvedt, L. L. Fujii-Lau, S. Komanduri, J. T. Maple, F. M. Murad, R. Pannala, and others, "Endoscopic mucosal resection," *Gastrointest. Endosc.*, vol. 82, no. 2, pp. 215–226, 2015.
- [259] G. J. Seo, D. K. Sohn, K. S. Han, C. W. Hong, B. C. Kim, J. W. Park, H. S. Choi, H. J. Chang, and J. H. Oh, "Recurrence after endoscopic piecemeal mucosal resection for large sessile colorectal polyps," *World J. Gastroenterol. WJG*, vol. 16, no. 22, p. 2806, 2010.
- [260] Y. Saito, M. Fukuzawa, T. Matsuda, S. Fukunaga, T. Sakamoto, T. Uraoka, T. Nakajima, H. Ikehara, K.-I. Fu, T. Itoi, and others, "Clinical outcome of endoscopic submucosal dissection versus endoscopic mucosal resection of large colorectal tumors as determined by curative

- resection,” *Surg. Endosc.*, vol. 24, no. 2, pp. 343–352, 2010.
- [261] S. Oka, S. Tanaka, I. Kaneko, R. Mouri, M. Hirata, T. Kawamura, M. Yoshihara, and K. Chayama, “Advantage of endoscopic submucosal dissection compared with EMR for early gastric cancer,” *Gastrointest. Endosc.*, vol. 64, no. 6, pp. 877–883, 2006.
- [262] J. T. Maple, B. K. A. Dayyeh, S. S. Chauhan, J. H. Hwang, S. Komanduri, M. Manfredi, V. Konda, F. M. Murad, U. D. Siddiqui, and S. Banerjee, “Endoscopic submucosal dissection,” *Gastrointest. Endosc.*, vol. 81, no. 6, pp. 1311–1325, 2015.
- [263] Y. Cao, C. Liao, A. Tan, Y. Gao, Z. Mo, and F. Gao, “Meta-analysis of endoscopic submucosal dissection versus endoscopic mucosal resection for tumors of the gastrointestinal tract,” *Endoscopy*, vol. 41, no. 09, pp. 751–757, 2009.
- [264] B.-H. Min, J. H. Lee, J. J. Kim, S. G. Shim, D. K. Chang, Y.-H. Kim, P.-L. Rhee, K.-M. Kim, C. K. Park, and J. C. Rhee, “Clinical outcomes of endoscopic submucosal dissection (ESD) for treating early gastric cancer: comparison with endoscopic mucosal resection after circumferential precutting (EMR-P),” *Dig. Liver Dis.*, vol. 41, no. 3, pp. 201–209, 2009.
- [265] H. Imaeda, N. Hosoe, K. Kashiwagi, T. Ohmori, N. Yahagi, T. Kanai, and H. Ogata, “Advanced endoscopic submucosal dissection with traction,” *World J. Gastrointest. Endosc.*, vol. 6, no. 7, p. 286, 2014.
- [266] K. Tsuji, N. Yoshida, H. Nakanishi, K. Takemura, S. Yamada, and H. Doyama, “Recent traction methods for endoscopic submucosal dissection,” *World J. Gastroenterol.*, vol. 22, no. 26, p. 5917, 2016.
- [267] T. Oyama, “Counter traction makes endoscopic submucosal dissection easier,” *Clin. Endosc.*, vol. 45, no. 4, p. 375, 2012.
- [268] C.-H. Li, P.-J. Chen, H.-C. Chu, T.-Y. Huang, Y.-L. Shih, W.-K. Chang, and T.-Y. Hsieh, “Endoscopic submucosal dissection with the pulley method for early-stage gastric cancer (with video),” *Gastrointest. Endosc.*, vol. 73, no. 1, pp. 163–167, 2011.
- [269] M. Yoshida, K. Takizawa, S. Suzuki, Y. Koike, S. Nonaka, Y. Yamasaki, T. Minagawa, C. Sato, C. Takeuchi, K. Watanabe, and others, “Conventional versus traction-assisted endoscopic submucosal dissection for gastric neoplasms: a multicenter, randomized controlled trial (with video),” *Gastrointest. Endosc.*, vol. 87, no. 5, pp. 1231–1240, 2018.
- [270] N. Sakamoto, T. Osada, T. Shibuya, K. Beppu, K. Matsumoto, H. Mori, M. Kawabe, A. Nagahara, M. Otaka, T. Ogihara, and others, “Endoscopic submucosal dissection of large

- colorectal tumors by using a novel spring-action SO clip for traction (with video)," *Gastrointest. Endosc.*, vol. 69, no. 7, pp. 1370–1374, 2009.
- [271] H. Ritsuno, N. Sakamoto, T. Osada, S. P. Goto, T. Murakami, H. Ueyama, H. Mori, K. Matsumoto, K. Beppu, T. Shibuya, and others, "Prospective clinical trial of traction device-assisted endoscopic submucosal dissection of large superficial colorectal tumors using the S--O clip," *Surg. Endosc.*, vol. 28, no. 11, pp. 3143–3149, 2014.
- [272] A. Parra-Blanco, D. Nicolas, M. R. Arnau, A. Z. Gimeno-Garcia, L. Rodrigo, and E. Quintero, "Gastric endoscopic submucosal dissection assisted by a new traction method: the clip-band technique. A feasibility study in a porcine model (with video)," *Gastrointest. Endosc.*, vol. 74, no. 5, pp. 1137–1141, 2011.
- [273] H. Mori, H. Kobara, N. Nishiyama, S. Fujihara, T. Matsunaga, and T. Masaki, "Novel effective and repeatedly available ring-thread counter traction for safer colorectal endoscopic submucosal dissection," *Surg. Endosc.*, vol. 31, no. 7, pp. 3040–3047, 2017.
- [274] P.-J. Chen, W.-C. Huang, H.-P. Wang, W.-K. Chang, T.-Y. Hsieh, S.-C. Shih, H.-Y. Wang, and C.-Y. Liu, "Percutaneous transgastric traction-assisted esophageal endoscopic submucosal dissection: a randomized controlled trial in a porcine model," *Scand. J. Gastroenterol.*, vol. 47, no. 11, pp. 1386–1393, 2012.
- [275] K. Okamoto, S. Okamura, N. Muguruma, S. Kitamura, T. Kimura, Y. Imoto, H. Miyamoto, T. Okahisa, and T. Takayama, "Endoscopic submucosal dissection for early gastric cancer using a cross-counter technique," *Surg. Endosc.*, vol. 26, no. 12, pp. 3676–3681, 2012.
- [276] T. Kobayashi, T. Gotohda, K. Tamakawa, H. Ueda, and T. Kakizoe, "Magnetic anchor for more effective endoscopic mucosal resection," *Jpn. J. Clin. Oncol.*, vol. 34, no. 3, pp. 118–123, 2004.
- [277] T. Gotoda, I. Oda, K. Tamakawa, H. Ueda, T. Kobayashi, and T. Kakizoe, "Prospective clinical trial of magnetic-anchor--guided endoscopic submucosal dissection for large early gastric cancer (with videos)," *Gastrointest. Endosc.*, vol. 69, no. 1, pp. 10–15, 2009.
- [278] I. Matsuzaki, S. Isobe, K. Hirose, T. Marukawa, and M. Esaki, "Magnetic anchor-guided endoscopic submucosal dissection for colonic tumor," *Video J. Encycl. GI Endosc.*, vol. 2, no. 4, pp. 74–75, 2017.
- [279] I. Matsuzaki, M. Hattori, K. Hirose, M. Esaki, M. Yoshikawa, T. Yokoi, M. Kobayashi, R. Miyahara, Y. Hirooka, and H. Goto, "Magnetic anchor--guided endoscopic submucosal dissection for gastric lesions (with video)," *Gastrointest. Endosc.*, vol. 87, no. 6, pp. 1576–

1580, 2018.

- [280] Y. Saito, F. Emura, T. Matsuda, T. Uraoka, T. Nakajima, H. Ikematsu, T. Gotoda, D. Saito, and T. Fujii, "A new sinker-assisted endoscopic submucosal dissection for colorectal cancer," *Gastrointest. Endosc.*, vol. 62, no. 2, pp. 297–301, 2005.
- [281] H. Kondo, T. Gotoda, H. Ono, I. Oda, T. Kozu, M. Fujishiro, D. Saito, and S. Yoshida, "Percutaneous traction-assisted EMR by using an insulation-tipped electrosurgical knife for early stage gastric cancer," *Gastrointest. Endosc.*, vol. 59, no. 2, pp. 284–288, 2004.
- [282] S. von Delius, A. Karagianni, C. H. von Weyhern, H. Feussner, T. Schuster, R. M. Schmid, and E. Frimberger, "Percutaneously assisted endoscopic surgery using a new PEG-minitrocar for advanced endoscopic submucosal dissection (with videos)," *Gastrointest. Endosc.*, vol. 68, no. 2, pp. 365–369, 2008.
- [283] H. Imaeda, Y. Iwao, H. Ogata, H. Ichikawa, M. Mori, N. Hosoe, T. Masaoka, M. Nakashita, H. Suzuki, N. Inoue, and others, "A new technique for endoscopic submucosal dissection for early gastric cancer using an external grasping forceps," *Endoscopy*, vol. 38, no. 10, pp. 1007–1010, 2006.
- [284] H. Imaeda, N. Hosoe, Y. Ida, H. Nakamizo, K. Kashiwagi, T. Kanai, Y. Iwao, T. Hibi, and H. Ogata, "Novel technique of endoscopic submucosal dissection by using external forceps for early rectal cancer (with videos)," *Gastrointest. Endosc.*, vol. 75, no. 6, pp. 1253–1257, 2012.
- [285] T. Uraoka, J. Kato, S. Ishikawa, K. Harada, M. Kuriyama, K. Takemoto, Y. Kawahara, Y. Saito, and H. Okada, "Thin endoscope-assisted endoscopic submucosal dissection for large colorectal tumors (with videos)," *Gastrointest. Endosc.*, vol. 66, no. 4, pp. 836–839, 2007.
- [286] K. Higuchi, S. Tanabe, M. Azuma, T. Sasaki, C. Katada, K. Ishido, A. Naruke, T. Mikami, and W. Koizumi, "Double-endoscope endoscopic submucosal dissection for the treatment of early gastric cancer accompanied by an ulcer scar (with video)," *Gastrointest. Endosc.*, vol. 78, no. 2, pp. 266–273, 2013.
- [287] J. Y. Ahn, K. D. Choi, J. Y. Choi, M.-Y. Kim, J. H. Lee, K.-S. Choi, D. H. Kim, H. J. Song, G. H. Lee, H.-Y. Jung, and others, "Transnasal endoscope-assisted endoscopic submucosal dissection for gastric adenoma and early gastric cancer in the pyloric area: a case series," *Endoscopy*, vol. 43, no. 03, pp. 233–235, 2011.
- [288] J. Yonezawa, M. Kaise, K. Sumiyama, K. Goda, H. Arakawa, and H. Tajiri, "A novel double-channel therapeutic endoscope ('R-scope') facilitates endoscopic submucosal dissection of

- superficial gastric neoplasms," *Endoscopy*, vol. 38, no. 10, pp. 1011–1015, 2006.
- [289] A. Loeve, P. Breedveld, and J. Dankelman, "Scopes too flexible... and too stiff," *IEEE Pulse*, vol. 1, no. 3, pp. 26–41, 2010.
- [290] S. K. Sharma, T. Hiratsuka, H. Hara, and J. W. Milsom, "Antigravity ESD--double-balloon-assisted underwater with traction hybrid technique," *Endosc. Int. open*, vol. 6, no. 06, pp. E739--E744, 2018.
- [291] S. Sharma, K. Momose, H. Hara, J. East, K. Sumiyama, K. Nakajima, G. Silbehumer, and J. Milsom, "Facilitating endoscopic submucosal dissection: double balloon endolumenal platform significantly improves dissection time compared with conventional technique (with video)," *Surg. Endosc.*, vol. 33, no. 1, pp. 315–321, 2019.
- [292] M. Runciman, A. Darzi, and G. P. Mylonas, "Deployable, Disposable, Self-Propelling and Variable Stiffness Devices for Minimally Invasive Surgery," in *2018 8th Joint Workshop on New Technologies for Computer/Robot Assisted Surgery*, 2018, pp. 17–18.
- [293] A. Repici, C. Hassan, D. D. P. Pessoa, N. Pagano, A. Arezzo, A. Zullo, R. Lorenzetti, and R. Marmo, "Efficacy and safety of endoscopic submucosal dissection for colorectal neoplasia: a systematic review," *Endoscopy*, vol. 44, no. 02, pp. 137–150, 2012.
- [294] T. Uraoka, S. Ishikawa, J. Kato, R. Higashi, H. Suzuki, E. Kaji, M. Kuriyama, S. Saito, M. Akita, K. Hori, and others, "Advantages of using thin endoscope-assisted endoscopic submucosal dissection technique for large colorectal tumors," *Dig. Endosc.*, vol. 22, no. 3, pp. 186–191, 2010.
- [295] M. A. Khashab, P. J. Pickhardt, D. H. Kim, and D. K. Rex, "Colorectal anatomy in adults at computed tomography colonography: normal distribution and the effect of age, sex, and body mass index," *Endoscopy*, vol. 41, no. 08, pp. 674–678, 2009.
- [296] S. Sadahiro, T. Ohmura, Y. Yamada, T. Saito, and Y. Taki, "Analysis of length and surface area of each segment of the large intestine according to age, sex and physique," *Surg. Radiol. Anat.*, vol. 14, no. 3, pp. 251–257, 1992.
- [297] R. M. Soetikno, T. Kaltenbach, R. V Rouse, W. Park, A. Maheshwari, T. Sato, S. Matsui, and S. Friedland, "Prevalence of nonpolypoid (flat and depressed) colorectal neoplasms in asymptomatic and symptomatic adults," *Jama*, vol. 299, no. 9, pp. 1027–1035, 2008.
- [298] Y. Saito, T. Uraoka, Y. Yamaguchi, K. Hotta, N. Sakamoto, H. Ikematsu, M. Fukuzawa, N. Kobayashi, J. Nasu, T. Michida, and others, "A prospective, multicenter study of 1111

- colorectal endoscopic submucosal dissections (with video)," *Gastrointest. Endosc.*, vol. 72, no. 6, pp. 1217–1225, 2010.
- [299] V. I. Egorov, I. V. Schastlivtsev, E. V. Prut, A. O. Baranov, and R. A. Turusov, "Mechanical properties of the human gastrointestinal tract," *J. Biomech.*, vol. 35, no. 10, pp. 1417–1425, 2002.
- [300] M. F. Traeger, D. B. Roppenecker, J. Coy, A. Fiolka, D. Wilhelm, A. Schneider, A. Meining, H. Feussner, and T. C. Lueth, "Forces in minimally invasive surgery: Reliable manipulation of gastric mucosa and the sigmoid colon," in *Robotics and Biomimetics (ROBIO), 2014 IEEE International Conference on*, 2014, pp. 408–412.
- [301] T. Ranzani, G. Ciuti, G. Tortora, A. Arezzo, S. Arolfo, M. Morino, and A. Menciassi, "A novel device for measuring forces in endoluminal procedures," *Int. J. Adv. Robot. Syst.*, vol. 12, no. 8, p. 116, 2015.
- [302] H. de Visser, E. a M. Heijnsdijk, J. L. Herder, and P. V. Pistecky, "Forces and displacements in colon surgery," *Surg. Endosc.*, vol. 16, no. 10, pp. 1426–1430, 2002.
- [303] D. K. Molina and V. J. M. DiMaio, "Normal organ weights in men: part II—the brain, lungs, liver, spleen, and kidneys," *Am. J. Forensic Med. Pathol.*, vol. 33, no. 4, pp. 368–372, 2012.
- [304] T. J. C. Oude Vrielink, M. Zhao, A. Darzi, and G. P. Mylonas, "Esd cyclops: A new robotic surgical system for gi surgery," in *2018 IEEE International Conference on Robotics and Automation (ICRA)*, 2018, pp. 150–157.
- [305] N. Yoshida, N. Yagi, Y. Naito, and T. Yoshikawa, "Safe procedure in endoscopic submucosal dissection for colorectal tumors focused on preventing complications," *World J. Gastroenterol. WJG*, vol. 16, no. 14, p. 1688, 2010.
- [306] T. A. Krouskop, T. M. Wheeler, F. Kallel, B. S. Garra, and T. Hall, "Elastic moduli of breast and prostate tissues under compression," *Ultrason. Imaging*, vol. 20, no. 4, pp. 260–274, 1998.
- [307] E. P. der Putten, R. H. M. Goossens, J. J. Jakimowicz, and J. Dankelman, "Haptics in minimally invasive surgery--a review," *Minim. Invasive Ther. Allied Technol.*, vol. 17, no. 1, pp. 3–16, 2008.
- [308] Y. Fong, W. Jarnagin, K. C. Conlon, R. DeMatteo, E. Dougherty, and L. H. Blumgart, "Hand-assisted laparoscopic liver resection: lessons from an initial experience," *Arch. Surg.*, vol. 135, no. 7, pp. 854–859, 2000.

- [309] P. Puangmali, K. Althoefer, L. D. Seneviratne, D. Murphy, and P. Dasgupta, "State-of-the-art in force and tactile sensing for minimally invasive surgery," *IEEE Sens. J.*, vol. 8, no. 4, pp. 371–381, 2008.
- [310] K. Tadano and K. Kawashima, "Development of 4-DOFs forceps with force sensing using pneumatic servo system," in *Robotics and Automation, 2006. ICRA 2006. Proceedings 2006 IEEE International Conference on*, 2006, pp. 2250–2255.
- [311] H. Sang, J. Yun, R. Monfaredi, E. Wilson, H. Fooladi, and K. Cleary, "External force estimation and implementation in robotically assisted minimally invasive surgery," *Int. J. Med. Robot. Comput. Assist. Surg.*, vol. 13, no. 2, p. e1824, 2017.
- [312] N. Yilmaz, M. Bazman, and U. Tumerdem, "External Force/Torque Estimation on a Dexterous Parallel Robotic Surgical Instrument Wrist," in *2018 IEEE/RSJ International Conference on Intelligent Robots and Systems (IROS)*, 2018, pp. 4396–4403.
- [313] S. Matich, C. Neupert, A. Kirschniak, H. F. Schlaak, and P. Pott, "3-D force measurement using single axis force sensors in a new single port parallel kinematics surgical manipulator," in *Intelligent Robots and Systems (IROS), 2016 IEEE/RSJ International Conference on*, 2016, pp. 3665–3670.
- [314] S. K. Prasad, M. Kitagawa, G. S. Fischer, J. Zand, M. A. Talamini, R. H. Taylor, and A. M. Okamura, "A modular 2-DOF force-sensing instrument for laparoscopic surgery," in *International Conference on Medical Image Computing and Computer-Assisted Intervention*, 2003, pp. 279–286.
- [315] N. Enayati, E. De Momi, and G. Ferrigno, "Haptics in robot-assisted surgery: challenges and benefits," *IEEE Rev. Biomed. Eng.*, vol. 9, pp. 49–65, 2016.
- [316] J. Konstantinova, A. Jiang, K. Althoefer, P. Dasgupta, and T. Nanayakkara, "Implementation of Tactile Sensing for Palpation in Robot-Assisted Minimally Invasive Surgery," *Sensors*, vol. 9090, no. R1, p. 1, 2013.
- [317] B. Kübler, U. Seibold, and G. Hirzinger, "Development of actuated and sensor integrated forceps for minimally invasive robotic surgery," *Int. J. Med. Robot. Comput. Assist. Surg.*, vol. 1, no. 3, pp. 96–107, 2005.
- [318] T. A. Dwarakanath, B. Dasgupta, and T. S. Mruthyunjaya, "Design and development of a Stewart platform based force--torque sensor," *Mechatronics*, vol. 11, no. 7, pp. 793–809, 2001.

- [319] D. R. Kerr, "Analysis, properties, and design of a Stewart-platform transducer," *J. Mech. Transm. Autom. Des.*, vol. 111, no. 1, pp. 25–28, 1989.
- [320] K. Miyashita, T. J. C. Oude Vrielink, and G. Mylonas, "A cable-driven parallel manipulator with force sensing capabilities for high-accuracy tissue endomicroscopy," *Int. J. Comput. Assist. Radiol. Surg.*, vol. 13, no. 5, pp. 659–669, 2018.
- [321] A. Saracino, T. J. C. Oude Vrielink, A. Menciassi, E. Sinibaldi, and G. Mylonas, "Haptic intracorporeal palpation using a cable-driven parallel robot: a user study," *Trans. Biomed. Eng. Submitt.*, 2019.
- [322] P. Gholami, M. M. Aref, and H. D. Taghirad, "On the control of the KNTU CDRPM: A cable driven redundant parallel manipulator," in *2008 IEEE/RSJ International Conference on Intelligent Robots and Systems*, 2008, pp. 2404–2409.
- [323] P. B. Stark and R. L. Parker, "Bounded-variable least-squares: an algorithm and applications," *Comput. Stat.*, vol. 10, p. 129, 1995.
- [324] V. Agrawal, W. J. Peine, and B. Yao, "Modeling of transmission characteristics across a cable-conduit system," *IEEE Trans. Robot.*, vol. 26, no. 5, pp. 914–924, 2010.
- [325] P. Pratt, A. Jaeger, A. Hughes-Hallett, E. Mayer, J. Vale, A. Darzi, T. Peters, and G.-Z. Yang, "Robust ultrasound probe tracking: initial clinical experiences during robot-assisted partial nephrectomy," *Int. J. Comput. Assist. Radiol. Surg.*, vol. 10, no. 12, pp. 1905–1913, 2015.
- [326] G. Pittiglio, A. Kogkas, T. J. C. Oude-Vrielink, and G. Mylonas, "Dynamic control of cable driven parallel robots with unknown cable stiffness: a joint space approach," in *2018 IEEE International Conference on Robotics and Automation (ICRA)*, 2018, pp. 948–955.
- [327] M. Maruthappu, B. J. Gilbert, M. A. El-Harasis, M. Nagendran, P. McCulloch, A. Duclos, and M. J. Carty, "The influence of volume and experience on individual surgical performance: a systematic review," *Ann. Surg.*, vol. 261, no. 4, pp. 642–647, 2015.
- [328] G. Ciuti, R. Donlin, P. Valdastri, A. Arezzo, A. Menciassi, M. Morino, and P. Dario, "Robotic versus manual control in magnetic steering of an endoscopic capsule," *Endoscopy*, vol. 42, no. 02, pp. 148–152, 2010.
- [329] P. R. Slawinski, A. Z. Taddese, K. B. Musto, K. L. Obstein, and P. Valdastri, "Autonomous retroflexion of a magnetic flexible endoscope," *IEEE Robot. Autom. Lett.*, vol. 2, no. 3, pp. 1352–1359, 2017.

- [330] J. M. Beer, A. D. Fisk, and W. A. Rogers, "Toward a framework for levels of robot autonomy in human-robot interaction," *J. Human-Robot Interact.*, vol. 3, no. 2, pp. 74–99, 2014.
- [331] G. P. Moustris, S. C. Hiridis, K. M. Deliparaschos, and K. M. Konstantinidis, "Evolution of autonomous and semi-autonomous robotic surgical systems: a review of the literature," *Int. J. Med. Robot. Comput. Assist. Surg.*, vol. 7, no. 4, pp. 375–392, 2011.
- [332] A. Wolf and M. Shoham, "Medical automation and robotics," in *Springer Handbook of Automation*, Springer, 2009, pp. 1397–1407.
- [333] G.-Z. Yang, J. Cambias, K. Cleary, E. Daimler, J. Drake, P. E. Dupont, N. Hata, P. Kazanzides, S. Martel, R. V Patel, and others, "Medical robotics—Regulatory, ethical, and legal considerations for increasing levels of autonomy," *Sci. Robot*, vol. 2, no. 4, p. 8638, 2017.
- [334] H. A. Paul, B. Mittlestadt, W. L. Bargar, B. Musits, R. H. Taylor, P. Kazanzides, J. Zuhars, B. Williamson, and W. Hanson, "A surgical robot for total hip replacement surgery," in *Proceedings 1992 IEEE International Conference on Robotics and Automation*, 1992, pp. 606–611.
- [335] B. L. Davies, F. M. y Baena, A. R. W. Barrett, M. Gomes, S. J. Harris, M. Jakopec, and J. P. Cobb, "Robotic control in knee joint replacement surgery," *Proc. Inst. Mech. Eng. Part H J. Eng. Med.*, vol. 221, no. 1, pp. 71–80, 2007.
- [336] M. H. L. Liow, P. L. Chin, H. N. Pang, D. K.-J. Tay, and S.-J. Yeo, "THINK surgical TSolution-One®(Robodoc) total knee arthroplasty," *SICOT-J*, vol. 3, 2017.
- [337] M. Jakopec, F. R. y Baena, S. J. Harris, P. Gomes, J. Cobb, and B. L. Davies, "The hands-on orthopaedic robot" Acrobot": Early clinical trials of total knee replacement surgery," *IEEE Trans. Robot. Autom.*, vol. 19, no. 5, pp. 902–911, 2003.
- [338] G. P. Mylonas, K.-W. Kwok, A. Darzi, and G.-Z. Yang, "Gaze-contingent motor channelling and haptic constraints for minimally invasive robotic surgery," in *International Conference on Medical Image Computing and Computer-Assisted Intervention*, 2008, pp. 676–683.
- [339] S. A. Bowyer, B. L. Davies, and F. R. y Baena, "Active constraints/virtual fixtures: A survey," *IEEE Trans. Robot.*, vol. 30, no. 1, pp. 138–157, 2014.
- [340] A. Sotiras, C. Davatzikos, and N. Paragios, "Deformable medical image registration: A survey," *IEEE Trans. Med. Imaging*, vol. 32, no. 7, p. 1153, 2013.
- [341] L. Leksell, "Stereotactic radiosurgery," *J. Neurol. Neurosurg. Psychiatry*, vol. 46, no. 9, pp.

797–803, 1983.

- [342] J. R. Adler Jr, S. D. Chang, M. J. Murphy, J. Doty, P. Geis, and S. L. Hancock, “The Cyberknife: a frameless robotic system for radiosurgery,” *Stereotact. Funct. Neurosurg.*, vol. 69, no. 1–4, pp. 124–128, 1997.
- [343] Y. Kim, H. Rhim, M. J. Choi, H. K. Lim, and D. Choi, “High-intensity focused ultrasound therapy: an overview for radiologists,” *Korean J. Radiol.*, vol. 9, no. 4, pp. 291–302, 2008.
- [344] R. Monfaredi, K. Cleary, and K. Sharma, “MRI robots for needle-based interventions: systems and technology,” *Ann. Biomed. Eng.*, vol. 46, no. 10, pp. 1479–1497, 2018.
- [345] K. Cleary, A. Melzer, V. Watson, G. Kronreif, and D. Stoianovici, “Interventional robotic systems: applications and technology state-of-the-art,” *Minim. Invasive Ther. Allied Technol.*, vol. 15, no. 2, pp. 101–113, 2006.
- [346] L. Maier-Hein, P. Mountney, A. Bartoli, H. Elhawary, D. Elson, A. Groch, A. Kolb, M. Rodrigues, J. Sorger, S. Speidel, and others, “Optical techniques for 3D surface reconstruction in computer-assisted laparoscopic surgery,” *Med. Image Anal.*, vol. 17, no. 8, pp. 974–996, 2013.
- [347] D. Hu, Y. Gong, B. Hannaford, and E. J. Seibel, “Path planning for semi-automated simulated robotic neurosurgery,” in *Intelligent Robots and Systems (IROS), 2015 IEEE/RSJ International Conference on*, 2015, pp. 2639–2645.
- [348] D. Hu, Y. Gong, B. Hannaford, and E. J. Seibel, “Semi-autonomous simulated brain tumor ablation with ravenii surgical robot using behavior tree,” in *Robotics and Automation (ICRA), 2015 IEEE International Conference on*, 2015, pp. 3868–3875.
- [349] A. Shademan, R. S. Decker, J. D. Opfermann, S. Leonard, A. Krieger, and P. C. W. Kim, “Supervised autonomous robotic soft tissue surgery,” *Sci. Transl. Med.*, vol. 8, no. 337, p. 337ra64–337ra64, 2016.
- [350] R. E. Goldman, A. Bajo, and N. Simaan, “Algorithms for autonomous exploration and estimation in compliant environments,” *Robotica*, vol. 31, no. 1, pp. 71–87, 2013.
- [351] L. Rozo, P. Jiménez, and C. Torras, “A robot learning from demonstration framework to perform force-based manipulation tasks,” *Intell. Serv. Robot.*, vol. 6, no. 1, pp. 33–51, 2013.
- [352] K. A. Nichols and A. M. Okamura, “Autonomous robotic palpation: Machine learning techniques to identify hard inclusions in soft tissues,” in *2013 IEEE International Conference on Robotics and Automation*, 2013, pp. 4384–4389.

- [353] K. A. Nichols and A. M. Okamura, "Methods to segment hard inclusions in soft tissue during autonomous robotic palpation," *IEEE Trans. Robot.*, vol. 31, no. 2, pp. 344–354, 2015.
- [354] M. Beccani, C. Di Natali, L. J. Sliker, J. A. Schoen, M. E. Rentschler, and P. Valdastrì, "Wireless tissue palpation for intraoperative detection of lumps in the soft tissue," *IEEE Trans. Biomed. Eng.*, vol. 61, no. 2, pp. 353–361, 2014.
- [355] F. Campisano, S. Ozel, A. Ramakrishnan, A. Dwivedi, N. Gkotsis, C. D. Onal, and P. Valdastrì, "Towards a soft robotic skin for autonomous tissue palpation," in *2017 IEEE International Conference on Robotics and Automation (ICRA)*, 2017, pp. 6150–6155.
- [356] M. Zhao, "Development of a Simulation Environment for a Novel Cable-driven Parallel Bimanual Robot for Single Access Surgery," Imperial College London, United Kingdom, 2016.
- [357] S.-E. Song, J. Tokuda, K. Tuncali, A. Yamada, M. Torabi, and N. Hata, "Design evaluation of a double ring RCM mechanism for robotic needle guidance in MRI-guided liver interventions," in *Intelligent Robots and Systems (IROS), 2013 IEEE/RSJ International Conference on*, 2013, pp. 4078–4083.
- [358] M. Camara, S. Dawda, E. Mayer, A. Darzi, and P. Pratt, "Subject-specific Modelling of Pneumoperitoneum: Model Implementation, Validation and Human Feasibility Assessment," *Press*, 2019.
- [359] G.-Z. Yang, J. Bellingham, P. E. Dupont, P. Fischer, L. Floridi, R. Full, N. Jacobstein, V. Kumar, M. McNutt, R. Merrifield, and others, "The grand challenges of Science Robotics," *Sci. Robot.*, vol. 3, no. 14, p. eaar7650, 2018.
- [360] C. Bergeles and G.-Z. Yang, "From passive tool holders to microsurgeons: safer, smaller, smarter surgical robots," *IEEE Trans. Biomed. Eng.*, vol. 61, no. 5, pp. 1565–1576, 2014.
- [361] W. Kraus, M. Kessler, and A. Pott, "Pulley friction compensation for winch-integrated cable force measurement and verification on a cable-driven parallel robot," in *Robotics and Automation (ICRA), 2015 IEEE International Conference on*, 2015, pp. 1627–1632.
- [362] J. P. Mulier, B. Dillemans, and S. Van Cauwenberge, "Impact of the patient's body position on the intraabdominal workspace during laparoscopic surgery," *Surg. Endosc.*, vol. 24, no. 6, pp. 1398–1402, 2010.
- [363] A. I. F. Vaz and L. N. Vicente, "A particle swarm pattern search method for bound constrained global optimization," *J. Glob. Optim.*, vol. 39, no. 2, pp. 197–219, 2007.

- [364] J. T. Bryson, X. Jin, and S. K. Agrawal, "Optimal design of cable-driven manipulators using particle swarm optimization," *J. Mech. Robot.*, vol. 8, no. 4, p. 41003, 2016.
- [365] G. Abbasnejad, J. Yoon, and H. Lee, "Optimum kinematic design of a planar cable-driven parallel robot with wrench-closure gait trajectory," *Mech. Mach. Theory*, vol. 99, pp. 1–18, 2016.
- [366] A. I. F. Vaz and L. N. Vicente, "PSwarm: a hybrid solver for linearly constrained global derivative-free optimization," *Optim. Methods Softw.*, vol. 24, no. 4–5, pp. 669–685, 2009.
- [367] F. Gustafsson, "Particle filter theory and practice with positioning applications," *IEEE Aerosp. Electron. Syst. Mag.*, vol. 25, no. 7, pp. 53–82, 2010.
- [368] Y. W. Pang, "Patient-specific Optimisation of a Surgical Robot," Imperial College London, United Kingdom, 2017.
- [369] J. Bano, a Hostettler, S. a Nicolau, S. Cotin, C. Doignon, H. S. Wu, M. H. Huang, L. Soler, and J. Marescaux, "Simulation of pneumoperitoneum for laparoscopic surgery planning.," *Med. Image Comput. Comput. Assist. Interv.*, vol. 15, no. Pt 1, pp. 91–8, 2012.
- [370] O. Oktay, L. Zhang, T. Mansi, P. Mountney, P. Mewes, S. Nicolau, L. Soler, and C. Chef d'hotel, "Biomechanically driven registration of pre- to intra-operative 3D images for laparoscopic surgery," *Lect. Notes Comput. Sci. (including Subser. Lect. Notes Artif. Intell. Lect. Notes Bioinformatics)*, vol. 8150 LNCS, no. PART 2, pp. 1–9, 2013.
- [371] P. A. Yushkevich, J. Piven, H. C. Hazlett, R. G. Smith, S. Ho, J. C. Gee, and G. Gerig, "User-guided 3D active contour segmentation of anatomical structures: significantly improved efficiency and reliability," *Neuroimage*, vol. 31, no. 3, pp. 1116–1128, 2006.
- [372] V. Vitiello, T. Cundy, A. Darzi, G. Yang, and G. Mylonas, "Augmented instrument control for the cyclops robotic system," in *The Hamlyn Symposium on Medical Robotics*, 2014, p. 29.
- [373] J.-H. Borchard, J. Kotlarski, and T. Ortmaier, "Workspace comparison of cooperating instruments in laparo-endoscopic single-site surgery," in *Advanced Intelligent Mechatronics (AIM), 2013 IEEE/ASME International Conference on*, 2013, pp. 1241–1248.
- [374] A. B. Kassam, J. A. Engh, A. H. Mintz, and D. M. Prevedello, "Completely endoscopic resection of intraparenchymal brain tumors," *J. Neurosurg.*, vol. 110, no. 1, pp. 116–123, 2009.
- [375] M. Brayda-Bruno and P. Cinnella, "Posterior endoscopic discectomy (and other procedures)," *Eur. Spine J.*, vol. 9, no. 1, pp. S024--S029, 2000.

- [376] F. A. Haji, A. Cenic, L. Crevier, N. Murty, and K. Reddy, "Minimally invasive approach for the resection of spinal neoplasm," *Spine (Phila. Pa. 1976)*, vol. 36, no. 15, pp. E1018--E1026, 2011.
- [377] G. Buess, K. Kipfmüller, D. Hack, R. Grüssner, A. Heintz, and T. Junginger, "Technique of transanal endoscopic microsurgery," *Surg. Endosc.*, vol. 2, no. 2, pp. 71–75, 1988.
- [378] "Titan Medical pushes FDA submission back to 2019, looks to US stock market cross listing." [Online]. Available: <https://www.massdevice.com/titan-medical-pushes-fda-submission-back-2019-looks-us-stock-market-cross-listing/>. [Accessed: 17-Dec-2018].
- [379] H. Inoue, H. Minami, Y. Kobayashi, Y. Sato, M. Kaga, M. Suzuki, H. Satodate, N. Odaka, H. Itoh, and S. Kudo, "Peroral endoscopic myotomy (POEM) for esophageal achalasia," *Endoscopy*, vol. 42, no. 04, pp. 265–271, 2010.

Copyright Permissions for usage of figures

The table below indicates for each figure the source and permissions. Specific letters for granting permission are added after the table.

Page no.	Figure	Name of work	Source of work	Copyright holder and contact	Permission requested on	I have permission yes/no	Permission Note
	1.2a	Image, Xi, Nurse at Patient Cart	Intuitive Surgical Online Community (behind login portal). https://www.davincisurgerycommunity.com	©2019 Intuitive Surgical, Inc.	-	yes	Terms of conditions Intuitive Surgery (Online Community webpage). “Reproduced images should be accompanied by the following copyright notice: ©[Year] Intuitive Surgical, Inc.”
	1.2b	Image, Xi, Surgeon Seated at Surgeon Console	https://www.davincisurgerycommunity.com	©2019 Intuitive Surgical, Inc.	-	yes	Idem as 1.2a.
	1.2c	Image, EndoWrist Instruments, Instrument Tip Size Comparison with US Penny	https://www.davincisurgerycommunity.com	©2019 Intuitive Surgical, Inc.	-	yes	Idem as 1.2a.
	1.3	Fig. 5. The CYCLOPS working prototype at its early stage of development.	Mylonas, G. P., Vitiello, V., Cundy, T. P., Darzi, A., & Yang, G. Z. (2014, May). CYCLOPS: A versatile robotic tool for bimanual single-access and natural-orifice endoscopic surgery. In <i>2014 IEEE International Conference on Robotics and Automation (ICRA)</i> (pp. 2436-2442). IEEE.	©2014 IEEE customercare@copyright.com	-	Yes	IEEE default permission for usage in thesis/dissertation (see letter bellow)

1.4a	Fig. 1. Epicardial wire robot for rapid accurate myocardial injection for gene therapy. (a) The manipulator collapses for endoscopic insertion and removal. (b) After insertion, it deploys in triangular shape, with its three corners grasping the epicardium with suction. By pulling the 3 cables that connect the injection head to the 3 suction bases, injections can be rapidly and accurately placed anywhere within the dotted triangle	Costanza, A. D., Wood, N. A., Passineau, M. J., Moraca, R. J., Bailey, S. H., Yoshizumi, T., & Riviere, C. N. (2014, August). A parallel wire robot for epicardial interventions. In <i>2014 36th Annual International Conference of the IEEE Engineering in Medicine and Biology Society</i> (pp. 6155-6158). IEEE.	©2014 IEEE customercare@copyright.com	-	Yes	IEEE default permission for usage in thesis/dissertation (see letter)
1.4b	Figure 5: Schematic of Endoscope Manipulator	Berkelman, P., Cinquin, P., Troccaz, J., Ayoubi, J., Letoublon, C., & Bouchard, F. (2002). A compact, compliant laparoscopic endoscope manipulator. In <i>Proceedings 2002 IEEE International Conference on Robotics and Automation</i> (Cat. No. 02CH37292) (Vol. 2, pp. 1870-1875). IEEE.	©2002 IEEE customercare@copyright.com	-	Yes	IEEE default permission for usage in thesis/dissertation (see letter)
1.4c	(b) The entire LPR robot.	Bricault, I., Zemiti, N., Jouniaux, E., Fouard, C., Taillant, E., Dorandeu, F., & Cinquin, P. (2008). Light puncture robot for CT and MRI interventions. <i>IEEE Engineering in Medicine and Biology Magazine</i> , 27(3), 42-50.	©2008 IEEE customercare@copyright.com	-	Yes	IEEE default permission for usage in thesis/dissertation (see letter)

	2.4a	RoboCrane®	https://www.nist.gov/image/manufacturingroboticsrobocrane174foraircraftmaintenancewideviewjpg-0	Credit: N.E. Wasson Jr./US Technologies	-	Yes	“Other organizations may use this image without charge for editorial articles that mention NIST in accompanying text or a caption. Correct photo credit must be provided. "Stock art" use requires permission and may require payment to the photographer. To receive a high resolution version send an email with the image title to inquiries@nist.gov .”
	2.4b	-	https://3dprint.com/wp-content/uploads/2017/04/20.jpg	Credit: IAAC - Institute for Advanced Architecture of Catalonia press@iaac.net	23-01-2019	Yes	Permission given by email (attached below)
	2.4c	-	Original image sent over email	Credit: Fraunhofer IPA teresa.mittner@ipa.fraunhofer.de	16-01-2019	Yes	Permission given by email (attached below)
	2.4d	-	Original image sent over email	Credit: Fraunhofer IPA, Philipp Miermeister teresa.mittner@ipa.fraunhofer.de	16-01-2019	Yes	Permission given by email (attached below)
	2.5a	A Skycam HD camera at Stanford Cardinals Stadium	https://commons.wikimedia.org/wiki/File:Sky_Cam_at_Stanford.jpg	Jrienstra (https://commons.wikimedia.org/wiki/File:Sky_Cam_at_Stanford.jpg), „Sky Cam at Stanford“, https://creativecommons.org/licenses/by-sa/3.0/legalcode	-	Yes	Licensed under the <i>Creative Commons Attribution-Share Alike 3.0 Unported</i>

	2.5b	Figure 1. The cable-driven parallel mechanism in action. The end-effector holds a SLR camera that is used to acquire images of the object from multiple viewpoints. The end-effector is suspended by six cables passing through pulleys attached to the walls of the room. The object is surrounded by a green enclosure to allow easy extraction of the object silhouette as well as precise positioning.	Deschênes, J. D., Lambert, P., Perreault, S., Martel-Brisson, N., Zoso, N., Zaccarin, A., ... & Gosselin, C. M. (2007, August). A cable-driven parallel mechanism for capturing object appearance from multiple viewpoints. In Sixth International Conference on 3-D Digital Imaging and Modeling (3DIM 2007) (pp. 367-374). IEEE.	©2007 IEEE customercare@copyright.com	-	Yes	IEEE default permission for usage in thesis/dissertation (see letter)
	2.5c	Scale model of FAST at the Five-Year Achievements Exhibition	https://commons.wikimedia.org/wiki/File:Scale_model_of_FAST_at_the_Five-Year_Achievements_Exhibition_(20171015151703).jpg	N509FZ (https://commons.wikimedia.org/wiki/File:Scale_model_of_FAST_at_the_Five-Year_Achievements_Exhibition_(20171015151703).jpg), https://creativecommons.org/licenses/by-sa/4.0/legalcode	-	Yes	Licensed under the <i>Creative Commons Attribution-Share Alike 4.0 International</i>
	2.6a	Fig. 1 Cable-driven parallel robot Mini-IPAnema3	Ho, W. Y., Kraus, W., Mangold, A., & Pott, A. (2015). Haptic interaction with a cable-driven parallel robot using admittance control. In Cable-Driven Parallel Robots (pp. 201-212). Springer, Cham.	© Springer International Publishing Switzerland 2015 customercare@copyright.com	16-01-2019	Yes	RightsLink® Licence Number 4511091224916
	2.6b	Fig. 6 Experimental setup and the coordinate systems	Jin, X., Jun, D. I., Jin, X., Seon, J., Pott, A., Park, S., ... & Ko, S. Y. (2015). Upper limb rehabilitation using a planar cable-driven parallel robot with various rehabilitation strategies. In Cable-Driven Parallel Robots (pp. 307-321). Springer, Cham.	© Springer International Publishing Switzerland 2015 customercare@copyright.com	16-01-2019	Yes	RightsLink® Licence Number 4511090974171

	2.6c	Figure 14. Test of the virtual envelope	Surdilovic, D., & Bernhardt, R. (2004, April). STRING-MAN: a new wire robot for gait rehabilitation. In IEEE International Conference on Robotics and Automation, 2004. Proceedings. ICRA'04. 2004 (Vol. 2, pp. 2031-2036). IEEE.	©2007 IEEE customercare@copyright.com	-	Yes	IEEE's default permission for usage in thesis/dissertation (see letter)
	2.6d	Fig. 1. A photograph of a user wearing CAREX. CAREX has three cuffs. The shoulder cuff is fixed on a chair.[...]	Mao, Y., Jin, X., Dutta, G. G., Scholz, J. P., & Agrawal, S. K. (2015). Human movement training with a cable driven ARm EXoskeleton (CAREX). IEEE Transactions on Neural Systems and Rehabilitation Engineering, 23(1), 84-92.	©2015 IEEE customercare@copyright.com	-	Yes	IEEE's default permission for usage in thesis/dissertation (see letter)
	2.6e	Fig. 1. The NeReBot 3 d.o.f. rehabilitation robot. Three wires are used to move the splint; each wire passes through a manually adjustable link and is pulled by a brushless motor located at the column base. The topmost link can be used to sustain the shoulder by means of a non-driven cable.	Rosati, G., Gallina, P., Masiero, S., & Rossi, A. (2005, June). Design of a new 5 dof wire-based robot for rehabilitation. In 9th International Conference on Rehabilitation Robotics, 2005. ICORR 2005. (pp. 430-433). IEEE.	©2005 IEEE customercare@copyright.com	-	Yes	IEEE's default permission for usage in thesis/dissertation (see letter)

2.6f	FIGURE 1. Robotic Physical Exercise and System (ROPES): A Cable-Driven Robotic Rehabilitation System For Lower-Extremity, T_i , t_i , K_{ji} , C_{ji} are cable tension, cable unit vector, internal torsion spring and damper constants at the hip, knee and ankle joints instead of joints' stiffness and damping, respectively, K_{ti} are external tensional and torsion springs for increasing the workspace of cable-driven system.	Alamdari, A., & Krovi, V. (2015, August). Robotic physical exercise and system (ROPES): A cable-driven robotic rehabilitation system for lower-extremity motor therapy. In ASME 2015 International Design Engineering Technical Conferences and Computers and Information in Engineering Conference (pp. V05AT08A032-V05AT08A032). American Society of Mechanical Engineers.	© 2015 by ASME darchib@asme.org	17-01-2019	Yes	Permission granted by ASME (See letter below)
3.1a	Fig. 2 The double parallelogram mechanism	Li, J., Xing, Y., Liang, K., & Wang, S. (2015). Kinematic design of a novel spatial remote center-of-motion mechanism for minimally invasive surgical robot. Journal of Medical Devices, 9(1), 011003.	© 2015 by ASME darchib@asme.org	23-01-2019	Yes	Permission granted by ASME (See letter below)
3.1b	(b) serial configuration	Lum, M. J., Rosen, J., Sinanan, M. N., & Hannaford, B. (2006). Optimization of a spherical mechanism for a minimally invasive surgical robot: theoretical and experimental approaches. IEEE Transactions on Biomedical Engineering, 53(7), 1440-1445.	© 2006 IEEE customercare@copyright.com	-	Yes	IEEE's default permission for usage in thesis/dissertation (see letter)
3.1c	Fig. 1. Mitsubishi PA10-7C generating an RCM.	Locke, R. C., & Patel, R. V. (2007, April). Optimal remote center-of-motion location for robotics-assisted minimally-invasive surgery. In Proceedings 2007 IEEE International Conference on Robotics and Automation (pp. 1900-1905). IEEE.	© 2007 IEEE customercare@copyright.com	-	Yes	IEEE's default permission for usage in thesis/dissertation (see letter)

	3.2a	Figure 1. VeSPA instruments and accessories. (A) curved cannulae; (B) multichannel single-port, 8.5-mm robotic scope, flexible instruments passed through the cannulae.	Haber, G. P., White, M. A., Autorino, R., Escobar, P. F., Kroh, M. D., Chalikonda, S., ... & Stein, R. J. (2010). Novel robotic da Vinci instruments for laparoendoscopic single-site surgery. <i>Urology</i> , 76(6), 1279-1282.	© 2010 Elsevier Inc. customercare@copyright.com	17-01-2019	Yes	RightsLink® Licence Number 4511500976234
	3.2b	FIGURE 1 Complete teleoperated robot system, including ViKY base with endoscope, additional support frame, instrument manipulators and robotic instruments	Isaac-Lowry, O. J., Okamoto, S., Pedram, S. A., Woo, R., & Berkelman, P. (2017). Compact teleoperated laparoendoscopic single-site robotic surgical system: Kinematics, control, and operation. <i>The International Journal of Medical Robotics and Computer Assisted Surgery</i> , 13(4), e1811.	© John Wiley & Sons, Ltd. customercare@copyright.com	17-01-2019	Yes	RightsLink® Licence Number 4511510214549
	3.3a	Fig. 10. Experiment: (a) 10 N weight pick up test; (b) peg board transfer test; and (c) suturing and knotting test.	Choi, H., Kwak, H. S., Lim, Y. A., & Kim, H. J. (2014). Surgical robot for single-incision laparoscopic surgery. <i>IEEE Transactions on Biomedical Engineering</i> , 61(9), 2458-2466.	© 2014 IEEE customercare@copyright.com	-	Yes	IEEE's default permission for usage in thesis/dissertation (see letter)
	3.3b	Fig. 1 – The da Vinci SP Surgical System (Model SP999; Intuitive Surgical Inc., Sunnyvale, CA, USA). (a) Detail of three articulating endoscopic instruments and an articulating endoscopic camera inserted through a single robotic port;	Kaouk, J. H., Haber, G. P., Autorino, R., Crouzet, S., Ouzzane, A., Flamand, V., & Villers, A. (2014). A novel robotic system for single-port urologic surgery: first clinical investigation. <i>European urology</i> , 66(6), 1033-1043.	© 2014 European Association of Urology customercare@copyright.com	17-01-2019	Yes	RightsLink® Licence Number 4511510884437

	3.3c	Figure 4. Application of the HVSPS for NOTES cholecystectomy: a) HVSPS manipulators in triangulated configuration with the flexible endoscope R-Scope (Olympus, Japan) b) [...]	Can, S., Fiolka, A., Mayer, H., Knoll, A., Schneider, A., Wilhelm, D., ... & Feussner, H. (2008). The mechatronic support system "HVSPS" and the way to NOTES. Minimally invasive therapy & allied technologies, 17(6), 341-345.	© 2008 Informa UK Ltd	10-04-2019	Not Yet	Taylor & Francis is pleased to offer reuses of its content for a thesis or dissertation free of charge contingent on resubmission of permission request if work is published First request letter added below. 2nd request letter added below.
	3.4a	https://www.ecnmag.com/article/2018/01/titan-medicals-sport-robotically-assisted-surgical-system-making-headway	https://abm-website-assets.s3.amazonaws.com/ecnmag.com/s3fs-public/styles/hero/public/feature_d_image/2018/01/titan%20medical%20nicholson.JPG?itok=uQY6zaY3	© Titan Medical Inc susan@titanmedicalinc.com	18-01-2019	Yes	Permission Titan medical (See letter below)
	3.4b	Fig.1. Constructed SURS robot: (a) folded configuration deployable through a ϕ 12-mm incision, (b) unfolded working configuration.	Xu, K., Zhao, J., & Fu, M. (2015). Development of the SJTU unfoldable robotic system (SURS) for single port laparoscopy. IEEE/ASME Transactions on Mechatronics, 20(5), 2133-2145.	© 2015 IEEE customercare@copyright.com	-	Yes	IEEE's default permission for usage in thesis/dissertation (see letter)
	3.5a	Fig. 11 Final prototype of PLAS	Cheon, B., Gezgin, E., Ji, D. K., Tomikawa, M., Hashizume, M., Kim, H. J., & Hong, J. (2014). A single port laparoscopic surgery robot with high force transmission and a large workspace. Surgical endoscopy, 28(9), 2719-2729.	© Springer Science+Business Media New York 2014 customercare@copyright.com	22-01-2019	Yes	RightsLink® Licence Number 4514471230244

	3.5b	Figure 7 Preliminary tests for system verification	Hwang, M., Yang, U. J., Kong, D., Chung, D. G., Lim, J. G., Lee, D. H., ... & Kwon, D. S. (2017). A single port surgical robot system with novel elbow joint mechanism for high force transmission. The International Journal of Medical Robotics and Computer Assisted Surgery, 13(4), e1808.	© John Wiley & Sons, Ltd. customercare@copyright.com	10-04-2019	Yes	RightsLink® Licence Number 4565241235529
	3.5c	Fig.2 Principle of bending motion	Ishii, C., & Kobayashi, K. (2007, April). Development of a new bending mechanism and its application to robotic forceps manipulator. In Proceedings 2007 IEEE International Conference on Robotics and Automation (pp. 238-243). IEEE.	©2007 IEEE customercare@copyright.com	-	Yes	IEEE's default permission for usage in thesis/dissertation (see letter)
	3.6a	Figure 2. Two arms are equipped at the tip portion of the EndoSAMURAI.	Ikeda, K., Sumiyama, K., Tajiri, H., Yasuda, K., & Kitano, S. (2011). Evaluation of a new multitasking platform for endoscopic full-thickness resection. Gastrointestinal endoscopy, 73(1), 117-122.	© 2011 American Society for Gastrointestinal Endoscopy customercare@copyright.com	17-01-2019	Yes	RightsLink® Licence Number 4511380918000
	3.6b	Figure 2. [...] B, The 2 separate, articulated working channels of the R-scope.	Moyer, M. T., Haluck, R. S., Gopal, J., Pauli, E. M., & Mathew, A. (2010). Transgastric organ resection solely with the prototype R-scope and the self-approximating transluminal access technique. Gastrointestinal endoscopy, 72(1), 170-176.	© 2010 American Society for Gastrointestinal Endoscopy customercare@copyright.com	17-01-2019	Yes	RightsLink® Licence Number 4511400666440

	3.6c	Figure 4. ANUBISCOPE (IRCAD & Karl Storz Endoskope).	Dallemagne, B., & Marescaux, J. (2010). The ANUBIS™ project. Minimally Invasive Therapy & Allied Technologies, 19(5), 257-261.	© 2010 Informa Healthcare	10-04-2019	Not Yet	<p><i>Taylor & Francis is pleased to offer reuses of its content for a thesis or dissertation free of charge contingent on resubmission of permission request if work is published</i></p> <p><i>First request letter added below. 2nd request letter added below.</i></p>
	3.7a	Medrobotics Flex® Robotic System	Original image provided by Samuel Straface (12-04-2019)	© Medrobotics Corporation kknightpr@gmail.com	11-04-2019	Yes	<p>The permission required proper acknowledgement of the Medrobotics Corporation and use of the full name Medrobotics Flex® Robotic System. Use for thesis only.</p> <p>See letter.</p>
	3.7b	Figure 7. The Cobra device features independently moving arms that allow the daughter scope to be elevated off the plane of the working arms and also permit traction/counter traction	Bardaro, S. J., & Swanström, L. (2006). Development of advanced endoscopes for natural orifice transluminal endoscopic surgery. Minimally Invasive Therapy & Allied Technologies, 15(6), 378-383.	© 2006 Taylor & Francis	10-04-2019	Not Yet	<p><i>Taylor & Francis is pleased to offer reuses of its content for a thesis or dissertation free of charge contingent on resubmission of permission request if work is published</i></p> <p><i>First request letter added below. 2nd request letter added below.</i></p>
	3.7c	Figure 1. Direct Drive Endoscopic System.	Thompson, C. C., Ryou, M., Soper, N. J., Hungess, E. S., Rothstein, R. I., & Swanstrom, L. L. (2009). Evaluation of a manually driven, multitasking platform for complex endoluminal and natural orifice transluminal endoscopic surgery applications (with video). Gastrointestinal endoscopy, 70(1), 121-125.	© 2009 American Society for Gastrointestinal Endoscopy customercare@copyright.com	17-01-2019	Yes	RightsLink® Licence Number 4511381220604

	3.8a	Figure 2: Slave Prototype	Phee, S. J., Low, S. C., Huynh, V. A., Kencana, A. P., Sun, Z. L., & Yang, K. (2009, September). Master and slave transluminal endoscopic robot (MASTER) for natural orifice transluminal endoscopic surgery. In 2009 Annual International Conference of the IEEE Engineering in Medicine and Biology Society (pp. 1192-1195). IEEE.	©2009 IEEE customercare@copyright.com	-	Yes	IEEE's default permission for usage in thesis/dissertation (see letter)
	3.8b	Figure 10 Experimental platform for scarless surgery developed by MiMed/TU München.	Feussner, H., Becker, V., Bauer, M., Kranzfelder, M., Schirren, R., Lüth, T., ... & WILHELM, D. (2015). Developments in flexible endoscopic surgery: a review. clinical and experimental gastroenterology, 8, 31.	©Feussner et al.	-	Yes	Licensed under the <i>Creative Commons Attribution – Non Commercial (unported, v3.0)</i> License
	3.9a	Fig. 3. Wire-reduction mechanism; (a) schematic diagram of the wire-reduction mechanism and (b) joint design using the wire-reduction mechanism	Roh, K. S., Yoon, S., Do Kwon, Y., Shim, Y., & Kim, Y. J. (2015, August). Single-Port surgical robot system with flexible surgical instruments. In International Conference on Intelligent Robotics and Applications (pp. 447-459). Springer, Cham.	© Springer International Publishing Switzerland 2015 customercare@copyright.com	23-01-2019	Yes	RightsLink® Licence Number 4514720217563
	3.9b	Fig. 1. [...] (b) Single-port surgical system using the variable neutral-line manipulator.	Kim, Y. J., Cheng, S., Kim, S., & Iagnemma, K. (2014). A stiffness-adjustable hyperredundant manipulator using a variable neutral-line mechanism for minimally invasive surgery. IEEE transactions on robotics, 30(2), 382-395.	©2014 IEEE customercare@copyright.com	-	Yes	IEEE's default permission for usage in thesis/dissertation (see letter)

	3.10a	Fig. 1 (A) Robot inserted through single incision. (B) Dexterous robot for advanced minimally invasive surgery	Lehman, A. C., Wood, N. A., Farritor, S., Goede, M. R., & Oleynikov, D. (2011). Dexterous miniature robot for advanced minimally invasive surgery. <i>Surgical endoscopy</i> , 25(1), 119-123.	© Springer Science+Business Media, LLC 2010 customercare@copyright.com	23-01-2019	Yes	RightsLink® Licence Number 4515020788979
	3.10b	Fig.1 Possible topologies of the modular robot in the stomach	Harada, K., Susilo, E., Menciassi, A., & Dario, P. (2009, May). Wireless reconfigurable modules for robotic endoluminal surgery. In 2009 IEEE International Conference on Robotics and Automation (pp. 2699-2704). IEEE.	©2009 IEEE customercare@copyright.com	-	Yes	IEEE's default permission for usage in thesis/dissertation (see letter)
	3.10c	Fig. 2. Internal unit of the endoluminal platform: miniature camera module anchored on the actuated triangular-shaped magnetic frame equipped with a dedicated docking mechanism.	Tognarelli, S., Salerno, M., Tortora, G., Quaglia, C., Dario, P., & Menciassi, A. (2012, June). An endoluminal robotic platform for Minimally Invasive Surgery. In 2012 4th IEEE RAS & EMBS International Conference on Biomedical Robotics and Biomechatronics (BioRob) (pp. 7-12). IEEE.	©2012 IEEE customercare@copyright.com	-	Yes	IEEE's default permission for usage in thesis/dissertation (see letter)
	3.11a	Fig. 2 LumenR retraction system. [...] B Close-up view of the LumenR operating chamber containing the distal tip of the colonoscope (black) and two colorcoded (red and black) instrument guides (LIG) with rat-tooth forceps (Color figure online)	Kantsevov, S. V., Bitner, M., & Piskun, G. (2016). New endoscopic platform for endoluminal enbloc tissue resection in the gastrointestinal tract (with videos). <i>Surgical endoscopy</i> , 30(7), 3145-3151.	© Springer Science+Business Media New York 2015 customercare@copyright.com	17-01-2019	Yes	RightsLink® Licence Number 4511400268119

3.11b	Fig. 1. The EndoLifter (Olympus). (A) The EndoLifter mounted on the tip of an endoscope. (B) Grasping forceps proceeding forward over the tip of the endoscope and opening.	Schölvinck, D. W., Goto, O., Bergman, J. J., Yahagi, N., & Weusten, B. L. (2015). The efficacy of an endoscopic grasp-and-traction device for gastric endoscopic submucosal dissection: an ex vivo comparative study (with video). <i>Clinical endoscopy</i> , 48(3), 221.	© 2015 Korean Society of Gastrointestinal Endoscopy	-	Yes	This is an Open Access article distributed under the terms of the <i>Creative Commons Attribution Non-Commercial License</i> (http://creativecommons.org/licenses/by-nc/3.0/)
3.12c	Fig.2 Close-up view of novel system of articulating devices. a Articulating forceps and knife [...]	Nakadate, R., Nakamura, S., Moriyama, T., Kenmotsu, H., Oguri, S., Arata, J., ... & Hashizume, M. (2015). Gastric endoscopic submucosal dissection using novel 2.6-mm articulating devices: an ex vivo comparative and in vivo feasibility study. <i>Endoscopy</i> , 47(09), 820-824.	© Georg Thieme Verlag KG Stuttgart · New York customercare@copyright.com	23-01-2019	Yes	RightsLink® Licence Number 4514720798473
3.12a	-	https://www.demcon.nl/wp-content/uploads/2016/04/definitief3507en3608-uitgesneden-620x350.jpg	© DEMCON advanced mechatronics B.V. renee.koekkoek.op.munsterhuis@demcon.nl	23-01-2019	Yes	Permission granted by DEMCON (see letter below, in Dutch)
3.12b	Figure 1. MrBot robot alongside the man on the magnetic resonance imaging table: computer-aided design rendering (left), and photo (right).	Mozer, P. C., Partin, A. W., & Stoianovici, D. (2009). Robotic image-guided needle interventions of the prostate. <i>Reviews in urology</i> , 11(1), 7.	© 2009 MedReviews, LLC mcroft@medreviews.com	11-04-2019	Yes	Reprinted with permission of MedReviews®, LLC. Mozer PC, Partin AW, Stoianovici D. Robotic image-guided needle interventions of the prostate. <i>Rev Urol.</i> 2009;11(1):7-15. All rights reserved. See letter below.

	3.13	Fig. 6: Eight possible morphologies of a CRISP robot consisting of one flexible tool and one to three snare needles. The tool and snares are highlighted in white for visibility.	Mahoney, A. W., Anderson, P. L., Swaney, P. J., Maldonado, F., & Webster, R. J. (2016, October). Reconfigurable parallel continuum robots for incisionless surgery. In 2016 IEEE/RSJ International Conference on Intelligent Robots and Systems (IROS) (pp. 4330-4336). IEEE.	©2016 IEEE customercare@copyright.com	-	Yes	IEEE's default permission for usage in thesis/dissertation (see letter)
	4.2a	Figure 2. The basic approach of traction-assisted endoscopic submucosal dissection according to the tumor location. Generally, the clip anchoring site is on the oral side if the endoscope is in straight position and on the anal side if it is in retroflex position. A , [...]. B , Clip anchoring to manage lesions in the greater curvature of the upper or middle third of the stomach. C , [...]	Yoshida, M., Takizawa, K., Suzuki, S., Koike, Y., Nonaka, S., Yamasaki, Y., ... & Kanzaki, H. (2018). Conventional versus traction-assisted endoscopic submucosal dissection for gastric neoplasms: a multicenter, randomized controlled trial (with video). Gastrointestinal endoscopy, 87(5), 1231-1240.	© 2018 by the American Society for Gastrointestinal Endoscopy customercare@copyright.com	24-01-2019	Yes	RightsLink® Licence Number 4515340623392
	4.2b	Figure 2. A, ESD with the pulley method. The distal loop is anchored on the edge of the resection mucosa with the first clip. The pulley loop is fixed on the opposite site of the gastric mucosa with the second clip, which is away from the distal loop to generate traction direction up and away from the resection plane. The edge of resection mucosa is elevated while pulling the floss out through the mouth. B, [...]	Li, C. H., Chen, P. J., Chu, H. C., Huang, T. Y., Shih, Y. L., Chang, W. K., & Hsieh, T. Y. (2011). Endoscopic submucosal dissection with the pulley method for early-stage gastric cancer (with video). Gastrointestinal endoscopy, 73(1), 163-167.	© 2011 American Society for Gastrointestinal Endoscopy customercare@copyright.com	24-01-2019	Yes	RightsLink® Licence Number 4515340942851

	4.2c	Fig. 4 Illustration depicting S–O clip-assisted ESD	Ritsuno, H., Sakamoto, N., Osada, T., Goto, S. P., Murakami, T., Ueyama, H., ... & Nagahara, A. (2014). Prospective clinical trial of traction device-assisted endoscopic submucosal dissection of large superficial colorectal tumors using the S–O clip. <i>Surgical endoscopy</i> , 28(11), 3143-3149.	© Springer Science+Business Media New York 2014 customercare@copyright.com	24-01-2019	Yes	RightsLink® Licence Number 4515341238544
	4.2d	Fig. 2 The typical picture and schema of ring-shaped thread counter traction. [...] C As submucosal dissection was continued and the traction force of the ring-shaped thread was decreased, a third hemoclip was added to hook and slide one side of the ring-shaped thread to obtain further counter traction. D [...]	Mori, H., Kobara, H., Nishiyama, N., Fujihara, S., Matsunaga, T., & Masaki, T. (2017). Novel effective and repeatedly available ring-thread counter traction for safer colorectal endoscopic submucosal dissection. <i>Surgical endoscopy</i> , 31(7), 3040-3047.	© The Author(s) 2016 Corresponding author: Hirohito Mori hiro4884@med.kagawa-u.ac.jp	-	Yes	This article is distributed under the terms of the Creative Commons Attribution 4.0 International License (http://creativecommons.org/licenses/by/4.0/)
	4.2e	Figure 1. Illustration of the PTT technique. The looped insertion wire is placed through a needle cannula and into the stomach. The PEG wire is affixed to the proximal edge of the resected mucosa with the clip and gently pulled out through the needle on the abdominal wall. The edge of resection mucosa is pulled away from the muscle layer.	Chen, P. J., Huang, W. C., Wang, H. P., Chang, W. K., Hsieh, T. Y., Shih, S. C., ... & Liu, C. Y. (2012). Percutaneous transgastric traction-assisted esophageal endoscopic submucosal dissection: a randomized controlled trial in a porcine model. <i>Scandinavian journal of gastroenterology</i> , 47(11), 1386-1393.	© 2012 Informa Healthcare	10-04-2019	Not Yet	<i>Taylor & Francis is pleased to offer reuses of its content for a thesis or dissertation free of charge contingent on resubmission of permission request if work is published</i> <i>First request letter added below.</i> <i>2nd request letter added below.</i>

4.2f	Fig. 2 Schema of the CC technique. [...] During submucosal dissection, the clip was continuously pulled very gently by an assistant. By pushing the scope toward the submucosa to be cut and pulling the thread in the opposite direction, the submucosa was lifted up enough and the “cross-counter” situation was configured (E, F)	Okamoto, K., Okamura, S., Muguruma, N., Kitamura, S., Kimura, T., Imoto, Y., ... & Takayama, T. (2012). Endoscopic submucosal dissection for early gastric cancer using a cross-counter technique. Surgical endoscopy, 26(12), 3676-3681.	© Springer Science+Business Media, LLC 2012 customercare@copyright.com	24-01-2019	Yes	RightsLink® Licence Number 4515360395946
4.3	-	https://mms.businesswire.com/media/20180529005316/en/659963/5/Lumendi_System_05-22-18_View_4.jpg?download=1	© Lumendi Ltd. deanneeagle@gmail.com	24-01-2019	Yes	Permission Lumendi Ltd (Letter below)
4.4 top-left	Fig. 1. Render of the ESD CYCLOPS system, without the soft silicone sleeve.	Oude Vrielink, T. J., Zhao, M., Darzi, A., & Mylonas, G. P. (2018, May). ESD CYCLOPS: A new robotic surgical system for GI surgery. In 2018 IEEE International Conference on Robotics and Automation (ICRA) (pp. 150-157). IEEE.	© 2018 IEEE customercare@copyright.com	-	Yes	IEEE's default permission for usage in thesis/dissertation (see letter)
4.4 right	Fig. 2. Overview of the mechatronics of the system. A. Deployable scaffold with silicon sleeve and two surgical instruments. [...]	Oude Vrielink, T. J., Zhao, M., Darzi, A., & Mylonas, G. P. (2018, May). ESD CYCLOPS: A new robotic surgical system for GI surgery. In 2018 IEEE International Conference on Robotics and Automation (ICRA) (pp. 150-157). IEEE.	© 2018 IEEE customercare@copyright.com	-	Yes	IEEE's default permission for usage in thesis/dissertation (see letter)

	4.5	Fig. 3. System schematic diagram	Oude Vrielink, T. J., Zhao, M., Darzi, A., & Mylonas, G. P. (2018, May). ESD CYCLOPS: A new robotic surgical system for GI surgery. In 2018 IEEE International Conference on Robotics and Automation (ICRA) (pp. 150-157). IEEE.	© 2018 IEEE customercare@copyright.com	-	Yes	IEEE's default permission for usage in thesis/dissertation (see letter)
	4.6	Fig. 4. Scaled-up version of the inflatable scaffold.	Oude Vrielink, T. J., Zhao, M., Darzi, A., & Mylonas, G. P. (2018, May). ESD CYCLOPS: A new robotic surgical system for GI surgery. In 2018 IEEE International Conference on Robotics and Automation (ICRA) (pp. 150-157). IEEE.	© 2018 IEEE customercare@copyright.com	-	Yes	IEEE's default permission for usage in thesis/dissertation (see letter)
	4.7	Fig.1 Three-dimensional colon maps from computed tomography colonography (CTC) demonstrating a range of colorectal length and tortuosity, including: a relatively short "textbook" colon (147cm length); [...]	Khashab, M. A., Pickhardt, P. J., Kim, D. H., & Rex, D. K. (2009). Colorectal anatomy in adults at computed tomography colonography: normal distribution and the effect of age, sex, and body mass index. Endoscopy, 41(08), 674-678.	© Georg Thieme Verlag KG Stuttgart · New York customercare@copyright.com	24-01-2019	Yes	RightsLink® Licence Number 4515560920420
	4.18	Fig. 8. Setup for force measurements on straight tool (left) and angled tool mimicking the curved tool (right). A and B represent the 6DOF loadcell and overtube, respectively.	Oude Vrielink, T. J., Zhao, M., Darzi, A., & Mylonas, G. P. (2018, May). ESD CYCLOPS: A new robotic surgical system for GI surgery. In 2018 IEEE International Conference on Robotics and Automation (ICRA) (pp. 150-157). IEEE.	© 2018 IEEE customercare@copyright.com	-	Yes	IEEE's default permission for usage in thesis/dissertation (see letter)

4.19	Fig. 9. The measured end-effector forces for the straight instrument, shown for movement in the x+ direction from the outer extremity. In this movement, tendons 1,2 and 5 retract, while the others are released. As the end-effector is fixed this motion results in an increase and decrease in tension, respectively.	Oude Vrielink, T. J., Zhao, M., Darzi, A., & Mylonas, G. P. (2018, May). ESD CYCLOPS: A new robotic surgical system for GI surgery. In 2018 IEEE International Conference on Robotics and Automation (ICRA) (pp. 150-157). IEEE.	© 2018 IEEE customercare@copyright.com	-	Yes	IEEE's default permission for usage in thesis/dissertation (see letter)
4.20	Fig. 7. left: The 15x20mm ellipse as seen during the task from the outside and endoscopic view. The pen is placed perpendicular to the paper with the tip placed at the same position as the curved instrument. right: The tracing task performed by the 7 subjects. The bottom right is the same task performed by the da vinci robot, by subject 4.	Oude Vrielink, T. J., Zhao, M., Darzi, A., & Mylonas, G. P. (2018, May). ESD CYCLOPS: A new robotic surgical system for GI surgery. In 2018 IEEE International Conference on Robotics and Automation (ICRA) (pp. 150-157). IEEE.	© 2018 IEEE customercare@copyright.com	-	Yes	IEEE's default permission for usage in thesis/dissertation (see letter)
4.22	Fig. 11. The system is currently undergoing in vivo pre-clinical validation on pigs.	Oude Vrielink, T. J., Zhao, M., Darzi, A., & Mylonas, G. P. (2018, May). ESD CYCLOPS: A new robotic surgical system for GI surgery. In 2018 IEEE International Conference on Robotics and Automation (ICRA) (pp. 150-157). IEEE.	© 2018 IEEE customercare@copyright.com	-	Yes	IEEE's default permission for usage in thesis/dissertation (see letter)

	5.2	Fig. 1. 3-DOF wrist mechanism	Yilmaz, N., Bazman, M., & Tumerdem, U. (2018, October). External Force/Torque Estimation on a Dexterous Parallel Robotic Surgical Instrument Wrist. In 2018 IEEE/RSJ International Conference on Intelligent Robots and Systems (IROS) (pp. 4396-4403). IEEE.	© 2018 IEEE customercare@copyright.com	-	Yes	IEEE default permission for usage in thesis/dissertation (see letter)
	5.3 Left	Fig. 2 The DLR MiroSurge robotic system	Hagn, U., Konietzschke, R., Tobergte, A., Nickl, M., Jörg, S., Kübler, B., ... & Le-Tien, L. (2010). DLR MiroSurge: a versatile system for research in endoscopic telesurgery. International journal of computer assisted radiology and surgery, 5(2), 183-193.	© CARS 2009 customercare@copyright.com	13-01-2019		RightsLink® Licence Number 4507120923763
	5.3 Center	Figure 6 Prototype of instrument tip and layout of the drive cables.	Kübler, B., Seibold, U., & Hirzinger, G. (2005). Development of actuated and sensor integrated forceps for minimally invasive robotic surger. The International Journal of Medical Robotics and Computer Assisted Surgery, 1(3), 96-107.	© 2005 John Wiley & Sons, Ltd. customercare@copyright.com	13-01-2019	Yes	RightsLink® Licence Number 4507121469532
	5.3 right	Figure 4 (a) [..]. (b) Average strain on force/torque sensor for load $F_x = 30$ N.	Kübler, B., Seibold, U., & Hirzinger, G. (2005). Development of actuated and sensor integrated forceps for minimally invasive robotic surger. The International Journal of Medical Robotics and Computer Assisted Surgery, 1(3), 96-107.	© 2005 John Wiley & Sons, Ltd. customercare@copyright.com	13-01-2019	Yes	RightsLink® Licence Number 4507121469532

	A.3.3	Fig. 2. Schematic diagram showing how an endoscopic port can be used to cannulate a deep tumor within the brain (in this case, a left transfrontal trajectory into a subcortical tumor). Left: The initial cannulation with the bullet-shaped dilator. Right: The conduit of the port within the tumor itself following dilator removal.	Kassam, A. B., Engh, J. A., Mintz, A. H., & Prevedello, D. M. (2009). Completely endoscopic resection of intraparenchymal brain tumors. <i>Journal of neurosurgery</i> , 110(1), 116-123.	© AANS	23-04-2019	Yes	See Letter below.
	A.4.1	Fig. 4 The developed instrument retro-fitted on a standard da Vinci instrument base. On the right, the instrument is shown mounted on the da Vinci's slave arm	Miyashita, K., Vrielink, T. O., & Mylonas, G. (2018). A cable-driven parallel manipulator with force sensing capabilities for high-accuracy tissue endomicroscopy. <i>International journal of computer assisted radiology and surgery</i> , 13(5), 659-669.	© The Author(s) 2018	-	Yes	This article is distributed under the terms of the <i>Creative Commons Attribution 4.0 International License</i> (http://creativecommons.org/licenses/by/4.0/)
	A.4.2	Fig.5 The test-setup to evaluate the contact force sensitivity of the system using a linear stage and ground truth load cell	Idem as A.4.1	© The Author(s) 2018	-	Yes	Idem as A.4.1.
	A.4.3	Fig.11 Contact force detection and endomicroscope image	Idem as A.4.1	© The Author(s) 2018	-	yes	Idem as A.4.1



RightsLink®

[Home](#)
[Create Account](#)
[Help](#)


Title: CYCLOPS: A versatile robotic tool for bimanual single-access and natural-orifice endoscopic surgery

Conference Proceedings: 2014 IEEE International Conference on Robotics and Automation (ICRA)

Author: George P. Mylonas

Publisher: IEEE

Date: May 2014

Copyright © 2014, IEEE

LOGIN

If you're a [copyright.com user](#), you can login to RightsLink using your copyright.com credentials.

Already a [RightsLink user](#) or want to [learn more?](#)

Thesis / Dissertation Reuse

The IEEE does not require individuals working on a thesis to obtain a formal reuse license, however, you may print out this statement to be used as a permission grant:

Requirements to be followed when using any portion (e.g., figure, graph, table, or textual material) of an IEEE copyrighted paper in a thesis:

- 1) In the case of textual material (e.g., using short quotes or referring to the work within these papers) users must give full credit to the original source (author, paper, publication) followed by the IEEE copyright line © 2011 IEEE.
- 2) In the case of illustrations or tabular material, we require that the copyright line © [Year of original publication] IEEE appear prominently with each reprinted figure and/or table.
- 3) If a substantial portion of the original paper is to be used, and if you are not the senior author, also obtain the senior author's approval.

Requirements to be followed when using an entire IEEE copyrighted paper in a thesis:

- 1) The following IEEE copyright/ credit notice should be placed prominently in the references: © [year of original publication] IEEE. Reprinted, with permission, from [author names, paper title, IEEE publication title, and month/year of publication]
- 2) Only the accepted version of an IEEE copyrighted paper can be used when posting the paper or your thesis on-line.
- 3) In placing the thesis on the author's university website, please display the following message in a prominent place on the website: In reference to IEEE copyrighted material which is used with permission in this thesis, the IEEE does not endorse any of [university/educational entity's name goes here]'s products or services. Internal or personal use of this material is permitted. If interested in reprinting/republishing IEEE copyrighted material for advertising or promotional purposes or for creating new collective works for resale or redistribution, please go to http://www.ieee.org/publications_standards/publications/rights/rights_link.html to learn how to obtain a License from RightsLink.

If applicable, University Microfilms and/or ProQuest Library, or the Archives of Canada may supply single copies of the dissertation.

[BACK](#)
[CLOSE WINDOW](#)

Copyright © 2019 [Copyright Clearance Center, Inc.](#) All Rights Reserved. [Privacy statement](#). [Terms and Conditions](#).
Comments? We would like to hear from you. E-mail us at customercare@copyright.com

From: [IAAC] Press Barcelona <press@iaac.net>
Sent: vrijdag 25 januari 2019 12:59
To: Oude Vrielink, Joric C
Subject: Re: Use image IAAC

Dear Timo,

Thanks for showing interest in the projects developed at IAAC. Here I share with you a [Google Drive folder](#) we usually send for press requests with the most relevant **Terraperforma** pictures and information. The main protocol we have for pictures citations is the following, the Institute asks that each picture goes accompanied with the following text (caption): **IAAC - Institute for Advanced Architecture of Catalonia**.

We would appreciate if, once the article has been published, you could share it with us for dissemination and save it in our publications archive.

Best regards,

On Wed, Jan 23, 2019 at 9:01 PM Oude Vrielink, Joric C <t.oude-vrielink15@imperial.ac.uk> wrote:

Dear Sir/Madam,

For my PhD thesis I would like to include an image that is part of IAAC property. The PhD thesis will be published on the Imperial College London Spiral repository (<http://spiral.imperial.ac.uk/>), hence I would like to ask permission for use of one of the images.

It is this image, from the Terraperforma project: <https://3dprint.com/wp-content/uploads/2017/04/20.jpg>

I found it in this article which cites IAAC as owner: <https://3dprint.com/169892/iaac-tecnalia-robotic-construction/>

Would it be possible, with the correct credits to IAAC, to use the image in my thesis?

I am looking forward to hear from you,

Best wishes,
Timo Oude Vrielink

Oude Vrielink, Joric C

From: Mittner, Teresa <teresa.mittner@ipa.fraunhofer.de>
Sent: vrijdag 18 januari 2019 7:49
To: Oude Vrielink, Joric C
Cc: Bez, Rainer; Nemitz, Fred
Subject: AW: Permission usage cable-robot pictures PhD thesis
Attachments: Fraunhofer IPA_Cable Robot_03.jpg; Fraunhofer IPA_Cable Simulator_01.jpg; Fraunhofer IPA_Cable Simulator_02.jpg

Dear Mr. Oude Vrielink,

you are welcome to use the attached pictures in your thesis provided there is a reference to the source in the publication and a free copy or pdf of the publication is sent to Fraunhofer IPA in Stuttgart. Please use the source "Fraunhofer IPA, Philipp Miermeister" for picture 01 and 02 and "Fraunhofer IPA" for picture 03. Alterating the images except for highlighting the main motif is not permitted.

Best regards

Teresa

--

Teresa Mittner, M.Sc.
Portfolio Marketing Manager

Fraunhofer Institute for
Manufacturing Engineering and Automation IPA
Department Robot and Assistive Systems

Nobelstrasse 12 | 70569 Stuttgart | Germany
Phone +49 711 970-1108
Fax +49 711 970-1008

teresa.mittner@ipa.fraunhofer.de
www.ipa.fraunhofer.de



Von: "Oude Vrielink, Joric C" <t.oude-vrielink15@imperial.ac.uk>
Datum: 16. Januar 2019 22:08:12 MEZ
An: "fred.nemitz@ipa.fraunhofer.de" <fred.nemitz@ipa.fraunhofer.de>
Betreff: Permission usage cable-robot pictures PhD thesis

Dear Mr Nemitz,

For my PhD thesis on cable robots I am interested in using images from Fraunhofer IPA, thus for non-commercial educational use. The thesis will eventually be published in the [Imperial College Spiral Depository](#).

It is regarding a high resolution image of the cable robots presented here:

- https://www.ipa.fraunhofer.de/en/press/2015-09-09_Cable-driven-parallel-robots.html
- <https://www.eu-nited.net/robotics/press-room/cable-robot-ipanema-extended-version-for-engineers.html>

The images will be used as literature study describing cable-driven parallel robots (CDPR) in general. My thesis is about use cable-driven robots in minimally invasive surgery hence the systems will be specifically used to indicate the versatility and unique features of such CDPRs.

Both sources are press releases, but at least the first one indicates the images are copyrighted, hence me contacting you. I have also contacted the contact persons at Fraunhofer listed in both articles, but the email addresses are void (Philipp Miermeister and Hubert Grosser, respectively).

Could you let me know whether it is possible to use the images for this purpose?

Best wishes,
Joric Oude Vrielink

Oude Vrielink, Joric C

From: Beth Darchi <DarchiB@asme.org>
Sent: donderdag 17 januari 2019 20:52
To: Oude Vrielink, Joric C
Subject: RE: Permissions figure ASME paper

Dear Mr. Oude Vrielink:

It is our pleasure to grant you permission to use the ASME **Figure 1 only** from “Robotic Physical Exercise and System (ROPES): A Cable-Driven Robotic Rehabilitation System for Lower-Extremity Motor Therapy,” by Aliakbar Alamdari and Venkat Krovi, Paper No. DETC2015-46393, cited in your letter for inclusion in a PhD Dissertation entitled Cable-driven parallel mechanisms for minimally invasive surgery to be published by Imperial College London.

As is customary, we request that you ensure full acknowledgment of this material, the author(s), source and ASME as original publisher. Acknowledgment must be retained on all pages printed and distributed.

Many thanks for your interest in ASME publications.

Sincerely,

Beth Darchi
Publishing Administrator
ASME
2 Park Avenue
New York, NY 10016-5990
Tel 1.212.591.7700
darchib@asme.org

From: Oude Vrielink, Joric C [mailto:t.oude-vrielink15@imperial.ac.uk]
Sent: Thursday, January 17, 2019 2:40 PM
To: Beth Darchi <DarchiB@asme.org>
Subject: Re: Permissions figure ASME paper

Apologies, I notices I didn't completely fill in the form. Find attached.

ASME CONFERENCE/JOURNAL/BOOKS PUBLICATIONS PERMISSION REQUEST FORM:

***Please TYPE in all required fields.** Please do not write in.

ASME Publication Title (Conference/Journal/Book)*: ASME

2015 International Design Engineering Technical Conferences
and Computers and Information in Engineering Conference

Complete List of ASME Authors*: Aliakbar Alamdari, Venkat
Krovi

ASME Paper Title (Conference or Journal) *: Robotic Physical Exercise and System (ROPES): A Cable-Driven
Robotic Rehabilitation System for Lower-Extremity Motor Therapy

Conference Paper Number (if conference)*:

DETC2015-46393

(Journal) paper number*: V05AT08A032

Volume Number Volume 5A:

39th Mechanisms and
Robotics Conference

DOI Number:

doi:10.1115/DETC2015-46393

Indicate Page(s) in the ASME publication: 10 pages

Year of Publication*: 2015

List ASME Figure Numbers: Figure 1

List ASME Table Numbers:

Number of Copies:

Usage (Please check box): ☐ Print ☒ Academic ☐ Online ☐ Intranet

Title of outside publication / Thesis*: Cable-driven parallel mechanisms for minimally invasive surgery
(PhD Dissertation)

Outside Publisher or University*: Imperial College London

Explanation of Usage: Part of the literature study of my PhD thesis includes an overview of cable-driven parallel mechanisms. I would like to use the figure as illustration for citing the paper.

First Name*: Timo

Last Name*: Oude
Vrielink

Address Line 1*:

3rd Floor Paterson
Wing, St Marys
Hospital, 20 South
Wharf Road

Address Line 2:

City*: London

State*: Greater London

Zip*: W2

1PF

Phone: Fax:

Email*: t.oude-vrielink15@imperial.ac.uk

Van: Oude Vrielink, Joric C

Verzonden: donderdag 17 januari 2019 19:38:13

Aan: Beth Darchi

Onderwerp: Re: Permissions figure ASME paper

Thank you Beth. Find below the form filled in:

ASME CONFERENCE/JOURNAL/BOOKS PUBLICATIONS PERMISSION REQUEST FORM:

***Please TYPE in all required fields.** Please do not write in.

ASME Publication Title (Conference/Journal/Book)*: ASME

2015 International Design Engineering Technical Conferences
and Computers and Information in Engineering Conference

Complete List of ASME Authors*: Aliakbar Alamdari, Venkat

Krovi

ASME Paper Title (Conference or Journal) *: Robotic Physical Exercise and System (ROPES): A Cable-Driven
Robotic Rehabilitation System for Lower-Extremity Motor Therapy

Conference Paper Number (if conference)*:

DETC2015-46393

(Journal) paper number *: V05AT08A032

Volume Number Volume 5A:

39th Mechanisms and
Robotics Conference

DOI Number:

doi:10.1115/DETC2015-46393

Indicate Page(s) in the ASME publication: 10 pages

Year of Publication*: 2015

List ASME Figure Numbers: Figure 1

List ASME Table Numbers:

Number of Copies:

Usage (Please check box): ☐ Print ☒ Academic ☐ Online ☐ Intranet

Title of outside publication / Thesis*: Cable-driven parallel mechanisms for minimally invasive surgery
(PhD Dissertation)

Outside Publisher or University*: Imperial College London

Explanation of Usage: Part of the literature study of my PhD thesis includes a literature overview of cable-
driven parallel mechanisms. I would like to use the

First Name*: Timo

Last Name*: Oude
Vrielink

Address Line 1*:

3rd Floor Paterson
Wing, St Marys
Hospital, 20 South
Wharf Road

Address Line 2:

City*: London
State*: Greater London
Zip*: W2
1PF
Phone: **Fax:**
Email*:
[t.oude-
vrielink15@
imperial.ac.
uk](mailto:t.oude-vrielink15@imperial.ac.uk)

Van: Beth Darchi <DarchiB@asme.org>
Verzonden: donderdag 17 januari 2019 19:19:38
Aan: Oude Vrielink, Joric C
Onderwerp: RE: Permissions figure ASME paper

In order for us to address permission requests to use ASME material, please be sure to fill out all required fields (*) to complete the form. Please send the form to permissions@asme.org.
Upon receipt of this form, I will be happy to give this matter my immediate attention and consideration, applying royalties if applicable.

ASME CONFERENCE/JOURNAL/BOOKS PUBLICATIONS PERMISSION REQUEST FORM:

*Please **TYPE** in all required fields. Please do not write in.

ASME Publication Title (Conference/Journal/Book)*:

Complete List of ASME Authors*:

ASME Paper Title (Conference or Journal) *:

Conference Paper Number (if conference)*:

(Journal) paper number *:

Volume Number

DOI Number:

Indicate Page(s) in the ASME publication:

Year of Publication*:

List ASME Figure Numbers:

List ASME Table Numbers:

Number of Copies:

Usage (Please check box): ☐ Print ☐ Academic ☐ Online ☐ Intranet

Title of outside publication / Thesis*:

Outside Publisher or University*:

Explanation of Usage:

First Name*:
Last Name*:
Address Line 1*:

Address Line 2:

City*:
State*:
Zip*:
Phone: Fax:
Email*:

Regards,

Beth Darchi
Publishing Administrator
ASME
2 Park Avenue
New York, NY 10016-5990
Tel 1.212.591.7700
darchib@asme.org

From: Oude Vrielink, Joric C [<mailto:t.oude-vrielink15@imperial.ac.uk>]
Sent: Wednesday, January 16, 2019 9:03 PM
To: permissions@asme.org
Subject: Permissions figure ASME paper

Dear Sir/Madam,
For my PhD thesis I am trying to obtain permissions for a figure in an [academic conference paper](#). However, the [usual steps](#) described on your website does not work for this specific paper, as it cannot be found on copyright.com. See hyperlinks in the text above.

I have tried several different search terms (ISB/doi/title) to find the paper, but to no avail.

Could you let me know how to obtain permission for the figure? It is regarding figure 1 of the paper.

Best wishes,
Joric Oude Vrielink

Oude Vrielink, Joric C

From: Beth Darchi <DarchiB@asme.org>
Sent: dinsdag 29 januari 2019 20:05
To: Oude Vrielink, Joric C
Subject: RE: Permission reprint figure

Dear Mr. Oude Vrielink:

It is our pleasure to grant you permission to use the ASME **Figure 2 only** from “Kinematic Design of a Novel Spatial Remote Center-of-Motion Mechanism for Minimally Invasive Surgical Robot,” by Jianmin Li, Yuan Xing, Ke Liang and Shuxin Wang, J. Med. Devices 9(1), 2015, cited in your letter for inclusion in a PhD Dissertation entitled Cable-driven parallel mechanisms for minimally invasive surgery to be published by Imperial College London.

As is customary, we request that you ensure full acknowledgment of this material, the author(s), source and ASME as original publisher. Acknowledgment must be retained on all pages printed and distributed.

Many thanks for your interest in ASME publications.

Sincerely,

Beth Darchi
Publishing Administrator
ASME
2 Park Avenue
New York, NY 10016-5990
Tel 1.212.591.7700
darchib@asme.org

From: Oude Vrielink, Joric C [mailto:t.oude-vrielink15@imperial.ac.uk]
Sent: Wednesday, January 23, 2019 9:16 PM
To: permissions@asme.org
Subject: Permission reprint figure

Dear Sir/Madam,

I would like to get permission to use a figure in a paper published by ASME in my PhD Thesis. I have previously already used the below form for requesting permission for an earlier paper.

Please let me know if any other information is required.

Best wishes,
Timo Oude Vrielink

ASME CONFERENCE/JOURNAL/BOOKS PUBLICATIONS PERMISSION REQUEST FORM:

***Please TYPE in all required fields.** Please do not write in.

ASME Publication Title (Conference/Journal/Book)*: Journa

I of Medical Devices

Complete List of ASME Authors*: Jianmin Li, Yuan Xing, Ke

Liang and Shuxin Wang

ASME Paper Title (Conference or Journal) *: Kinematic Design of a Novel Spatial Remote Center-of-Motion Mechanism for Minimally Invasive Surgical Robot

Conference Paper Number (if conference) *:

(Journal) paper number *: MED-14-1153

Volume Number: Volume 9

DOI Number:

10.1115/1.4028651

Indicate Page(s) in the ASME publication: 8 pages

Year of Publication*: 2015

List ASME Figure Numbers: Figure 2

List ASME Table Numbers:

Number of Copies:

Usage (Please check box): ☐ Print ☒ Academic ☐ Online ☐ Intranet

Title of outside publication / Thesis*: Cable-driven parallel mechanisms for minimally invasive surgery (PhD Dissertation)

Outside Publisher or University*: Imperial College London

Explanation of Usage: Part of the literature study of my PhD thesis includes an overview of cable-driven parallel mechanisms. I would like to use the figure as illustration for citing the paper.

First Name*: Timo

Last Name*: Oude

Vrielink

Address Line 1*:

3rd Floor Paterson

Wing, St Marys

Hospital, 20 South

Wharf Road

Address Line 2:

City*: London

State*: Greater London

Zip*: W2

1PF

Phone: Fax:

Email*: t.oude-vrielink15@imperial.ac.uk

Oude Vrielink, Joric C

From: Susan Wilkins <susan@titanmedicalinc.com>
Sent: vrijdag 18 januari 2019 14:41
To: Oude Vrielink, Joric C
Subject: RE: Permission Image for PhD thesis

Timo,

Please go ahead and use the image.

Susan

From: Oude Vrielink, Joric C <t.oude-vrielink15@imperial.ac.uk>
Sent: January 17, 2019 4:10 PM
To: Susan Wilkins <susan@titanmedicalinc.com>
Subject: Permission Image for PhD thesis

Dear Sir/Madam,

For my PhD thesis on Surgical Robotics I would like to include a image of the SPORT robot in my literature review section. The thesis will be published in the Imperial College London Spiral Repository: <https://spiral.imperial.ac.uk/>.

The name of the thesis is *Cable-driven parallel mechanisms in Minimally Invasive Robotic Surgery*. I am particularly interested in a image of the surgical instruments, such as the one seen [here](#) in the header.

Would it be possible to use this or any other image supplied by you for in the thesis?

Best wishes,
Timo (Joric) Oude Vrielink

Oude Vrielink, Joric C

From: Oude Vrielink, Joric C
Sent: vrijdag 12 april 2019 0:18
To: Samuel Straface
Subject: Re: Permission usage figure PhD Thesis

Dear Samuel,

Thank you for the permission and the updated picture. I agree with all the conditions of use as stated in your email.

Thanks again,

Timo Oude Vrielink

From: Samuel Straface
Sent: Friday, 12 April, 00:10
Subject: FW: Permission usage figure PhD Thesis
To: Oude Vrielink, Joric C
Cc: Michelle Martin

Dear Timo. The image you have requested permission to use is very old, circa 2015, and the robot system in that photo has been superseded. We are willing to approve the use of our product photo (attached) if you agree to the following in your reply email:

Use the current photo only (attached); Represent that authorization to use photos was granted by **Medrobotics Corporation** in your thesis (please do not misspell corporate name by using capitals where they are not represented in this email (e.g., MedRobotics is not acceptable)); Clearly represent the name of the product as **Medrobotics Flex® Robotic System**, with the registered trademark (R) after Flex; The use of the photo and Medrobotics name is strictly for your PhD thesis and associated publications and no other rights are granted or implied by this email.

Please respond by stating that you agree to all the conditions of use.

Thank you and best of luck in the pursuit of your Ph.D.

Sincerely,

SAMUEL STRAFACE, PH. D.

President & CEO
Medrobotics Corporation
475 Paramount Drive,
Raynham, Massachusetts 02767 USA

Email: SStraface@Medrobotics.com
Company: +1-508-692-6460
Direct Telephone: +1-617-818-4466
Facsimile: +1-508-823-1703
www.Medrobotics.com

This message is intended for the addressee only as it contains private and confidential information. The contents are not to be disclosed to anyone other than the addressee. Unauthorized recipients are requested to comply with the above and to inform the sender immediately of any errors in transmission.

Begin forwarded message:

From: "Oude Vrielink, Joric C" <t.oude-vrielink15@imperial.ac.uk>
Subject: Permission usage figure PhD Thesis
Date: April 11, 2019 at 12:59:00 AM MST
To: "kknightpr@gmail.com" <kknightpr@gmail.com>

Dear Kevin,

I am contacting you as I would like to use an image of the Flex Robotic system for my PhD thesis at Imperial College London. The thesis is entitled 'Cable-driven Parallel Mechanisms for Minimally Invasive Robotic Surgery', with specific focus on flexible endoscopic systems. As the Medrobotics Flex Robotic system is at the frontline of developments, it would be very useful for the readers to include a figure. I found a figure in an [earlier publication](#) (Figure 3b, also added below this email). Would it be possible to use this figure for my PhD thesis?

The thesis will be made public on Spiral, Imperial College's institutional repository <http://spiral.imperial.ac.uk/> and therefore I will require permission to reprint the figure. The thesis will be published under a Creative Commons Attribution Non Commercial 4.0 International Licence. The appropriate credits will be given to Medrobotics for use of the figure.

Best wishes,

Timo Oude Vrielink



Oude Vrielink, Joric C

From: Renée Koekkoek op Munsterhuis <renee.koekkoek.op.munsterhuis@demcon.nl>
Sent: donderdag 24 januari 2019 21:50
To: Oude Vrielink, Joric C
Subject: RE: Gebruik afbeelding MIRIAM robot in PhD proefschrift

Dat lijkt me goed.

Grt,
Renée

From: Oude Vrielink, Joric C <t.oude-vrielink15@imperial.ac.uk>
Sent: 24 January 2019 21:42
To: Renée Koekkoek op Munsterhuis <renee.koekkoek.op.munsterhuis@demcon.nl>
Subject: RE: Gebruik afbeelding MIRIAM robot in PhD proefschrift

Heel erg bedankt Renée, dan zal ik de afbeelding gebruiken.

Het leek me het beste om de bronvermelding "DEMCON advanced mechatronics B.V." te gebruiken.
Mocht het toch beter zijn om een andere naam te vermelden, zou je me dat dan kunnen laten weten?

Met vriendelijke groeten,
Timo

From: Renée Koekkoek op Munsterhuis [<mailto:renee.koekkoek.op.munsterhuis@demcon.nl>]
Sent: donderdag 24 januari 2019 16:32
To: Oude Vrielink, Joric C <t.oude-vrielink15@imperial.ac.uk>
Subject: RE: Gebruik afbeelding MIRIAM robot in PhD proefschrift

Beste Timo,

Dank voor je mail. Dat is geen probleem.

Wanneer je meer informatie wenst, hoor ik dat graag.

Met vriendelijke groet,
Renée Koekkoek op Munsterhuis
Public Relations Demcon
06-52631185

From: Oude Vrielink, Joric C <t.oude-vrielink15@imperial.ac.uk>
Sent: woensdag 23 januari 2019 19:39
To: Demcon Managementsupport <Managementsupport@demcon.nl>
Subject: Gebruik afbeelding MIRIAM robot in PhD proefschrift

Beste Heer/Mevrouw,
Voor mijn literatuurstudie van mijn promotieonderzoek ben zou ik graag een afbeelding van het MIRIAM system willen gebruiken. Het liefst deze: <https://www.demcon.nl/wp-content/uploads/2016/04/definitief3507en3608-uitgesneden-620x350.jpg>

Het proefschrift zal gepubliceerd worden op de online [repository](#) van de universiteit Imperial College London. Het proefschrift heet "Cable-driven parallel mechanisms for Minimally Invasive Surgical Robotics".

Graag hoor ik of dit mogelijk is.

Met vriendelijke groeten,
Timo Oude Vrielink

Oude Vrielink, Joric C

From: Merilee Croft <mcraft@medreviews.com>
Sent: donderdag 11 april 2019 15:34
To: Oude Vrielink, Joric C
Subject: RE: Reprint permissions figure PhD Thesis

Hi, Timo,

Permission to reproduce the image in your PhD thesis is granted gratis. Please run a credit line as follows:

Reprinted with permission of MedReviews®, LLC. Mozer PC, Partin AW, Stoianovici D. Robotic image-guided needle interventions of the prostate. *Rev Urol.* 2009;11(1):7-15. All rights reserved.

Please don't hesitate to contact me if you have any questions,

Best,
Meri

Merilee Croft
Director, Editorial Production
MedReviews, LLC
2585 Broadway, Suite 221
New York, NY 10025

mcraft@medreviews.com
917-781-7535

From: Oude Vrielink, Joric C <t.oude-vrielink15@imperial.ac.uk>
Sent: Thursday, April 11, 2019 5:05 AM
To: Merilee Croft <mcraft@medreviews.com>
Subject: Reprint permissions figure PhD Thesis

Dear Merilee,

I am contacting you for reprint permissions for a figure use in my PhD thesis. The thesis will be made publically available on Spiral, Imperial College 's institutional repository <http://spiral.imperial.ac.uk/> and therefore I will require permission to reprint the figure. The thesis will be published under a Creative Commons Attribution Non Commercial 4.0 International Licence.

The thesis is entitled 'Cable-Driven Parallel Mechanisms for Minimally Invasive Robotic Surgery'. The details of the figure are found in the following publication:

Journal: Reviews in Urology
Paper title: Robotic Image-Guided Needle Interventions of the Prostate
Authors: Pierre C Mozer, Alan W Partin and Dan Stoianovici
Year of Publication: 2009
Volume: 11 (1)

Regarding **Figure 1 (right)**

Please let me know whether I have the permission to reprint the figure.

Best wishes,

Timo Oude Vrielink

Oude Vrielink, Joric C

From: Deanne Eagle <deanneeagle@gmail.com>
Sent: zaterdag 26 januari 2019 1:47
To: Oude Vrielink, Joric C
Subject: Re: DiLumen C2

Dear Timo,

You have permission to use the image! Please credit it to: " Lumendi Ltd."

Also, could you send me a link when it is published? We all want to see it!

Wishing you the best of luck; please let me know if there's anything else I can help with.

Best, Deanne

Deanne Eagle
(917) 837-5866

From: t.oude-vrielink15@imperial.ac.uk
Sent: January 25, 2019 9:41 AM
To: deanneeagle@gmail.com
Subject: RE: DiLumen C2

Hi Deanne,

Great, thank you.

Best,
Timo

From: Deanne Eagle [mailto:deanneeagle@gmail.com]
Sent: vrijdag 25 januari 2019 12:38
To: Oude Vrielink, Joric C <t.oude-vrielink15@imperial.ac.uk>
Subject: Re: DiLumen C2

Hi Timo,

I'll get this to the company and get back to you. I don't think there will be a problem; they just want to see it.

But I'll keep you informed.

Best, Deanne

Deanne Eagle
[\(917\) 837-5866](tel:(917)837-5866)

From: t.oude-vrielink15@imperial.ac.uk

Sent: January 25, 2019 9:31 AM

To: deanneeagle@gmail.com

Subject: RE: DiLumen C2

Hi Deanne,

Of course, I am still writing the chapter and can supply it once I have a final version. In the meanwhile, to provide a context I have placed the page with a (preliminary) image of the DiLumen C2 system, see below. The image will be directly removed if no permission is granted.

The DiLumen C2 is mentioned as it combines two important aspects – a stable endoscope and a stable tissue surface – with bimanual control. The combination is essential for ESD, and in light with the many systems developed over the last few years it seems that the DiLumen C2 is the only which combines these aspects.

My own work is focused on the development of cable-driven parallel mechanisms for minimally invasive robotic surgery. One chapter is about ESD and the development of an academic system for performing the procedure, called the ESD CYCLOPS.

If it is already clear that Lumendi does not want the image to be included, please let me know so I can already include this in future version.

Also let me know if you have any specific questions or comments.

Best wishes,
Timo

for tissue retraction. The balloon offers stability to the colonoscope, but can also be used to straighten colonic folds for improved visualisation of the tissue surface. This is important for the detection of polyps, which can be missed when hidden behind tissue, and is yet another important reason leading to the introduction of new add-on devices such as EndoCuff Vision® (Olympus Corp.). Instead of a balloon, the EndoCuff uses flexible 'arms' to straighten colonic folds and provide endoscope stabilization.

The DiLumen™ EIP oversheath (Lumendi Ltd) is a recent development that uses a double balloon technique specifically for therapeutic interventions. The first balloon is integrated into the oversheath and affixed just before the steerable section of the endoscope's tip, and is used for endoscope stabilization. The second balloon is located at the tip of the endoscope and can be extended forwards along two rails. By inflating both balloons, the DiLumen EIP device creates a working area around the lesion (the so-called 'therapeutic zone') which can be used to inflate and stretch the colonic folds. Additionally, the distal balloon can be equipped with clips to provide mucosal traction by extending the balloon further along the guides. In 2018, this system with clips was compared to conventional cap-assisted ESD in *ex vivo* animal trials and one *in vivo* animal trial, demonstrating a significant decrease in operating time [ref dilum-1]. A similar result was found when performing the ESD in *ex vivo* tissue when the therapeutic zone was filled with water [ref dilum-2]. The system has been FDA-approved and CE-marked (2018), and a bimanual version of the system is being developed for ESD (DiLumen C2™).



Figure 4.3 – The DiLumen C2™ system for ESD. Image credit: Lumendi Ltd. ASKING FOR PERMISSION.

The combination of endoscope stabilisation and tissue counter-traction, as seen in the DiLumen system, are important to reduce the complexity of ESD procedures. Another important aspect is the dexterity of the surgical instruments. This current chapter discusses

From: Deanne Eagle [mailto:deanneeagle@gmail.com]
Sent: vrijdag 25 januari 2019 11:57
To: Oude Vrielink, Joric C <t.oude-vrielink15@imperial.ac.uk>
Subject: RE: DiLumen C2

Dear Timo,

The company is wondering if it would be possible to see a draft of the dissertation before agreeing to supply the image. I know these things have to be carefully kept in confidence until publication, but is there any chance we could see even an early draft—under confidentiality, of course?

Best, Deanne



Deanne Eagle
Planet Communications. LLC
[917-837-5866](tel:917-837-5866) cellular

www.planetcommunications.nyc

From: Oude Vrielink, Joric C [mailto:t.oude-vrielink15@imperial.ac.uk]
Sent: Thursday, January 24, 2019 9:47 AM
To: deanneeagle@gmail.com
Subject: DiLumen C2

Dear Deanne,

For my PhD dissertation I would like to include a picture of the DiLumen C2 system. Would it be possible to get permission for the use of an image from Lumendi and if yes, get a high resolution image from the system? The thesis will be published in the Imperial College London Spiral repository: <https://spiral.imperial.ac.uk>.

The image will be supplied with credits to Lumendi Ltd (please let me know if specific crediting is required).

Best wishes,
Timo Oude Vrielink

Oude Vrielink, Joric C

From: permissions <permissions@thejns.org>
Sent: vrijdag 26 april 2019 14:59
To: Oude Vrielink, Joric C
Subject: Re: Permissions

Non-exclusive permission is granted at no charge for the use you describe, provided proper credit is given as determined by style guidelines of the publisher of the new work, or by some accepted style such as AP or Chicago. Please save this communication as proof of permission grant.

Best of luck to you!

Gillian

From: Oude Vrielink, Joric C <t.oude-vrielink15@imperial.ac.uk>
Sent: Thursday, April 25, 2019 5:07:08 PM
To: permissions
Subject: RE: Permissions

Dear Gillian,
It would be about Figure 2, on page 118 of the paper.

Best wishes,
Timo

From: permissions [mailto:permissions@thejns.org]
Sent: donderdag 25 april 2019 15:47
To: Oude Vrielink, Joric C <t.oude-vrielink15@imperial.ac.uk>
Subject: Fw: Permissions

Dear Timo,

Can you please let me know which figure from our paper you wish to reuse?

thank you,

Gillian

From: jnsonline@thejns.org <jnsonline@thejns.org>
Sent: Tuesday, April 23, 2019 4:57 PM
To: permissions
Subject: Permissions

A user submitted the Permissions form with the following values:

Address1: 3rd Floor, Paterson Wing, 20 South Wharf Road
Address2:
Article Title: Completely endoscopic resection of intraparenchymal brain tumors

Authors: Amin B. Kassam, Johnathan A. Engh, Arlan H. Mintz and Daniel M. Prevedello
City: London
Country Code: -1
Custom Form Id: Permissions
Email: t.oude-vrielink15@imperial.ac.uk
Fax:
First Name: Timo
Institution: Imperial College London
Issue: 1
Language: English (as originally published)
Last Name: Oude Vrielink
Media: Not listed/other
Media Type: Electronic
Middle Name:
My Title: PhD Candidate
Other Company:
Page Range: 116–123
Permission Note: Usage for PhD Thesis (published at University repository: <http://spiral.imperial.ac.uk/>)
Phone: +447492906800
Pub Month: Jan
Pub Year: 2009
Publication: Journal of Neurosurgery
Publisher: Imperial College
Quantity: 1
Ref Number:
Repub Date: July 2019
Spec:
State: Greater London
Title: Mr.
Title Edition: Cable-driven parallel mechanisms for minimally invasive surgical robotics
Translation:
Volume: 110
Website:
Zip Code: W1 2PF
Thank you.

Oude Vrielink, Joric C

From: Oude Vrielink, Joric C
Sent: woensdag 10 april 2019 10:45
To: permissionrequest@tandf.co.uk
Subject: Copyright usage figures

Dear Sir/Madam,

In my PhD dissertation several of images are being used that have copyright held by Taylor and Francis. In general I understand it should not be a problem to use the images as Rightslink gives the following message regarding the material:

"Taylor & Francis is pleased to offer reuses of its content for a thesis or dissertation free of charge contingent on resubmission of permission request if work is published."

The PhD thesis, however, will be 'published' on the Imperial College London [Spiral Repository](#). Does this require a other licence from T&F?

Best wishes,
Timo Oude Vrielink

From: Oude Vrielink, Joric C
Sent: donderdag 16 mei 2019 12:29
To: permissionrequest@tandf.co.uk
Subject: Copyright permission usage in PhD dissertation

Dear Sir/Madam,

I have completed my PhD thesis at Imperial College London entitled 'Cable-driven parallel mechanisms for minimally invasive robotic surgery'.

I seek your permission to reprint, in my thesis an extract from:

Can, S., Fiolka, A., Mayer, H., Knoll, A., Schneider, A., Wilhelm, D., ... & Feussner, H. (2008). The mechatronic support system "HVSPS" and the way to NOTES. Minimally invasive therapy & allied technologies, 17(6), 341-345.

The extract to be reproduced is:

Figure 4, Page 344

I would like to include the extract in my thesis which will be added to Spiral, Imperial's institutional repository <http://spiral.imperial.ac.uk/> and made available to the public under ***Creative Commons AttributionNon Commercial 4.0 International Licence (CC BY-NC)***.

If you are happy to grant me all the permissions requested, please return a signed copy of this letter. If you wish to grant only some of the permissions requested, please list these and then sign.

Yours sincerely,

Timo Oude Vrielink

From: Oude Vrielink, Joric C
Sent: donderdag 16 mei 2019 12:27
To: permissionrequest@tandf.co.uk
Subject: Copyright permission usage in PhD dissertation

Dear Sir/Madam,

I have completed my PhD thesis at Imperial College London entitled 'Cable-driven parallel mechanisms for minimally invasive robotic surgery'.

I seek your permission to reprint, in my thesis an extract from:

Dallemagne, B., & Marescaux, J. (2010). The ANUBIS™ project. Minimally Invasive Therapy & Allied Technologies, 19(5), 257-261.

The extract to be reproduced is:

Figure 4, Page 259

I would like to include the extract in my thesis which will be added to Spiral, Imperial's institutional repository <http://spiral.imperial.ac.uk/> and made available to the public under ***Creative Commons AttributionNon Commercial 4.0 International Licence (CC BY-NC)***.

If you are happy to grant me all the permissions requested, please return a signed copy of this letter. If you wish to grant only some of the permissions requested, please list these and then sign.

Yours sincerely,

Timo Oude Vrielink

From: Oude Vrielink, Joric C
Sent: donderdag 16 mei 2019 12:30
To: permissionrequest@tandf.co.uk
Subject: Copyright permission usage in PhD dissertation

Dear Sir/Madam,

I have completed my PhD thesis at Imperial College London entitled 'Cable-driven parallel mechanisms for minimally invasive robotic surgery'.

I seek your permission to reprint, in my thesis an extract from:

Bardaro, S. J., & Swanström, L. (2006). Development of advanced endoscopes for natural orifice transluminal endoscopic surgery. *Minimally Invasive Therapy & Allied Technologies*, 15(6), 378-383.

The extract to be reproduced is:

Figure 7, Page 382

I would like to include the extract in my thesis which will be added to Spiral, Imperial's institutional repository <http://spiral.imperial.ac.uk/> and made available to the public under ***Creative Commons AttributionNon Commercial 4.0 International Licence (CC BY-NC)***.

If you are happy to grant me all the permissions requested, please return a signed copy of this letter. If you wish to grant only some of the permissions requested, please list these and then sign.

Yours sincerely,

Timo Oude Vrielink

From: Oude Vrielink, Joric C
Sent: donderdag 16 mei 2019 12:31
To: 'permissionrequest@tandf.co.uk'
Subject: Copyright permission usage in PhD dissertation

Dear Sir/Madam,

I have completed my PhD thesis at Imperial College London entitled 'Cable-driven parallel mechanisms for minimally invasive robotic surgery'.

I seek your permission to reprint, in my thesis an extract from:

Chen, P. J., Huang, W. C., Wang, H. P., Chang, W. K., Hsieh, T. Y., Shih, S. C., ... & Liu, C. Y. (2012). Percutaneous transgastric traction-assisted esophageal endoscopic submucosal dissection: a randomized controlled trial in a porcine model. *Scandinavian journal of gastroenterology*, 47(11), 1386-1393.

The extract to be reproduced is:

Figure 1, Page 1388

I would like to include the extract in my thesis which will be added to Spiral, Imperial's institutional repository <http://spiral.imperial.ac.uk/> and made available to the public under ***Creative Commons AttributionNon Commercial 4.0 International Licence (CC BY-NC)***.

If you are happy to grant me all the permissions requested, please return a signed copy of this letter. If you wish to grant only some of the permissions requested, please list these and then sign.

Yours sincerely,

Timo Oude Vrielink